Master's thesis

NTNU
Norwegian University of Science and Technology
Faculty of Natural Sciences
Department of Chemical Engineering

Hauna Fathmadinda Hosen

Combined Effect of Surfactant Presence and Gas Dissolution on Coalescence in Chemical- and Bioreactors

Master's thesis in Chemical Engineering
Supervisor: Professor Hugo Atle Jakobsen
Co-supervisor: Suat Canberk Ozan
June 2021

NTNU
Norwegian University of
Science and Technology

Hauna Fathmadinda Hosen

Combined Effect of Surfactant Presence and Gas Dissolution on Coalescence in Chemical- and Bioreactors

Master's thesis in Chemical Engineering
Supervisor: Professor Hugo Atle Jakobsen
Co-supervisor: Suat Canberk Ozan
June 2021

Norwegian University of Science and Technology
Faculty of Natural Sciences
Department of Chemical Engineering

NTNU
Norwegian University of
Science and Technology

Combined Effect of Surfactant Presence and Gas Dissolution on Coalescence in Chemical- and Bioreactors

Abstract

In this work, coalescence of gas bubbles is investigated in the presence of gas dissolution and surfactants through a film drainage model. The study on dissolution is carried out for three cases considering low Pe, constant mass flux, and variable mass flux applying for all ranges of Pe. It is seen through the low Pe case that any involved reactions in the system have no noticeable impact on coalescence. The last two cases indicate that gas dissolution delays the coalescence time under specific conditions. While the extent of the dissolution effect for the constant mass flux case depends on the contact time of the two bubbles, the one for the variable mass flux case considers the important impact of the film saturation in addition to the gas solubility and Pe. The effect of dissolution seems to be dependent of the tangential mobility which is strongly influenced by the presence of surfactants. The study is summarized in a map which exhibits the conditions for negligible effect of surfactants and the complete immobilization, depending on the extent of the surface tension changes with the total amount of the surfactants present in the system and how unevenly the surfactants are distributed along the interface. It is found that some realistic cases require other immobilization mechanisms in addition to the Marangoni stresses to reach complete immobilization.

Preface

This thesis is written to partly fulfill the requirement for the degree of the Master of Science (MSc) in the Department of Chemical Engineering – Norwegian University of Science and Technology (NTNU). The research presented here has been started since the Autumn semester of 2020 through the Specialization Project within the Environmental Engineering and Reactor Technology Research Group.

I would like to express my gratitude to Professor Hugo Atle Jakobsen for his invaluable encouragement and guidance during my two years here. I would also like to thank Suat Canberk Ozan for introducing this field to me and for all of his endless supports and meaningful feedback in supervising me for the last three semesters. My special thanks also go to Maria Fanebust who shares the same interest, personalities, mindset, enthusiasm, and dreams as me during the up-and-down moments.

I hope this thesis can be a good insight for all readers who share the same interest within the field.

Trondheim, June 2021
Hauna Fathmadinda Hosen

Contents

List of Figures

List of Tables

Nomenclature

$\mathbf{e}$	Unit base vectors of the space coordinate system
$\mathbf{g}$	Gravity forces vector
$\mathbf{j}$	Diffusive mass flux vector
$\mathbf{N}$	Total mass flux vector
$\mathbf{n}$	Unit normal vector
$\mathbf{r}$	Position vector
$\mathbf{t}$	Unit tangent vector
$\mathbf{u}$	Interfacial velocity vector
$\mathbf{v}$	Velocity vector
I	Identity tensor
I_s	Surface identity tensor
P	Pressure tensor
T	Total stress tensor
T_I	Interfacial stress tensor
A	Hamaker constant
A^*	Dimensionless Hamaker constant
D	Molecular diffusivity
H	Mean curvature
h	Film thickness
$\bar{h}$	Characteristic length of film thickness
h_{00}	Initial minimum thickness of the film
K'	Bubble solubility
k_H	Henry's law constant
k_0	Zero-order reaction rate constant
k_1	First-order reaction rate constant
M	Interface displacement rate due to mass transfer
N	Mass flux
P	Excess pressure in the film
$\bar{P}$	Characteristic pressure scale
Pe	Bulk Péclet number
Pe_s	Surface Péclet number

Q	Dimensionless reaction rate
R_1, R_2	Bubble radii
R_p	Equivalent bubble radius
r_A	Reaction rate of substance A
r	Radial coordinate
$\bar{r}$	Characteristic length of film radius
r_d	Deformed radius of the interface
r_∞	A large radial distance
t	Time
$\bar{t}$	Characteristic time scale
t_c	Coalescence time
$t_{drainage}$	Drainage time
$t_{contact}$	Contact time
U_n	Normal velocity of the interface
U_t	Tangential velocity of the interface
V_1, V_2	Approach velocities of the bubbles
V_{app}	Relative approach velocity of the bubbles
v	Bulk velocity
$\bar{v}$	Characteristic velocity scale
z	Axial coordinate
λ_c	Coalescence time efficiency
δ	Kronecker's delta
ϵ	A small parameter
τ	Deviatoric stress tensor
μ	Viscosity
Π	Disjoining pressure
ρ	Density
σ	Surface tension
ω	Mass fraction
Γ	Surface excess concentration
∇	Vector differential operator
∇_s	Surface gradient operator

D_r Differentiation matrix for r coordinate

D_z Differentiation matrix for z coordinate

N_r Number of grids for r coordinate

N_z Number of grids for z coordinate

Δt Time step

1 Introduction

Multiphase reactors have been commonly used in many industrial processes, such as hydrogenation, oxidation, and bioreactions. These reactors usually involve gas, liquid, and solid components which interact with each other, resulting in complex hydrodynamic behaviors that may influence the effectiveness of the processes. Such systems can be visualized in Figure 1, where gas bubbles are dispersed in a bubble column reactor filled with a liquid continuous phase together with solid presence. The gas bubbles may serve either as nutrients for bioreactors or reactants for chemical reactors, which are distributed with various sizes and velocities. These bubbles interact through collisions which may lead to coalescence and affect the bubble distribution along the reactor. During this interaction, the bubbles dissolve into the surrounding liquid medium due to concentration difference. This mechanism potentially changes the local jump conditions across the bubble interfaces which affects the bubble coalescence. The complexity of these systems arises with the existence of solid phases, e.g., cells in bioreactors and impurities in chemical reactors. As solid phases may act like surfactants, they tend to attach along the bubble interfaces and change the interfacial properties, such as the surface tension. This may cause the bubble interfaces to become immobilized, which eventually affects the coalescence behavior. As coalescence is one of key mechanisms affecting the distribution of bubbles along a reactor, it is important to study the effects of the gas dissolution and the surfactant presence on bubble coalescence.

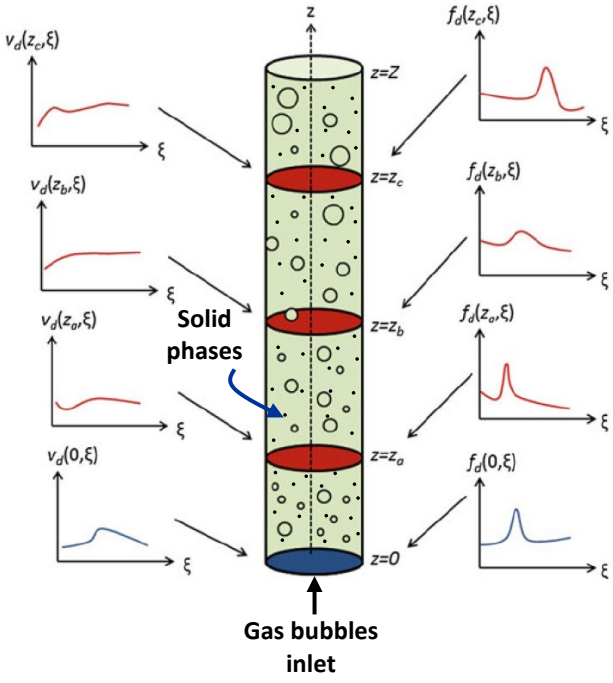

Figure 1: Evolution of gas bubbles in a multiphase reactor (adapted from Jakobsen, 2008)

1.1 Studies on Coalescence of Fluid Particles

Coalescence behavior was studied for the first time by Shinnar and Church (1960) and Shinnar (1961) through a film drainage approach. In their experimental setup, they found that coalescence occurs within several consecutive mechanisms: a collision between two fluid particles entraps the continuous phase as a thin film between the particles, the film drains out due to pressure buildup during the bubbles approach, and the distance between the particles reaches a critical thickness at which the attractive intermolecular forces start to become significant and destabilize the interface, leading to a film rupture and resulting in coalescence. This mechanism implies that coalescence is delayed by the drainage of the film, which seemed to be inconsistent with the rapid coalescence proposed by Howarth (1964). Instead of the delayed coalescence, he found that coalescence occurs rapidly when the approaching bubble velocities are higher than a critical value. Liao and Lucas (2010) clarified this issue by discussing that the two findings correspond to different approaches of estimating coalescence behavior based on the film drainage and the energy models, respectively. In comparison to the critical velocity found by Howarth (1964), Lehr et al. (2002) discovered another critical approach velocity above which the fluid particles bounce off instead of coalescing. This analysis seemed to agree with Kirkpatrick and Lockett (1974) and Chesters and Hofman (1982) who formulated the critical velocity theoretically based on the film drainage approach and the energy model, respectively. These discrepant arguments were identified to be valid under different velocity spectrums according to Yaminsky et al. (2010) and Horn et al. (2011). In Yaminsky et al. (2010)'s study, they observed three different behaviors of air bubble collisions in water, which were distinguishable based on two approach velocities: 1 μm/s and 150 μm/s. The first one corresponded to a critical speed under which the film tended to stay stable and after which the coalescence occurred. When the velocities were between 1 μm/s and 150 μm/s, the delayed coalescence was found with apparent dimple. As for the velocities higher than 150 μm/s, the dimple was no longer visible and the coalescence tended to occur rapidly. Horn et al. (2011) completed the analysis with the fourth behavior indicated as bounce which appeared at even higher velocities. They summarized the four regimes based on Chesters and Hofman (1982); Klaseboer et al. (2000); Yaminsky et al. (2010); and Del Castillo et al. (2011). The four behaviors were theoretically studied by Ozan et al. (2021) through their film drainage model which was coupled with a force balance. In their investigation, the steady-state, the coalescence, and the rebound are possible to appear depending on the collision kinetic energy. The film tends to stay stable when the collision energy is low enough to dissipate rapidly. Then,

coalescence occurs within intermediate collision energies and rebound show up at even larger energies which enable the stored film force to blow up, resulting in the kinetic energy acting reversely to the approach of the particles. They also came up with a formula to determine the critical velocity at which the rebound starts to occur, which is in accordance with the experimental results of Duineveld, (1997); Lehr et al., (2002); Ribeiro and Mewes, (2007).

In macro scale, the coalescence behavior is analyzed by estimating the coalescence efficiency which depends on the drainage time compared to the contact time. When the drainage time is longer than the contact time, the two colliding fluid particles are estimated to coalesce. Based on the film drainage approach, Coulaloglou (1975) suggested a formula to estimate the coalescence efficiency of a gentle collision as

$$\lambda_c = exp\left(-\frac{t_{drainage}}{t_{contact}}\right) \quad (1)$$

The importance of estimating the drainage time leads to multiple types of modelling which can be grouped based on its deformability and its tangential mobility as suggested by Chesters (1991); Lee and Hodgson (1968); and Liao and Lucas (2010). Based on the deformability criterion, the modelling of deformable interfaces is more preferable as they are able to exhibit dimples which were observed in experimental studies (Klaseboer et al., 2000; Yaminsky et al., 2010), whereas the non-deformable interface modelling is inadequate for this purpose. Further investigations were done by Chan et al. (2011) who revealed other possible shapes of deformed interfaces with the emergence of an additional rim, a local maximum, and multiple maxima and minima at the interface, called as the pimple, wimple, and ripple, respectively. The deformable models can be sub-categorized into immobile, partially mobile, and fully mobile, depending on the mechanisms controlling the drainage (Chesters, 1991; Lee and Hodgson, 1968; Liao and Lucas, 2010). The immobile interfaces are indicated by zero tangential velocity due to dominating pressure gradients, which give the parabolic flow to the system. When the tangential velocity appears, the interfaces become partially mobile with an additional flow from the plug component. When this component overpower the pressure gradients, the parabolic flow dissipates and the interfaces become fully mobile. Chesters (1991) distinguished the fully and partially mobile interfaces from their zero and non-zero tangential stresses, respectively. Although this definition was commonly used, Bazhlekov et al. (2000) introduced different levels of interfacial mobility through their model based on the extent of the viscous forces by varying the ratio of the dispersed phase to the continuous phase viscosities.

Regardless of the tangential mobility of the interfaces, Yiantsios and Davis (1991) revealed that it is impossible to model coalescence without the inclusion of attractive van der Waals forces. They also established two rupturing phenomena in their study. One arises with strong van der Waals forces, which result in film rupture occurring at the centerline, called nose rupture. The other one, identified as rim rupture, appears with weak van der Waals forces which allow the capillary forces to act during the film drainage and promote the emergence of dimple at which the rupture takes place. Further studies were examined by Abid and Chesters (1994) and Saboni et al. (1995) who considered the van der Waals interactions through the Hamaker constant to analyze its effect on the coalescence for constant approach velocity and constant van der Waals forces, respectively. Klaseboer et al. (2000) investigated similar works for immobile and fully mobile interfaces considering constant approach velocity. Although their immobile model fits the experimental results, their solution for the fully mobile interface seems to be inconsistent with the experiment, which was analyzed to have immobilized interfaces due to contamination to impurities in the system. To complete the model, Ozan and Jakobsen (2019a) merged the works of Klaseboer et al. (2000) with the one done by Bazhlekov et al. (2000) to investigate the effects of the van der Waals forces and different degrees of mobility for constant approach velocity. They introduced three velocity regimes corresponding to the nose rupture, the rim rupture with dimple and with multiple rims. In their study, the nose rupture occurs within low velocities where the coalescence time decreases with the approach velocity. At sufficiently higher velocities, the regime shifts into rim rupture with the emergence of dimple which slows down the drainage process, indicated by the less significant decreasing trend of the coalescence time. The third regime was found out when the coalescence time starts to increase with the approach velocity with multiple rims emerging along the interfaces. In their first two regimes, the relation between the coalescence time and the approach velocity seem to match the power law formula suggested by Del Castillo et al. (2011) and Orvalho et al. (2015) through their experiments.

1.2 Studies on Coalescence with Surfactant Presence

Surfactants are frequently found as impurities in typical chemical reactors. Even in bioreactors which require a hygienic system, the cells involved in these reactors may also act as surfactants. These surfactants are able to attach and spread unevenly along the bubble interface, which creates the surface tension gradient, induces Marangoni flows, and eventually influences the coalescence behavior. The effect of surfactants on coalescence was theoretically studied by Alexandrova (2014) and Alexandrova et al. (2018). Alexandrova (2014) considered the

presence of insoluble surfactants by including a surfactant balance across the interface and investigated their effects on the film drainage for a constant force. Her study showed that the drainage rate decreases with higher surface Péclet number and their model with very high surface Péclet number resulted in no rims. Alexandrova et al. (2018) extended the study by also investigating the effects of the initial surfactant concentration with different Hamaker constant to determine the conditions at which the effects of the Marangoni and the van der Waals forces are more influential. They found two critical limits of initial surfactant concentration. Below the low limit, the van der Waals forces always become dominant while above the high limit, the Marangoni forces start to dominate the film drainage and hinder coalescence. Lu et al. (2018) investigated the surfactant transport mechanisms and their effect on micro-bubble coalescence. They came up with two mechanisms of surfactant transport, governed by the Marangoni flows and the local contraction of the meniscus bridge connecting the interfaces. The two phenomena strongly affect the drainage rate by influencing the local pull of the surface tension along the bubble interface. While the small-sized bubble tends to keep the surfactants accumulated within the curved area due to its strong local contraction, the Marangoni flows appears to pull the fluid away from the joining meniscus, resulting in the migration of the surfactants towards the back of the bubbles. Ozan and Jakobsen (2019b) studied the film drainage of viscous interfaces with constant approach velocity in the presence of low surfactant concentrations to investigate the effects of the Marangoni stresses and the surface viscosities on the immobilization of the interface. In their conclusion, they proposed regime maps showing different conditions of the surface Péclet number and the Boussinesq number under which the Marangoni flows and the surface viscosities predominate the drainage behavior. In addition to the viscous component of the surface rheology, Ozan and Jakobsen (2020a) extended their model by considering the viscoelasticity of the interface which is assumed equivalent to the Upper Convected Maxwell model. They found that the elastic forces appearing on the interface delay the viscous response of the interface which causes the drainage behavior to initially follow the inviscid interface. The drainage begins to deviate from the inviscid interface behavior and approach to the Newtonian one after some time, depending on the surface Weissenberg number and the Boussinesq number. This delay results in the shifting tangential mobility which may cause the coalescence time to differ from both inviscid and Newtonian interfaces, implying that the viscoelasticity of the interface plays an important role on the coalescence time.

1.3 Studies on Coalescence with Mass Transfer

There are several types of mass transfer studied in the coalescence of fluid particles. One refers to the migration of solutes in oil-liquid systems which have been studied experimentally and theoretically by Ban et al. (2000); Chevaillier et al. (2006); Gourdon and Casamatta (1991); Kamp and Kraume (2014); Kourio et al. (1989), Kourio et al. (1994); Saboni (2002); and Saboni et al. (1999). All studies agree to the same conclusion that the solute transfer have two different effects, either stimulating or hindering coalescence, depending on the direction of the solute transfer, the surface-activity, and the dominating properties. The former effect appears when the solute transfers from the dispersed to the continuous phase while the latter one is caused by the Marangoni stresses emerging due to the contrary direction of the solute transfer (Gourdon and Casamatta, 1991 ; Kourio et al., 1994). The transfer direction was found to be not the only factor affecting the coalescence behavior as Saboni (2002) revealed that the solute transferring from the dispersed to the continuous phase may also decrease the coalescence tendency when the surface-activity is taken into account. Further works were done by Ban et al. (2000) and Chevaillier et al. (2006) who found that the solute transferring from the continuous to the dispersed phase can slow down the drainage rate by stimulating the tangential velocity to the opposite direction of the film drainage. They also clarified that the effect of solute transfer from the continuous to the dispersed phase is strongly affected by the approach velocity while the opposite direction depends more on the concentration gradient of the solute.

Another type of the mass transfer phenomenon corresponds to the dissolution of gas bubbles in a liquid phase which were studied with various methods. Katsir and Marmur (2014) examined the impact of CO_2 dissolution on the coalescence time for a system with purified water. They analyzed that the dissolved CO_2 tends to dissociate in water, which then induces surface charges and promotes electric double layer repulsion, resulting in longer coalescence time. Farajzadeh et al. (2014) investigated the effect of gas solubility on foam drainage for pure gases and mixed gases. In their experimental setup, they measured the decreasing volume of the foam due to coalescence with time. They concluded that the foam drainage rate increases considerably with the gas solubility. Furthermore, the foams with two components of gases were found to have a drainage rate between the ones for the two individual components. Li et al. (2019) studied theoretically and experimentally the behavior of a single rising CO_2 bubble for different sizes and found that the mass flux becomes lower with larger bubbles. In addition, they observed the behavior of two bubbles rising side-by-side to determine their critical interval, defined as the furthest initial distance between the bubbles which allows coalescence.

Compared to their setups without mass transfer, the ones with the mass transfer have lower critical interval which indicates that the mass transfer may decrease the coalescence tendency with various extents, depending on the mass transfer efficiency. They came up with a conclusion that the mass transfer phenomena have considerable impacts on bubble behaviors.

1.4 Project Objective

This study aims to investigate the combined effect of gas dissolution and surfactant presence on bubble coalescence through a film drainage model. The effect of gas dissolution is taken into account by coupling the model with a component mass balance. This model is initially examined in the absence of surfactants for three cases: low Pe where the convective mass transfer is negligible, constant mass flux, and variable mass flux which is applicable to the entire range of Pe values. While first two cases are carried under constant fluxes, the third case is investigated by varying Pe and the gas solubility. Then, the effect of surfactants is included by adding a surfactant balance to the model. In this case, the extent of Marangoni flows emerging due to surfactants is evaluated through the surface Péclet number (Pe_s), the initial concentration of surfactants (Γ_0), and the effectivity of surfactants in changing the surface tension (σ_Γ').

2 Physical System and Mathematical Model

This study considers two inviscid bubbles of a single substance A, which collide in a liquid phase as visualized in Figure 2. The bubbles approach each other with a constant relative approach velocity, $V_{app} = V_2 - V_1$, enclosing a thin film of the continuous phase between them. The system contains surfactants which are confined to the bubble interfaces, i.e., insoluble in the dispersed and the continuous phases. The mass transfer occurs from the dispersed to the continuous phase due to the dissolution of the gas with flux of $\mathbf{N}_{A,D\to C}$. This phenomenon results in the dwindling bubbles and moves the interface position by Δz_{mt} as depicted in Figure 2 (c) where $\omega_{A,d}$ and $\omega_{A,c}$ denote the mass fraction of A in the dispersed and the continuous phases, respectively. As the bubbles move closer, the film gets squeezed until the minimum thickness is small enough to stimulate the attractive intermolecular forces to destabilize the interface, leading to film rupture and consequently coalescence.

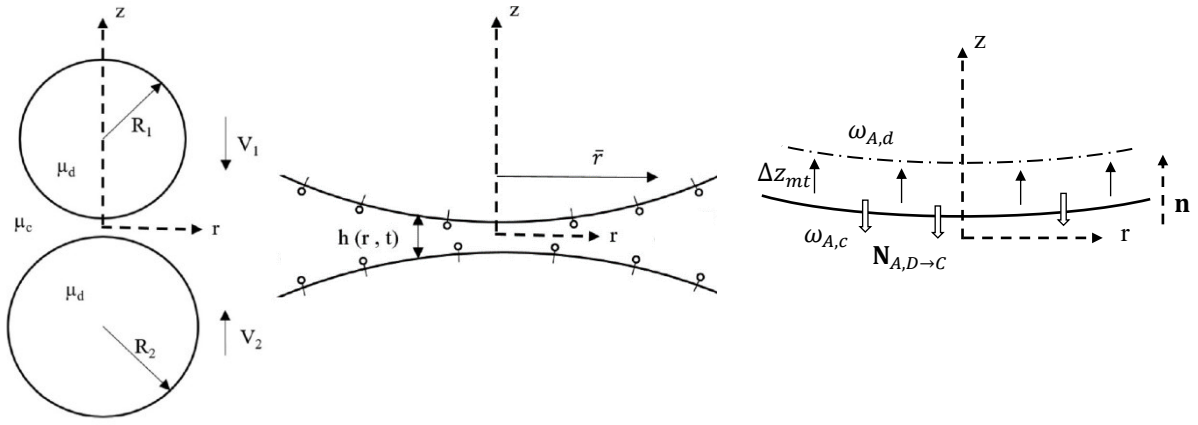

(a) (b) (c)

Figure 2: (a) - (b) The physical configuration of a thin film between two gas bubbles confined by surfactants (adapted from Ozan and Jakobsen, 2019a) and (c) the dissolution of gas bubbles from the dispersed phase to the continuous phase

The dispersed and the continuous phases are assumed incompressible and follow the Newtonian behavior with constant μ_d and μ_c, respectively. Following Chesters (1991), the collision is assumed to occur gently, implying that the bubble radii, R_1 and R_2, are much larger than the film radius, $\bar{r}$. This justifies the two unequal size bubbles to have the same interfacial curvature as for a particle with an equivalent radius of R_p:

$$R_p = 2\left(\frac{1}{R_1} + \frac{1}{R_2}\right)^{-1} \tag{2}$$

This relationship originates from the summation of the normal stress balances between two different size bubbles as given in App. A.2.

The implementation of R_p in the model indicates a symmetrical system around r axis which holds together with the axisymmetry assumption around the center line, creating equivalent behaviors within the four quadrants. Therefore, the solution for one quadrant in $r \geq 0$ and $z \geq 0$ is evaluated through this study to represent the behaviors of the other quadrants. The model performs the cylindrical coordinates to describe the flow within the film while the curvature of the interface is described by a curvilinear coordinate system as illustrated in Figure 3.

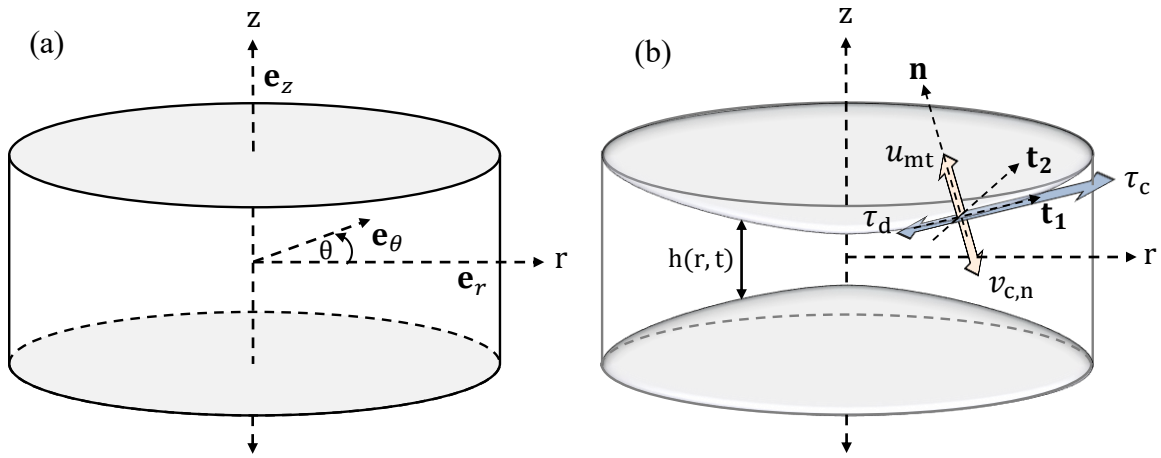

Figure 3: Cylindrical coordinates where the top and the bottom surfaces of a cylindrical disk in (a) are transformed into curvilinear surfaces in (b), representing the gas bubble interfaces

Figure 3 (a) shows cylindrical coordinates with $\mathbf{e}_r$, $\mathbf{e}_\theta$, and $\mathbf{e}_z$ as the base vectors which are applicable for the bulk flow in the continuous phase. The curved surfaces in Figure 3 (b) represent the bubble interfaces which are described in terms of surface coordinates having tangent and a normal unit vectors, $\mathbf{t_1}$, $\mathbf{t_2}$, and $\mathbf{n}$, which are perpendicular to each other. The behaviors at the interface equate the jump conditions between the dispersed and the continuous phases which are decomposed into tangential and normal components. As an illustration, τ_{c} and τ_{d} exhibit the tangential component of the bulk stresses acting within the film and the bubble, while $v_{\mathrm{c,n}}$ and u_{mt} represent the normal component of the bulk velocity and the interface displacement rate due to mass transfer. To connect the interface conditions with the bulk conditions, the unit vectors are expressed as functions of cylindrical coordinates and all operators, e.g., the surface gradient operator, are transformed into cylindrical coordinates.

For positive r and z coordinates, the interface position at $z = h(r,t)/2$ is defined in the surface coordinates as $\mathbf{r}_s = r\mathbf{e}_r(\theta) + z\mathbf{e}_z = r\mathbf{e}_r(\theta) + \frac{h(r,t)}{2}\mathbf{e}_z$. The unit vector $\mathbf{n}$ is chosen to direct from the continuous to the dispersed phase, which is the same direction as positive z in this case. By choosing $\mathbf{t}_1$ to direct in positive r, the right-hand rule gives $\mathbf{t}_2$ in counterclockwise

direction which also yields the coordinate permutation of $\mathrm{r}, \theta, \mathrm{z}$ as the base permutation. According to Johns and Narayanan (2007) and Ozan and Jakobsen (2019b), the tangent vectors are obtained from the partial derivative of $\mathbf{r}_s$ with respect to r and θ, divided by each length. Then, the cross product of these tangent vectors yields the normal vector as derived in App. A.1, giving:

$$\mathbf{t}_1 = \frac{\frac{\partial \mathbf{r}_s}{\partial r}}{\left|\frac{\partial \mathbf{r}_s}{\partial r}\right|} = \frac{\mathbf{e}_r + \frac{1}{2}\frac{\partial h}{\partial r}\mathbf{e}_z}{\sqrt{1 + \frac{1}{4}\left(\frac{\partial h}{\partial r}\right)^2}}, \qquad \mathbf{t}_2 = \frac{\frac{\partial \mathbf{r}_s}{\partial \theta}}{\left|\frac{\partial \mathbf{r}_s}{\partial \theta}\right|} = \mathbf{e}_\theta \tag{3}$$

$$\mathbf{n} = \mathbf{t}_1 \times \mathbf{t}_2 = \frac{\mathbf{e}_r + \frac{1}{2}\frac{\partial h}{\partial r}\mathbf{e}_z}{\sqrt{1 + \frac{1}{4}\left(\frac{\partial h}{\partial r}\right)^2}} \times \mathbf{e}_\theta = \frac{\mathbf{e}_z - \frac{1}{2}\frac{\partial h}{\partial r}\mathbf{e}_r}{\sqrt{1 + \frac{1}{4}\left(\frac{\partial h}{\partial r}\right)^2}} \tag{4}$$

In the right-hand side of Eq. (4), the positive sign of $\mathbf{e}_z$ comes from the cross product between $\mathbf{e}_r$ and $\mathbf{e}_\theta$ which follows the base permutation of coordinates $\mathrm{r}, \theta, \mathrm{z}$. Meanwhile, the negative sign of $\mathbf{e}_r$ is the result of the cross product between $\mathbf{e}_z$ and $\mathbf{e}_\theta$ which gives the reversed permutation. These signs are consistent with the direction of $\mathbf{n}$ from the continuous phase towards the dispersed phase, as depicted in Figure 3. When the bubble interfaces deform during the film drainage, $\mathbf{r}_s$ also changes which consequently changes the unit vectors as Figure 4.

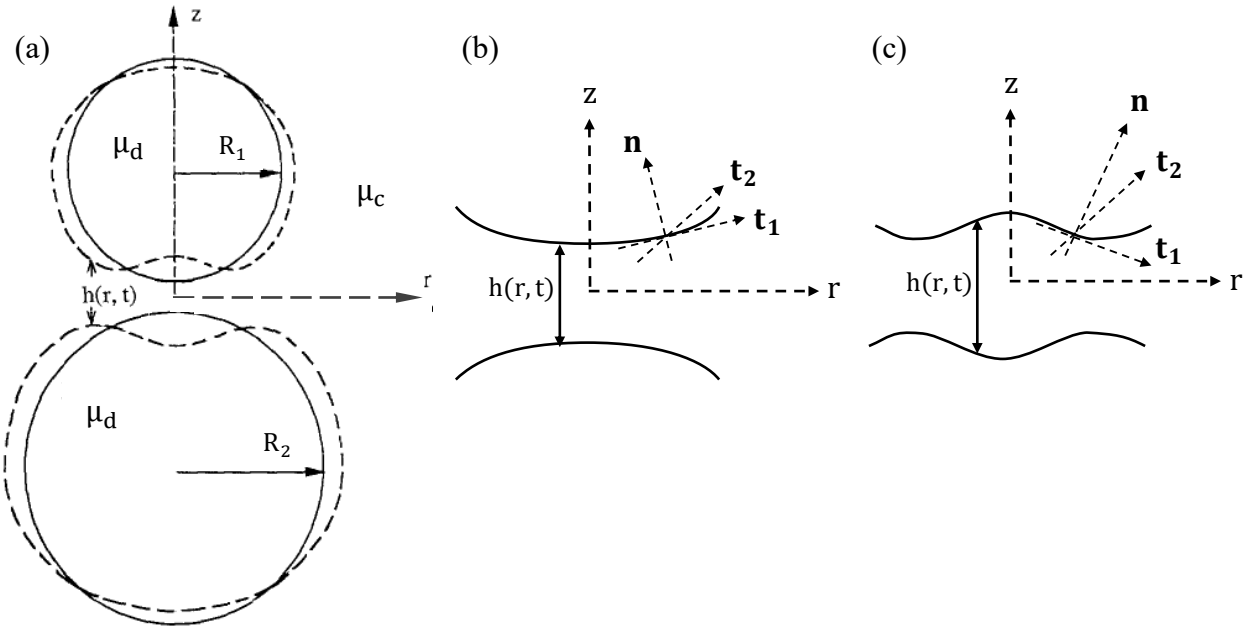

Figure 4: (a) Perfect spherical and deformed bubbles represented by solid and dashed lines, respectively (adapted from Yiantsios and Davis (1991)), (b) the unit vectors at a certain interface position for the perfect spherical interface, and (c) the unit vectors at a corresponding position for the deformed interface

The coalescence behavior is investigated through a film drainage model which is derived from the governing equations and the interface conditions. The governing equations describe the flow condition within the bulk phases where the bubble interfaces become the boundaries described by the interface conditions.

2.1 Governing Equations

The governing equations hold for the bulk phases in which the film side flows are formulated in cylindrical coordinates. In the presence of the mass transfer, a component mass balance is required in addition to the continuity and the Navier-Stokes equations.

2.1.1 The Continuity Equation

The continuity equation stems from the mass conservation where the rate of mass change in a system equals to the difference between the mass rates flowing into and out of the system, described as:

$$\frac{\partial \rho_c}{\partial t} + \nabla \cdot (\rho_c \mathbf{v}_c) = 0 \tag{5}$$

The first term in the left-hand side indicates the rate of the mass loss or accumulation in a unit volume, where ρ_c denotes the mass density of the continuous phase. The convective component in the second term represents the divergence of the mass entering and leaving the system, driven by the fluid motion in the continuous phase with the bulk velocity of $\mathbf{v}_c$. The incompressible fluid assumption gives constant ρ_c, i.e., $\frac{\partial \rho_c}{\partial t} = 0$ and $\nabla \rho_c = 0$, simplifying Eq. (5) into

$$\nabla \cdot \mathbf{v}_c = 0 \tag{6}$$

In the cylindrical coordinate system, the vector differential operator, ∇, is defined as

$$\nabla = \mathbf{e}_r \frac{\partial}{\partial r} + \mathbf{e}_\theta \frac{1}{r} \frac{\partial}{\partial \theta} + \mathbf{e}_z \frac{\partial}{\partial z} \tag{7}$$

while $\mathbf{v}_c$ is assumed to have no θ-component, giving

$$\mathbf{v}_c = v_r \mathbf{e}_r + v_z \mathbf{e}_z \tag{8}$$

By taking the dot product between Eqs. (7) and (8), Eq. (6) becomes

$$\frac{1}{r} \frac{\partial}{\partial r} (r v_r) + \frac{\partial v_z}{\partial z} = 0 \tag{9}$$

The complete derivation is discussed in App. A.3.

2.1.2 The Navier-Stokes Equation

The Navier-Stokes equation originates from the equation of motion for Newtonian fluids which equates the acceleration/deceleration of a fluid motion with the rate of momentum change due to the effect of forces acting upon the system, expressed as

$$\frac{\partial}{\partial t}(\rho_c \mathbf{v}_c) + \nabla \cdot (\rho_c \mathbf{v}_c \mathbf{v}_c) = -\nabla \mathrm{P}_c - \nabla \cdot \tau_c + \rho_c \mathbf{g} \tag{10}$$

The two terms in the left hand-side represent the change of motion comprising the time-dependent and the convective components. The time-dependent term describes the rate of momentum accumulation/loss, whereas the convective term shows the momentum transport in a unit volume ($\rho_c\ \mathbf{v}_c$) which is driven by the fluid motion (represented by $\mathbf{v}_c$). In the right-hand side, the terms containing P_c, τ_c, and $\mathbf{g}$ respectively describe the effects of the pressure, the viscous stress tensor, and the gravitational acceleration on the momentum change. For a Newtonian fluid, τ_c is expressed in terms of the fluid viscosity, μ_c, and $\mathbf{v}_c$:

$$\tau_c = -\mu_c(\nabla \mathbf{v}_c + (\nabla \mathbf{v}_c)^T) + \frac{2}{3}\mu_c(\nabla \cdot \mathbf{v}_c)\mathrm{I} \tag{11}$$

The superscript T and the notation I denote the transpose operator and the identity tensor, respectively. For a thin film system, the gravity term appears to be negligible compared to the other terms as shown in App. A.4. Therefore, the last term of Eq. (10) is cancelled out and the substitution of Eq. (11) to Eq. (10) yields

$$\rho_c \frac{\partial \mathbf{v}_c}{\partial t} + \mathbf{v}_c \cdot \nabla \mathbf{v}_c = -\nabla \mathrm{P}_c + \mu_c \nabla^2 \mathbf{v}_c \tag{12}$$

Specifying ∇ and $\mathbf{v}_c$ as Eqs. (7) and (8), with constant ρ_c and μ_c give the r- and z-components of the Navier-Stokes equation:

r-component: $$\rho_c\left(\frac{\partial v_r}{\partial t} + v_r\frac{\partial v_r}{\partial r} + v_z\frac{\partial v_r}{\partial z}\right) = -\frac{\partial P_c}{\partial r} + \mu_c\left[\frac{\partial}{\partial r}\left(\frac{1}{r}\frac{\partial}{\partial r}(r v_r)\right) + \frac{\partial^2 v_r}{\partial z^2}\right] \tag{13}$$

z-component: $$\rho_c\left(\frac{\partial v_z}{\partial t} + v_r\frac{\partial v_z}{\partial r} + v_z\frac{\partial v_z}{\partial z}\right) = -\frac{\partial P_c}{\partial z} + \mu_c\left[\frac{1}{r}\frac{\partial}{\partial r}\left(r\frac{\partial v_z}{\partial r}\right) + \frac{\partial^2 v_z}{\partial z^2}\right] \tag{14}$$

The full derivation is explained in more detail through App. A.4.

2.1.3 The Component Mass Balance Equation

The component mass balance describes the distribution of substance A in the continuous phase due to mass transfer, which is expressed in terms of the mass fraction, $\omega_{A,c}$, as

$$\frac{\partial(\rho_c \omega_{A,c})}{\partial t} + \nabla \cdot (\rho_c \mathbf{v}_c \omega_{A,c}) = -\nabla \cdot \mathbf{j}_A + r_A \tag{15}$$

In left-hand side, the first term indicates the rate of mass accumulation of species A while the second term represents the mass rate change of A due to convection. The right-hand side represents the contribution of the diffusion and the reaction on the mass balance. Following the Fick's law, the diffusive mass flux, $\mathbf{j}_A$, is defined as a function of the concentration gradient:

$$\mathbf{j}_A = -\rho_c D_{AB} \nabla \omega_{A,c} \tag{16}$$

with D_{AB} denoting the molecular diffusivity, which is considered constant. By applying Eqs. (7), (8), and (16) to Eq. (15), the final expression of the component mass balance for the incompressible fluid is obtained according to App. A.5 as

$$\frac{\partial \omega_{A,c}}{\partial t} + v_r \frac{\partial \omega_{A,c}}{\partial r} + v_z \frac{\partial \omega_{A,c}}{\partial z} = D_{AB} \left[\frac{1}{r} \frac{\partial}{\partial r} \left(r \frac{\partial \omega_{A,c}}{\partial r} \right) + \frac{\partial^2 \omega_{A,c}}{\partial z^2} \right] + \frac{r_A}{\rho_c} \tag{17}$$

2.2 Interface Conditions

The interface conditions are derived according to the law of conservation where the total mass and the total momentum passing through the interface are conserved. The mass conservation is described in terms of the velocity fields while the momentum conservation yields the stress balance across the interface. These conditions are decomposed into the tangential and the normal components by taking the dot product of each balance with the tangent and the normal unit vectors.

For a system without mass transfer and surfactants, the mass conservation gives:

$$\begin{aligned} \mathbf{v}_c|_{z=h/2} &= \mathbf{u} \\ &= U_n \mathbf{n} + U_t \mathbf{t}_1 \end{aligned} \tag{18}$$

where $\mathbf{u}$ describes the rate of interfacial displacement with U_n and U_t standing for the normal and the tangential velocities of the interface. The tangential element gives the no-slip condition whereas the normal component results in the kinematic condition. Meanwhile, the momentum conservation yields:

$$\begin{aligned} \|\mathrm{T}\| \cdot \mathbf{n} = \nabla_s \cdot \mathrm{T}_I &= (\nabla_s \cdot \mathrm{I}_s)\sigma + \mathrm{I}_s \cdot \nabla_s \sigma \\ &= 2H\sigma \mathbf{n} + \nabla_s \sigma \end{aligned} \tag{19}$$

Here, ∇_s and T_I denote the surface gradient operator and the interfacial stress tensor:

$$\nabla_s = \frac{\mathbf{t}_1}{\sqrt{1 + \frac{1}{4}\left(\frac{\partial h}{\partial r}\right)^2}} \frac{\partial}{\partial r} + \frac{\mathbf{t}_2}{r} \frac{\partial}{\partial \theta}; \qquad \mathrm{T}_I = \mathrm{I}_s \sigma \tag{20}$$

where I_s is the surface identity tensor:

$$\mathrm{I}_s = \mathbf{t}_1 \mathbf{t}_1 + \mathbf{t}_2 \mathbf{t}_2 \tag{21}$$

The double brackets in Eq. (19) indicate the jump condition between the bulk phases which defines the bulk stress tensor $\|\mathrm{T}\|$ as $\left[\mathrm{T}_c|_{z=h/2} - \mathrm{T}_d|_{z=h/2}\right]$. In this case, the signs of the film side and the bubble side tensors, $+\mathrm{T}_c$ and $-\mathrm{T}_d$, refer to the same and the opposite directions of $\mathbf{n}$. The two terms in the right-hand side of Eq. (19) respectively represent the effect of the curvature and the surface tension gradient on the balance.

The inclusion of the mass transfer leads to a jump condition across the interface, i.e., normal to the interface, which affects the normal component of the interface conditions: the kinematic condition and the normal stress balance. Meanwhile, the surfactant presence creates the surface tension gradient along the interface, which changes the tangential mobility of the interface, i.e., the tangential stress balance and the no-slip condition.

Although the interface is described by the surface coordinates, the unit vectors $\mathbf{t}_1$, $\mathbf{t}_2$, and $\mathbf{n}$ are formulated in terms of cylindrical coordinates, as given in Eqs. (3) and (4). Therefore, the final formulation of the interface conditions only contain cylindrical coordinates: r, θ, and z.

2.2.1 No-slip Condition

The no-slip condition refers to the equality of the movement in tangential direction between the interface and the bulk phase, which is formulated by taking the tangential component of Eq. (18):

$$\mathbf{v}_c|_{z=h/2} \cdot \mathbf{t}_1 = \mathbf{u} \cdot \mathbf{t}_1 \tag{22}$$

As derived in App. A.6, applying $\mathbf{t}_1$ in Eq. (3) to Eq. (22) gives the no-slip condition:

$$\frac{v_r|_{z=h/2} + \frac{1}{2}\frac{\partial h}{\partial r} v_z|_{z=h/2}}{\sqrt{1 + \frac{1}{4}\left(\frac{\partial h}{\partial r}\right)^2}} = U_t \tag{23}$$

The effect of the mass transfer is initially investigated for tangentially immobile interfaces which have zero U_t. Then, the mobility of the interface is included afterwards with non-zero U_t, which is a function of the tangential stress of the dispersed phase, τ_d, according to the boundary integral method (Davis et al., 1989; Ladyzhenskaya, 1969; Pozrikidis, 1992):

$$U_t = \frac{1}{\mu_d}\int_0^{r_\infty} \emptyset(r', \theta)\ \tau_d\ dr' \tag{24}$$

$$\emptyset(r', \theta) = \frac{r'}{2\pi}\int_0^{\pi} \frac{cos\theta}{\sqrt{r^2 + (r')^2 - 2rr'cos\theta}} d\theta \tag{25}$$

Substituting Eq. (25) to Eq. (24) results in

$$U_t = \frac{1}{\mu_d}\int_0^{r_\infty} \frac{r'}{2\pi}\int_0^{\pi} \frac{cos\theta}{\sqrt{r^2 + (r')^2 - 2rr'cos\theta}} d\theta \;\; \tau_d \;\; dr' \tag{26}$$

where τ_d is obtained from the tangential stress balance, discussed in Section 2.2.4.

2.2.2 Kinematic Condition

The name of kinematic originates from the branch of dynamics that study the motion of bodies without considering the forces causing the motion. By this definition, the kinematic condition for a film system refers to the rate of the interface displacement which is analyzed through the normal component of Eq. (18). In the absence of the mass transfer, the kinematic condition indicates the equality between the normal velocity of the interface, $U_n = \mathbf{u} \cdot \mathbf{n}$, and the normal bulk velocity, $\mathbf{v} \cdot \mathbf{n}$, at the interface position. The mass transfer causes a discrepancy between the two speeds, which is proportional to the mass flux passing through the interface, $N|_{z=h/2}$, giving a modified balance:

$$\begin{aligned} N|_{z=h/2} &= -\rho(\mathbf{u} - \mathbf{v}) \cdot \mathbf{n} \\ &= -\rho \mathbf{u}_{mt} \cdot \mathbf{n} \end{aligned} \tag{27}$$

with $\mathbf{u}_{mt}$ referring to the rate of interface displacement caused by the mass transfer across the interface. The negative sign in front of ρ implies that the mass flux moves to the reversed direction of $\mathbf{n}$, as illustrated in Figure 2 (c). Meanwhile, the negative sign between $\mathbf{u}$ and $\mathbf{v}$ represents the speed difference between the bubble interface displacement and the fluid motion. Equation (27) yields a relation among $\mathbf{u}$, $\mathbf{v}$, and $\mathbf{u}_{mt}$ in normal direction as

$$\mathbf{u} \cdot \mathbf{n} = (\mathbf{u}_{mt} + \mathbf{v}) \cdot \mathbf{n} \tag{28}$$

where $\mathbf{u}_{mt} \cdot \mathbf{n} = u_{mt}$ and $\mathbf{v}_c \cdot \mathbf{n} = v_{c,n}$ are visualized in Figure 3. Following the physical configuration in Figure 2 (c) and Figure 3, the direction of u_{mt} is the same as Δz_{mt} which points to positive $\mathbf{n}$. Meanwhile, $v_{c,n}$ has the same direction as V_1 described in Figure 2, which is in negative $\mathbf{n}$.

The mass conservation for the dissolution of gas defines $N|_{z=h/2}$ as the total mass flux transferred from the dispersed phase, which has the same amount as the mass flux entering the continuous phase. This reformulates Eq. (27) into:

$$N|_{z=h/2} = -\rho \mathbf{u}_{mt} \cdot \mathbf{n} = -\rho_d(\mathbf{u} - \mathbf{v}_d) \cdot \mathbf{n} = -\rho_c(\mathbf{u} - \mathbf{v}_c) \cdot \mathbf{n} \tag{29}$$

with ρ_d and $\mathbf{v}_d$ representing the mass density and the bulk velocity of the dispersed phase.

The general formulation of $N|_{z=h/2}$ is composed by the mass flux of the substances involved in the system, which are driven by the diffusion and the convection mechanisms. Therefore, the total mass flux is analyzed through a balance between the last term of Eq. (29) and the total of the diffusive and convective fluxes for all substances, i:

$$-\rho_c(\mathbf{u}-\mathbf{v}_c)\cdot\mathbf{n}=\sum_{i=1}^{n}\left(-\rho_c D_{AB}\nabla\omega_{i,c}\cdot\mathbf{n}-\rho_c\omega_{i,c}(\mathbf{u}-\mathbf{v}_c)\cdot\mathbf{n}\right) \tag{30}$$

Considering pure component of gas bubbles, as indicated in Figure 2 (c), the dissolution of gas only gives A as the only substance transferring through the interfaces. Applying this assumption to Eq. (30) yields:

$$-\rho_c(\mathbf{u}-\mathbf{v}_c)\cdot\mathbf{n}=-\rho_c D_{AB}\nabla\omega_{A,c}\cdot\mathbf{n}-\rho_c\omega_{A,c}(\mathbf{u}-\mathbf{v}_c)\cdot\mathbf{n} \tag{31}$$

where $\omega_{A,c}$ indicates the mass fraction of substance A in the continuous phase. With some re-arrangements, the analysis of Eq. (31) at the interface position, $z=h/2$, gives:

$$\left(1-\omega_{A,c}\big|_{z=h/2}\right)\left(\mathbf{v}_c|_{z=h/2}-\mathbf{u}\right)\cdot\mathbf{n}=-D_{AB}\nabla\omega_{A,c}\big|_{z=h/2}\cdot\mathbf{n}$$

$$\mathbf{u}\cdot\mathbf{n}=\mathbf{v}_c|_{z=h/2}\cdot\mathbf{n}+\frac{D_{AB}\nabla\omega_{A,c}\big|_{z=h/2}\cdot\mathbf{n}}{\left(1-\omega_{A,c}\big|_{z=h/2}\right)} \tag{32}$$

In the left-hand side, $\mathbf{u}\cdot\mathbf{n}=U_n$, represents the normal velocity of the interface, which is defined as $U_n=\frac{1}{2}\frac{\partial h}{\partial t}$ (Johns and Narayanan, 2007; Ozan and Jakobsen, 2019b). The full derivation in App. A.7 results in:

$$U_n=\frac{1}{2}\frac{\partial h}{\partial t}=\frac{v_z|_{z=h/2}-\frac{1}{2}\frac{\partial h}{\partial r}v_r|_{z=h/2}}{\sqrt{1+\frac{1}{4}\left(\frac{\partial h}{\partial r}\right)^2}}$$

$$+\frac{1}{\sqrt{1+\frac{1}{4}\left(\frac{\partial h}{\partial r}\right)^2}}\frac{D_{AB}}{\left(1-\omega_{A,c}\big|_{z=h/2}\right)}\left(\frac{\partial\omega_{A,c}}{\partial z}\Big|_{z=h/2}-\frac{1}{2}\frac{\partial h}{\partial r}\frac{\partial\omega_{A,c}}{\partial r}\Big|_{z=h/2}\right) \tag{33}$$

where the right-hand side indicates the normal bulk velocity in the continuous phase and the displacement rate of the interface due to the mass transfer.

2.2.3 Normal Stress Balance

The normal stress balance originates from the normal component of Eq. (19) which describes the conservation of momentum across the interface. The effect of the mass transfer appears on the balance as a convective term to describe the momentum jump condition driven by $\mathbf{u}_{mt}=\mathbf{u}-\mathbf{v}$ which is specified in Eq. (28). This yields the normal stress balance as

$$2H\sigma\mathbf{n}\cdot\mathbf{n}+\nabla_s\sigma\cdot\mathbf{n}=\|\mathrm{T}\|:\mathbf{nn}-\left\|\rho\left((\mathbf{u}-\mathbf{v})\cdot\mathbf{n}\right)^2\right\| \tag{34}$$

The first term in the left-hand side contains $2H$ which describes the twice of the mean curvature of deformable interfaces. This term is specified as the surface divergence of $\mathbf{n}$:

$$2H=-\nabla_{\mathrm{s}}\cdot\mathbf{n}=\frac{1}{2r}\frac{\partial}{\partial r}\left(r\frac{\partial h}{\partial r}\right) \tag{35}$$

The negative sign in front of the surface gradient operator indicates that the interface curves to negative $\mathbf{n}$ direction. The detail derivation of $2H$ can be referred to Chesters and Hofman (1982) and Ozan and Jakobsen (2020b), which is also provided in App. A.8. As the dot product of two identical vectors results in $\mathbf{n}\cdot\mathbf{n}=1$, the left-hand side of Eq. (34) simplifies to $2H\sigma=\frac{\sigma}{2r}\frac{\partial}{\partial r}\left(r\frac{\partial h}{\partial r}\right)$.

The second term in the left-hand side of Eq. (34) takes ∇_s from Eq. (20) to yield

$$\nabla_s\sigma\cdot\mathbf{n}=\left[\frac{\mathbf{t}_1}{\sqrt{1+\frac{1}{4}\left(\frac{\partial h}{\partial r}\right)^2}}\frac{\partial\sigma}{\partial r}+\frac{\mathbf{t}_2}{r}\frac{\partial\sigma}{\partial\theta}\right]\cdot\mathbf{n}=0 \tag{36}$$

Note that $\mathbf{t}_1\cdot\mathbf{n}=0$ and $\mathbf{t}_2\cdot\mathbf{n}=0$ since the two vectors are perpendicular to each other.

In the first term of the right-hand side of Eq. (34), T denotes the bulk stress tensors for Newtonian fluids, which are given as

$$\mathrm{T}=-P\mathrm{I}+\mu(\nabla\mathbf{v}+(\nabla\mathbf{v})^T) \tag{37}$$

whereas the double brackets indicate the jump condition between the bulk phases as explained for Eq. (19). Thus, Eq. (34) becomes:

$$2H\sigma=[(\mathrm{T}_c\cdot\mathbf{n})\cdot\mathbf{n}-(\mathrm{T}_d\cdot\mathbf{n})\cdot\mathbf{n}]-\|\rho(U_n-v_n)^2\| \tag{38}$$

The last term of Eq. (38) describes the normal stress caused by the mass transfer which is treated further in Section 2.3. Expanding the first term of the right-hand side in Eq. (38) as derived in App. A.8 yields

$$\frac{\sigma}{2r}\frac{\partial}{\partial r}\left(r\frac{\partial h}{\partial r}\right)=-P_c+\frac{\mu_c}{1+\frac{1}{4}\left(\frac{\partial h}{\partial r}\right)^2}\left[\frac{1}{2}\left(\frac{\partial h}{\partial r}\right)^2\frac{\partial v_r}{\partial r}+\left(\frac{\partial v_r}{\partial z}+\frac{\partial v_z}{\partial r}\right)\left(-\frac{\partial h}{\partial r}\right)+2\frac{\partial v_z}{\partial z}\right]$$
$$+P_d-\|\rho(U_n-v_n)^2\| \tag{39}$$

Notice that the normal stress emerging in the dispersed phase only considers the pressure contribution, P_d, since $\mu_d\ll\mu_c$ for bubbles in liquid system. In addition, the surface tension changes only to a very small extent. Thus, although the surface tension gradient is important in the tangential stress balance, as discussed in Section 2.2.4, the change in its value is negligible, meaning that the surface tension is assumed constant in the normal stress balance, i.e., $\sigma\approx\sigma_0$.

2.2.4 Tangential Stress Balance

The tangential stress balance equates the interfacial stress and the bulk phases stresses along the interface which is described as the tangential component of Eq. (19):

$$2H\sigma\mathbf{n}\cdot\mathbf{t}_1 + \nabla_s\sigma\cdot\mathbf{t}_1 = \|\mathrm{T}\|:\mathbf{n}\mathbf{t}_1 \tag{40}$$

The dot product $\mathbf{n}\cdot\mathbf{t}_1 = 0$ due to their orthogonality, giving no curvature term in the left-hand side. By applying ∇_s in Eq. (20), the second term of the left-hand side in Eq. (40) becomes

$$\begin{aligned}\nabla_s\sigma\cdot\mathbf{t}_1 &= \left[\frac{\mathbf{t}_1}{\sqrt{1+\frac{1}{4}\left(\frac{\partial h}{\partial r}\right)^2}}\frac{\partial\sigma}{\partial r} + \frac{\mathbf{t}_2}{r}\frac{\partial\sigma}{\partial\theta}\right]\cdot\mathbf{t}_1 \\ &= \frac{1}{\sqrt{1+\frac{1}{4}\left(\frac{\partial h}{\partial r}\right)^2}}\frac{\partial\sigma}{\partial r}\end{aligned} \tag{41}$$

Here, σ describes the surface tension that changes with r for non-uniform distribution of surfactants. By denoting the tangential stress of the dispersed phase as $\tau_d = -(\mathrm{T}_d\cdot\mathbf{n})\cdot\mathbf{t}_1$ and referring to App. A.9, the tangential stress balance is formulated as

$$\begin{aligned}&\frac{1}{\sqrt{1+\frac{1}{4}\left(\frac{\partial h}{\partial r}\right)^2}}\frac{\partial\sigma}{\partial r} \\ &\quad= \frac{\mu_c}{1+\frac{1}{4}\left(\frac{\partial h}{\partial r}\right)^2}\left[-\frac{\partial h}{\partial r}\frac{\partial v_r}{\partial r} + \left(\frac{\partial v_r}{\partial z}+\frac{\partial v_z}{\partial r}\right)\left(1-\frac{1}{4}\left(\frac{\partial h}{\partial r}\right)^2\right) + \frac{\partial h}{\partial r}\frac{\partial v_z}{\partial z}\right] + \tau_d\end{aligned} \tag{42}$$

The surface tension gradient, $\partial\sigma/\partial r$, appearing in the left-hand side represents the Marangoni effects due to concentration gradient, $\partial\Gamma/\partial r$, that is caused by uneven distribution of surfactants on the interface. This implies that the change in the surface tension depends on the change in the surface excess concentration, which is expressed as

$$\begin{aligned}\frac{\partial\sigma}{\partial r} &= \frac{\partial\sigma}{\partial\Gamma}\frac{\partial\Gamma}{\partial r} \\ &\approx \frac{\Delta\sigma}{\Delta\Gamma}\frac{\partial\Gamma}{\partial r} = \sigma_\Gamma\frac{\partial\Gamma}{\partial r}\end{aligned} \tag{43}$$

The term $\partial\sigma/\partial\Gamma$ describes the dependency of the surface tension on the surface excess concentration which is assumed to be constant and introduced as σ_Γ. Substituting Eq. (43) to Eq. (42) yields

$$\frac{\sigma_\Gamma\frac{\partial\Gamma}{\partial r}}{\sqrt{1+\frac{1}{4}\left(\frac{\partial h}{\partial r}\right)^2}} = \frac{\mu_c}{1+\frac{1}{4}\left(\frac{\partial h}{\partial r}\right)^2}\left[-\frac{\partial h}{\partial r}\frac{\partial v_r}{\partial r} + \left(\frac{\partial v_r}{\partial z}+\frac{\partial v_z}{\partial r}\right)\left(1-\frac{1}{4}\left(\frac{\partial h}{\partial r}\right)^2\right) + \frac{\partial h}{\partial r}\frac{\partial v_z}{\partial z}\right] + \tau_d \tag{44}$$

2.2.5 Surface Excess Concentration Balance

This balance describes the distribution of the surfactants along the interface, which is expressed in terms of the surface excess concentration, Γ. Since the surfactants are assumed to be confined to the interfaces, the surfactant excess concentration balance reads:

$$\frac{\partial \Gamma}{\partial t} + \nabla_s \cdot (\Gamma \mathbf{u}) + \nabla_s \cdot (\mathbf{J}_I \cdot \mathrm{I}_s) = 0 \tag{45}$$

In the left-hand side, the first term represents the rate of accumulation of Γ, the second term where $\mathbf{u}$ is defined as Eq. (18) describes the rate of change due to the convection, and the last term corresponds to the diffusion, where $\mathbf{J}_I$ stands for the interfacial mass flux of the surfactant:

$$\mathbf{J}_I = -D_I \nabla_s \Gamma \tag{46}$$

The right-hand side of Eq. (45) describes the concentration jump condition between the bulk phases, which appears to be zero since the surfactants are assumed to be confined at the interface. Implementing $\mathbf{u}$, I_s, and $\mathbf{J}_I$ in Eqs. (18), (21), and (46) expands Eq. (45) into

$$\frac{\partial \Gamma}{\partial t} + \nabla_s \cdot \left[\Gamma(U_n \mathbf{n} + U_t \mathbf{t}_1)\right] + \nabla_s \cdot \left[(-D_I \nabla_s \Gamma) \cdot (\mathbf{t}_1 \mathbf{t}_1 + \mathbf{t}_2 \mathbf{t}_2)\right] = 0 \tag{47}$$

By substituting $\mathbf{t}_1$, $\mathbf{t}_2$, $\mathbf{n}$, and ∇_s in Eqs. (3), (4), and (20) to Eq. (47), taking the dot product rules as App. A.1 derives the surface excess concentration balance as

$$\frac{\partial \Gamma}{\partial t} + \frac{\frac{1}{r}\frac{\partial}{\partial r}(r\Gamma U_t)}{\sqrt{1+\frac{1}{4}\left(\frac{\partial h}{\partial r}\right)^2}} - \frac{1}{2}\frac{\Gamma U_n}{\left[1+\frac{1}{4}\left(\frac{\partial h}{\partial r}\right)^2\right]^{\frac{3}{2}}}\frac{\partial^2 h}{\partial r^2} - \frac{\Gamma U_n}{2r}\frac{\frac{\partial h}{\partial r}}{\sqrt{1+\frac{1}{4}\left(\frac{\partial h}{\partial r}\right)^2}}$$
$$- \frac{D_I}{1+\frac{1}{4}\left(\frac{\partial h}{\partial r}\right)^2}\left[\frac{1}{r}\frac{\partial}{\partial r}\left(r\frac{\partial \Gamma}{\partial r}\right) - \frac{1}{4}\frac{\partial \Gamma}{\partial r}\frac{\frac{\partial h}{\partial r}\frac{\partial^2 h}{\partial r^2}}{1+\frac{1}{4}\left(\frac{\partial h}{\partial r}\right)^2}\right] = 0 \tag{48}$$

2.3 Non-dimensionalization

The model equations are non-dimensionalized to determine the dominant terms based on the lubrication theory. The transformation requires the characteristic scales to link the dimensional and non-dimensional variables with a relation:

$$\varphi = \bar{\varphi}\tilde{\varphi} \tag{49}$$

where the left-hand side indicates the dimensional variable and the signs bar and tilde represent the characteristic scale and the dimensionless variable, respectively. The characteristic scales are analyzed by taking a clean system without mass transfer as the default case. This implies that the surfactant effect on the tangential stress balance, Eq. (42), and the mass transfer effect on the kinematic condition and the normal stress balance, Eqs. (33) and (39), are not considered

when determining the characteristic scales. Then, the determined scales are used to evaluate the importance of the surfactant presence and the mass transfer on the corresponding equations.

Since the film is thin, the thickness of the film is smaller than the film radius. Introducing epsilon, ϵ, as a parameter having a small value gives $\bar{h}/\bar{r} = \epsilon \ll 1$. The film radius is justified to be much smaller than the equivalent radius of the bubble, R_p, for a gentle collision. This results in:

$$\bar{r} = \epsilon R_p, \qquad \bar{h} = \epsilon \bar{r} = \epsilon^2 R_p \tag{50}$$

The radial and axial velocity scales, $\bar{v}_r$ and $\bar{v}_z$, are analyzed by evaluating the continuity equation in Eq. (9) which signifies the equality of the rate of mass flowing throughout the system. In terms of dimensionless variables, Eq. (9) is written as

$$\frac{\bar{v}_r}{\bar{r}}\left[\ \frac{1}{\tilde{r}}\frac{\partial}{\partial \tilde{r}}(\tilde{r}\tilde{v}_r)\ \right] + \frac{\bar{v}_z}{\bar{h}}\left[\ \frac{\partial \tilde{v}_z}{\partial \tilde{z}}\ \right] = 0 \tag{51}$$

The mass conservation indicates that the two terms in the left-hand side should stay, meaning that both terms have comparable magnitudes:

$$\frac{\bar{v}_r}{\bar{r}} = \frac{\bar{v}_z}{\bar{h}} \tag{52}$$

Substituting Eq. (50) to Eq. (53) yields

$$\bar{v}_z = \frac{\bar{h}}{\bar{r}}\bar{v}_r = \epsilon \bar{v}_r \tag{53}$$

This transforms the continuity equation in Eq. (51) into the dimensionless form:

$$\frac{1}{\tilde{r}}\frac{\partial}{\partial \tilde{r}}(\tilde{r}\tilde{v}_r) + \frac{\partial \tilde{v}_z}{\partial \tilde{z}} = 0 \tag{54}$$

The time scale is determined through the kinematic condition in Eq. (33) which describes the displacement of the interfaces with time due to the fluid motion. Since the coalescence time stems from the drainage of the film which moves the interface position, the relationship among the length, the velocity, and the time scales are well described in the kinematic condition. In terms of dimensionless variables, Eq. (33) can be written as

$$\frac{\bar{h}}{\bar{t}}\left[\ \frac{1}{2}\frac{\partial \tilde{h}}{\partial \tilde{t}}\ \right] = \frac{\bar{v}_z\left[\ \tilde{v}_z\ \right] - \frac{\bar{h}\bar{v}_r}{\bar{r}}\left[\ \frac{1}{2}\frac{\partial \tilde{h}}{\partial \tilde{r}}\tilde{v}_r\ \right]}{\sqrt{1+\left(\frac{\bar{h}}{\bar{r}}\right)^2\left[\ \frac{1}{4}\left(\frac{\partial \tilde{h}}{\partial \tilde{r}}\right)^2\ \right]}} + \frac{D_{AB}}{\left(1-\omega_{A,c}\right)}\frac{\left[\ \frac{1}{\bar{h}}\left(\frac{\partial \omega_{A,c}}{\partial \tilde{z}}\right) - \frac{\bar{h}}{\bar{r}^2}\left(\frac{1}{2}\frac{\partial \tilde{h}}{\partial \tilde{r}}\frac{\partial \omega_{A,c}}{\partial \tilde{r}}\right)\ \right]}{\sqrt{1+\left(\frac{\bar{h}}{\bar{r}}\right)^2\left[\ \frac{1}{4}\left(\frac{\partial \tilde{h}}{\partial \tilde{r}}\right)^2\ \right]}} \tag{55}$$

By implementing the length and the velocity scales in Eqs. (50) and (53), Eq. (55) becomes

$$\frac{\bar{h}}{\bar{t}}\left[\ \frac{1}{2}\frac{\partial\tilde{h}}{\partial\tilde{t}}\ \right]=\frac{\bar{v}_z\left[\ \tilde{v}_z-\frac{1}{2}\frac{\partial\tilde{h}}{\partial\tilde{r}}\tilde{v}_r\ \right]}{\sqrt{1+\epsilon^2\left[\ \frac{1}{4}\left(\frac{\partial\tilde{h}}{\partial\tilde{r}}\right)^2\ \right]}}+\frac{D_{AB}}{\left(1-\omega_{A,c}\right)}\frac{\left[\ \frac{1}{\bar{h}}\left(\frac{\partial\omega_{A,c}}{\partial\tilde{z}}\right)-\frac{\epsilon^2}{\bar{h}}\left(\frac{1}{2}\frac{\partial\tilde{h}}{\partial\tilde{r}}\frac{\partial\omega_{A,c}}{\partial\tilde{r}}\right)\ \right]}{\sqrt{1+\epsilon^2\left[\ \frac{1}{4}\left(\frac{\partial\tilde{h}}{\partial\tilde{r}}\right)^2\ \right]}} \tag{56}$$

The small value of ϵ^2 appearing in the second term inside the square roots makes this term omitted ($\epsilon^2 \ll 1$). In addition, the last term of the right-hand side indicates that the radial component of the diffusive flux is insignificant compared to the axial component $\left(\frac{\epsilon^2}{\bar{h}} \ll \frac{1}{\bar{h}}\right)$, which simplifies Eq. (56) into

$$\frac{\bar{h}}{\bar{t}}\left[\ \frac{1}{2}\frac{\partial\tilde{h}}{\partial\tilde{t}}\ \right]=\bar{v}_z\left[\ \tilde{v}_z-\frac{1}{2}\frac{\partial\tilde{h}}{\partial\tilde{r}}\tilde{v}_r\ \right]+\frac{D_{AB}}{\left(1-\omega_{A,c}\right)}\frac{1}{\bar{h}}\left[\ \frac{\partial\omega_{A,c}}{\partial\tilde{z}}\ \right] \tag{57}$$

The significant terms are analyzed based on the default case without mass transfer which is then used to evaluate the importance of the mass transfer. i.e., the last term of Eq. (57). Since the mass should be conserved, the left-hand side and the first term of the right-hand side in Eq. (57) should stay as two significant terms with comparable magnitudes, $\frac{\bar{h}}{\bar{t}}=\bar{v}_z$, which yields

$$\bar{t}=\frac{\bar{h}}{\bar{v}_z} \tag{58}$$

Substituting Eq. (58) into Eq. (57) gives the dimensionless normal velocity of the interface $\widetilde{U}_n$:

$$\widetilde{U}_n=\frac{1}{2}\frac{\partial\tilde{h}}{\partial\tilde{t}}=\tilde{v}_z|_{\tilde{z}=\tilde{h}/2}-\frac{1}{2}\frac{\partial\tilde{h}}{\partial\tilde{r}}\tilde{v}_r|_{\tilde{z}=\tilde{h}/2}+\frac{1}{Pe}\frac{1}{\left(1-\omega_{A,c}\big|_{\tilde{z}=\tilde{h}/2}\right)}\frac{\partial\omega_{A,c}}{\partial\tilde{z}}\Big|_{\tilde{z}=\tilde{h}/2} \tag{59}$$

The first two terms in the right-hand side represent the axial and the radial components of the dimensionless normal velocity in the continuous phase, $\tilde{\mathrm{v}}_{c,n}$. Meanwhile, the last term corresponds to the contribution of the mass transfer in the interface displacement rate which scales with $1/Pe=\frac{D_{AB}}{\bar{v}_z\bar{h}}$, giving the bulk Péclet number, Pe, as

$$Pe=\frac{\bar{v}_z\bar{h}}{D_{AB}} \tag{60}$$

where Pe signifies the ratio between the convective and the diffusive mass transfer rates in the bulk phase.

The analysis of the pressure scale is based on the film drainage mechanism in which the movement of the approaching bubbles squeezes the film and results in the pressure gradient in r-direction. This justifies that the pressure scale stems from the r-component of the Navier-Stokes equation in Eq. (13) which can be expressed in terms of dimensionless variables by implementing Eqs. (50), (53), and (58) to give

$$\frac{\epsilon\rho_c\bar{v}_r{}^2}{\bar{h}}\left[\frac{\partial\tilde{v}_r}{\partial\tilde{t}}+\tilde{v}_r\frac{\partial\tilde{v}_r}{\partial\tilde{r}}+\tilde{v}_z\frac{\partial\tilde{v}_r}{\partial\tilde{z}}\right]=\frac{\bar{P}\epsilon}{\bar{h}}\left[-\frac{\partial\tilde{P}_c}{\partial\tilde{r}}\right]+\frac{\mu_c\bar{v}_r\epsilon^2}{\bar{h}^2}\left[\frac{\partial}{\partial\tilde{r}}\left(\frac{1}{\tilde{r}}\frac{\partial}{\partial\tilde{r}}(\tilde{r}\tilde{v}_r)\right)\right]+\frac{\mu_c\bar{v}_r}{\bar{h}^2}\left[\frac{\partial^2\tilde{v}_r}{\partial\tilde{z}^2}\right] \quad (61)$$

Comparing the last two terms in the right-hand side indicates that the radial deviatoric stress is insignificant compared to the axial component $\left(\frac{\mu_c\bar{v}_r\epsilon^2}{\bar{h}^2}\ll\frac{\mu_c\bar{v}_r}{\bar{h}^2}\right)$. This yields the remaining terms after the division by $\frac{\mu_c\bar{v}_r}{\bar{h}^2}$ as

$$\frac{\epsilon\rho_c\bar{v}_r\bar{h}}{\mu_c}\left[\frac{\partial\tilde{v}_r}{\partial\tilde{t}}+\tilde{v}_r\frac{\partial\tilde{v}_r}{\partial\tilde{r}}+\tilde{v}_z\frac{\partial\tilde{v}_r}{\partial\tilde{z}}\right]=\frac{\bar{P}\bar{h}\epsilon}{\mu_c\bar{v}_r}\left[-\frac{\partial\tilde{P}_c}{\partial\tilde{r}}\right]+\left[\frac{\partial^2\tilde{v}_r}{\partial\tilde{z}^2}\right] \quad (62)$$

The scales in the left-hand side, $\frac{\epsilon\rho_c\bar{v}_r\bar{h}}{\mu_c}$, reflect a Reynolds number which is estimated to be small for a thin film according to experimental studies. Thus, the left-hand side of Eq. (62) can be omitted, leaving the remaining terms in the right-hand side as the significant terms with comparable magnitudes, $\frac{\bar{P}\bar{h}\epsilon}{\mu_c\bar{v}_r}=1$, to comply with the momentum conservation. This formulates the pressure scale as

$$\bar{P}=\frac{\mu_c\bar{v}_r}{\bar{h}\epsilon} \quad (63)$$

and simplifies Eq. (62) into

$$0=-\frac{\partial\tilde{P}_c}{\partial\tilde{r}}+\frac{\partial^2\tilde{v}_r}{\partial\tilde{z}^2} \quad (64)$$

The characteristic scales acquired in Eqs. (50), (53), (58), and (63) are implemented to non-dimensionalize the remaining equations. For the z-component of the Navier-Stokes, expressing Eq. (14) in terms of dimensionless variables give

$$\frac{\epsilon^2\rho_c\bar{v}_r{}^2}{\bar{h}}\left[\frac{\partial\tilde{v}_z}{\partial\tilde{t}}+\tilde{v}_r\frac{\partial\tilde{v}_z}{\partial\tilde{r}}+\tilde{v}_z\frac{\partial\tilde{v}_z}{\partial\tilde{z}}\right]=\frac{\mu_c\bar{v}_r}{\bar{h}^2\epsilon}\left[-\frac{\partial\tilde{P}_c}{\partial\tilde{z}}\right]+\frac{\mu_c\bar{v}_r\epsilon^3}{\bar{h}^2}\left[\frac{1}{\tilde{r}}\frac{\partial}{\partial\tilde{r}}(\tilde{r}\tilde{v}_r)\right]+\frac{\mu_c\bar{v}_r\epsilon}{\bar{h}^2}\left[\frac{\partial^2\tilde{v}_z}{\partial\tilde{z}^2}\right] \quad (65)$$

The right-hand side considers the pressure term as the only significant term since the last two terms are negligible $\left(\frac{\mu_c\bar{v}_r\epsilon^3}{\bar{h}^2}\ll\frac{\mu_c\bar{v}_r}{\bar{h}^2\epsilon};\frac{\mu_c\bar{v}_r\epsilon}{\bar{h}^2}\ll\frac{\mu_c\bar{v}_r}{\bar{h}^2\epsilon}\right)$. Dividing the remaining terms with $\frac{\mu_c\bar{v}_r}{\bar{h}^2\epsilon}$ yields a Reynolds number, $\frac{\epsilon^3\rho_c\bar{v}_r\bar{h}}{\mu_c}$, in the left-hand side which gives a small magnitude as justified for Eq. (62). Therefore, Eq. (65) becomes

$$0=-\frac{\partial\tilde{P}_c}{\partial\tilde{z}} \quad (66)$$

The non-dimensionalization of the component balance for the dissolution of gas transforms Eq. (17) into

$$\frac{\bar{v}_z}{\bar{h}}\left(\frac{\partial\omega_{A,c}}{\partial\tilde{t}}+\tilde{v}_r\frac{\partial\omega_{A,c}}{\partial\tilde{r}}+\tilde{v}_z\frac{\partial\omega_{A,c}}{\partial\tilde{z}}\right)=D_{AB}\left[\frac{\epsilon^2}{\bar{h}^2}\frac{1}{\tilde{r}}\frac{\partial}{\partial\tilde{r}}\left(\tilde{r}\frac{\partial\omega_{A,c}}{\partial\tilde{r}}\right)+\frac{1}{\bar{h}^2}\frac{\partial^2\omega_{A,c}}{\partial\tilde{z}^2}\right]+\frac{r_A}{\rho_c} \quad (67)$$

The radial diffusive term appears to be negligible compared to the axial component $\left(\frac{\epsilon^2}{\bar{h}^2} \ll \frac{1}{\bar{h}^2}\right)$. The remaining terms are divided with $\frac{\bar{v}_z}{\bar{h}}$ to simplify Eq. (67) into

$$\frac{\partial \omega_{A,c}}{\partial \tilde{t}} + \tilde{v}_r \frac{\partial \omega_{A,c}}{\partial \tilde{r}} + \tilde{v}_z \frac{\partial \omega_{A,c}}{\partial \tilde{z}} = \frac{1}{Pe} \frac{\partial^2 \omega_{A,c}}{\partial \tilde{z}^2} + Q \tag{68}$$

where Pe is defined in Eq. (60) and Q is introduced as the dimensionless reaction term:

$$Q = \frac{\bar{h}}{\bar{v}_z} \frac{r_A}{\rho_c} = \bar{t} \frac{r_A}{\rho_c} \tag{69}$$

The no-slip condition is evaluated by scaling $\widetilde{U}_t$ with $\bar{v}_r$, transforming Eq. (23) into

$$\frac{\bar{v}_r[\tilde{v}_r] + \epsilon^2 \bar{v}_r \left[\frac{1}{2} \frac{\partial \tilde{h}}{\partial \tilde{r}} \tilde{v}_z \right]}{\sqrt{1 + \epsilon^2 \left[\frac{1}{4} \left(\frac{\partial \tilde{h}}{\partial \tilde{r}} \right)^2 \right]}} = \bar{v}_r \widetilde{U}_t \tag{70}$$

In the numerator part of the left-hand side, the axial velocity term appears to be insignificant compared to the radial velocity. Additionally, the second term inside the square root is negligible compared to 1, simplifying Eq. (70) into

$$\tilde{v}_r|_{\tilde{z}=\tilde{h}/2} = \widetilde{U}_t \tag{71}$$

The normal stress balance is assessed by re-writing Eq. (39) as

$$-\frac{\mu_c \bar{v}_r}{\bar{h}\epsilon} \left\| \tilde{P} \right\| + \frac{\frac{\mu_c \bar{v}_r \epsilon^3}{\bar{h}} \left[\frac{1}{2} \left(\frac{\partial \tilde{h}}{\partial \tilde{r}} \right)^2 \frac{\partial \tilde{v}_r}{\partial \tilde{r}} \right] + \left[\frac{\mu_c \bar{v}_r \epsilon^2}{\bar{h}} \left(\frac{\partial \tilde{v}_r}{\partial \tilde{z}} \right) + \frac{\mu_c \bar{v}_r \epsilon^3}{\bar{h}} \left(\frac{\partial \tilde{v}_z}{\partial \tilde{r}} \right) \right] \left(-\frac{\partial \tilde{h}}{\partial \tilde{r}} \right) + \frac{\mu_c \bar{v}_r \epsilon}{\bar{h}} \left(2 \frac{\partial \tilde{v}_z}{\partial \tilde{z}} \right)}{1 + \epsilon^2 \left[\frac{1}{4} \left(\frac{\partial \tilde{h}}{\partial \tilde{r}} \right)^2 \right]}$$

$$-\bar{v}_z{}^2 \left\| \rho \left(\widetilde{U}_n - \tilde{v}_n \right)^2 \right\| = \frac{\epsilon^2 \sigma_0}{\bar{h}} \left[\frac{1}{2\tilde{r}} \frac{\partial}{\partial \tilde{r}} \left(\tilde{r} \frac{\partial \tilde{h}}{\partial \tilde{r}} \right) \right] \tag{72}$$

The right-hand side indicates that the surface tension is assumed constant, i.e., $\sigma \approx \sigma_0$, as mentioned in Section 2.2.3. In the second term of the left-hand side, the denominator is noticeably close to 1 since $\epsilon^2 \ll 1$. Then, comparing all terms containing $\frac{\mu_c \bar{v}_r}{\bar{h}}$ leaves the pressure terms as the significant term, hence, reduces Eq. (72) into

$$-\frac{\mu_c \bar{v}_r}{\bar{h}\epsilon} \left\| \tilde{P} \right\| - \epsilon^2 \bar{v}_r{}^2 \left\| \rho \left(\widetilde{U}_n - \tilde{v}_n \right)^2 \right\| = \frac{\epsilon^2 \sigma_0}{\bar{h}} \left[\frac{1}{2\tilde{r}} \frac{\partial}{\partial \tilde{r}} \left(\tilde{r} \frac{\partial \tilde{h}}{\partial \tilde{r}} \right) \right] \tag{73}$$

Notice that $\bar{v}_z{}^2$ in the third terms of the left-hand side of Eq. (72) transforms into $\epsilon^2 \bar{v}_r{}^2$. By dividing both sides with $\frac{\mu_c \bar{v}_r}{\bar{h}\epsilon}$, Eq. (73) becomes

$$-\left\|\tilde{P}\right\| - \frac{\epsilon^3 \bar{v}_r \bar{h}}{\mu_c} \left\| \rho\left(\tilde{U}_n - v_n\right)^2 \right\| = \frac{\epsilon^3 \sigma_0}{\mu_c \bar{v}_r} \left[\frac{1}{2\tilde{r}} \frac{\partial}{\partial \tilde{r}} \left(\tilde{r} \frac{\partial \tilde{h}}{\partial \tilde{r}} \right) \right] \tag{74}$$

The momentum conservation should hold for cases without mass transfer. This requires the pressure and the curvature terms to stay as significant terms with comparable magnitudes. Equating both magnitudes yields $\bar{v}_r$ in terms of the physical properties as

$$\bar{v}_r = \frac{\sigma_0}{\mu_c} \epsilon^3 \tag{75}$$

and transforms Eq. (74) into

$$-\left\|\tilde{P}\right\| - \frac{\epsilon^3 \bar{v}_r \bar{h}}{\mu_c} \left\| \rho\left(\tilde{U}_n - \tilde{v}_n\right)^2 \right\| = \frac{1}{2\tilde{r}} \frac{\partial}{\partial \tilde{r}} \left(\tilde{r} \frac{\partial \tilde{h}}{\partial \tilde{r}} \right) \tag{76}$$

Re-evaluating Eq. (76) with $\bar{v}_r$ and $\bar{h}$ in Eqs. (75) and (50) estimates the magnitude in the second term of the left hand-side to be 10^{-4}, which is less significant than the coefficient of the pressure and the curvature terms that is around 1. This implies that the role of the mass transfer on the normal stress balance is negligible. By referring to section 2.2.3, the double bracket defines the jump condition in the pressure term as $\left\|\tilde{P}\right\| = \tilde{P}_c - \tilde{P}_d$ which expands Eq. (76) into

$$\tilde{P}_d\big|_{\tilde{z}=\tilde{h}/2} - \tilde{P}_c\big|_{\tilde{z}=\tilde{h}/2} = \frac{1}{2\tilde{r}} \frac{\partial}{\partial \tilde{r}} \left(\tilde{r} \frac{\partial \tilde{h}}{\partial \tilde{r}} \right) \tag{77}$$

Based on Eq. (75), all remaining characteristic scales and the dimensionless numbers in Eqs. (53), (58), (60), (63), and (69) can be formulated in terms of the physical properties as summarized in Eq. (91).

The non-dimensionalization of the tangential stress balance re-writes Eq. (44) as

$$\frac{\frac{\sigma_0}{\bar{r}} \left[\tilde{\sigma}_{\tilde{\Gamma}} \frac{\partial \tilde{\Gamma}}{\partial \tilde{r}} \right]}{\sqrt{1 + \epsilon^2 \left[\frac{1}{4} \left(\frac{\partial \tilde{h}}{\partial \tilde{r}} \right)^2 \right]}}$$

$$= \frac{\mu_c}{1 + \epsilon^2 \left[\frac{1}{4} \left(\frac{\partial \tilde{h}}{\partial \tilde{r}} \right)^2 \right]} \left\{ \frac{\bar{v}_r \epsilon^2}{\bar{h}} \left[-\frac{\partial \tilde{h}}{\partial \tilde{r}} \frac{\partial \tilde{v}_r}{\partial \tilde{r}} \right] + \left(\frac{\bar{v}_r}{\bar{h}} \left[\frac{\partial \tilde{v}_r}{\partial \tilde{z}} \right] + \frac{\bar{v}_r \epsilon^2}{\bar{h}} \left[\frac{\partial \tilde{v}_z}{\partial \tilde{r}} \right] \right) \left(1 - \epsilon^2 \left[\frac{1}{4} \left(\frac{\partial \tilde{h}}{\partial \tilde{r}} \right)^2 \right] \right) \right.$$

$$\left. + \frac{\bar{v}_r \epsilon^2}{\bar{h}} \left[\frac{\partial \tilde{h}}{\partial \tilde{r}} \frac{\partial \tilde{v}_z}{\partial \tilde{z}} \right] \right\} + \bar{\tau}_d \tilde{\tau}_d \tag{78}$$

Notice that the numerator in the left-hand side stems from $\frac{\partial \sigma}{\partial r}$ which scales with $\frac{\sigma_0}{\bar{r}}$ where σ_0 stands for the initial surface tension. All terms having a magnitude of ϵ^2, which is smaller than 1, are omitted. This reduces Eq. (78) into

$$\frac{\sigma_0}{\bar{r}}\left[\tilde{\sigma}_{\tilde{\Gamma}}\frac{\partial\tilde{\Gamma}}{\partial\tilde{r}}\right]=\mu_c\left\{\frac{\bar{v}_r\epsilon^2}{\bar{h}}\left[-\frac{\partial\tilde{h}}{\partial\tilde{r}}\frac{\partial\tilde{v}_r}{\partial\tilde{r}}\right]+\frac{\bar{v}_r}{\bar{h}}\left[\frac{\partial\tilde{v}_r}{\partial\tilde{z}}\right]+\frac{\bar{v}_r\epsilon^2}{\bar{h}}\left[\frac{\partial\tilde{v}_z}{\partial\tilde{r}}\right]+\frac{\bar{v}_r\epsilon^2}{\bar{h}}\left[\frac{\partial\tilde{h}}{\partial\tilde{r}}\frac{\partial\tilde{v}_z}{\partial\tilde{z}}\right]\right\}+\bar{\tau}_d\tilde{\tau}_c \quad (79)$$

In the right-hand side, the three terms containing $\bar{v}_r\epsilon^2/\bar{h}$ are negligible compared to the one with a magnitude of $\bar{v}_r/\bar{h}$, simplifying Eq. (79) into

$$\frac{\sigma_0}{\bar{r}}\left[\tilde{\sigma}_{\tilde{\Gamma}}\frac{\partial\tilde{\Gamma}}{\partial\tilde{r}}\right]=\mu_c\frac{\bar{v}_r}{\bar{h}}\left[\frac{\partial\tilde{v}_r}{\partial\tilde{z}}\right]+\bar{\tau}_d\tilde{\tau}_d \quad (80)$$

The important terms in this stage are analyzed by taking a clean system without surfactants as the default case, i.e., $\Gamma=0$, which needs to satisfy the law of momentum conservation. This requires the two terms in the right-hand side to stay significant with equal magnitudes:

$$\bar{\tau}_d=\mu_c\frac{\bar{v}_r}{\bar{h}} \quad (81)$$

Evaluating Eq. (80) with Eq. (81) gives

$$\frac{\sigma_0}{\bar{r}}\frac{\bar{h}}{\mu_c\bar{v}_r}\left[\tilde{\sigma}_{\tilde{\Gamma}}\frac{\partial\tilde{\Gamma}}{\partial\tilde{r}}\right]=\left.\frac{\partial\tilde{v}_r}{\partial\tilde{z}}\right|_{\tilde{z}=\tilde{h}/2}+\tilde{\tau}_d|_{\tilde{z}=\tilde{h}/2} \quad (82)$$

where $\bar{h}$, $\bar{r}$, and $\bar{v}_r$ are defined in Eqs. (50) and (75), transforming Eq. (82) into

$$\frac{1}{\epsilon^2}\left[\tilde{\sigma}_{\tilde{\Gamma}}\frac{\partial\tilde{\Gamma}}{\partial\tilde{r}}\right]=\left.\frac{\partial\tilde{v}_r}{\partial\tilde{z}}\right|_{\tilde{z}=\tilde{h}/2}+\tilde{\tau}_d|_{\tilde{z}=\tilde{h}/2} \quad (83)$$

Here, the magnitude of the left-hand side appears to be larger than the ones for the two terms in the right-hand side ($1/\epsilon^2\gg1$). This indicates that the left-hand side is more dominant than the other two terms. However, neglecting the terms in the right-hand side results in $\frac{1}{\epsilon^2}\left[\tilde{\sigma}_{\tilde{\Gamma}}\frac{\partial\tilde{\Gamma}}{\partial\tilde{r}}\right]=0$, which is unreasonable for this term to become the largest term and also zero at the same time. Thus, the right-hand side of Eq. (83) cannot be neglected in this case. By merging $\tilde{\sigma}_{\tilde{\Gamma}}$ with $1/\epsilon^2$, Eq. (83) becomes

$$\tilde{\sigma}'_{\tilde{\Gamma}}\frac{\partial\tilde{\Gamma}}{\partial\tilde{r}}=\left.\frac{\partial\tilde{v}_r}{\partial\tilde{z}}\right|_{\tilde{z}=\tilde{h}/2}+\tilde{\tau}_d|_{\tilde{z}=\tilde{h}/2} \quad (84)$$

where $\tilde{\sigma}'_{\tilde{\Gamma}}=\frac{1}{\epsilon^2}\tilde{\sigma}_{\tilde{\Gamma}}=\frac{1}{\epsilon^2}\frac{\Delta\tilde{\sigma}}{\Delta\tilde{\Gamma}}$ is called as the dimensionless dependence hereafter. Equation (84) is required to determine U_t for tangentially mobile interfaces through Eq. (26) which can be expressed in terms of dimensionless variables:

$$\bar{v}_r\tilde{U}_t=\frac{1}{\mu_d}\bar{\tau}_d\bar{r}\int_0^{\tilde{r}_\infty}\frac{\tilde{r}'}{2\pi}\int_0^{\pi}\frac{cos\theta}{\sqrt{\tilde{r}^2+(\tilde{r}')^2-2\tilde{r}\tilde{r}'cos\theta}}d\theta\ \ \tilde{\tau}_d\ d\tilde{r}' \quad (85)$$

where the integration variable r' scales with $\bar{r}$. Substituting Eq. (81) to Eq. (85) results in

$$\tilde{U}_t=\frac{1}{\lambda^*}\int_0^{\tilde{r}_\infty}\frac{\tilde{r}'}{2\pi}\int_0^{\pi}\frac{cos\theta}{\sqrt{\tilde{r}^2+(\tilde{r}')^2-2\tilde{r}\tilde{r}'cos\theta}}d\theta\ \tilde{\tau}_d\ d\tilde{r}' \quad (86)$$

The notation $\lambda^* = \frac{\epsilon\mu_d}{\mu_c}$ denotes the viscosity ratio of the dispersed phase to the continues phase, which signifies the level of interfacial mobility. Since this study concerns on a collision of gas bubbles in water, the value of λ^* is relatively small, which indicates that it is easier for the interface to move tangentially, reflecting high mobility (high $\widetilde{U}_t$) when the system is free from surfactants. For an initial investigation, this study considers the interfaces to be tangentially immobile, $\widetilde{U}_t = 0$, and the tangential stress balance in Eq. (84) is not required.

The non-dimensionalization of the surfactant excess concentration balance estimates the term $1+\frac{1}{4}\left(\frac{\partial h}{\partial r}\right)^2 = 1 + \epsilon^2\left[\frac{1}{4}\left(\frac{\partial \tilde{h}}{\partial \tilde{r}}\right)^2\right]$ as 1 due to the small parameter, $\epsilon^2 \ll 1$, which reduces Eq. (48) into

$$\frac{\Gamma_m}{\bar{t}}\left[\frac{\partial \tilde{\Gamma}}{\partial \tilde{t}}\right] + \frac{\bar{v}_r\Gamma_m}{\bar{r}}\left[\frac{1}{\tilde{r}}\frac{\partial}{\partial \tilde{r}}\left(\tilde{r}\tilde{\Gamma}\widetilde{U}_t\right)\right] - \frac{\bar{v}_z\Gamma_m\epsilon}{\bar{r}}\left[\frac{1}{2}\tilde{\Gamma}\widetilde{U}_n\frac{\partial^2\tilde{h}}{\partial\tilde{r}^2}\right] - \frac{\bar{v}_z\Gamma_m\epsilon}{\bar{r}}\left[\frac{\tilde{\Gamma}\widetilde{U}_n}{2\tilde{r}}\frac{\partial\tilde{h}}{\partial\tilde{r}}\right] - D_I\left\{\frac{\Gamma_m}{\bar{r}^2}\left[\frac{1}{\tilde{r}}\frac{\partial}{\partial\tilde{r}}\left(\tilde{r}\frac{\partial\tilde{\Gamma}}{\partial\tilde{r}}\right)\right] - \frac{\Gamma_m\epsilon^2}{\bar{r}^2}\left[\frac{1}{4}\frac{\partial\tilde{\Gamma}}{\partial\tilde{r}}\frac{\partial\tilde{h}}{\partial\tilde{r}}\frac{\partial^2\tilde{h}}{\partial\tilde{r}^2}\right]\right\} = 0 \quad (87)$$

Notice that U_n and Γ scale with $\bar{v}_z$ and Γ_m, respectively, where Γ_m denotes the surface excess concentration when the critical micelle concentration is reached. Rearranging Eq. (87) and applying $\bar{v}_r$, $\bar{r}$, $\bar{h}$, and $\bar{t}$ summarized in Eq. (91) gives

$$\frac{\sigma_0\Gamma_m\epsilon^2}{\mu_c R_p}\left[\frac{\partial\tilde{\Gamma}}{\partial\tilde{t}} + \frac{1}{\tilde{r}}\frac{\partial}{\partial\tilde{r}}\left(\tilde{r}\tilde{\Gamma}\widetilde{U}_t\right)\right] + \frac{\sigma_0\Gamma_m\epsilon^4}{\mu_c R_p}\left[-\frac{1}{2}\tilde{\Gamma}\widetilde{U}_n\frac{\partial^2\tilde{h}}{\partial\tilde{r}^2} - \frac{\tilde{\Gamma}\widetilde{U}_n}{2\tilde{r}}\frac{\partial\tilde{h}}{\partial\tilde{r}}\right] - D_I\frac{\Gamma_m}{{R_p}^2\epsilon^2}\left[\frac{1}{\tilde{r}}\frac{\partial}{\partial\tilde{r}}\left(\tilde{r}\frac{\partial\tilde{\Gamma}}{\partial\tilde{r}}\right)\right] + D_I\frac{\Gamma_m}{{R_p}^2}\left[\frac{1}{4}\frac{\partial\tilde{\Gamma}}{\partial\tilde{r}}\frac{\partial\tilde{h}}{\partial\tilde{r}}\frac{\partial^2\tilde{h}}{\partial\tilde{r}^2}\right] = 0 \quad (88)$$

In the left-hand side, the second and the fourth terms are negligible compared to the first and the third terms, respectively. Thus, Eq. (88) becomes

$$\frac{\sigma_0\Gamma_m\epsilon^2}{\mu_c R_p}\left[\frac{\partial\tilde{\Gamma}}{\partial\tilde{t}} + \frac{1}{\tilde{r}}\frac{\partial}{\partial\tilde{r}}\left(\tilde{r}\tilde{\Gamma}\widetilde{U}_t\right)\right] - D_I\frac{\Gamma_m}{{R_p}^2\epsilon^2}\left[\frac{1}{\tilde{r}}\frac{\partial}{\partial\tilde{r}}\left(\tilde{r}\frac{\partial\tilde{\Gamma}}{\partial\tilde{r}}\right)\right] = 0 \quad (89)$$

Dividing all terms with $D_I\frac{\Gamma_m}{{R_p}^2\epsilon^2}$ results in

$$Pe_s\left[\frac{\partial\tilde{\Gamma}}{\partial\tilde{t}} + \frac{1}{\tilde{r}}\frac{\partial}{\partial\tilde{r}}\left(\tilde{r}\tilde{\Gamma}\widetilde{U}_t\right)\right] - \frac{1}{\tilde{r}}\frac{\partial}{\partial\tilde{r}}\left(\tilde{r}\frac{\partial\tilde{\Gamma}}{\partial\tilde{r}}\right) = 0 \quad (90)$$

with $Pe_s = \frac{\sigma_0 R_p}{\mu_c D_I}\epsilon^4$ denoting the surface Péclet number.

All characteristic scales and the produced dimensionless numbers are expressed in Table 1 whereas the non-dimensionalized equations are presented in Table 2.

Table 1: The characteristic scales and the dimensionless numbers of the model equations

Characteristic scales:

$$\bar{r} = \epsilon R_p; \quad \bar{h} = \epsilon^2 R_p; \quad \bar{v}_r = \frac{\sigma_0}{\mu_c}\epsilon^3; \quad \bar{v}_z = \frac{\sigma_0}{\mu_c}\epsilon^4; \quad \bar{V}_{app} = \frac{\sigma_0}{\mu_c}\epsilon^4;$$

$$\bar{t} = \frac{R_p \mu_c}{\sigma_0 \epsilon^2}; \quad \bar{P} = \frac{\sigma_0}{R_p}; \quad \bar{\tau}_d = \frac{\sigma_0}{R_p}\epsilon; \quad \bar{U}_t = \frac{\sigma_0}{\mu_c}\epsilon^3 \tag{91}$$

Dimensionless numbers:

$$\lambda^* = \frac{\epsilon \mu_d}{\mu_c}; \quad \tilde{\sigma}'_{\tilde{\Gamma}} = \frac{1}{\epsilon^2}\frac{\Delta\tilde{\sigma}}{\Delta\tilde{\Gamma}}; \quad Q = \frac{R_p \mu_c}{\sigma_0 \epsilon^2}\frac{r_A}{\rho_c}; \quad Pe = \frac{\sigma_0 R_p}{\mu_c D_{AB}}\epsilon^6; \quad Pe_s = \frac{\sigma_0 R_p}{\mu_c D_I}\epsilon^4 \tag{92}$$

Table 2: The dimensionless thin film equations

The governing equations	
Continuity:	$\frac{1}{\tilde{r}}\frac{\partial}{\partial\tilde{r}}(\tilde{r}\tilde{v}_r) + \frac{\partial\tilde{v}_z}{\partial\tilde{z}} = 0$
Navier-Stokes:	r-component: $0 = -\frac{\partial\tilde{P}_c}{\partial\tilde{r}} + \frac{\partial^2\tilde{v}_r}{\partial\tilde{z}^2}$, z-component: $0 = -\frac{\partial\tilde{P}_c}{\partial\tilde{z}}$
Component mass balance of gas A:	$\frac{\partial\omega_{A,c}}{\partial\tilde{t}} + \tilde{v}_r\frac{\partial\omega_{A,c}}{\partial\tilde{r}} + \tilde{v}_z\frac{\partial\omega_{A,c}}{\partial\tilde{z}} = \frac{1}{Pe}\frac{\partial^2\omega_{A,c}}{\partial\tilde{z}^2} + Q$
Interface conditions	
No-slip condition:	$\tilde{v}_r\vert_{\tilde{z}=\tilde{h}/2} = \widetilde{U}_t$
Tangential velocity:	$\widetilde{U}_t = \frac{1}{\lambda^*}\int_0^{\tilde{r}_\infty} \frac{\tilde{r}'}{2\pi}\int_0^{\pi} \frac{cos\theta}{\sqrt{\tilde{r}^2 + (\tilde{r}')^2 - 2\tilde{r}\tilde{r}'cos\theta}} d\theta \;\; \tilde{\tau}_d \;\; d\tilde{r}'$
Kinematic condition:	$\frac{1}{2}\frac{\partial\tilde{h}}{\partial\tilde{t}} = \tilde{v}_z\vert_{\tilde{z}=\frac{\tilde{h}}{2}} - \frac{1}{2}\frac{\partial\tilde{h}}{\partial\tilde{r}}\tilde{v}_r\vert_{\tilde{z}=\tilde{h}/2} + \frac{1}{Pe}\frac{1}{\left(1-\omega_{A,c}\vert_{\tilde{z}=\tilde{h}/2}\right)}\frac{\partial\omega_{A,c}}{\partial\tilde{z}}\Big\vert_{\tilde{z}=\frac{\tilde{h}}{2}}$
Stress balance:	Normal component: $\tilde{P}_d\vert_{\tilde{z}=\frac{\tilde{h}}{2}} - \tilde{P}_c\vert_{\tilde{z}=\frac{\tilde{h}}{2}} = \frac{1}{2\tilde{r}}\frac{\partial}{\partial\tilde{r}}\left(\tilde{r}\frac{\partial\tilde{h}}{\partial\tilde{r}}\right)$, Tangential component: $\tilde{\sigma}'_{\tilde{\Gamma}}\frac{\partial\tilde{\Gamma}}{\partial\tilde{r}} = \frac{\partial\tilde{v}_r}{\partial\tilde{z}}\Big\vert_{\tilde{z}=\tilde{h}/2} + \tilde{\tau}_d\vert_{\tilde{z}=\tilde{h}/2}$
Surfactant balance:	$Pe_s\left[\frac{\partial\tilde{\Gamma}}{\partial\tilde{t}} + \frac{1}{\tilde{r}}\frac{\partial}{\partial\tilde{r}}\left(\tilde{r}\tilde{\Gamma}\widetilde{U}_t\right)\right] - \frac{1}{\tilde{r}}\frac{\partial}{\partial\tilde{r}}\left(\tilde{r}\frac{\partial\tilde{\Gamma}}{\partial\tilde{r}}\right) = 0$

2.4 Analytical Treatment and The Boundary Conditions

In the absence of the mass transfer, the z-component of the model equations are able to be solved analytically, resulting in a set of 1-dimensional equations. When the mass transfer is taken into account, it requires the component mass balance to be solved in 2 dimensions. This part is treated specifically through the numerical technique, which is discussed further in Section 3.

2.4.1 The Thinning Equation

The thinning equation expresses the time evolution of the interface displacement, $\frac{\partial h}{\partial t}$, which originates from the evaluation of the kinematic condition by determining the bulk velocity at the interface. The radial velocity profile is acquired from the r-component of the Navier-Stokes in Eq. (64) by integrating it twice with respect to z. Then, the radial velocity is applied to the continuity equation in Eq. (54) to obtain the axial velocity.

According to the z-component of the Navier-Stokes in Eq. (66), there is no pressure gradient in z-direction. This implies that $\tilde{P}$ stays constant when integrating Eq. (64) with respect to z, which yields

$$\tilde{v}_r = \frac{1}{2}\frac{\partial \tilde{P}}{\partial \tilde{r}}\tilde{z}^2 + C_1\tilde{z} + C_2 \tag{93}$$

Notice that all $\partial \tilde{P}_c/\partial r$ terms transform into $\partial \tilde{P}/\partial r$ which represents the gradient of the excess pressure as explained in Section 2.4.2. Equation (93) is substituted into Eq. (54) to obtain

$$\frac{\partial \tilde{v}_z}{\partial \tilde{z}} = -\frac{1}{\tilde{r}}\frac{\partial}{\partial \tilde{r}}\left(\frac{\tilde{r}}{2}\frac{\partial \tilde{P}}{\partial \tilde{r}}\right)\tilde{z}^2 - \frac{1}{\tilde{r}}\frac{\partial}{\partial \tilde{r}}\left(\tilde{r}C_1\right)\tilde{z} - \frac{1}{\tilde{r}}\frac{\partial}{\partial \tilde{r}}\left(\tilde{r}C_2\right) \tag{94}$$

which can be integrated with respect to $\tilde{z}$ by noticing that $\tilde{P}_c$, $\tilde{r}$, C_1, and C_2 are independent of $\tilde{z}$, resulting in

$$\tilde{v}_z = -\frac{1}{3}\frac{1}{\tilde{r}}\frac{\partial}{\partial \tilde{r}}\left(\frac{\tilde{r}}{2}\frac{\partial \tilde{P}}{\partial \tilde{r}}\right)\tilde{z}^3 - \frac{1}{2}\frac{1}{\tilde{r}}\frac{\partial}{\partial \tilde{r}}\left(\tilde{r}C_1\right)\tilde{z}^2 - \frac{1}{\tilde{r}}\frac{\partial}{\partial \tilde{r}}\left(\tilde{r}C_2\right)\tilde{z} + C_3 \tag{95}$$

The symmetry condition around $\tilde{r}$ axis, i.e., at $\tilde{z} = 0$, indicates that the radial velocity gradient in z-direction and the axial velocity are zero:

$$\left.\frac{\partial \tilde{v}_r}{\partial \tilde{z}}\right|_{\tilde{z}=0} = 0, \qquad \tilde{v}_z|_{\tilde{z}=0} = 0 \tag{96}$$

The implementation of Eq. (96) into Eqs. (93) and (95) determines the two constants, $C_1 = 0$ and $C_3 = 0$, which give the velocity profiles:

$$\tilde{v}_r = \frac{1}{2}\frac{\partial \tilde{P}}{\partial \tilde{r}}\tilde{z}^2 + C_2 \tag{97}$$

$$\tilde{v}_z = -\frac{1}{3}\frac{1}{\tilde{r}}\frac{\partial}{\partial \tilde{r}}\left(\frac{\tilde{r}}{2}\frac{\partial \tilde{P}}{\partial \tilde{r}}\right)\tilde{z}^3 - \frac{1}{\tilde{r}}\frac{\partial}{\partial \tilde{r}}\left(\tilde{r}C_2\right)\tilde{z} \tag{98}$$

The constant C_2 is identified by substituting the no-slip condition from Eq. (71) into Eq. (97), giving $C_2 = \widetilde{U}_t - \frac{1}{2}\frac{\partial \tilde{P}}{\partial \tilde{r}}\left(\frac{\tilde{h}}{2}\right)^2$. Implementing the constant C_2 to Eqs. (97) and (98) formulates the radial and axial velocity profiles as

$$\tilde{v}_r = \frac{1}{2}\frac{\partial \tilde{P}}{\partial \tilde{r}}\left[\tilde{z}^2 - \left(\frac{\tilde{h}}{2}\right)^2\right] + \widetilde{U}_t \tag{99}$$

$$\tilde{v}_z = -\frac{1}{3}\frac{1}{\tilde{r}}\frac{\partial}{\partial \tilde{r}}\left(\frac{\tilde{r}}{2}\frac{\partial \tilde{P}}{\partial \tilde{r}}\right)\tilde{z}^3 - \frac{1}{\tilde{r}}\frac{\partial}{\partial \tilde{r}}\left(\tilde{r}\widetilde{U}_t\right)\tilde{z} + \frac{1}{\tilde{r}}\frac{\partial}{\partial \tilde{r}}\left[\frac{\tilde{r}}{2}\frac{\partial \tilde{P}}{\partial \tilde{r}}\left(\frac{\tilde{h}}{2}\right)^2\right]\tilde{z} \tag{100}$$

Finally, evaluating Eqs. (99) and (100) at the interface, $\tilde{z} = \tilde{h}/2$, expands the kinematic condition in Eq. (59) which is derived in App. A.11 to yield the thinning equation:

$$\frac{\partial \tilde{h}}{\partial \tilde{t}} = \frac{1}{12\tilde{r}}\frac{\partial}{\partial \tilde{r}}\left(\tilde{r}\frac{\partial \tilde{P}}{\partial \tilde{r}}\tilde{h}^3\right) - \frac{1}{\tilde{r}}\frac{\partial}{\partial \tilde{r}}\left(\tilde{r}\widetilde{U}_t\tilde{h}\right) + M \tag{101}$$

The two first terms in the right-hand side represent the parabolic and the plug components of the flow which are caused by the pressure gradient and the tangential velocity, respectively. The last term, describing the role of the mass transfer in the balance, is proportional to the mass flux and defined as

$$M = \frac{2}{Pe}\frac{1}{\left(1 - \omega_{A,c}\big|_{\tilde{z}=\tilde{h}/2}\right)}\frac{\partial \omega_{A,c}}{\partial \tilde{z}}\bigg|_{\tilde{z}=\tilde{h}/2} \tag{102}$$

Notice that positive M refers to mass transfer from the dispersed to the continuous phase.

The solution of Eq. (101) requires two boundary conditions, which follow the symmetry condition and the gentle collision assumption:

$$\frac{\partial \tilde{h}}{\partial \tilde{r}}\bigg|_{\tilde{r}=0} = 0, \qquad \frac{\partial \tilde{h}}{\partial \tilde{t}}\bigg|_{\tilde{r}=\tilde{r}_\infty} = -\tilde{V}_{app} + M|_{\tilde{r}=\tilde{r}_\infty} \tag{103}$$

The symmetry condition applies at the center of the radial coordinate, $\tilde{r} = 0$, where the gradient of the interface position with r is zero. Meanwhile, the gentle collision refers to the equivalence between the rate of the interface displacement at large radial distance, at $\tilde{r}_\infty$, and the approach velocity, $\tilde{V}_{app}$, where M is also considered. The initial film thickness, $h(r, 0)$, signifying the initial distance of two spherical bubbles is expressed as

$$h(r,0) = h_{00} + \frac{r^2}{R_p} \tag{104}$$

with h_{00} denoting the initial minimum distance of the two bubbles, which takes place at $r = 0$, and the term r^2/R_p resembling a perfect sphere. Applying the characteristic scales in Table 1 transforms Eq. (104) into

$$\tilde{h}(\tilde{r},0) = \tilde{h}_{00} + \tilde{r}^2 \tag{105}$$

where the value of $\tilde{h}_{00}$ should be sufficiently large to represent a perfect spherical shape, i.e., the interface is not deformed yet.

For the immobile case, there is no tangential velocity, $\widetilde{U}_t = 0$, which eliminates the second term of the right-hand side in Eq. (101), giving

$$\frac{\partial \tilde{h}}{\partial \tilde{t}} = \frac{1}{12\tilde{r}}\frac{\partial}{\partial \tilde{r}}\left(\tilde{r}\frac{\partial \tilde{P}}{\partial \tilde{r}}\tilde{h}^3\right) + M \tag{106}$$

When the interface is fully mobile, the viscosity ratio goes to zero, $\lambda^* \to 0$, and the boundary integral equation in Eq. (86) needs to be rearranged into

$$\widetilde{U}_t\,\lambda^* = \int_0^{\tilde{r}_\infty} \frac{\tilde{r}'}{2\pi}\int_0^{\pi} \frac{cos\theta}{\sqrt{\tilde{r}^2 + (\tilde{r}')^2 - 2\tilde{r}\tilde{r}'cos\theta}}\,d\theta\;\tilde{\tau}_d\,d\tilde{r}' \tag{107}$$

Introducing $\widehat{U}_t = \lambda^*\widetilde{U}_t$ as the tangential velocity for the fully mobile case reformulates Eq. (101) into

$$\lambda^*\frac{\partial \tilde{h}}{\partial \tilde{t}} = \frac{\lambda^*}{12\tilde{r}}\frac{\partial}{\partial \tilde{r}}\left(\tilde{r}\frac{\partial \tilde{P}}{\partial \tilde{r}}\tilde{h}^3\right) - \frac{1}{\tilde{r}}\frac{\partial}{\partial \tilde{r}}\left(\,\tilde{r}\widehat{U}_t\tilde{h}\,\right) + \lambda^* M$$

$$\frac{\partial \tilde{h}}{\partial \tilde{t}_{\lambda^*}} = -\frac{1}{\tilde{r}}\frac{\partial}{\partial \tilde{r}}\left(\,\tilde{r}\widehat{U}_t\tilde{h}\,\right) \tag{108}$$

implying that the contribution of the pressure gradient is omitted and the effect of the mass transfer becomes negligible. Here, λ^* in the left-hand side of Eq. (108) merges into the dimensionless time, giving $\tilde{t}_{\lambda^*} = \frac{\tilde{t}}{\lambda^*} = \frac{t}{\bar{t}\lambda^*}$. This rearrangement consequently re-defines the boundary condition at $\tilde{r} = \tilde{r}_\infty$ as

$$\left.\frac{\partial \tilde{h}}{\partial \tilde{t}_{\lambda^*}}\right|_{\tilde{r}=\tilde{r}_\infty} = -\tilde{V}_{app,\lambda^*} \tag{109}$$

with $\tilde{V}_{app,\lambda^*} = \tilde{V}_{app}\,\lambda^* = \frac{V_{app}}{\bar{V}_{app}}\lambda^*$.

2.4.2 The Pressure Equation

The pressure equation stems from the normal stress balance in Eq. (77) which is expressed in terms of the excess pressure, describing the pressure deviation of the bubble interface to a perfect sphere. This requires the normal stress balance for a perfect sphere:

$$-P_{c,0} + P_{d,0} = 2H\sigma_0 = \frac{2\sigma_0}{R_p} \tag{110}$$

which is transformed into dimensionless variables by implementing the pressure scale from Table 1 to obtain

$$-\tilde{P}_{c,0} + \tilde{P}_{d,0} = 2 \tag{111}$$

Taking the difference between Eq. (111) and Eq. (77) results in the pressure equation:

$$-\tilde{P}_{c,0} - \left(-\tilde{P}_c\right) + \tilde{P}_{d,0} - \tilde{P}_d = 2 - \frac{1}{2\tilde{r}}\frac{\partial}{\partial\tilde{r}}\left(\tilde{r}\frac{\partial\tilde{h}}{\partial\tilde{r}}\right)$$

$$\tilde{P} = 2 - \frac{1}{2\tilde{r}}\frac{\partial}{\partial\tilde{r}}\left(\tilde{r}\frac{\partial\tilde{h}}{\partial\tilde{r}}\right) \tag{112}$$

Notice that $\tilde{P}_d$ is approximately the same as $\tilde{P}_{d,0}$ for a gentle collision, hence, $\tilde{P}_{d,0} - \tilde{P}_d \approx 0$. Therefore, $\tilde{P} = \tilde{P}_c - \tilde{P}_{c,0}$ stands for the film side excess pressure. This definition is introduced to all model equations containing $\partial\tilde{P}_c/\partial r$ which turns into $\partial\tilde{P}/\partial r$ since $\frac{\partial\tilde{P}_c}{\partial r} = \frac{\partial\tilde{P}}{\partial r}$. In addition, this model requires a disjoining pressure to account for the attractive intermolecular forces which enable coalescence. For a thin film, the disjoining pressure is given as

$$\Pi_D = A/6\pi h^3 \tag{113}$$

with A standing for the Hamaker constant which represents the strength of the van der Waals interactions between the two bubbles. As the film becomes thinner, the van der Waals interactions get more impactful and accelerate the drainage rate significantly, which leads to a film rupture, followed by coalescence. The non-dimensionalization of Eq. (113) gives an additional term to Eq. (112) to become the pressure equation:

$$\tilde{P} = 2 - \frac{1}{2\tilde{r}}\frac{\partial}{\partial\tilde{r}}\left(\tilde{r}\frac{\partial\tilde{h}}{\partial\tilde{r}}\right) + \frac{A^*}{\tilde{h}^3} \tag{114}$$

with $A^* = \frac{A}{6\pi\sigma {R_p}^2 \epsilon^6}$ reflecting the dimensionless Hamaker constant. The boundary conditions are defined through the symmetry condition and the gentle collision:

$$\left.\frac{\partial\tilde{P}}{\partial\tilde{r}}\right|_{\tilde{r}=0} = 0, \qquad \tilde{P}\big|_{\tilde{r}=\tilde{r}_\infty} = 0 \tag{115}$$

The symmetry condition indicates that the pressure gradient is zero at the center of r-coordinate whereas the gentle collision implies that the interface at large radial distance stays undeformed (no excess pressure).

2.4.3 The Component Mass Balance Equation

The solution of the component mass balance in Eq. (68) requires two boundary conditions for each r- and z-direction. In r-direction, the axisymmetry and the gentle collision indicate zero concentration gradient at the center line and at large radial distance, respectively:

$$\left.\frac{\partial \omega_{A,c}}{\partial \tilde{r}}\right|_{\tilde{r}=0} = 0, \qquad \left.\frac{\partial \omega_{A,c}}{\partial \tilde{r}}\right|_{\tilde{r}=\tilde{r}_\infty} = 0 \tag{116}$$

Meanwhile, in z-direction, the boundary conditions stem from the symmetry condition around r-axis and the solubility condition:

$$\left.\frac{\partial \omega_{A,c}}{\partial \tilde{z}}\right|_{\tilde{z}=0} = 0, \qquad \omega_{A,c}\big|_{\tilde{z}=\tilde{h}/2} = \frac{k_H P_{A,d}}{\rho_c} = K' \tag{117}$$

The symmetry condition holds for $\tilde{z} = 0$ where there is no concentration gradient with z whereas the solubility condition signifies the mass fraction of gas A at the interface as the solubility of gas A in the continuous phase, introduced as K'. Following Henry's law, K' is proportional to the Henry's law constant and the partial pressure of species A, notated by k_H and $P_{A,d}$, respectively. As the bubbles are assumed to have a single component, $P_{A,d}$ is the same as the total pressure of the dispersed phase. The implementation of the second boundary condition of Eq. (117) formulates Eq. (102) into

$$M = \frac{2}{Pe}\frac{1}{(1-K')}\left.\frac{\partial \omega_{A,c}}{\partial \tilde{z}}\right|_{\tilde{z}=\tilde{h}/2} \tag{118}$$

The estimation of M in Eq. (118) considers 3 cases: low Pe which omits the left-hand side of Eq. (68), constant mass flux where Eq. (68) is not necessary, and variable mass flux which requires Eq. (68) to be solved in 2 dimensions.

2.4.3.1 Case 1: Low Péclet Number

Low Pe values imply that the diffusive transport dominates the mass transfer mechanism, and eliminates the left-hand side of Eq. (68):

$$0 = \frac{1}{Pe}\frac{\partial^2 \omega_{A,c}}{\partial \tilde{z}^2} + Q \tag{119}$$

This case estimates the reaction term, Q, with a zero- and a first-order kinetics. The zero-order reaction has no dependence on the mass fraction, $\omega_{A,c}$, which allows Q to stay constant. Therefore, Eq. (119) can be solved analytically by assigning the boundary conditions in Eq. (117), yielding:

$$\omega_{A,c} = -\frac{1}{2} PeQ \left[\tilde{z}^2 - \left(\frac{\tilde{h}}{2} \right)^2 \right] + K' \tag{120}$$

By referring to App. A.12, evaluating the first derivative of Eq. (120) with $\tilde{z}$ at the interface approximates M in Eq. (118) with Pe canceling out each other, resulting in

$$M = -\frac{Q\tilde{h}}{(1-K')} \tag{121}$$

Substituting Eq. (121) to the thinning equation in Eq. (101) formulates

$$\frac{\partial \tilde{h}}{\partial \tilde{t}} = \frac{1}{12\tilde{r}} \frac{\partial}{\partial \tilde{r}} \left(\tilde{r} \frac{\partial \tilde{P}}{\partial \tilde{r}} \tilde{h}^3 \right) - \frac{1}{\tilde{r}} \frac{\partial}{\partial \tilde{r}} \left(\tilde{r} \tilde{U}_t \tilde{h} \right) - \frac{Q\tilde{h}}{(1-K')} \tag{122}$$

Notice that Q has a negative value since the substance A acts as a reactant, which gives positive M in Eq. (121), reflecting mass transfer from the dispersed to the continuous phase.

When the reaction follows a first-order kinetic, Q becomes a linear function of $\omega_{A,c}$ and the analytic solution of Eq. (119) derived in App. A.12 yields

$$M = 2 \frac{\sqrt{-\bar{t}k_1 Pe}}{Pe} \frac{K'}{(1-K')} \frac{e^{\sqrt{-\bar{t}k_1 Pe}\frac{\tilde{h}}{2}} - e^{-\sqrt{-\bar{t}k_1 Pe}\frac{\tilde{h}}{2}}}{e^{\sqrt{-\bar{t}k_1 Pe}\frac{\tilde{h}}{2}} + e^{-\sqrt{-\bar{t}k_1 Pe}\frac{\tilde{h}}{2}}} \tag{123}$$

Applying Eq. (123) to Eq. (101) results in the thinning equation for a first-order reaction:

$$\begin{aligned} \frac{\partial \tilde{h}}{\partial \tilde{t}} = {} & \frac{1}{12\tilde{r}} \frac{\partial}{\partial \tilde{r}} \left(\tilde{r} \frac{\partial \tilde{P}}{\partial \tilde{r}} \tilde{h}^3 \right) - \frac{1}{\tilde{r}} \frac{\partial}{\partial \tilde{r}} \left(\tilde{r} \tilde{U}_t \tilde{h} \right) \\ & + 2 \frac{\sqrt{-\bar{t}k_1 Pe}}{Pe} \frac{K'}{(1-K')} \frac{e^{\sqrt{-\bar{t}k_1 Pe}\frac{\tilde{h}}{2}} - e^{-\sqrt{-\bar{t}k_1 Pe}\frac{\tilde{h}}{2}}}{e^{\sqrt{-\bar{t}k_1 Pe}\frac{\tilde{h}}{2}} + e^{-\sqrt{-\bar{t}k_1 Pe}\frac{\tilde{h}}{2}}} \end{aligned} \tag{124}$$

with k_1 denoting the first-order reaction rate constant.

2.4.3.2 Case 2: Constant Mass Flux

This case considers the mass flux across the interface, $N|_{z=h/2}$ in Eq. (29), to stay constant, i.e., constant M in Eq. (118). The effect of the mass transfer is examined by specifying positive constant values for M without requiring the component mass balance in Eq. (68). To evaluate some real systems, the estimation of M values for O_2 and CO_2 are based on Apps. B.1-B.2.

2.4.3.3 Case 3: Variable Mass Flux (2D Model)

The variable mass flux in this case considers both convective and diffusive terms in Eq. (68) to be significant. As the investigation in case 1 reveals insignificant effect of Q, as explained in Section 4.1, Eq. (68) simplifies into

$$\frac{\partial \omega_{A,c}}{\partial \tilde{t}} + \tilde{v}_r \frac{\partial \omega_{A,c}}{\partial \tilde{r}} + \tilde{v}_z \frac{\partial \omega_{A,c}}{\partial \tilde{z}} = \frac{1}{Pe} \frac{\partial^2 \omega_{A,c}}{\partial \tilde{z}^2} \tag{125}$$

where $\tilde{v}_r$ and $\tilde{v}_z$ are expressed in Eqs. (99) and (100). Equation (125) requires the boundary conditions in Eqs. (116) and (117) to obtain the $\omega_{A,c}$ profiles in 2 dimensions, from which the name '2D model' originates. The solution for $\omega_{A,c}$ at a given time are used to estimate M based on Eq. (118):

$$M = \frac{2}{Pe} \frac{1}{(1-K')} \frac{\partial \omega_{A,c}}{\partial \tilde{z}}\bigg|_{\tilde{z}=\tilde{h}/2} \tag{126}$$

which is applied to Eqs. (101) and (103). Here, Pe is able to cover all values and K' changes with P_d according to Eq. (117).

2.4.4 The Tangential Velocity

The tangential velocity is formulated by substituting $\tilde{\tau}_d|_{\tilde{z}=\tilde{h}/2}$ from Eq. (84) to Eq. (86)

$$\widetilde{U}_t = \frac{1}{\lambda^*} \int_0^{\tilde{r}_\infty} \frac{\tilde{r}'}{2\pi} \int_0^{\pi} \frac{cos\theta}{\sqrt{\tilde{r}^2 + (\tilde{r}')^2 - 2\tilde{r}\tilde{r}'cos\theta}} d\theta \left[\tilde{\sigma}'_{\tilde{\Gamma}} \frac{\partial \tilde{\Gamma}}{\partial \tilde{r}} - \frac{\partial \tilde{v}_r}{\partial \tilde{z}}\bigg|_{\tilde{z}=\tilde{h}/2} \right] d\tilde{r}' \tag{127}$$

where $\frac{\partial \tilde{v}_r}{\partial \tilde{z}}\Big|_{\tilde{z}=\tilde{h}/2}$ is taken from the first derivative of Eq. (99) with $\tilde{z}$ as

$$\begin{aligned} \frac{\partial \tilde{v}_r}{\partial \tilde{z}}\bigg|_{\tilde{z}=\tilde{h}/2} &= \frac{\partial}{\partial \tilde{z}} \left\{ \frac{1}{2} \frac{\partial \tilde{P}}{\partial \tilde{r}} \left[\tilde{z}^2 - \left(\frac{\tilde{h}}{2} \right)^2 \right] + \widetilde{U}_t \right\} \bigg|_{\tilde{z}=\tilde{h}/2} \\ &= \frac{\partial \tilde{P}}{\partial \tilde{r}} \tilde{z} \bigg|_{\tilde{z}=\tilde{h}/2} = \frac{\partial \tilde{P}}{\partial \tilde{r}} \frac{\tilde{h}}{2} \end{aligned} \tag{128}$$

Substituting Eq. (128) to Eq. (127) gives

$$\widetilde{U}_t = \frac{1}{\lambda^*} \int_0^{\tilde{r}_\infty} \frac{\tilde{r}'}{2\pi} \int_0^{\pi} \frac{cos\theta}{\sqrt{\tilde{r}^2 + (\tilde{r}')^2 - 2\tilde{r}\tilde{r}'cos\theta}} d\theta \left[\tilde{\sigma}'_{\tilde{\Gamma}} \frac{\partial \tilde{\Gamma}}{\partial \tilde{r}} - \frac{\partial \tilde{P}}{\partial \tilde{r}} \frac{\tilde{h}}{2} \right] d\tilde{r}' \tag{129}$$

with $\tilde{\sigma}'_{\tilde{\Gamma}}$ is the parameter having the estimated values as discussed in Section 4.2 and the term $\frac{\partial \tilde{\Gamma}}{\partial \tilde{r}}$ requires the solution of the surface excess concentration balance. The symmetry conditions give no tangential velocity at the center and no velocity gradient at the boundary, which read:

$$\widetilde{U}_t\big|_{\tilde{r}=0} = 0, \qquad \frac{\partial \widetilde{U}_t}{\partial \tilde{r}}\bigg|_{\tilde{r}=\tilde{r}_\infty} = 0 \tag{130}$$

2.4.5 The Surface Excess Concentration Balance

Equation (90) is solved by applying the symmetry conditions giving no gradients:

$$\left.\frac{\partial\tilde{\Gamma}}{\partial\tilde{r}}\right|_{\tilde{r}=0} = 0, \qquad \left.\frac{\partial\tilde{\Gamma}}{\partial\tilde{r}}\right|_{\tilde{r}=\tilde{r}_\infty} = 0 \tag{131}$$

Then, the initial condition is defined as

$$\tilde{\Gamma}(\tilde{r},0) = \tilde{\Gamma}_0 = \frac{\Gamma_0}{\Gamma_m} \tag{132}$$

The overall model equations are summarized in Table 3. Notice that all equations, except the component mass balance, are valid at the interface.

Table 3: The dimensionless equations and the boundary conditions

<table>
<tr><td rowspan="2">Thinning equation:</td><td colspan="2">$\frac{\partial\tilde{h}}{\partial\tilde{t}} = \frac{1}{12\tilde{r}}\frac{\partial}{\partial\tilde{r}}\left(\tilde{r}\frac{\partial\tilde{P}}{\partial\tilde{r}}\tilde{h}^3\right) - \frac{1}{\tilde{r}}\frac{\partial}{\partial\tilde{r}}\left(\tilde{r}\tilde{U}_t\tilde{h}\right) + M$</td></tr>
<tr><td>Boundary conditions:
$\left.\frac{\partial\tilde{h}}{\partial\tilde{r}}\right|_{\tilde{r}=0} = 0\,; \quad \left.\frac{\partial\tilde{h}}{\partial\tilde{t}}\right|_{\tilde{r}=\tilde{r}_\infty} = -\tilde{V}_{app} + M|_{\tilde{r}=\tilde{r}_\infty}$</td><td>Initial condition:
$\tilde{h}(\tilde{r},0) = \tilde{h}_{00} + \tilde{r}^2$</td></tr>
<tr><td rowspan="2">Pressure equation:</td><td colspan="2">$\tilde{P} = 2 - \frac{1}{2\tilde{r}}\frac{\partial}{\partial\tilde{r}}\left(\tilde{r}\frac{\partial\tilde{h}}{\partial\tilde{r}}\right) + \frac{A^*}{\tilde{h}^3}$</td></tr>
<tr><td colspan="2">Boundary conditions:
$\left.\frac{\partial\tilde{P}}{\partial\tilde{r}}\right|_{\tilde{r}=0} = 0\,; \quad \tilde{P}\big|_{\tilde{r}=\tilde{r}_\infty} = 0$</td></tr>
<tr><td rowspan="2">Component mass balance for gas A</td><td colspan="2">$\frac{\partial\omega_{A,c}}{\partial\tilde{t}} + \tilde{v}_r\frac{\partial\omega_{A,c}}{\partial\tilde{r}} + \tilde{v}_z\frac{\partial\omega_{A,c}}{\partial\tilde{z}} = \frac{1}{Pe}\frac{\partial^2\omega_{A,c}}{\partial\tilde{z}^2} + Q$</td></tr>
<tr><td>Boundary conditions in r:
$\left.\frac{\partial\omega_{A,c}}{\partial\tilde{r}}\right|_{\tilde{r}=0} = 0\,; \ \left.\frac{\partial\omega_{A,c}}{\partial\tilde{r}}\right|_{\tilde{r}=\tilde{r}_\infty} = 0$</td><td>Boundary conditions in z:
$\left.\frac{\partial\omega_{A,c}}{\partial\tilde{z}}\right|_{\tilde{z}=0} = 0\,; \ \omega_{A,c}\big|_{\tilde{z}=\tilde{h}/2} = K'$</td></tr>
<tr><td rowspan="2">Tangential velocity:</td><td colspan="2">$\tilde{U}_t = \frac{1}{\lambda^*}\int_0^{\tilde{r}_\infty}\frac{\tilde{r}'}{2\pi}\int_0^{\pi}\frac{cos\theta}{\sqrt{\tilde{r}^2+(\tilde{r}')^2-2\tilde{r}\tilde{r}'cos\theta}}d\theta\left[\tilde{\sigma}'_{\tilde{\Gamma}}\frac{\partial\tilde{\Gamma}}{\partial\tilde{r}} - \frac{\partial\tilde{P}}{\partial\tilde{r}}\frac{\tilde{h}}{2}\right]d\tilde{r}'$</td></tr>
<tr><td colspan="2">Boundary conditions:
$\tilde{U}_t\big|_{\tilde{r}=0} = 0\,; \qquad \left.\frac{\partial\tilde{U}_t}{\partial\tilde{r}}\right|_{\tilde{r}=\tilde{r}_\infty} = 0$</td></tr>
<tr><td rowspan="2">Surfactant balance:</td><td colspan="2">$Pe_s\left[\frac{\partial\tilde{\Gamma}}{\partial\tilde{t}} + \frac{1}{\tilde{r}}\frac{\partial}{\partial\tilde{r}}\left(\tilde{r}\tilde{\Gamma}\tilde{U}_t\right)\right] - \frac{1}{\tilde{r}}\frac{\partial}{\partial\tilde{r}}\left(\tilde{r}\frac{\partial\tilde{\Gamma}}{\partial\tilde{r}}\right) = 0$</td></tr>
<tr><td>Boundary conditions:
$\left.\frac{\partial\tilde{\Gamma}}{\partial\tilde{r}}\right|_{\tilde{r}=0} = 0, \qquad \left.\frac{\partial\tilde{\Gamma}}{\partial\tilde{r}}\right|_{\tilde{r}=\tilde{r}_\infty} = 0$</td><td>Initial condition:
$\tilde{\Gamma}(\tilde{r},0) = \tilde{\Gamma}_0 = \frac{\Gamma_0}{\Gamma_m}$</td></tr>
</table>

Since all variables are transformed into dimensionless, tildes in the dimensionless variables are omitted after this section.

3 Method

The mathematical problems in this study are solved using numerical computation to estimate the drainage behavior. The model is initially investigated in the absence of surfactants for three cases: low Pe, constant mass flux, and variable mass flux which is applicable for any Pe values. Then, the effect of the surfactant presence is taken into account by including the tangential mobility to the model and coupling it with the surface excess concentration balance. The complete model, i.e., Case 3, contains radial and axial components which are solved by applying a two-step solver. The first part of the solver computes Γ, P, h, and U_t, at a given time by solving the r-component of Eqs. (90), (101), (114) and (129) simultaneously. In this part, M is taken from the previous time step (assigned as zero initially). The second part of the solver takes the solutions obtained from the first part to solve the z-component of Eq. (125), resulting in the 2-dimensional mass fraction profiles. These solutions are used to compute M which is required in the first part to determine Γ, P, h, and U_t for the next time step. While the two parts of the solver are required for Case 3, the first two cases do not need the second part since M is estimated via analytical calculation or assigned as a constant.

In the first step of the solver, the thinning, the pressure, the tangential velocity, and the surface excess concentration balance equations summarized in Table 3 are solved simultaneously using the corresponding boundary and initial conditions. In addition, the initial values of P, U_t, and M are taken as zero. The discretization of the time derivative follows the second-order backward differentiation by assigning the initial conditions in the first and the second time steps. To obtain higher resolution, the spatial derivatives in r-direction are approximated via a spectral method based on the Chebyshev polynomials (Guo et al., 2013). The tangential velocity in Eq. (129) is solved by employing the integration matrix $[A]$ as suggested by Ozan and Jakobsen (2019a) to handle the singularity in the boundary integral kernel, yielding

$$U_t = \frac{[A]}{\lambda^*}\left[\sigma_\Gamma' \frac{\partial \Gamma}{\partial r} - \frac{\partial P}{\partial r}\frac{h}{2}\right] \tag{133}$$

By omitting the subscript t in U_t, the discretization of the domain in r-direction into N_r grids, i.e., N_r+1 grid points, turns the four evaluated variables into an array of size (N_r+1) x 1 and yields the discretized equations as follows.

The discretized thinning equation in Eq. (101):

$$\frac{3}{2\Delta t}\left[\delta_{ij}\right]h_i^{k+1}-\frac{2}{\Delta t}h_i^{k}+\frac{1}{2\Delta t}h_i^{k-1} = \left[\frac{1}{12}\left[diag\left(\frac{1}{r_i}\right)\right]\left[D_{r,ij}\right]\left[diag(r_i)\right]\left[diag\left(h_i^{k}\right)^3\right]\left[D_{r,i}\right]\right]P_i^{k+1} - \left[\left[diag\left(\frac{1}{r_i}\right)\right]\left[D_{r,ij}\right]\left[diag(r_i)\right]\left[diag\left(h_i^{k}\right)\right]\right]U_i^{k+1}+M_i^{k} \quad (134)$$

The discretized pressure equation in Eq. (114):

$$\left[\delta_{ij}\right]P_i^{k+1} = 2\left[1,1,1,\dots,1\right]_{(N_r+1)} - \left[\frac{1}{2}\left[diag\left(\frac{1}{r_i}\right)\right]\left[D_{r,ij}\right]\left[diag(r_i)\right]\left[D_{r,ij}\right]\right]h_i^{k+1}+\frac{A^*}{\left(h_i^{k}\right)^3} \quad (135)$$

The discretized tangential velocity equation in Eq. (133):

$$\left[\delta_{ij}\right]U_i^{k+1}=\frac{1}{\lambda^*}\left[A_i\right]\left[\sigma_\Gamma'\left[D_{r,ij}\right]\right]\Gamma_i^{k+1}-\frac{1}{\lambda^*}\left[A_i\right]\left[\left[diag\left(\frac{h_i^{k}}{2}\right)\right]\left[D_{r,ij}\right]\right]P_i^{k+1} \quad (136)$$

The discretized surface excess concentration balance in Eq. (90):

$$Pe_s\left\{\frac{3}{2\Delta t}\left[\delta_{ij}\right]\Gamma_i^{k+1}-\frac{2}{\Delta t}\Gamma_i^{k}+\frac{1}{2\Delta t}\Gamma_i^{k-1}\right\} + Pe_s\left[diag\left(\frac{1}{r_i}\right)\right]\left[D_{r,ij}\right]\left[diag(r_i)\right]\left[diag\left(\Gamma_i^{k}\right)\right]U_i^{k+1} - \left[diag\left(\frac{1}{r_i}\right)\right]\left[D_{r,ij}\right]\left[diag(r_i)\right]\left[D_{r,ij}\right]\Gamma_i^{k+1}=0 \quad (137)$$

Here, k denotes the time step, i.e., the terms in the $(k+1)^{th}$ time step are unknown. The subscripts $i=1,\dots,(N_r+1)$ and $j=1,\dots,(N_r+1)$ respectively describe the row and the column positions of the corresponding elements. The spectral differentiation matrix, D_r, is obtained from the Chebyshev polynomial function and applied to take the derivative with respect to r. The notations δ_{ij} and $diag$ respectively describe the identity matrix of size (N_r+1 x N_r+1) and the diagonalization function that arranges its input with size (N_r+1) x 1 into a diagonal square matrix. All matrix operators multiplying the unknown terms are grouped into $\left[\ B_{qr,ij}\ \right]$, where $q=1,2,3,4$ corresponds to the sequence of Eqs. (134)-(137) and $r=1,2,3,4$ specifies the sequence of the unknown variables h_i^{k+1}, P_i^{k+1}, U_i^{k+1}, and Γ_i^{k+1}. The known parts of the transient term are defined as $h_{kt,i}=-\frac{2}{\Delta t}h_i^{k}+\frac{1}{2\Delta t}h_i^{k-1}$ and $\Gamma_{kt,i}=-\frac{2}{\Delta t}\Gamma_i^{k}+\frac{1}{2\Delta t}\Gamma_i^{k-1}$. By arranging the unknown and the known terms into the left-hand and the right-hand sides, Eqs. (134)-(137) are rewritten into

$$\left[\ B_{11,ij}\ \right]h_i^{k+1} - \left[\ B_{12,ij}\ \right]P_i^{k+1} + \left[\ B_{13,ij}\ \right]U_i^{k+1} = -h_{kt,i} + M_i^k \tag{138}$$

$$\left[\ B_{21,ij}\ \right]h_i^{k+1} + \left[\ B_{22,ij}\ \right]P_i^{k+1} = 2\left[1,1,1,\dots,1\right]_{(N_r+1)} + \frac{A^*}{\left(h_i^k\right)^3} \tag{139}$$

$$\left[\ B_{32,ij}\ \right]P_i^{k+1} + \left[\ B_{33,ij}\ \right]U_i^{k+1} - \left[\ B_{34,ij}\ \right]\Gamma_i^{k+1} = 0 \tag{140}$$

$$\left[\ B_{43,ij}\ \right]U_i^{k+1} + \left[\ B_{44,ij}\ \right]\Gamma_i^{k+1} = -\Gamma_{kt,i} \tag{141}$$

Then, by specifying the known terms in the right-hand side as $\left[\ RHS_{q,i}\ \right]$, Eqs. (138)-(141) are merged into one equation:

$$\begin{bmatrix} \left[B_{11,ij}\right] & \left[B_{12,ij}\right] & \left[B_{13,ij}\right] & \left[B_{14,ij}\right] \\ \left[B_{21,ij}\right] & \left[B_{22,ij}\right] & \left[B_{23,ij}\right] & \left[B_{24,ij}\right] \\ \left[B_{31,ij}\right] & \left[B_{32,ij}\right] & \left[B_{33,ij}\right] & \left[B_{34,ij}\right] \\ \left[B_{41,ij}\right] & \left[B_{42,ij}\right] & \left[B_{43,ij}\right] & \left[B_{44,ij}\right] \end{bmatrix} \begin{bmatrix} h_i^{k+1} \\ P_i^{k+1} \\ U_i^{k+1} \\ \Gamma_i^{k+1} \end{bmatrix} = \begin{bmatrix} rhs_{1,i} \\ rhs_{2,i} \\ rhs_{3,i} \\ rhs_{4,i} \end{bmatrix} \tag{142}$$

Here, the matrices $\left[B_{14,ij}\right]$, $\left[B_{23,ij}\right]$, $\left[B_{24,ij}\right]$, $\left[B_{31,ij}\right]$, $\left[B_{41,ij}\right]$, and $\left[B_{42,ij}\right]$ contain a value of zero in all of their elements. Combining all matrices $\left[B_{qr,ij}\right]$ and $\left[rhs_{q,i}\right]$ respectively into $\left[C_{fg}\right]$ and $\left[RHS_f\right]$ yields

$$\begin{bmatrix} \\ C_{fg} \\ \\ \\ \end{bmatrix} \begin{bmatrix} h_i^{k+1} \\ P_i^{k+1} \\ U_i^{k+1} \\ \Gamma_i^{k+1} \end{bmatrix} = \begin{bmatrix} \\ RHS_f \\ \\ \\ \end{bmatrix} \tag{143}$$

with $f = 1, \dots, 4x(N_r+1)$ and $g = 1, \dots, 4x(N_r+1)$ denoting the indices of the corresponding elements. The boundary conditions in Eqs. (103), (115), (130), and (131) are discretized into

$$\left[D_{r,1j}\right]h_i^{k+1} = 0, \qquad \frac{3}{2\Delta t}h_{(N_r+1)}^{k+1} - \frac{2}{\Delta t}h_{(N_r+1)}^{k} + \frac{1}{2\Delta t}h_{(N_r+1)}^{k-1} = -V_{app} + M_{(N_r+1)}^k \tag{144}$$

$$\left[D_{r,1j}\right]P_i^{k+1} = 0, \qquad P_{(N_r+1)}^{k+1} = 0 \tag{145}$$

$$U_1^{k+1} = 0, \qquad \left[D_{r,(N_r+1)j}\right]U_i^{k+1} = 0 \tag{146}$$

$$\left[D_{r,1j}\right]\Gamma_i^{k+1} = 0, \qquad \left[D_{r,(N_r+1)j}\right]\Gamma_i^{k+1} = 0 \tag{147}$$

The rearrangement of the unknown and the known terms of Eq. (144) into the left-hand and the right-hand sides yields

$$\left[D_{r,1j}\right] h_i^{k+1} = 0, \qquad h_{(N_r+1)}^{k+1} = \frac{-h_{kt,(N_r+1)} - V_{app} + M_{(N_r+1)}^{k}}{\frac{3}{2\Delta t}} \tag{148}$$

where h_{kt} is defined as in Eq. (138). The boundary conditions are implemented by substituting Eqs. (145)-(148) to the first and the last rows of the corresponding matrices $\left[B_{qr,ij}\right]$ and $\left[rhs_{q,i}\right]$ in Eq. (142) which are re-expressed as $\left[C_{fg}\right]$ and $\left[RHS_f\right]$ in Eq. (143).

For the thinning equation, the left-hand sides of Eq. (148) is taken to replace $\left[B_{11,1j}\right]$ and $\left[B_{11,(N_r+1)j}\right]$ while the right-hand side of Eq. (148) replaces $\left[rhs_{1,1}\right]$ and $\left[rhs_{1,(N_r+1)}\right]$. Defining these conditions in Eq. (143) replaces the 1^{st} and the $(N_r+1)^{th}$ rows of $\left[C_{fg}\right]$ and $\left[RHS_f\right]$ into

$$\begin{aligned} C_{1g} &= \left[D_{r,1j}\ \ 0\ 0\ 0\ \dots\ 0\right]_{4x(N_r+1)}, \\ RHS_1 &= 0 \end{aligned} \tag{149}$$

$$\begin{aligned} C_{(N_r+1)g} &= \left[\left[0\ 0\ 0\ \dots\ 0\ 0\ 1\right]_{(N_r+1)} \left[0\ 0\ 0\ \dots\ 0\right]_{3x(N_r+1)}\right], \\ RHS_{(N_r+1)} &= \frac{-h_{kt,(N_r+1)} - V_{app} + M_{(N_r+1)}^{k}}{\frac{3}{2\Delta t}} \end{aligned} \tag{150}$$

The boundary conditions for the pressure equation are implemented by replacing $\left[B_{22,1j}\right]$ and $\left[B_{22,(N_r+1)j}\right]$ with the left-hand sides of Eq. (145) together with the replacement of $\left[rhs_{2,1}\right]$ and $\left[rhs_{2,(N_r+1)}\right]$ by the right-hand side of Eq. (145). Introducing them into Eq. (143) substitutes the $(N_r+2)^{th}$ and the $(2N_r+2)^{th}$ rows of $\left[C_{fg}\right]$ and $\left[RHS_f\right]$, resulting in

$$\begin{aligned} C_{(N_r+2)g} &= \left[\left[0\ 0\ 0\ \dots\ 0\right]_{(N_r+1)} \left[D_{r,1j}\ \ 0\ 0\ 0\ \dots\ 0\right]_{3x(N_r+1)}\right], \\ RHS_{(N_r+2)} &= 0 \end{aligned} \tag{151}$$

$$\begin{aligned} C_{(2N_r+2)g} &= \left[\left[0\ 0\ 0\ \dots\ 0\ 0\ 1\right]_{2x(N_r+1)} \left[0\ 0\ 0\ \dots\ 0\right]_{2x(N_r+1)}\right], \\ RHS_{(2N_r+2)} &= 0 \end{aligned} \tag{152}$$

The same procedure is applied for the tangential velocity equation by assigning the left-hand sides of Eq. (146) to $\left[B_{33,1j}\right]$ and $\left[B_{33,(N_r+1)j}\right]$, and the right-hand side ones to $\left[rhs_{3,1}\right]$ and

$[rhs_{3,(N_r+1)}]$, which define the $(2N_r+3)^{th}$ and the $(3N_r+3)^{th}$ rows of $[C_{fg}]$ and $[RHS_f]$ in Eq. (143) as

$$C_{(2N_r+3)g} = \left[\left[0\ 0\ 0\ \dots\ 0\right]_{2x(N_r+1)}\left[1\ 0\ 0\ \dots\ 0\right]_{2x(N_r+1)}\right],$$
$$RHS_{2N_r+3} = 0 \tag{153}$$

$$C_{(3N_r+3)g} = \left[\left[0\ 0\ 0\ \dots\ 0\right]_{2x(N_r+1)}\left[D_{r,(N_r+1)j}\ \ 0\ 0\ 0\ \dots\ 0\right]_{2x(N_r+1)}\right],$$
$$RHS_{(3N_r+3)} = 0 \tag{154}$$

Lastly, the boundary conditions for the surface excess concentration balance are implemented by taking the left-hand sides of Eq. (147) to $[B_{44,1j}]$ and $[B_{44,(N_r+1)j}]$ and substituting the right-hand side ones to $[rhs_{4,1}]$ and $[rhs_{4,(N_r+1)}]$, which replace the $(3N_r+4)^{th}$ and the $(4N_r+4)^{th}$ rows of $[C_{fg}]$ and $[RHS_f]$ in Eq. (143), giving

$$C_{(3N_r+4)g} = \left[0\ 0\ 0\ \dots\ 0\ 0\ \ D_{r,1j}\right]_{4x(N_r+1)},$$
$$RHS_{3N_r+4} = 0 \tag{155}$$

$$C_{(4N_r+4)g} = \left[0\ 0\ 0\ \dots\ 0\ 0\ \ D_{r,(N_r+1)j}\right]_{4x(N_r+1)},$$
$$RHS_{(4N_r+4)} = 0 \tag{156}$$

By applying Eqs. (149)-(156), Eq. (143) is solved to obtain the film thickness, the excess pressure, the tangential velocity, and the surface excess concentration profiles along r-axis as

$$\begin{bmatrix} h_i^{k+1} \\ P_i^{k+1} \\ U_i^{k+1} \\ \Gamma_i^{k+1} \end{bmatrix} = \begin{bmatrix} \\ C_{fg} \\ \\ \end{bmatrix}^{-1} \begin{bmatrix} \\ RHS_f \\ \\ \end{bmatrix} \tag{157}$$

The magnitude of M_i^k in Eqs. (134) and (150) is assumed to be constant, i.e., $M_i^k \approx M$, for the first two cases. Specifically for the first case, M is estimated through Eqs. (121) and (123) for the zero- and the first-order reactions, respectively. Meanwhile, the third case takes M_i^k from Eq. (126) which requires Eq. (125) to be solved numerically in two dimensions. Although it involves 2-dimensional components, the solver is developed in a specific way as described in Figure 5 where the r- and z- components are solved separately. In this section, the subscript A, c in $\omega_{A,c}$ is omitted for the discretization purposes.

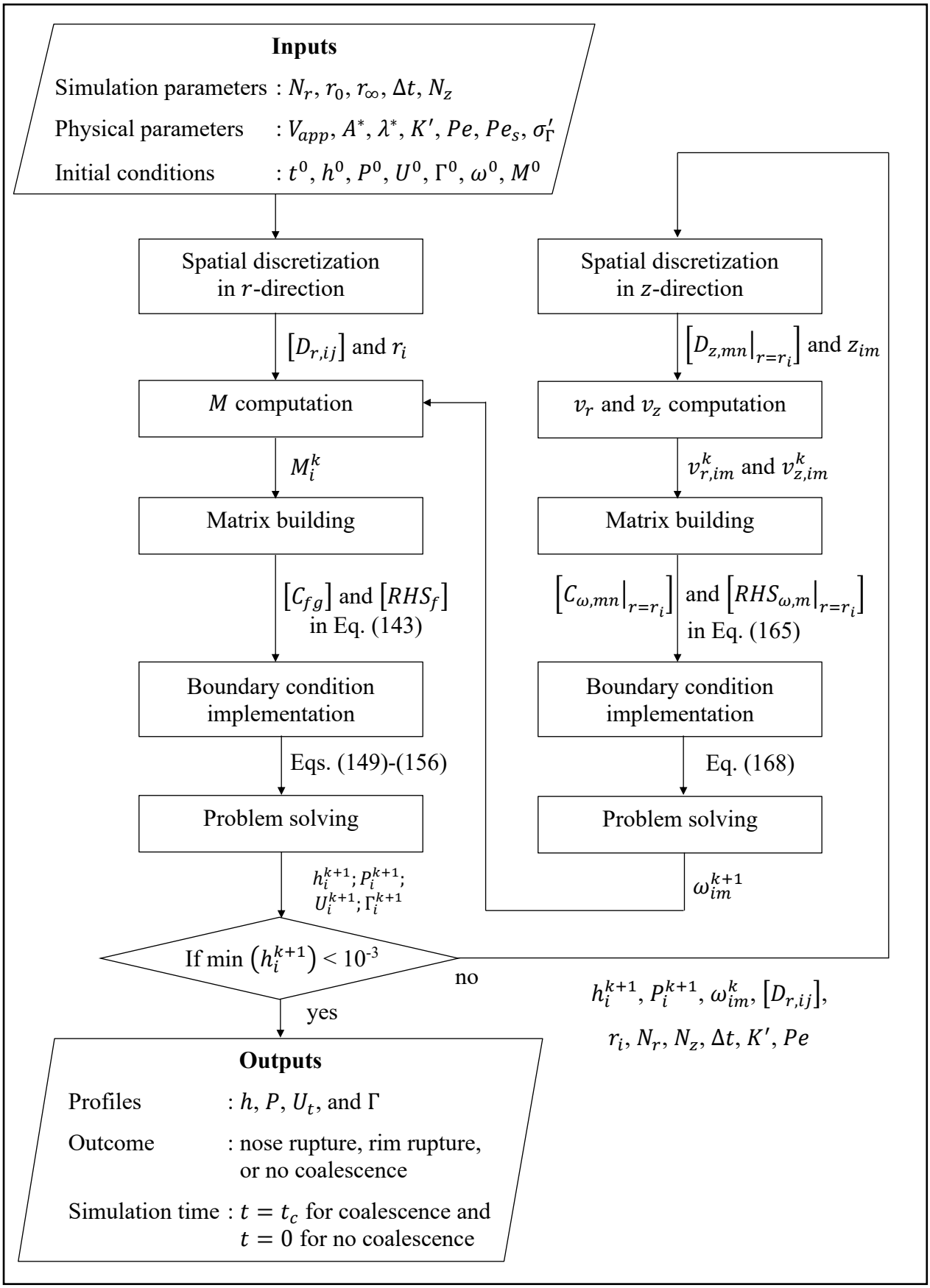

Figure 5: Algorithm of the first and the second parts of the solver. The subscripts $i = 1, \dots, N_r+1$ and $m = 1, \dots, N_z+1$ correspond to the nodes in r- and z- directions, respectively.

As summarized in Figure 5, the second step of the solver is constructed in addition to the first step to determine the bulk velocities and the mass fraction profiles within the film. In this step, the radial discretization component and the solutions for h_i^{k+1} and P_i^{k+1} obtained in the first step are taken to solve a one-dimensional problem in z direction for a fixed value of r. The dependence of the upper boundary, $z = h/2$, on r implies that each problem is solved for a different domain size.

Following the first step of the solver, the spatial derivatives in z-direction are discretized using the Chebyshev spectral method. The differentiation matrix $[D_z]$ and z positions are obtained for each r value and denoted as $\left[D_z|_{r=r_i}\right]$ and $z|_{r=r_i}$. The time derivative is approximated by the first-order backward differentiation. Then, by specifying N_z as the number of grids for z-coordinate, Eq. (125) is discretized at $r = r_i$ as

$$\frac{1}{\Delta t}\left[\delta_{mn}\right]\omega_m^{k+1}|_{r=r_i} - \frac{1}{\Delta t}\omega_m^k|_{r=r_i} + diag\left(v_{r,m}^k\big|_{r=r_i}\right) d\omega_m^k|_{r=r_i} + diag\left(v_{z,m}^k\big|_{r=r_i}\right)\left[D_{z,mn}\big|_{r=r_i}\right]\omega_m^{k+1}|_{r=r_i} = \frac{1}{Pe}\left[D_{z,mn}\big|_{r=r_i}\right]\left[D_{z,mn}\big|_{r=r_i}\right]\omega_m^{k+1}|_{r=r_i} \quad (158)$$

Here, $m = 1, \dots, (N_z{+}1)$ and $n = 1, \dots, (N_z{+}1)$ are the row and the column positions of the corresponding elements. This defines $\left[D_{z,mn}\big|_{r=r_i}\right]$ as a spectral differentiation matrix of sizes $(N_z{+}1)$ x $(N_z{+}1)$ evaluated at $r = r_i$ which takes the derivative with respect to z at $r = r_i$. The term $d\omega_m^k|_{r=r_i}$ describes the derivative of ω with respect to r which is evaluated at $r = r_i$. In other words, $d\omega_m^k|_{r=r_i}$ is the i^{th} element of $\left[d\omega_m^k|_{r=1} \ \dots \ d\omega_m^k|_{r=r_{N_r+1}}\right] = \left[d\omega_{im}^k\right]^T$ which is computed from

$$d\omega_{im}^k = \left[D_{r,ij}\right]\omega_{im}^k \quad ; i = 1, \dots, (N_r{+}1); j = 1, \dots, (N_r{+}1); \ m = 1, \dots, (N_z{+}1) \quad (159)$$

where $\left[D_{r,ij}\right]$ is taken from the first step of the solver. The bulk velocities, $v_{r,m}^k\big|_{r=r_i}$ and $v_{z,m}^k\big|_{r=r_i}$, in Eq. (158) are obtained by determining the velocity profiles within the film, $v_{r,im}^k$ and $v_{z,im}^k$, from the discretization of Eqs. (99) and (100):

$$v_{r,im}^k = \frac{1}{2}\left[\left[D_{r,ij}\right]P_i^{k+1}\right] \odot \left[{z_{im}}^2 - \left(\frac{h_i^{k+1}}{2}\right)^2\right] \quad (160)$$

$$v_{z,im}^k = -\frac{1}{3}\frac{1}{r_i} \odot dP_{1,i} \odot {z_{im}}^3 + \frac{1}{r_i} \odot dP_{2,i} \odot z_{im} \quad (161)$$

The solutions for h_i^{k+1} and P_i^{k+1} are taken from the first part of the solver. The element-wise notation ($\odot$) multiplies each element of the corresponding matrices or arrays located in the same row, i. The terms $dP_{1,i}$ and $dP_{2,i}$ are defined as

$$dP_{1,i} = \left[D_{r,ij} \right] \left[\frac{r_i}{2} \odot \left[\left[D_{r,ij} \right] P_i^{k+1} \right] \right] \tag{162}$$

$$dP_{2,i} = \left[D_{r,ij} \right] \left[\frac{r_i}{2} \odot \left[\left[D_{r,ij} \right] P_i^{k+1} \right] \odot \left(\frac{h_i^{k+1}}{2} \right)^2 \right] \tag{163}$$

The rearrangement of Eq. (158) into the matrix operator, the unknown, and the known terms yields

$$\left[\frac{1}{\Delta t} \left[\delta_{mn} \right] + diag \left(v_{z,m}^k \big|_{r=r_i} \right) \left[D_{z,mn} \big|_{r=r_i} \right] - \frac{1}{Pe} \left[D_{z,mn} \big|_{r=r_i} \right] \left[D_{z,mn} \big|_{r=r_i} \right] \right] \omega_m^{k+1} |_{r=r_i}$$

$$= \left[\frac{1}{\Delta t} \omega_m^k |_{r=r_i} - diag \left(v_{r,m}^k \big|_{r=r_i} \right) d_r \omega_m^k |_{r=r_i} \right] \tag{164}$$

By defining the matrix operator and the known terms as $\left[C_{\omega,mn} \big|_{r=r_i} \right]$ and $\left[RHS_{\omega,m} \big|_{r=r_i} \right]$, Eq. (164) is rewritten into

$$\left[\ C_{\omega,mn} \big|_{r=r_i} \ \right] \left[\omega_m^{k+1} |_{r=r_i} \right] = \left[\ RHS_{\omega,m} \big|_{r=r_i} \ \right] \tag{165}$$

The boundary conditions in r-direction are taken from Eq. (116), which are expressed as

$$\omega_m^{k+1} |_{r=1} = \omega_m^{k+1} |_{r=2}, \qquad \omega_m^{k+1} |_{r=r_{N_r}} = \omega_m^{k+1} |_{r=r_{(N_r+1)}} \tag{166}$$

while the boundary conditions in z-direction stem from the discretization of Eq. (117):

$$\left[D_{z,1n} \big|_{r=r_i} \right] \omega_m^{k+1} |_{r=r_i} = 0, \qquad \omega_{N_z+1}^{k+1} \big|_{r=r_i} = K' \tag{167}$$

Equation (166) implies that the problem is solved for $i = 2, \dots, N_r$ since the solutions for $i = 1$ and $i = N_{r+1}$ are equivalent to the solutions for $i = 2$ and $i = N_r$, respectively. Then, Eq. (167) is implemented by replacing the first and last rows of $\left[\ C_{\omega,mn} \big|_{r=r_i} \ \right]$ and $\left[\ RHS_{\omega,m} \big|_{r=r_i} \ \right]$ in Eq. (165), resulting in

$$C_{\omega,1n} \big|_{r=r_i} = \left[D_{z,1n} \big|_{r=r_i} \right], \qquad \left[\ RHS_{\omega,1} \big|_{r=r_i} \ \right] = 0$$

$$C_{\omega,(N_z+1)n} \big|_{r=r_i} = \left[0 \dots 0 \ 0 \ 1 \right]_{(N_z+1)}, \quad \left[\ RHS_{\omega,N_z+1} \big|_{r=r_i} \ \right] = \mathrm{K}';\ i = 2, \dots, N_r\ ;$$

$$n = 1, \dots, (N_z+1) \tag{168}$$

Finally, Eq. (165) is solved together with the boundary conditions in Eq. (168) by determining

$$\left[\omega_m^{k+1}|_{r=r_i}\right] = \left[\ C_{\omega,mn}\big|_{r=r_i}\ \right]^{-1}\left[\ RHS_{\omega,m}\big|_{r=r_i}\ \right];\ i = 2,\dots,N_r\ ;\quad m = 1,\dots,(N_z{+}1);\quad n = 1,\dots,(N_z{+}1) \qquad (169)$$

and executing Eq. (166). The solution for $\omega_m^{k+1}|_{r=r_i}$ is used by taking the m^{th} element of its derivative with respect to z, which gives $\frac{\partial\omega}{\partial z}\Big|_{z=h/2}$. The result is then used to compute M_i^k in the first step of the solver which is required to solve the thinning equation at the next time step.

The procedure discussed so far considers the complete model with gas dissolution and surfactant presence. When a specific case is examined, the model equations are adjusted according to Table 4.

Table 4: The model equations for specific cases

Cases	Adjustment to the Model
Immobile interfaces (U_t = 0)	- The thinning equation becomes Eq. (106) - Eqs. (90) and (133) are not required
Fully mobile interfaces ($\lambda^* \to 0$)	- The thinning equation turn into Eq. (107) - The velocity equation becomes Eq. (108) - The boundary condition in Eq. (109) is applied
Absence of gas dissolution (M = 0)	- Eq. (125) is not required - The second part of the solver is not required
Absence of surfactants (Γ_0 = 0)	- Eq. (90) is not required

The solver computes iteratively to give solutions for the next time steps until the coalescence is estimated to occur. This behavior is indicated by quick decreases in the dimensionless minimum film thickness, min (h_i^{k+1}), which may reach negative values in the simulation. Therefore, the simulation is set to stop the iteration when min (h_i^{k+1}) reaches below 10^{-3} as an indicator of coalescence. The time required for one single simulation to satisfy this condition is considered as the coalescence time. When the gas dissolution is taken into account, it may cause some increases in min (h_i^{k+1}) to a larger value than the initial one. In this case, the outcome is considered as no coalescence.

4 Results and Discussion

In this study, the film drainage behavior is examined by considering two phenomena: the dissolution of gas and the surfactant presence. Each phenomenon is studied separately in Sections 4.1 and 4.2 by investigating their physical behaviors, i.e., mass fluxes in the presence of dissolution and tangential mobility for systems with surfactants, and their impacts on the drainage behavior. Then, the combined effect of both phenomena is analyzed in Section 4.3.

The model is validated by executing four cases which are then compared to the solutions obtained by Ozan and Jakobsen (2019a). Two of these cases consider the constant mass flux and the variable mass flux to validate the first and the second parts of the solver, respectively, for the immobile case. Similarly for the mobile case, each part of the solver is validated by taking the tangential mobility into account.

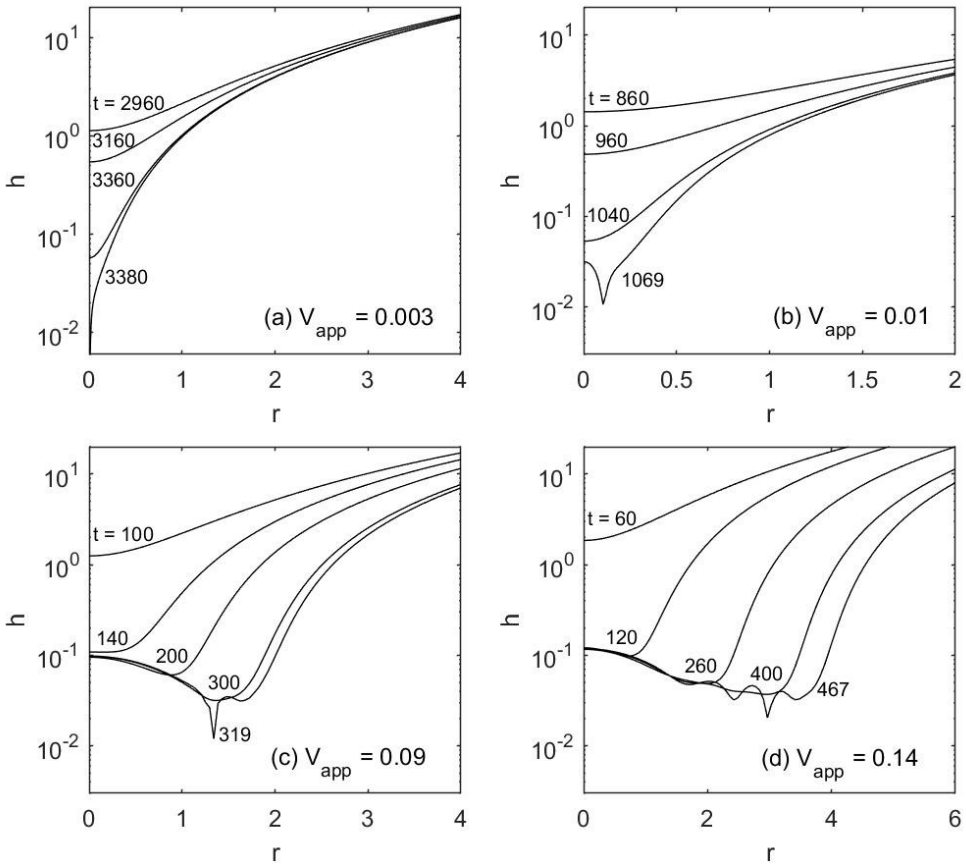

Figure 6: Time evolution of the film thickness profiles reproduced from Figure 5 of Ozan and Jakobsen (2019a) for validation of the first part of the solver without considering the mass transfer (M = 0). The four types of behavior in (a)-(d) respectively correspond to the nose rupture, the rim rupture with dimple formation and with multiple rims formation (the pimple and the ripple shapes). The results are obtained at A^* = 10^{-4}, h_{00} = 10, and r_∞ = 15.

Figure 6 presents the time evolution of the film thickness profiles at different V_{app} values, which are obtained from the first part of the solver for no-flux case ($M = 0$). Overall, the results seem to be identical to Figure 5 of Ozan and Jakobsen (2019a). In all subplots, the film thickness decreases with time due to the drainage until the film ruptures at different times, shown in the last profiles, after which coalescence is estimated to occur. In Figure 6 (a), the rupture occurs at the center which is indicated as the nose rupture. This type of behavior occurs at relatively low V_{app} where the attractive van der Waals forces start to become significant to destabilize the film and results in coalescence before the capillary forces act upon the system. As V_{app} increases, the capillary forces become sufficiently stronger to promote rims formation at the interface before the film is thin enough to allow the van der Waals forces to act substantially. In these cases, the film ruptures at the position of the rim, which is called the rim rupture as represented in Figure 6 (b)-(d). The dimple shape in case (b) is commonly known whereas the other two shapes are discussed further by Chan et al. (2011). According to their Section 3.1.2, the pimple in case (c) refers to an additional minimum emerging locally at the interface while the ripple in case (d) is indicated by the multiple minima and maxima appearing along the interface.

The second part of the solver is validated together with the first part by setting K' into zero, i.e., no mass flux, and comparing the results with the constant flux case for $M = 0$. The comparison in Figure 7 shows that the results with the two-step solver, i.e., the 2D solver, fit perfectly with the constant flux solver. Therefore, all results for the no-flux case in this section are obtained from the constant flux solver.

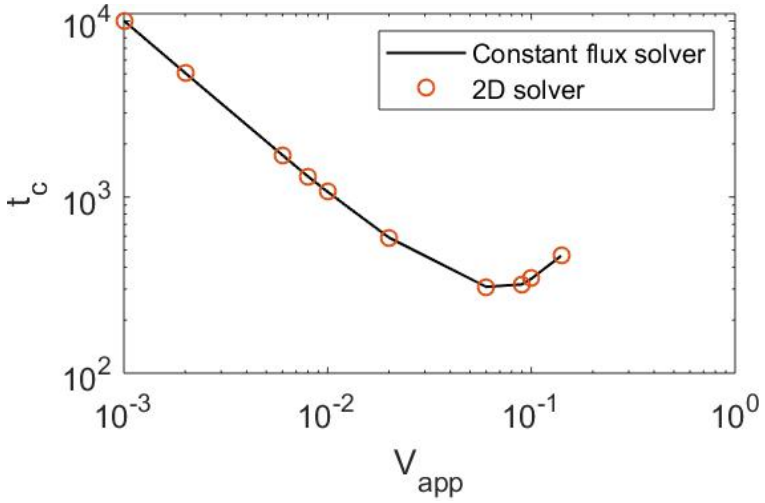

Figure 7: Coalescence time as a function of V_{app} for validation of the 2D solver. All results are obtained at $A^* = 10^{-4}$, $h_{00} = 10$, and $r_\infty = 15$.

To compare with Figure 4 of Ozan and Jakobsen (2019a), the t_c curves in Figure 7 seem to match well with their $A^* = 10^{-4}$ case. The linear decreasing trend of t_c within the low V_{app} values is found to give the nose rupture as described in Figure 6 (a). Then, the slope of $\log(t_c)/\log(V_{app})$ decreases at around $V_{app} = 0.01$ where the dimple starts to grow along the interface as represented in Figure 6 (b). This decreasing slope indicates that the drainage rate is slowed down by the emergence of the dimple which tend to strengthen the resistance of the interface to the drainage process. Then, the decreases in t_c become less significant until t_c passes its minimum point and starts to increase with V_{app}. In this regime, the multiple rims appear along the interface as shown in Figure 6 (c)-(d), which delay the drainage rate even more, resulting in the increasing trend of t_c.

The mobile solver is validated by reproducing Figures 7 (a) and 10 of Ozan and Jakobsen (2019a) using the first-step of the solver and the two steps of the solver, respectively. In their work, the time is scaled with μ_d instead of μ_c that is used in this study. This results in the different transformation of the dimensionless time, i.e., t_c. To yield the same transformation as their work, the coalescence time obtained in this study needs to be divided by the viscosity ratio, λ^*. The results are presented in Figure 8 which seem to be in good agreement with Figure 7 (a) of Ozan and Jakobsen (2019a). The decreasing-increasing trend of t_c is similarly found in the mobile case for different extents of mobility. As λ^* values get smaller, i.e., more mobile interfaces, the coalescence times approach to the fully mobile case which fits with the results for $\lambda^* = 0.1$.

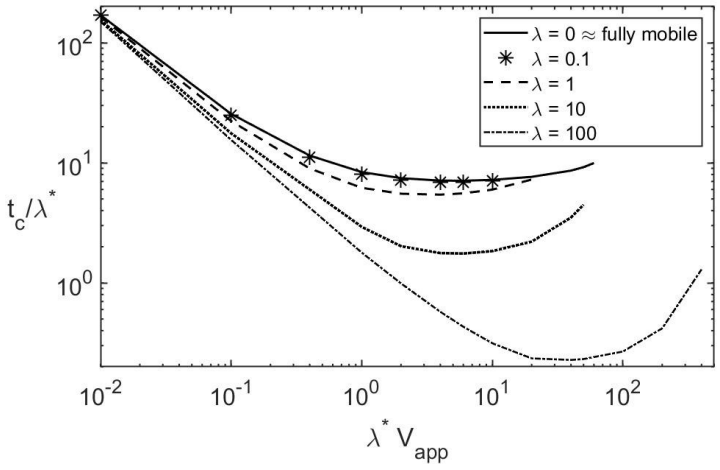

Figure 8: Reproduction of Fig. 7 (a) of Ozan and Jakobsen (2019a) using the first-step of the solver showing coalescence time for different λ^* as a function of V_{app} evaluated at $A^* = 10^{-4}$, $h_{00} = 2$, $r_\infty = 30$, and $M = 0$.

Figure 9 shows the time evolution of the film thickness profiles for partially and fully mobile cases that are obtained from the two-step solver. The results seem to be in accordance with the ones obtained in Ozan and Jakobsen (2019a)'s Figure 10 where the pimpling and the wimpling behaviors in their figure are also found here. While the pimple shape in case (a) is similarly shown in Figure 6 (c) for immobile case, the wimple shape in Figure 9 (b) only shows up when the interface is fully mobile ($\lambda^* \to 0$). This corresponds to the contribution of the parabolic flow ($\lambda^* \neq 0$) in hindering the emergence of the wimple as discussed in Ozan and Jakobsen (2019a).

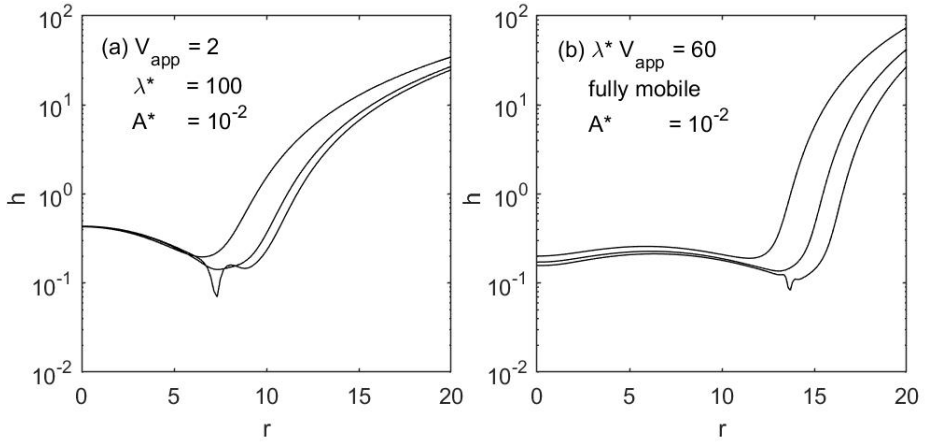

Figure 9: Reproduction of Fig. 10 of Ozan and Jakobsen (2019a) using the two-step solver which shows the time evolution of the film thickness for (a) partially mobile and (b) fully mobile interfaces, exhibiting the pimpling and the wimpling behaviors, respectively. All results are obtained at $h_{00} = 2$, $r_\infty = 30$, and $K' = 0$.

4.1 The Effect of Gas Dissolution on Coalescence

The effect of the gas dissolution is investigated for three cases based on 1 mm bubbles in water. The first case considers low Pe where the convective transport is assumed to be negligible. In the second case, the mass flux is assumed to be constant and its effect is investigated by varying M. The third case applies for variable mass fluxes which hold for any Pe values. This case is studied by observing the behavior of the mass transfer, i.e., the time evolution of M, before the effects of the gas solubility and Pe on the drainage rate are examined. As the default case, all results are evaluated for immobile interfaces ($U_t = 0$) with the absence of surfactants. Specifically for the first case, the negligible convection assumption implies that the reaction term should stay to balance the diffusive term. This means that the first case only holds for systems which involve reactions.

4.1.1 Case 1: Low Péclet Number

The model in this case is evaluated by estimating M for the zero- and the first-order reactions as expressed in Eqs. (121) and (123). A typical bioreactor system is taken as the base case, where O_2 is commonly used as nutrients for cells. Following the typical bioreactor systems discussed in Lopes et al. (2014), the O_2 solubility in water at 1-15 bar is taken to estimate K' which is on the order of $10^{-5} - 10^{-4}$. Then, by assuming that the dimensionless film thickness is roughly at $h \ll 0.1$, M is estimated to be around $10^{-14} - 10^{-9}$ for the zero-order reactions and $10^{-16} - 10^{-10}$ for the first-order reactions. These values are assigned as constant M to estimate the coalescence times for different V_{app}, which are summarized in Figure 10.

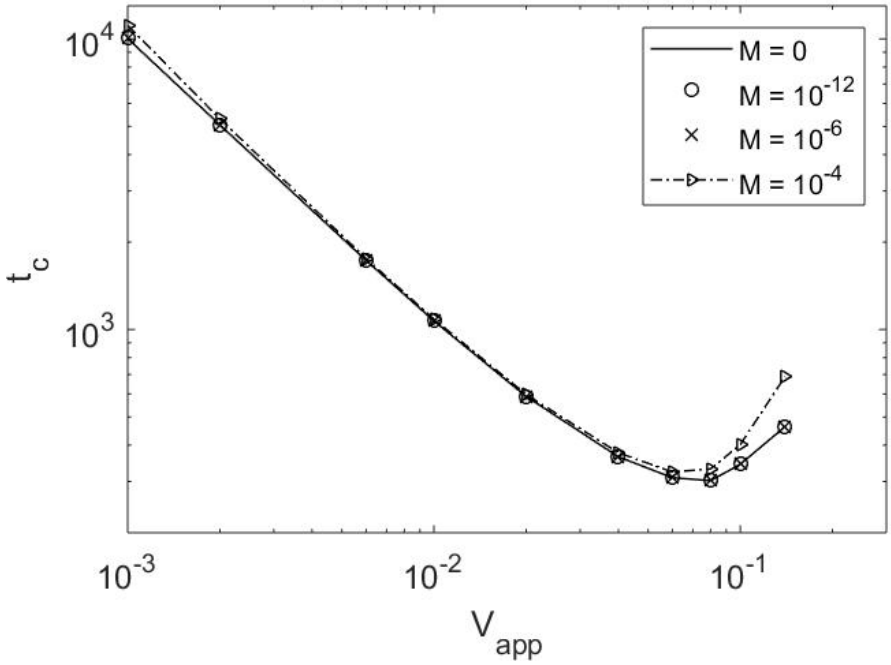

Figure 10: Coalescence time for different M values as a function of V_{app}. All results are evaluated at A^* = 10^{-4}, h_{00} = 10, and r_∞ = 15.

Compared to the no-flux case ($M = 0$), the coalescence time for $M < 10^{-4}$ seems to be indistinguishable. As expected from Eq. (101), when M is too small, the effect of dissolution on the film drainage becomes insignificant. In this case, M depends on the gas solubility, K', and the consumption rate of the gas, r_A, which are relatively low for bioreactions. The low K' value results in low concentration gradient within the film, which restricts the diffusive transfer of the substance. In addition, r_A, which serves as the sink term in this case, is expected to promote larger flux compared to the non-reactive systems by increasing the concentration gradient. However, this effect becomes less significant when r_A is low. According to Eqs. (121) and (123), M seems to be quite insensitive to the changes in K' and r_A. Thus, changing these

two parameters to larger values for a system with chemical reactions still yields small M values, which are below 10^{-4}.

In comparison to reactive systems assumed in this case, Li et al. (2019) observed that gas dissolution also occurs and influences coalescence in the absence of reactions. In their experiments, they used CO_2 which has a solubility of 100 times higher than the O_2 solubility and came up with their Eq. (3.2) which describes the relationship between the mass flux of CO_2 and the bubble size. According to their expression, the values of M for 1 mm CO_2 bubbles are estimated to be on the order of $10^{-6} - 10^{-2}$ (further details are derived in App. 0). Based on Figure 10, the values of $M \geq 10^{-4}$ for CO_2 bubbles are seen to be influential on the coalescence time. This implies that the effect of dissolution may not be neglected for gases with high solubility. In addition, the considerable effect of dissolution also applies for non-reactive systems according to Li et al. (2019), which cannot be simulated using the low Pe case since M in this case disappears when there are no reactions. This indicates that the model for low Pe case may be inadequate to represent the dissolution phenomena on film drainage.

4.1.2 Case 2: Constant Mass Flux

In this case, M is assigned as a constant value which may represent any values of Pe, K', and reactive or non-reactive systems. The values of M are varied between 10^{-8} and $5\ x\ 10^{-4}$ with the results given in Figure 11. While the curves for $M < 10^{-4}$ match the no-flux case, the results for $M \geq 10^{-4}$ show slower drainage time compared to the no-flux case. The gas transfer from the dispersed to the continuous phase shrinks the bubbles out which displaces the interfaces away from each other. This implies that the rate of the film drainage becomes slower with higher M. As also described in Eq. (101), when M is constant, the film thickness increases more with larger M.

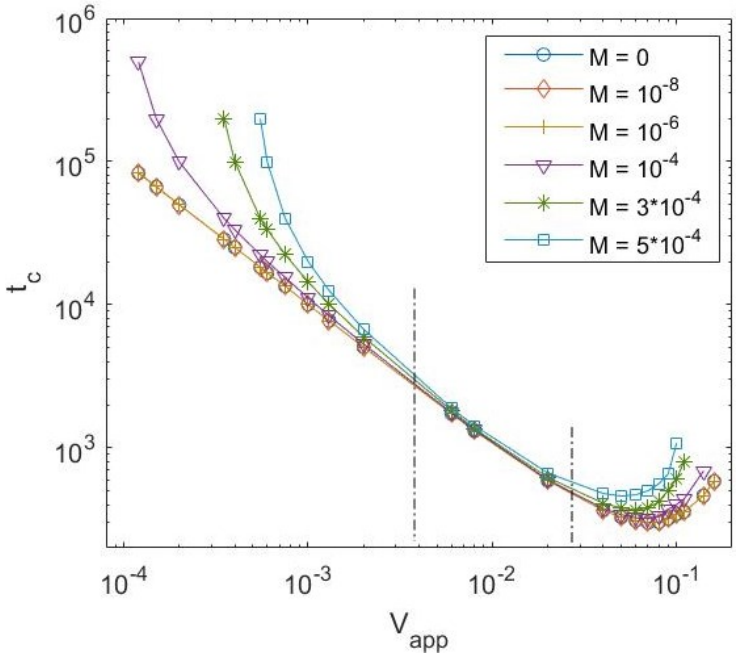

Figure 11: Coalescence time for different M as a function of V_{app}, showing three different patterns. All curves are obtained at $A^* = 10^{-4}$, $h_{00} = 10$, and $r_\infty = 15$.

For $M \geq 10^{-4}$, the extent of M effect on t_c seems to change with V_{app}, revealing three patterns which are separated roughly by the dot-dashed lines. At low V_{app} values, the effect of M in slowing the drainage rate becomes less significant with V_{app} until the curves merge at intermediate V_{app} values, starting from $V_{app} \approx 0.006$. These cases occur in the decreasing trend of t_c where the contact time between the bubbles gets faster with V_{app}. This reduces the period for the mass flux to occur, which consequently decreases the significance of M effect in prolonging t_c. As M is assumed constant here, the extent of M effect can be connected directly to the contact time. This is also shown through the boundary condition at $r = r_\infty$ in Eq. (103) where M becomes less dominant on the rate of the interface displacement when V_{app} is larger. After passing the intermediate values, at $V_{app} \geq 0.02$, the drainage rate is slowed down by the emergence of the dimple. This implies that the contact time begins to increase with V_{app}, thus, the curves start to separate again as discussed further in Figure 14.

The slowing down effect of M is also found for very low M values when they are comparable to V_{app}. As shown in Figure 12, the t_c curves for $M = 10^{-8}$ and $M = 10^{-6}$ appear to deviate from the no-flux case within very low V_{app} values. However, according to Yaminsky et al. (2010), the coalescence hardly occurs in such low V_{app} since the film tends to stay stable at

$V_{app} < 1$ μm/s. This value corresponds to a dimensionless V_{app} of 10^{-4} below which the visible effect of the mass transfer for $M < 10^{-4}$ may be unrealistic.

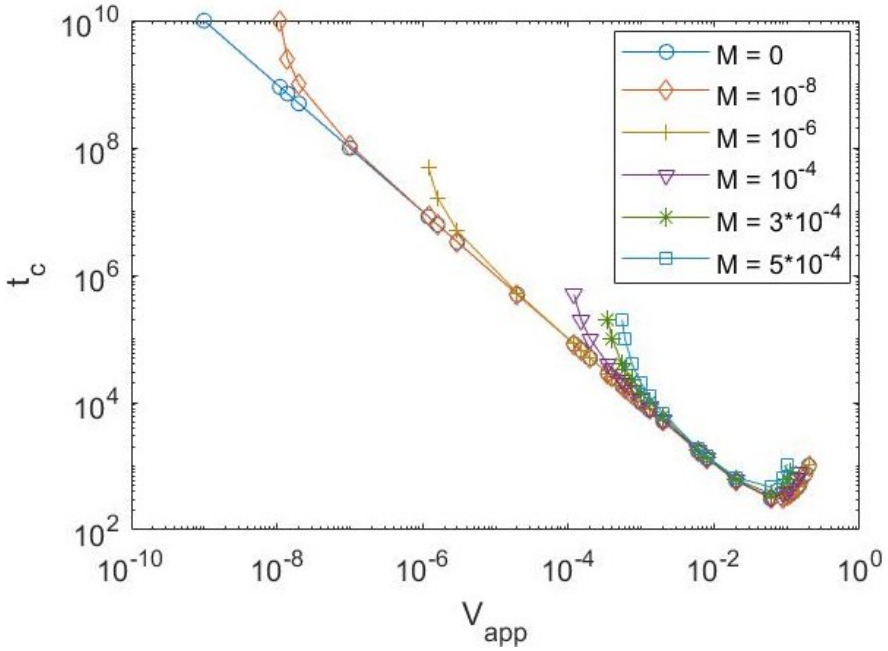

Figure 12: Coalescence time as a function of the approach velocity at very low V_{app} regime, showing that smaller M affects the coalescence time when M values are comparable to V_{app}

At intermediate V_{app} values, the effect of M in increasing t_c can be seen clearer in Figure 13. All curves for $M < 10^{-4}$ show similar t_c which are indicated the same as t_c for the no-flux case. Then, t_c starts to increase with M by around 1%-2% for $M = 10^{-4}$ and 8%-14% for $M = 5\ x\ 10^{-4}$. After this value, higher M seems to give asymptotic trend which may indicate that the gas dissolves completely into the continuous phase. However, there is no apparent reason for this behavior to occur in real systems, especially since the mass transfer should reach an equilibrium state. At this stage, there is no concentration difference between the dispersed phase and the continuous phase, i.e., no further phase change.

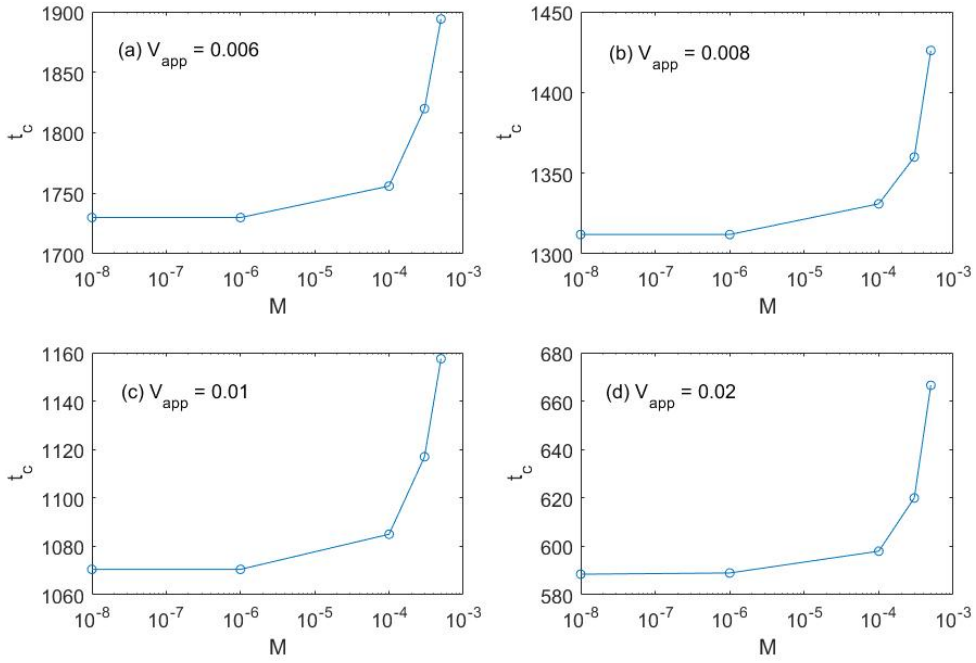

Figure 13: Coalescence time as a function of M at (a) V_{app} = 0.006, (b) V_{app} = 0.008, (c) V_{app} = 0.01, and (d) V_{app} = 0.02 with A^* = 10^{-4}, h_{00} = 10, and r_∞ = 15

At high V_{app} values, $V_{app} > 0.02$, the curves for $M \geq 10^{-4}$ separate from the no-flux case as shown clearer in Figure 14. The decreasing trend correspond to the dimple formation at the interface, which delays the drainage process compared to the linear trend in the first two patterns discussed above. This allows the mass transfer to occur for longer period and affect the drainage behavior more significantly. As V_{app} becomes larger, the dimple becomes more pronounced, which decreases the drainage rate more, provides longer contact time, and results in more visible effect of M until multiple rims appear in the increasing trend of t_c. In this regime, all curves increase with approximately the same slope of $\log(t_c)$ /log (V_{app}).

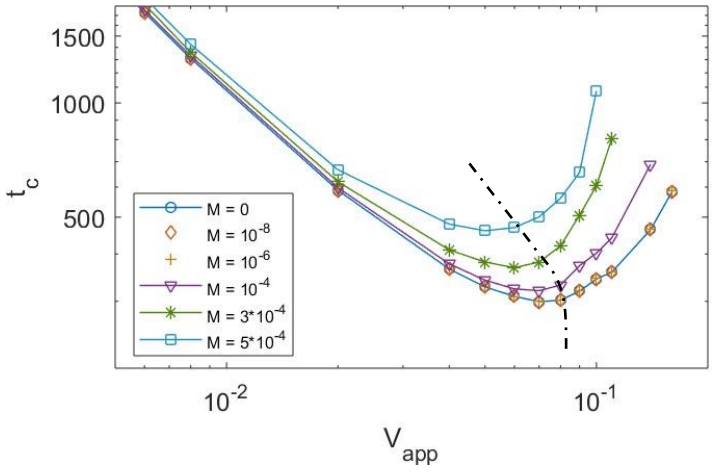

Figure 14: Coalescence time as a function of V_{app} at high V_{app} regime, showing that the minimum t_c is obtained at lower V_{app} for higher M

It can be seen respectively from the decreasing and the increasing trends that the curves for larger M separate at lower V_{app} and reach the minimum t_c at lower V_{app} as well. These behaviors show that the mass transfer favors the interfaces to deform to a larger extent, as can be seen in Figure 15. In both cases, the thickness profiles show similar behavior until $t = 200$ at which the interface starts to deform. After this stage, the two cases show different behavior where the no-flux case gives film rupture already at $t = 305$ with the deformed radius of $r_d \approx 1$ while at the same time, the film for $M = 5\,x\,10^{-4}$ has not reached its critical thickness. Consequently, the interface for $M = 5\,x\,10^{-4}$ keeps deforming to a larger r_d until the film ruptures at around $t = 465$ and $r_d \approx 1.8$. Therefore, the drainage for higher M reaches the multiple rim regime, i.e., passes min (t_c), at lower V_{app}.

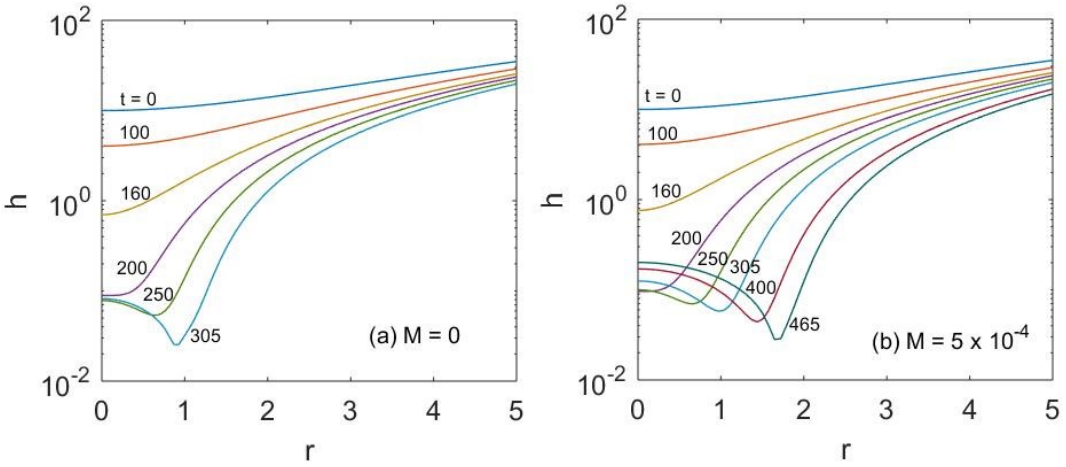

Figure 15: Time evolution of the film thickness profiles for (a) the no-flux case (M = 0) and (b) M = 5 x 10^{-4} showing wider deformed radius, r_d, caused by the gas dissolution. All results are obtained at V_{app} = 0.06, A^* = 10^{-4}, h_{00} = 10, and r_∞ = 15.

The results with constant mass flux show that the gas dissolution starts to affect the film drainage when $M \geq 10^{-4}$ which is in the range of the approximated M for CO_2 bubbles. Meanwhile, the dissolution of gasses with low solubility, such as O_2, seems to have no effect on the drainage. However, mass fluxes in real systems may not stay constant along the interfaces and during the interaction. Therefore, an analysis on the variable mass flux case with 2D model is required to conclude the effect of the gas dissolution on coalescence.

4.1.3 Case 3: Variable Mass Flux (2D Model)

In this section, M is computed throughout the simulation as a function of r and t which requires the second part of the solver in addition to the first part. As the default case, the convective and the diffusive transfer rates are considered to be equally significant by setting $Pe = 1$. The gas solubility is taken as $K' = 10^{-3}$ which represent systems such as CO_2 bubbles dispersed in

water at 1 bar or O_2 bubbles dispersed in water at 100 bar. The results are initially examined by analyzing the bulk velocities and the mass fraction profiles within the film as presented in Figure 16.

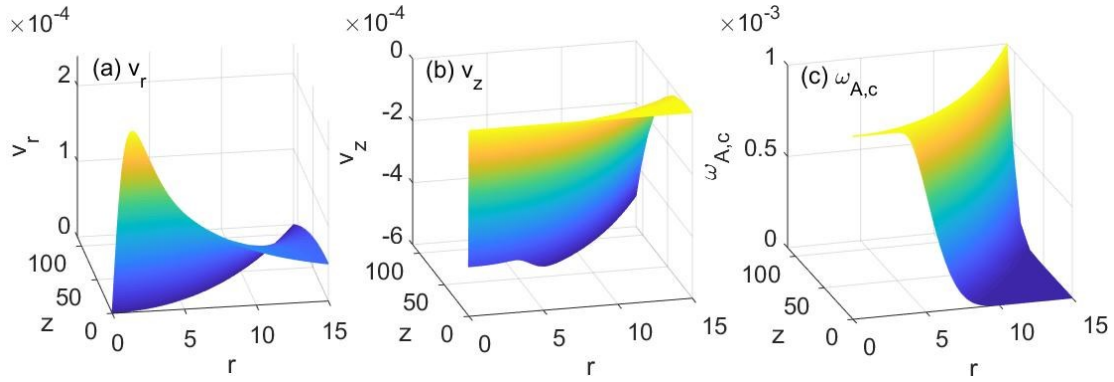

Figure 16: Surface profiles of (a)-(b) the bulk velocities and (c) the mass fraction at t = 100. The results are obtained at K' = 10^{-3}, Pe = 1, V_{app} = 0.001, A^* = 10^{-4}, h_{00} = 2, and r_∞ = 15.

All profiles are obtained at $t = 100$ which show the film behaviors before the bubbles deform. The radial bulk velocity, v_r, along the interface (the dark-blue area in (a)) shows zero values which is expected for immobile case (U_t = 0). These values increase along z-direction and attain their maximum at $z = 0$, indicating that there is no further velocity gradient in z-direction, which is also consistent with the first symmetry condition in Eq. (96). The axial bulk velocity, v_z, follows the second symmetry condition in Eq. (96) which is zero at z = 0 (the yellow area in (b)). Then, v_z decreases to negative values towards the interface which represents the movement of the upper bubble to negative z. The mass fraction, $\omega_{A,c}$, at the interface (the yellow area in (c)) has the same value as $K' = 10^{-4}$ which then decreases in both z- and r-directions towards $\omega_{A,c} = 0$, showing the concentration difference within the film.

The surface profiles presented in Figure 16 seem to fit the expected physical behavior. However, there are some numerical stability issues encountered during the evaluation of M behavior, particularly in the rim rupture regime and the mobile solver. The film drainage behavior presented in Section 4.1.3.1 is obtained from the 2D solver after the numerical issues are resolved to a certain stage, as discussed further in Section 4.1.3.2. During the attempts of resolving these issues, some alternative methods of estimating the coalescence time were examined and discussed in Section 4.1.3.3.

4.1.3.1 Film Drainage with the 2D Solver

The time evolution of M is introduced in this section to understand the physical behavior of the variable mass flux across the interface. In Figure 17 (a), it is shown that M decreases with time throughout the simulation until coalescence is estimated to occur at $t_c \approx 2100$. For all r positions, M initially falls by around 10 times to a value of $M \approx 5\,x\,10^{-4}$ before its behavior becomes dependent of r. The decreasing trend of M indicates that the mass flux diminishes during the film drainage. As the gas transfers to the continuous phase, the concentration of the gas within the film, $\omega_{A,c}$, increases with time. This reduces the concentration difference of the gas inside the film which appears in the last term of Eq. (102), resulting in the decreasing M throughout the time.

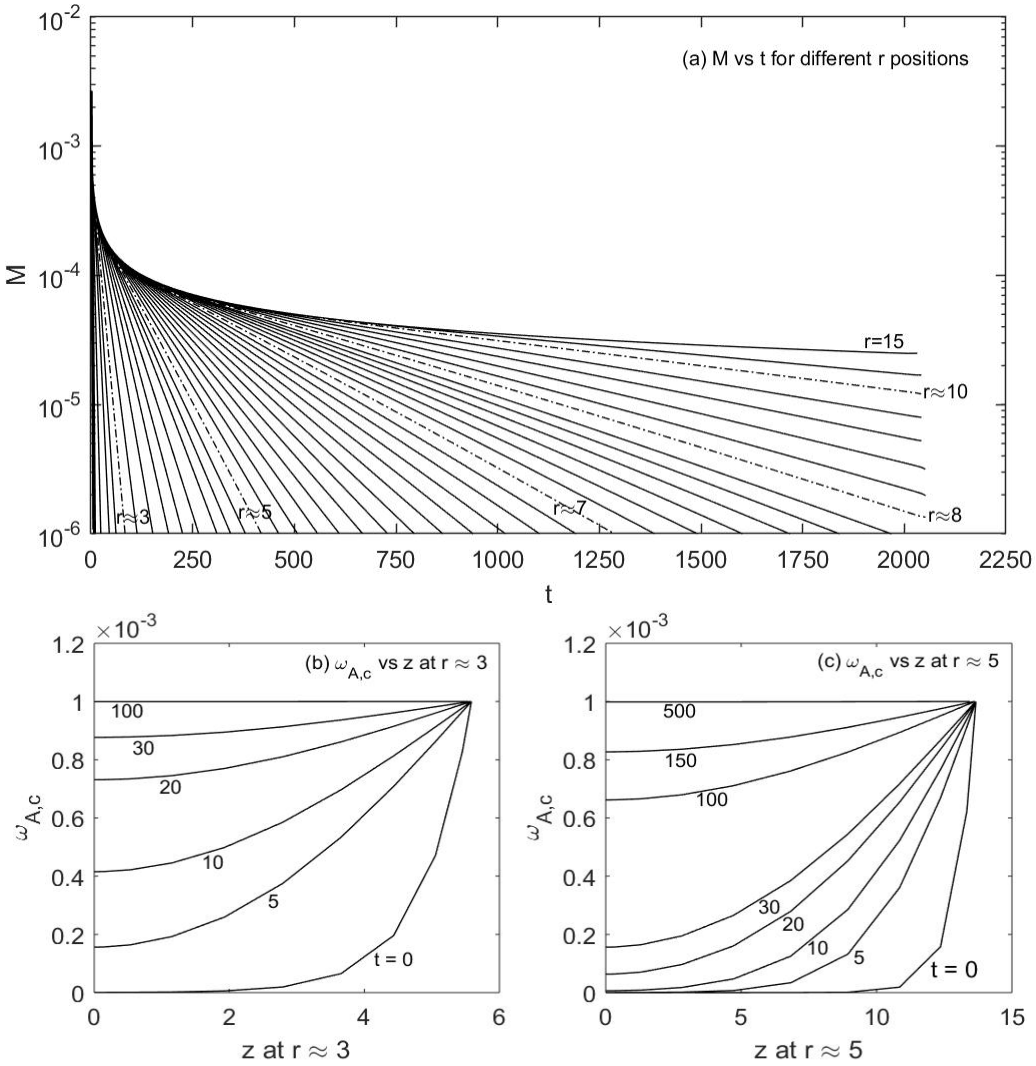

Figure 17: (a) M as a function of time from the smallest to the largest r positions where the leftmost to the rightmost dashed-dot curves indicate $r \approx 3$, $r \approx 5$, $r \approx 7$, $r \approx 8$, and $r \approx 10$, (b)-(c) time evolution of the mass fraction of A within the film against z for $r \approx 3$ and $r \approx 5$. All results are obtained at $K' = 10^{-3}$, $Pe = 1$, $V_{app} = 0.001$, $A^* = 10^{-4}$, $h_{00} = 2$, and $r_\infty = 15$.

Compared to large r positions, M decreases more significantly at smaller r. This can be explained through Figure 17 (b)-(c) where $\omega_{A,c}$ grows faster for smaller r, which reduces the concentration gradient more quickly. This happens because the film within smaller r is relatively thinner, which enables the gas to fill these domains more quickly. The dissolved gas accumulates inside the film until its concentration at the given r reaches $\omega_{A,c} = K'$, which is indicated as local film saturation. In this case, the gas cannot dissolve further, i.e., no mass flux, since there is no concentration gradient along z. Therefore, the last term of Eq. (102) becomes zero, resulting in $M = 0$. The film saturation locally occurs at different time for different r. As described in Figure 17 (b)-(c), the local saturation for $r \approx 3$ is obtained at $t \approx 100$ while at a larger position, at $r \approx 5$, the film saturates at $t \approx 500$. These conditions are detected in Figure 17 (a) where M for the corresponding r and times reaches below 10^{-6}. This implies that $M \leq 10^{-6}$ is small enough to consider that the film is locally saturated, which also shows that the film saturates more quickly at smaller r.

The M behavior is evaluated further for higher V_{app} values, where the decreasing M also holds as shown in Figure 18 (a)-(c). In all cases, M at a given time decreases with smaller r and reaches its minimum value at $r = 0$. Then, the film saturates locally ($M \leq 10^{-6}$) starting from the center, which matches the analysis of Figure 17. The local saturation seems to occur at wider r for larger V_{app}, reaching $r \approx 2.1$, $r \approx 2.2$, and $r \approx 2.7$ at $t = 35$ for the three velocities in cases (a)-(c), respectively. This behavior can be seen more clearly in Figure 18 (d) which presents the width of saturated film, r_{sat}, for the three corresponding V_{app} as a function of time. The areas under the three curves represent the saturated domains which increase during the drainage process. It is clearly seen that r_{sat} is relatively wider for larger V_{app} which implies that V_{app} favors the film to saturate more easily. This happens because the film thins out faster with larger V_{app} before the interfaces deform and start to affect the drainage behavior. As a consequence, the film is filled by the gas more quickly and reaches the solubility at earlier time. This effect is magnified by the role of V_{app} in enforcing the film to flow out of the collision zone which expands r_{sat} wider. Especially for the cases with comparable convective and diffusive transfer rates as investigated here, M is affected by the flow of the film which gets stronger with the velocity, allowing the film to reach the local saturation more easily.

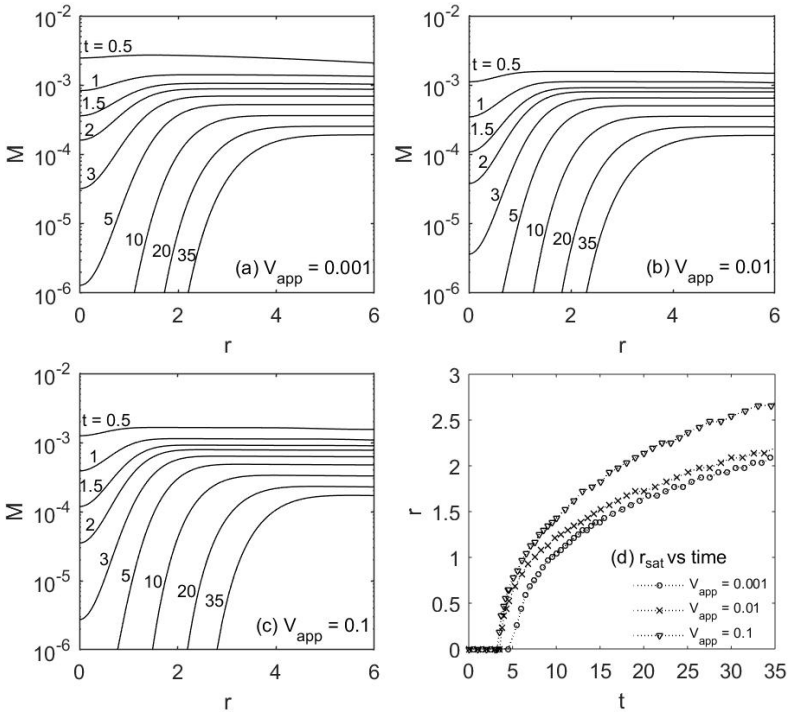

Figure 18: Time evolution of (a) - (c) M profiles for different V_{app} values and (d) the radial position which separates the saturated and unsaturated film domains. All results are obtained at K' = 10^{-3}, Pe = 1, A^* = 10^{-4}, h_{00} = 2, and r_∞ = 15.

To compare with small r positions, the behavior in large r can be examined from the maximum values of M which are estimated to occur at $r = r_\infty$ according to Figure 17. The results in Figure 19 show that max(M) increases with decreasing V_{app} and it converges to the same value for $V_{app} = 10^{-3}$ and $V_{app} = 10^{-4}$. This indicates that the rate of decreasing M is relatively faster for larger V_{app}, which is consistent with the analysis of easier local saturation for larger V_{app}.

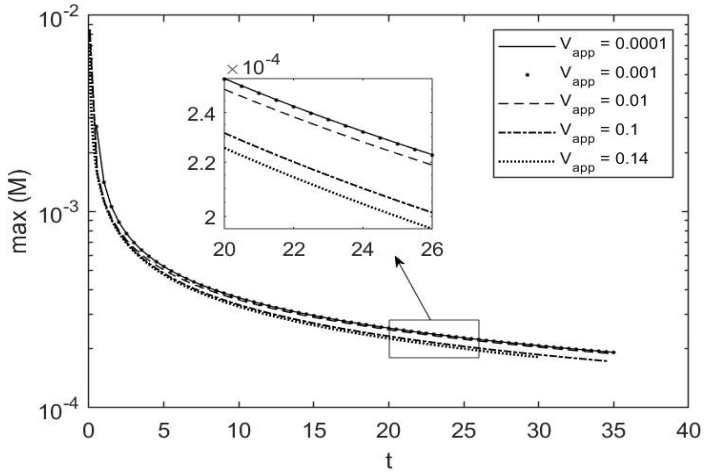

Figure 19: Time evolution of maximum M for different V_{app}. All results are obtained at K' = 10^{-3}, Pe = 1, A^* = 10^{-4}, h_{00} = 2, and r_∞ = 15.

After observing the dissolution behavior, now its effect on the film drainage is evaluated by varying Pe and K'. Figure 20 shows the effect of Pe on max(M) and t_c. It can be seen in case (a) that max(M) behaves differently with Pe, which rises until $Pe = 0.004$ and declines afterwards. When $Pe \leq 0.004$, the convective transport may not be strong enough to promote film saturation. Therefore, larger Pe results in more amount of mass crossing the interface without significantly promoting film saturation, which yields the increasing trend of max(M). This behavior changes after $Pe = 0.004$ when the convection is estimated to be influential enough to favor film saturation. In this case, higher Pe promotes larger mass flux which allow the film to reach local saturation more easily and eventually stops the mass transfer at earlier time. Consequently, larger Pe results in the decreasing trend of max(M) due to the implication from the film saturation. This is also noticed through Eq. (102) where the terms $2/Pe$ and $\partial\omega_{A,c}/\partial z$ give opposite effects on M. When the former term dominates, larger Pe yields lower M as indicated by the decreasing trend of max(M). This only occurs when Pe is sufficiently large to favor saturation. On the other hand, when the term $\partial\omega_{A,c}/\partial z$ dominates, larger Pe results in higher M, which corresponds to the increasing trend when the convection is too weak to influence the amount of the mass flux, i.e., harder for the film to saturate. Depending on the dominating term, the behavior of M may change with Pe as described in Eq. (102).

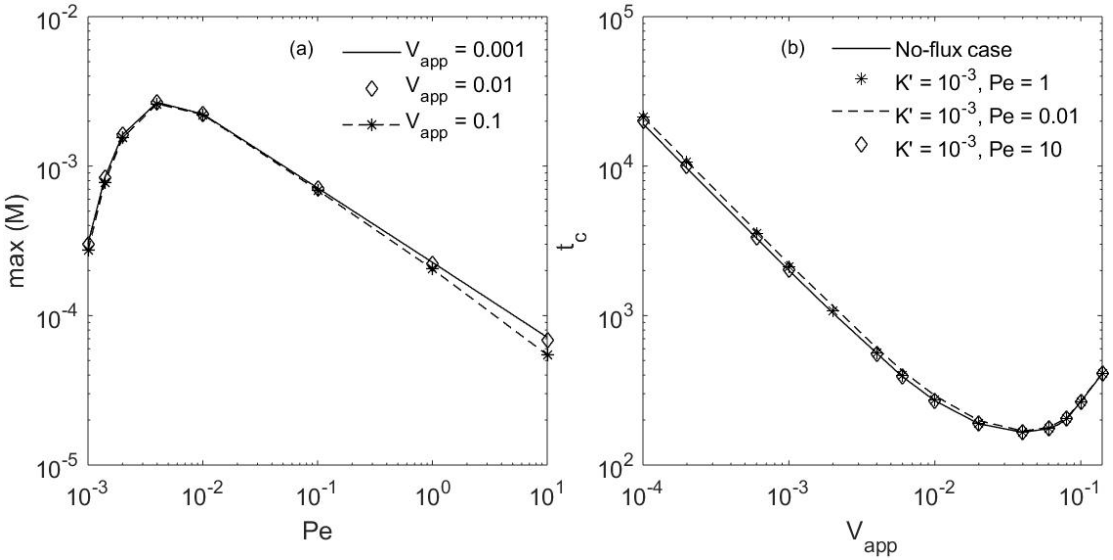

Figure 20: (a) Maximum M at t = 25 as a function of Pe for different V_{app} and (b) coalescence time for different Pe as a function of V_{app} with K' = 10^{-3}, A^* = 10^{-4}, h_{00} = 2, and r_∞ = 15

The effect of Pe on M appears to be insignificant on t_c as presented in Figure 20 (b). Considering that the mass transfer from the dispersed to the continuous phase displaces the interface to the reversed direction of the approach of the bubbles, it is expected for the mass

transfer to slow down the drainage rate of the film. However, the film saturation may be impactful on the drainage mechanism in this case. As larger M favors film saturation in the collision domain, the effect of dissolution disappears already at earlier time, resulting in the same behavior as the no-flux case afterwards. Thus, the coalescence time for $K' = 10^{-3}$ is not really affected by the gas dissolution.

In comparison to $K' = 10^{-3}$, the results for different K' are presented in Figure 21. It is shown that the t_c curves differ from the no-flux case only when $K' = 10^{-2}$ and $Pe \leq 1$. Since the gas concentration needs to reach the solubility for the film to saturate, a system with larger K' allows more amount of gas to transfer before reaching the film saturation. This implies that the dissolution occurs for a longer period and becomes more influential to the drainage process when K' is large enough to delay the saturation. In addition to K', the dynamic behavior of saturation is also influenced by Pe and V_{app}. As discussed in Figure 20, the film saturation is promoted by Pe and V_{app}, which explains the disappearance of the mass transfer effect at larger values of both parameters. Based on this analysis, the effect of gas dissolution associated with the role of film saturation needs to be considered when K' is sufficiently high and the values of Pe and V_{app} are relatively low.

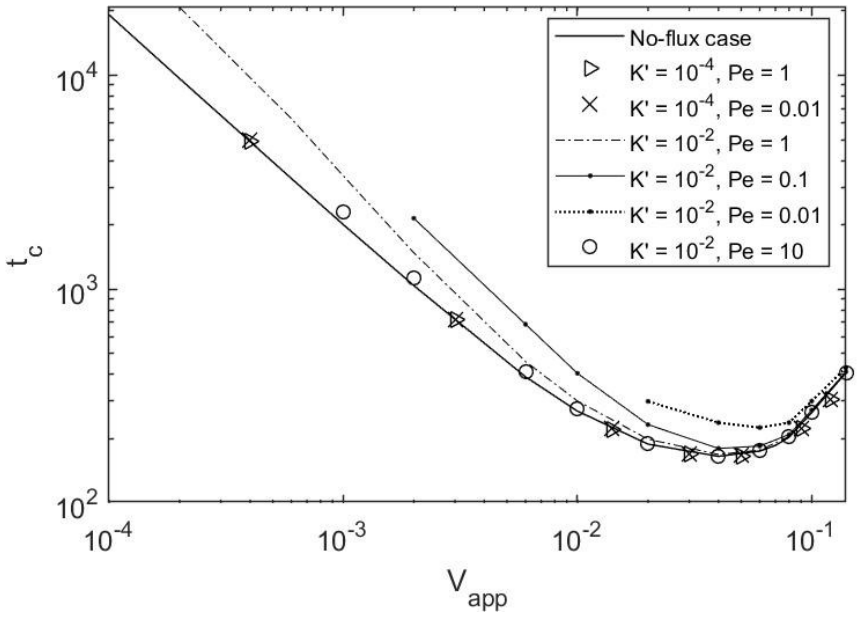

Figure 21: Coalescence time for different K' and different Pe as a function of V_{app} with A^* = 10^{-4}, h_{00} = 2, and r_∞ = 15

The drainage behavior discussed so far is based on the default case with immobile interfaces. Specifically for bubble collisions, the low viscosity of the bubbles compared to the continuous

phase result in high mobility of the interfaces. Nevertheless, the drainage behavior is found to be similar in the mobile cases when the gas dissolution is considered. When the interfaces are highly mobile, the tangential velocity appears to increase the drainage rate, which thins the film faster compared to the immobile one. This implies that the film saturates more easily which reduces the significance of the dissolution effect on t_c. Combining this condition with the other parameters leads to a conclusion that the gas dissolution influences the film drainage when the local saturation is delayed, which is only possible under specific conditions:

- The systems involve gasses with high solubility at relatively high pressure to give $K' \geq 10^{-2}$, which corresponds to the solubility of, for instance, CO_2 in water at 10 bar.
- The transport mechanism needs to be less influenced by the convection, i.e., $Pe \leq 1$.
- The approach velocity of the bubbles are sufficiently low.
- The tangential mobility of the interfaces are relatively low, which may imply a requirement for immobilization mechanisms to be involved in the system.

The analysis of the 2D case also shows the inadequacy of the model with constant mass flux as it is not capable to simulate the film saturation occurring during the bubble collision.

As mentioned previously, the results discussed in this section are obtained from the 2D solver which encountered some stability issues and numerical difficulties for some cases, such as M behavior for the rim rupture regime or the mobile interface. These issues are discussed further in Section 4.1.3.2 together with the attempts of resolving them.

4.1.3.2 Several Attempts to Resolve the Numerical Issues

Although the two-step solver is constructed to solve 1D problems separately, there are some numerical issues encountered during the initial simulations. One is related to small values involved in this study, such as the computed $\omega_{A,c}$ and M. Another challenge appears due to different grid points of z coordinate for each r since the domain size in z direction changes with r due to the interface's shape.

Implementation of $\omega_{A,c}$ and M Criteria to Handle Small Numbers

As $\omega_{A,c}$ varies between 0 and K', it may attain very small values close to zero, that are smaller than the machine accuracy and may be misinterpreted by the solver as small negative values. This error may accumulate throughout the next computations, resulting in significant negative values, which are not physical. Therefore, a command is added to the solver to set all small values, $\omega_{A,c} \leq 10^{-15}$, into zero, hereafter is called as the $\omega_{A,c}$ criterion. A similar issue was

found in the computed M. Despite the physical existence of negative M values, their presence in this study is contradictory to the assumption that the mass transfer occurs from the dispersed to the continuous phase. Therefore, a similar command as the $\omega_{A,c}$ criterion is applied in this case, mentioned as the M criterion. At a later stage of the simulation, the M criterion seems to cause some inconsistencies in the solver, particularly in the rim rupture regime. One example of the cases is shown in Figure 22 where the time evolution of the minimum film thickness, min (h), is compared for three different cases. The no-flux case $(K' = 0)$ represents the expected behavior while the other two cases, marked with the circle and the triangle symbols, are obtained for $K' = 10^{-3}$ with the inclusion and exclusion of the M criterion, respectively. The thickness at which the curve starts to drop rapidly is defined as the critical min (h) and the final time obtained at each curve represents the estimated t_c.

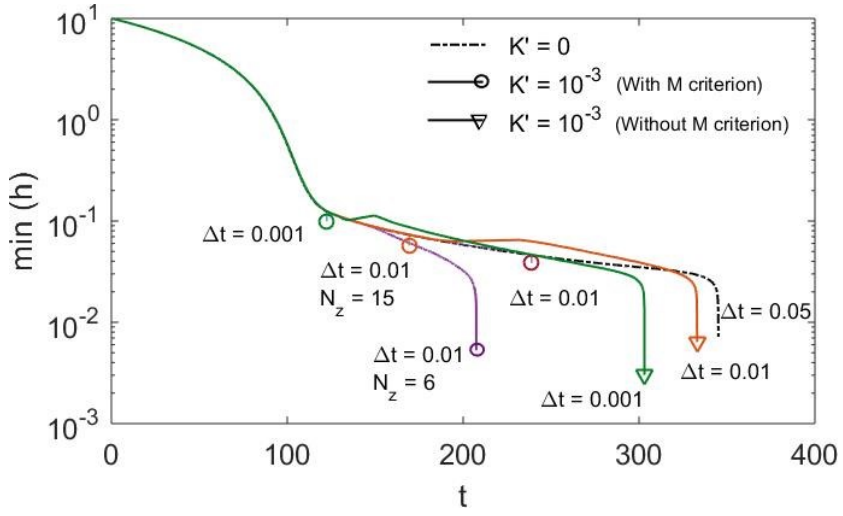

Figure 22: The time evolution of the minimum thickness for $K' = 10^{-3}$ at $V_{app} = 0.1$ evaluated at different parameter settings in comparison to the expected behavior represented by the dot-dashed curve (obtained for $K' = 0$)

Unlike the dot-dashed curve which decreases smoothly, the min (h) for $K' = 10^{-3}$ with M criterion seems to be broken off suddenly. In addition, it can be seen that different parameter settings such as the time step Δt and the spatial grid N_z give inconsistent t_c with various critical min (h) values. Meanwhile, min (h) for no M criterion cases look smoother and their critical min (h) are approximately the same as the one obtained in the no-flux case. By excluding the M criterion from the particular problematic cases, the estimated t_c for the whole simulation are compared to the results before excluding the M criterion, which are shown in Figure 23.

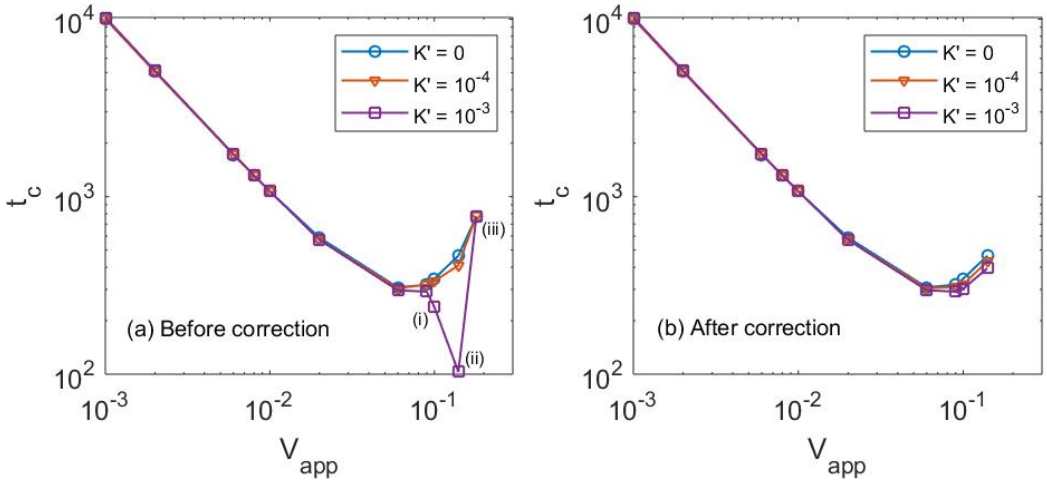

Figure 23: Coalescence time as a function of V_{app} when (a) M criterion is applied to the whole simulation, showing suspicious results: (i) and (ii) show unexpected decreasing t_c for $K' = 10^{-3}$ while (iii) shows unreasonable merging curves of t_c for all K' values, (b) M criterion is excluded from the problematic cases (i)-(ii). All results are obtained at $A^* = 10^{-4}$, $h_{00} = 10$, and $r_\infty = 15$.

In Figure 23 (a), t_c for $K' = 10^{-3}$ at (i) $V_{app} = 0.1$ and (ii) $V_{app} = 0.14$ are suspected to be inaccurate, which therefore, are re-evaluated without including the M criterion. Although it means that the mass transfer is allowed to occur in the opposite direction of the assumed one, the behavior inside the film may be unpredictable when the dimple emerges, e.g., the concentration gradients in r-direction, $\partial\omega_{A,c}/\partial r$, may change into negative values. Thus, the exclusion of the M criterion is still acceptable for the problematic cases. The last results at (iii) $V_{app} = 0.18$ also seems suspicious since there is no argument that can explain the merging curves after they separate at around the minimum t_c. Moreover, the deformed radius of the interface for case (iii) appears to be too large (above 50% of r_∞) to be considered as the gentle collision assumed in this study. Therefore, the result for case (iii) is excluded and the corrected version is given in Figure 23 (b). All of the inconsistencies occurred during the simulation are explained further in App. C.1.

Re-evaluation of *M* Criterion to Improve the Numerical Stabilities

Although the corrected results in Figure 23 (b) looks reasonable, there are some other issues appearing during the simulation. One of them is related to the convergence issues for mobile cases which are similar to Figure 22. In this case, the estimation of t_c does not converge to one value when the simulation parameters, such as Δt and N_z, are changed, which makes it hard to estimate t_c.

Beside the convergence issues, there are some other suspicious behaviors even for immobile case, such as the time evolution of M for a fixed r value. As presented in Figure 24 (a), some increases in M appear after $t \approx 180$ while M is expected to stay as zero due to film saturation. This behavior also appears in Figure 24 (b) after the M criterion is excluded from the solver with some decreases in M during the local saturation. These small decreases affect the behaviors significantly which may mislead the entire analysis of the effect of gas dissolution as discussed in Figure 25 and 26.

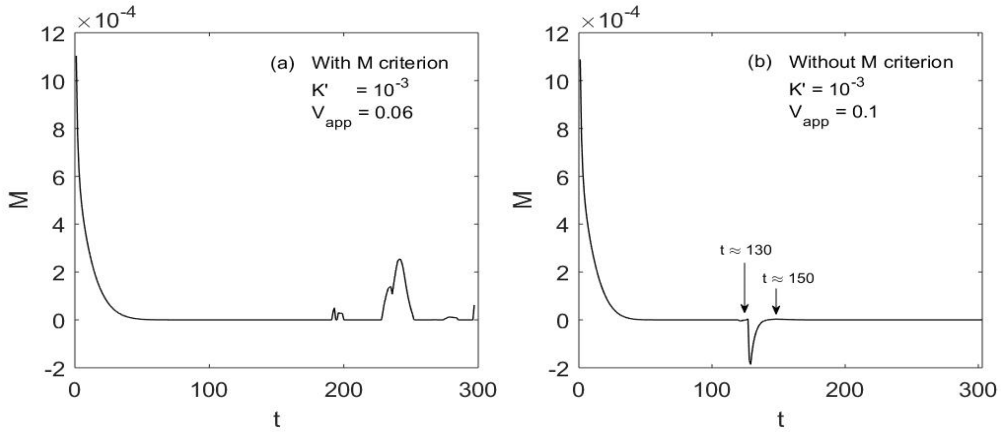

Figure 24: Time evolution of M evaluated at r = 1 for (a) with M criterion and (b) without M criterion. All results are obtained at A^* = 10^{-4}, h_{00} = 10, and r_∞ = 15.

Figure 25 shows the change of behaviors when the type of the rupture shift from the nose to the rim rupture. As discussed in Section 4.1.3.1, the effect of the mass transfer is found to consistently increase t_c. Meanwhile, in Figure 25, the increasing t_c due to mass transfer only holds for the nose rupture regime as if the mass transfer is also able to decrease t_c when the rim rupture occurs in case (d). These competing effects unfortunately can be misinterpreted as a physical phenomenon through Figure 26. In these film thickness profiles, the final value of the deformed radius, r_d, seems to be a requirement for the film rupture to occur. As the dimple emerges due to the capillary forces, the same V_{app} gives the same capillary forces, resulting in the same final value of r_d for both cases at $r_{d,final} \approx 2.2$. When $K' = 10^{-3}$ increases the film thickness after the interface deforms, at $h \approx 0.1$, r_d becomes larger compared to the no-flux case. This causes the case with $K' = 10^{-3}$ to reach $r_{d,final}$ faster and gives earlier t_c. However, the increasing thickness after $t = 120$ is found to occur due to computational errors instead of the physical effect of the mass transfer. This can be detected from the increasing min (h) in Figure 26 (a) which occurs at approximately the same time as the decreasing M in Figure 24 (b). This type of connection is similarly found in the mobile cases where the increases in min (h) also begin at min $(h) \approx 0.1$ as presented in App. C.1.

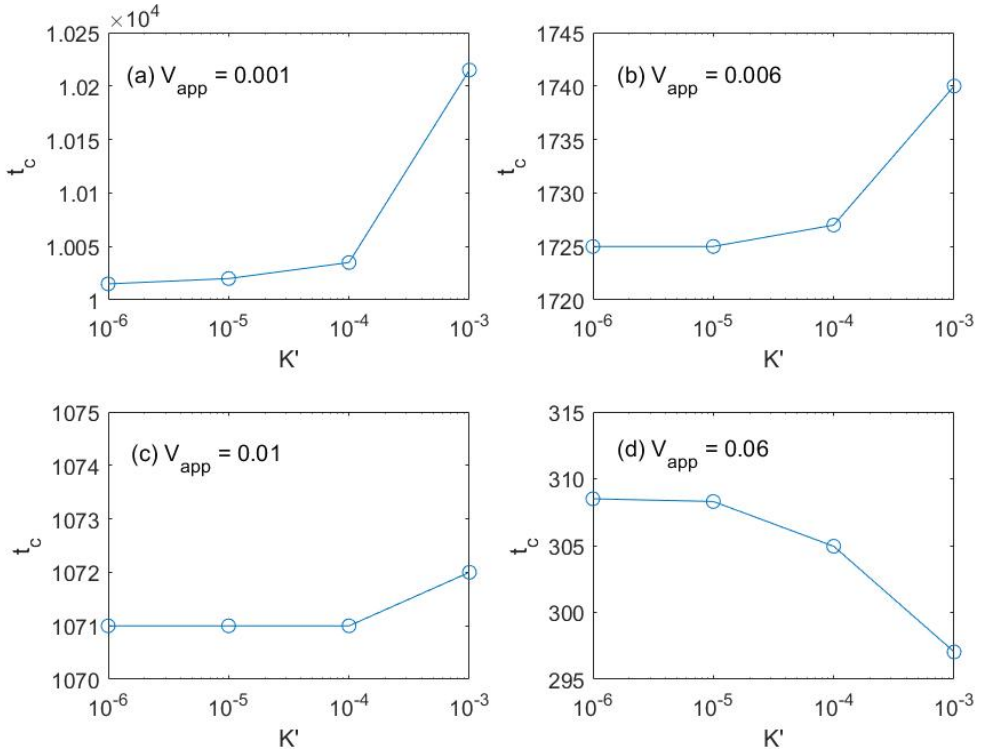

Figure 25: Examples of incorrect results for $K' = 10^{-3}$ obtained from unstable solver in comparison to the no-flux case, showing coalescence time as a function of K' for the nose rupture regime at (a) $V_{app} = 0.001$ and (b) $V_{app} = 0.006$, and for the rim rupture regime at (c) $V_{app} = 0.01$ and (d) $V_{app} = 0.06$. All results are obtained at $A^* = 10^{-4}$, $h_{00} = 10$, and $r_\infty = 15$.

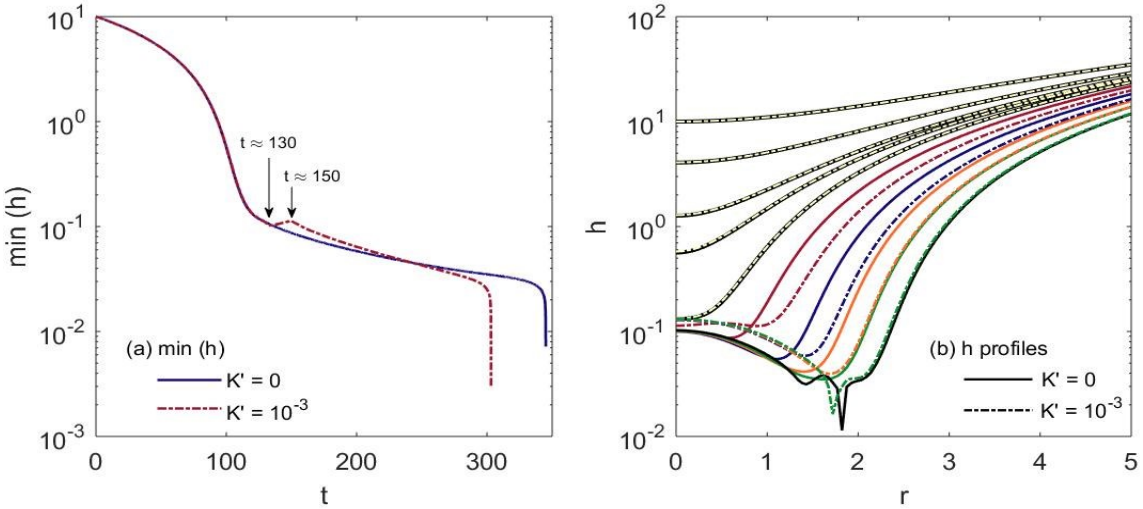

Figure 26: Examples of incorrect results for $K' = 10^{-3}$ obtained from unstable solver in comparison to the no-flux case, showing (a) some increases in min (h) for $K' = 10^{-3}$ and (b) the same value of $r_{d,final}$ reached faster for $K' = 10^{-3}$. The same color in subplot (b) represents the same dimensionless time at which the thickness profiles are obtained and the first five profiles (from $t = 0$ to $t = 120$) show the same behavior between the two cases. All results are obtained at $V_{app} = 0.1$, $A^* = 10^{-4}$, $h_{00} = 10$, and $r_\infty = 15$.

The reason behind the instabilities in M, i.e., Figure 24, is because the current M criterion only applies for a given time step at certain r values. Meanwhile, the computation for the next time steps may be influenced by the applied M criterion in the neighboring r from the previous time steps. In other words, the fluctuations in Figure 24 (a) might not come from small numbers anymore but due to some significant differences in M between the neighboring r values after setting one of them into $M = 0$. In the meantime, there seems to be no physical reasoning for M to raise again once it reaches zero as expected for dissipating flux. Therefore, the M criterion is changed into a new rule, which is, when M reaches below the limit value at any given time, it will be set to zero for the rest of the simulation without the possibility of gaining a non-zero value again. This rule is applied by creating an array of size $N_r + 1$, i.e., the same size as M, which multiplies M in every time steps. This array is initially set to have a value of one in all elements. When $M(r) \leq 10^{-15}$, the elements of the array at the corresponding r are changed into zero which enables the corresponding M to stay as zero for the rest of the simulation. After applying this method, the instabilities of M for small r disappear together with the convergence issues.

Implementation of Saturation Condition to Solve the Discontinuity of the Solutions

The instability issues discussed so far only concern on $r = 1$ which are solved already by the new M criterion. However, similar problems are also found at large r which are shown through the time evolution of M for different r given in Figure 27. Although the fluctuations in M are not seen any more in this case, M behaves differently at different positions where it increases for even nodes and decreases for odd nodes. These different behaviors between the neighboring r indicate discontinuities in the solutions which are unexpected for a continuous model in this study. One attempt to solve this issue is by applying a saturation condition. In this condition, when the value of $\omega_{A,c}$ at a given location is close to K', the film is accepted to be saturated locally and $\omega_{A,c}$ is set equal to K'. Specifically for this study, the saturation condition is given as $\frac{|\omega_{A,c} - K'|}{K'} \leq 10^{-5}$. After applying this condition, the discontinuities for some r points dissapear, unfortunately they still exist in large r values as can be seen in Figure 28.

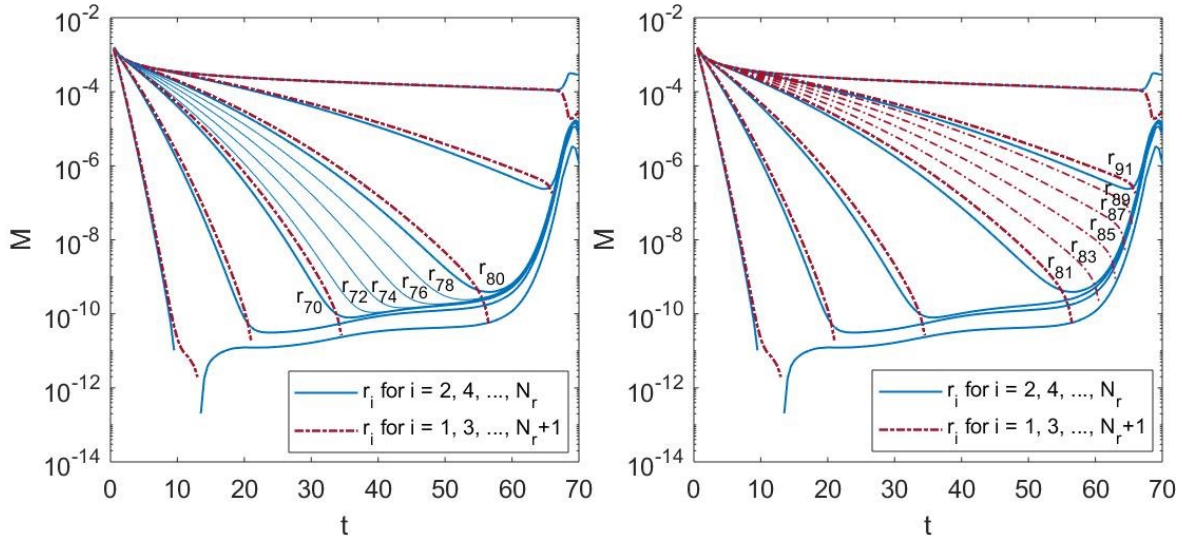

Figure 27: Time evolution of M after the implementation of the new M criterion. Both plots are obtained from the same case. The left and the right plots respectively show more specific data for even and odd values of r_i.

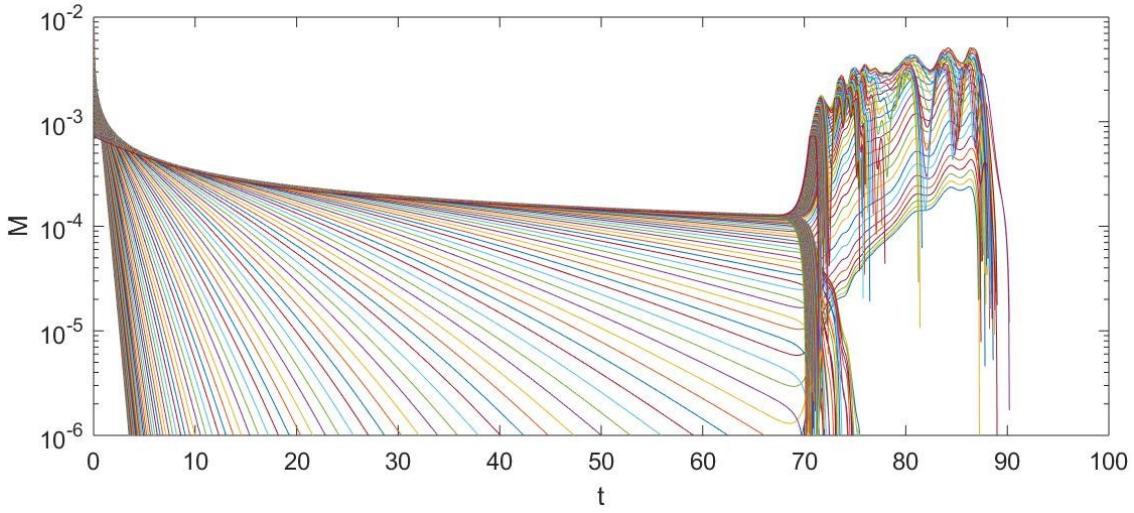

Figure 28: Time evolution of M with the implementation of saturation condition in addition to the new M criterion. The leftmost to the rightmost curves represent M for the smallest to the largest r.

Implementation of the Continuity Equation for v_z Computation

The discontinuity described in Figure 28 seems to be related to v_z computation. In further analysis provided in App. C.2, the pressure gradient in the first term of Eq. (95) may be the main source of the problem. Since the pressure along the interface is found to oscillate, taking its derivative with r twice magnifies the oscillation. When this term meets z^3 in the first term of Eq. (95), the oscillation becomes more significant especially since the grids of z are different for each r, hence, having z on the order of 3 increases the difference in the grids.

One of the attempts was applied by expanding the pressure gradient term and evaluating the significance of the second derivative. The results show that the second derivative is the main source of the problem while it cannot be neglected compared to the first derivative. Therefore, another way was executed by computing v_z using the continuity equation in Table 2 with v_r as the input.

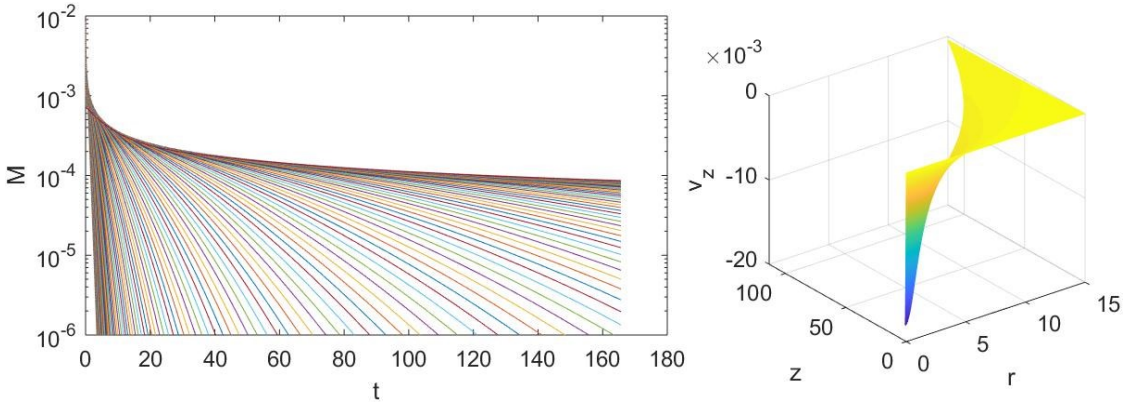

Figure 29: Time evolution of M and surface profiles of v_z at $t = 100$ with the implementation of the new M criterion, the saturation condition, and the continuity equation for v_z computation

The results in Figure 29 show that the discontinuities in the time evolution of M disappear completely. However, the surface profiles of v_z indicate a discrepancy in the boundary condition at the interface, i.e., $v_z|_{z=h/2} \neq \frac{1}{2}\frac{\partial h}{\partial t}$. This may happen because of the different domain of z for each r. In the analytical calculation, since z is a coordinate, i.e., z does not depend on r, it can be taken out from the derivative operation with respect to r. However, in the numerical computation, since v_r contains z, using the differentiation matrix to take the derivative of v_r with respect to r in the continuity equation may imply that z is considered to be dependent of r. As z nodes are different for each r, the term $\partial z/\partial r$ that should be zero is computed as non-zero in this case. As a result, v_z approaches zero towards the boundary instead of following the interface displacement rate at $r = r_\infty$.

4.1.3.3 Alternative Estimation of Coalescence Time

The 2D solver developed so far still encounters some unresolved numerical issues as discussed in Section 4.1.3.2 which makes the solver unable to determine the complete solutions. In addition, it takes quite long time for one simulation to finish since the two steps of the solver iterate the computation consecutively throughout the simulation. There are some alternative methods can be implemented when the 2D model is specifically used to estimate t_c.

Saturation Time Criterion

Considering that the film saturation ($M \rightarrow 0$) may occur before the film rupture, it is possible to estimate the coalescence time by neglecting the mass flux after some time. In this case, the time at which the film saturation is estimated to occur is mentioned as t_{sat} and the condition applied to the code is called as the saturation time condition. In Figure 30, some cases are taken as samples to show at what time approximately K' can be assumed zero. When K' is set to zero at $t = t_{sat}$, the resulting coalescence time, $t_c{}'$, can be plotted against t_{sat}/t_c where t_c is the estimated coalescence time without neglecting the mass flux. The results in Figure 30, except for cases (c) and (f), imply that t_c' goes to t_c when $t_{sat}/t_c \approx 0.5$, meaning that neglecting K' after roughly half of the simulation time may result in the same t_c as the one without neglecting K'. This method seems to be applicable for different V_{app}, λ^*, and Pe. Although the sampled cases are taken when the convergence issues still occurred (notice that t_c for $K' = 10^{-3}$ is lower than t_c for the no-flux case in cases (a), (b), and (f)), the general idea can be adapted for time consideration.

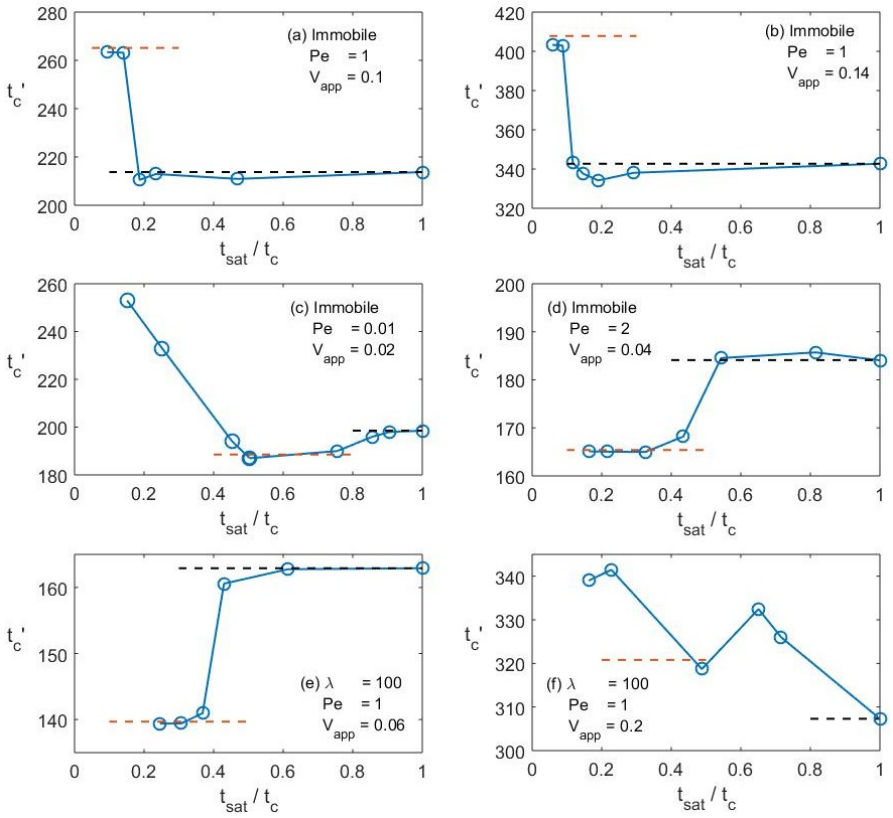

Figure 30: Coalescence times, $t_c{}'$, obtained when K' is set into zero after some time (t_{sat}) as a function of t_{sat}/t_c for different V_{app}, Pe, and λ^*. The red dashed lines represent t_c for the no-flux case and the black dashed lines show t_c for $K' = 10^{-3}$ without including the saturation time criterion.

M Expression

This expression enables the solutions for variable mass flux case to be estimated without applying the second-step of the solver. The results obtained from the 2D solver show how M decreases during the film thins out and how the rate of the decreasing M changes with r. These behaviors can be summarized to estimate M as a function of h and r. As a sample, the results are taken from one case that gives reliable results, i.e., the nose rupture regime. Then, M for a single r is plotted in terms of $\log(M)$ against h to estimate their relationship for one fixed r value by using a linear regression. The same procedure is applied for several r positions to obtain several equations for $\log(M) = a\,h + b$. The constants a and b are then formulated as functions of r using suitable regressions. Further details on the estimation of the M expression are given in Appendix D. Finally, $\log(M)$ can be expressed in terms of h and r which is estimated as

$$\log(M_0) = 58290\, r^{-4.362} h - 68100\, r^{-2.4} \tag{170}$$

The notation M_0 refers to the M expression for the base case, i.e., $K' = 10^{-3}$ and $Pe = 1$. In addition to the M expression, a saturation condition is applied by setting $M = 0$ for small r values. This M expression can be rewritten as

$$M = c\, M_0 = 10^{58290\, r^{-4.362} h - 68100\, r^{-2.4}} \tag{171}$$

where c is a multiplicator that can be varied to evaluate different magnitudes of M, i.e., various extent of the mass transfer. The M expression is evaluated at $c = 1$ as the default case and the results are compared to the ones obtained from the 2D solver.

Figure 31 presents the time evolution of the film thickness profiles obtained from the 2D solver and the M expression which shows good agreement between the two cases. The estimated t_c from the M expression deviates by 0.5% which is considered to be insignificant. Further evaluation on the behavior of the mass transfer is presented in Figure 32 where M for different r is plotted with time. The results from the M expression seem to follow the 2D case with decreasing trend of M. For the 2D case, M initially reach around $4x10^{-4}$ before declining quickly. Compared to this value, the maximum initial M given by the M expression reaches approximately $4x10^{-5}$, which is ten times lower than the one for the 2D case. As the film drains out, the maximum value of M for the M expression becomes slightly higher than the 2D case, which may counterbalance the difference in the initial M, resulting in similar t_c.

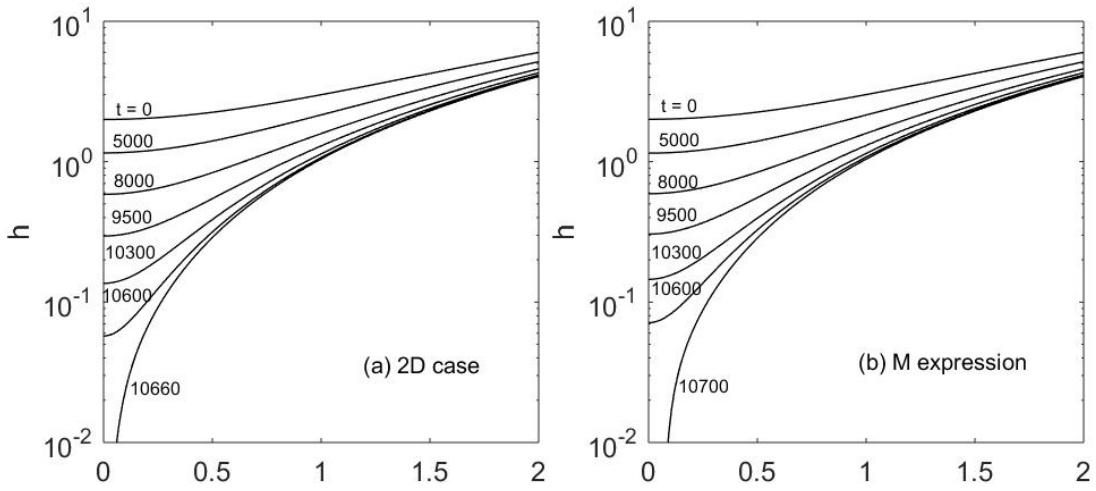

Figure 31: Time evolution of the film thickness profiles obtained from (a) the 2D case and (b) the M expression. All results are obtained at V_{app} = 0.0002, A^* = 10^{-4}, h_{00} = 2, and r_∞ = 15, based on K' = 10^{-3} and Pe = 1.

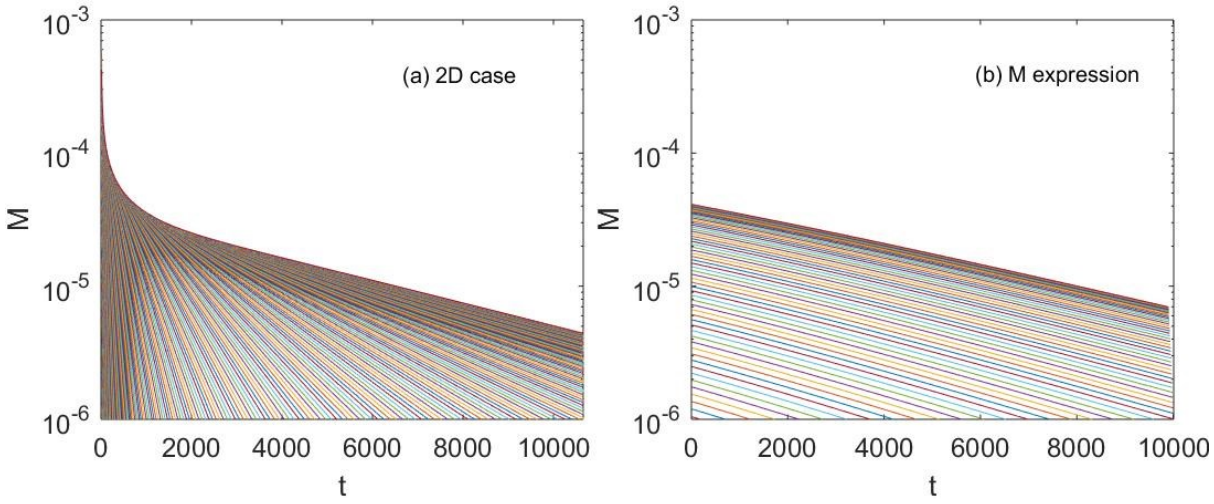

Figure 32: Time evolution of M for different r, obtained from (a) the 2D case and (b) the M expression. M from the smallest to the largest r is represented by the leftmost to the rightmost curves in case (a) and the bottom to the top curves in case (b). All results are obtained at V_{app} = 0.0002, A^* = 10^{-4}, h_{00} = 2, and r_∞ = 15, based on K' = 10^{-3} and Pe = 1.

The M expression is evaluated further for different V_{app} where the results in Figure 33 show that the rate of the decreasing M gets faster with V_{app}. This seems to fit with the analysis in Figure 19 where the slope of max(M) increases with V_{app}. This results in M disappearing faster for larger V_{app}. The disappearance of M in Figure 33 is indicated as the film saturation. This implies that higher V_{app} favors film saturation, which is in accordance with the 2D case discussed in Figure 18.

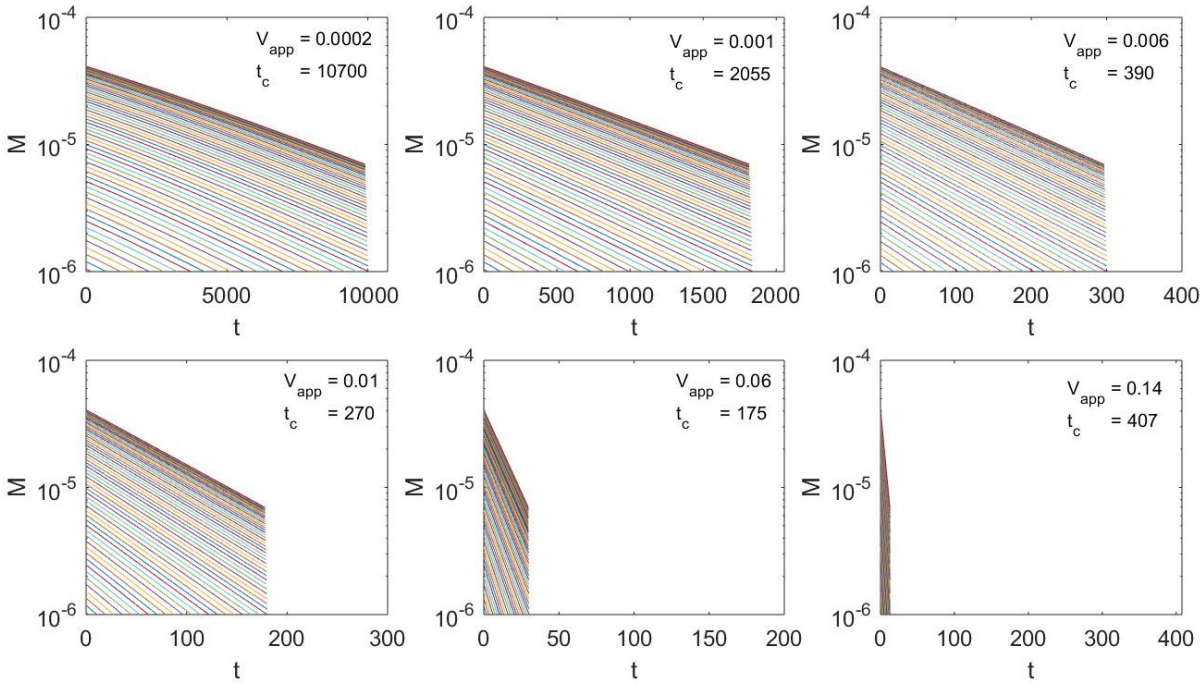

Figure 33: Time evolution of M profiles for different V_{app} obtained from the M expression, showing the time required for local saturation to occur. All results are obtained at $A^* = 10^{-4}$, $h_{00} = 2$, and $r_\infty = 15$, based on $K' = 10^{-3}$ and $Pe = 1$.

Figure 34 summarizes t_c as a function of V_{app} for the 2D case and the M expression. It can be seen that the estimated t_c from the M expression fits well with the curve for the 2D case. This implies that the M expression is applicable for different V_{app}, which means that the variable mass flux model may be solved without using the second step of the solver to save more time in obtaining the solutions.

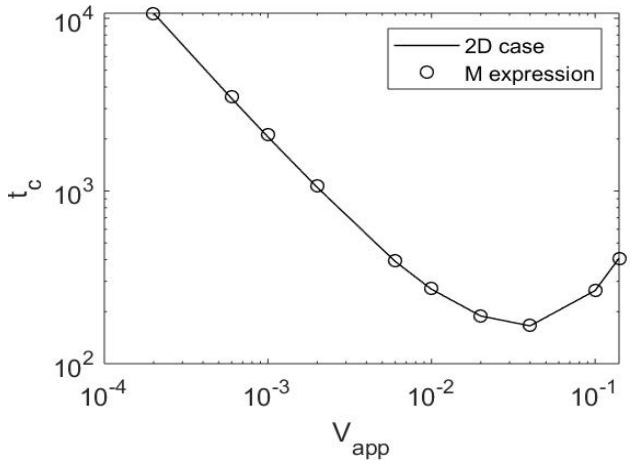

Figure 34: Coalescence time as a function of V_{app} obtained from (a) the 2D case and (b) the M expression. All results are obtained at $A^* = 10^{-4}$, $h_{00} = 2$, and $r_\infty = 15$, based on $K' = 10^{-3}$ and $Pe = 1$.

The M expression is evaluated further by varying c to estimate t_c for different extent of mass transfer, given in Figure 35. It is seen that larger M gives higher t_c and the influence of M on t_c gets more significant with decreasing V_{app}. These behaviors seem to follow the 2D case as represented by Figure 21.

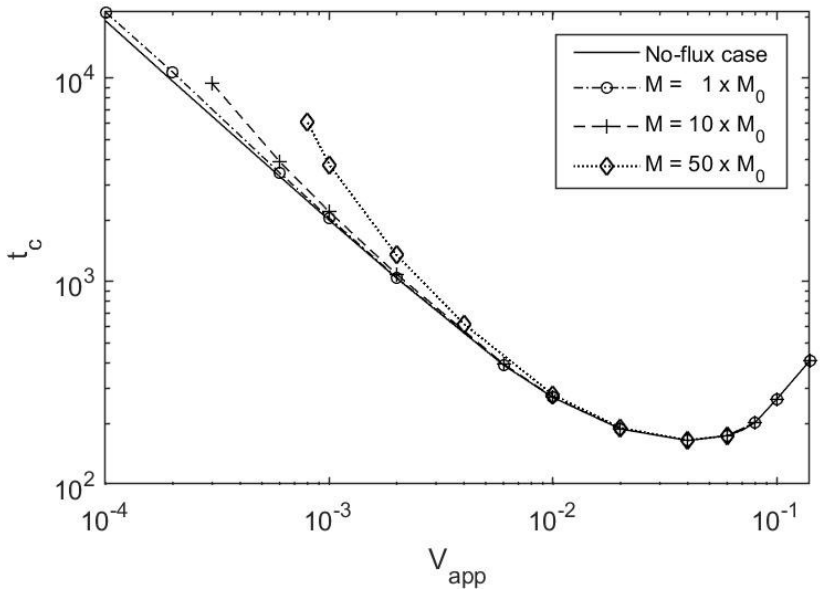

Figure 35: Coalescence time as a function of V_{app} for different M expression. All results are obtained at $A^* = 10^{-4}$, $h_{00} = 2$, and $r_\infty = 15$.

All results obtained from the M expression seem to follow the behaviors in the 2D case, which may indicate the M expression as a good approach to estimate the film drainage behaviors for the variable mass flux case by only using a 1D solver, i.e., the first part of the solver. The implementation of the M expression does not only give faster solutions compared to the 2D solver but may also be helpful to avoid any numerical issues encountered in the 2D solver when solving other cases. Despite its applicability, it may be important to determine the relationship between c and the physical properties, i.e., K' and P.

4.2 The Effect of Surfactant Presence on Coalescence

The model for surfactant cases is validated by comparing the results with Figures 8-11 of Ozan and Jakobsen (2019b). In their work, they investigated the effect of the surface viscosity, which is represented by the Boussinesq number, Bo, in the presence of surfactants. By extracting their results with $Bo = 0$, i.e., no surface viscosities considered, the coalescence times can be compared with the ones obtained in this study. It should be noticed that the surface Péclet number, Pe_s, in their study is scaled with μ_d as the implication of the time scale they used. To match their transformation, Pe_s in this study should be divided by λ^* as presented in Figure 36. It can be shown that the results fit the ones obtained in Ozan and Jakobsen (2019b) both for $\mu_d \approx \mu_c$ and for $\mu_d \ll \mu_c$.

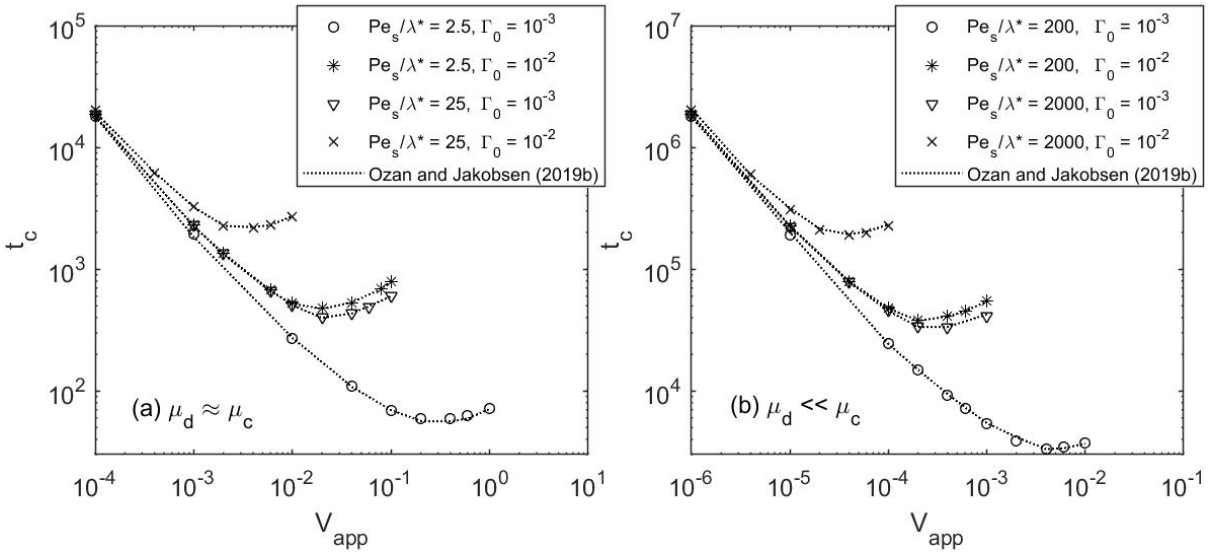

Figure 36: Reproduction of Ozan and Jakobsen (2019b)'s Fig. 8-11 showing coalescence time for their Bo = 0 system as a function of V_{app} for (a) $\mu_d \approx \mu_c$ with $\lambda^* = 10^{-2}$ and (b) $\mu_d \ll \mu_c$ with $\lambda^* = 10^{-4}$. All results are obtained at $\sigma'_\Gamma = -5000$, A^* = 10^{-4}, h_{00} = 2, and r_∞ = 30.

The study with surfactant presence is conducted by setting the viscosity ratio based on air bubbles dispersed in water using $\epsilon = 10^{-2}$ which yields $\lambda^* = 10^{-4}$. In the absence of surfactants, the estimated value λ^* here represents highly mobile interfaces. The interfaces may be immobilized by the presence of surfactants with varying degrees, depending on Γ_0, σ'_Γ, and Pe_s. The three parameters respectively describe the amount of surfactants present in the system, the strength of the surfactants in changing the surface tension, and the non-uniformity of the distribution of the surfactants along the interfaces. By varying these three parameters, the results are compared to the immobile and fully mobile cases as presented in Figure 37. For $|\sigma'_\Gamma| = 5000$ in cases (a) and (b), the effect of surfactants appears when $\Gamma_0 > 10^{-5}$, which

seems to be in accordance with Figures 8-11 of Ozan and Jakobsen (2019b) for their $Bo = 0$ case. As the magnitude of σ_Γ' decreases by 10 times to $|\sigma_\Gamma'| = 500$ in cases (c) and (d), the surfactants start to affect the system when $\Gamma_0 > 10^{-4}$, which is 10 times higher than the one in cases (a) and (b). This behavior is similarly found in cases (e) and (f) where the surfactants need to be present at $\Gamma_0 > 10^{-3}$ to change t_c of a system with $|\sigma_\Gamma'| = 50$. These results imply that the surfactants become influential only after the product of $|\sigma_\Gamma'\Gamma_0| > 0.05$. When this rule is satisfied, the surfactants start to immobilize the system and change t_c.

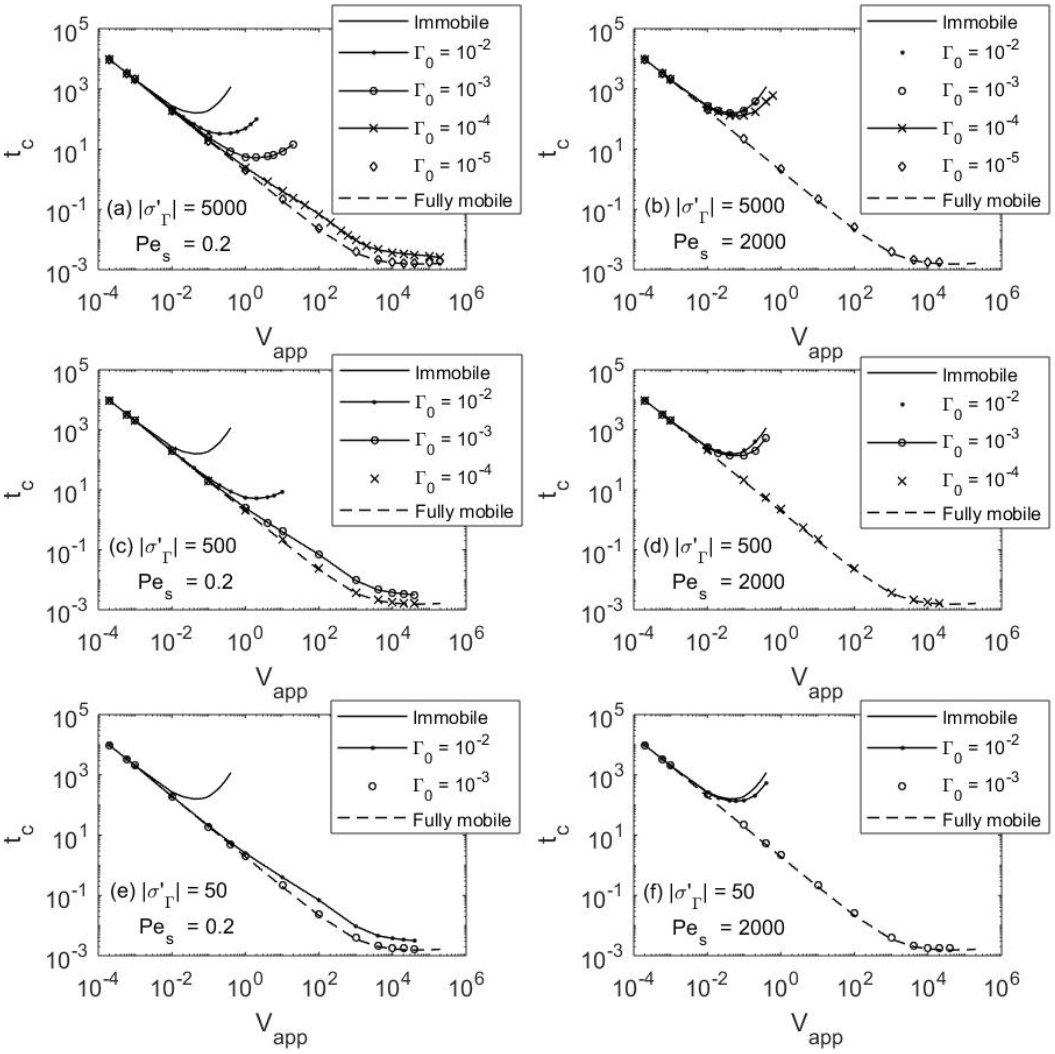

Figure 37: Coalescence time as a function of V_{app} for different values of Γ_0, $|\sigma_\Gamma'|$, and Pe_s. All results are obtained at $\lambda^* = 10^{-4}$, $A^* = 10^{-4}$, $h_{00} = 2$, and $r_\infty = 30$.

The merged parameter $|\sigma_\Gamma'\Gamma_0|$ appears to represent how much the surface tension changes with the total amount of surfactants present in the system. When the dependence is weaker, i.e., smaller $|\sigma_\Gamma'|$, the changes in the surface tension becomes less sensitive to the surfactant presence, which implies that the system requires more surfactants, i.e., higher Γ_0, to change the

surface tension. As the dependence becomes stronger (larger $|\sigma_\Gamma'|$), the surface tension may change more significantly only by small quantities of surfactants in the system. This relationship is also described by the term $\sigma_\Gamma' \frac{\partial \Gamma}{\partial r}$ in Eq. (129). Since Γ scales with Γ_0, the product of $\sigma_\Gamma' \Gamma_0$ may result in the same behavior as shown in Figure 38. Therefore, $|\sigma_\Gamma' \Gamma_0|$ can be used as a single parameter to be investigated in the next section.

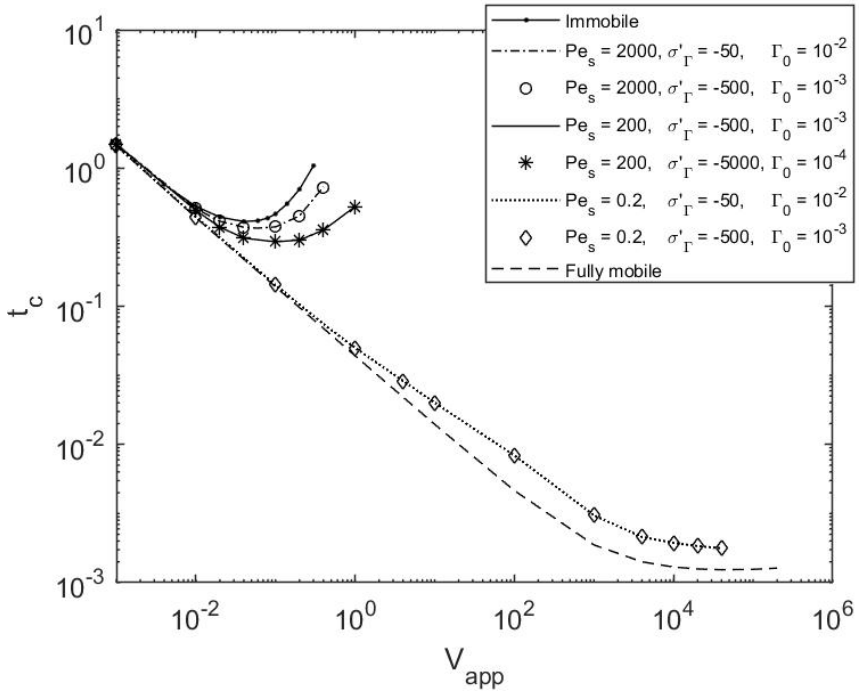

Figure 38: Coalescence time as a function of V_{app} showing identical curves for fixed values of the product $|\sigma_\Gamma' \Gamma_0|$. All results are obtained at $\lambda^* = 10^{-4}$, $A^* = 10^{-4}$, $h_{00} = 2$, and $r_\infty = 30$.

The effect of the surfactant presence is initially investigated by varying Pe_s for $|\sigma_\Gamma'| = 0.5$. The effect of Pe_s change the distribution of the surfactants along the interface where higher Pe_s results in more uneven distribution of the surfactants on the interfaces. As can be shown in Figure 39, $Pe_s = 0.2$ in case (a) results in the nose rupture with $t_c \approx 20.1$. When Pe_s increases to $Pe_s = 2000$ in case (b), the interface deforms with the emergence of the dimple, resulting in the rim rupture at $t_c \approx 131$, which indicates slower drainage rate compared to case (a). The delayed drainage rate implies that Pe_s reduces the tangential mobility of the interfaces. Since Pe_s represents the ratio of the convective to the diffusive transfer rates, higher Pe_s provides stronger convection to distribute the surfactants more nonuniformly along the interface. This yields larger excess concentration gradients, which result in larger surface tension gradients, i.e., stronger Marangoni stresses, and eventually immobilizes the interfaces more significantly.

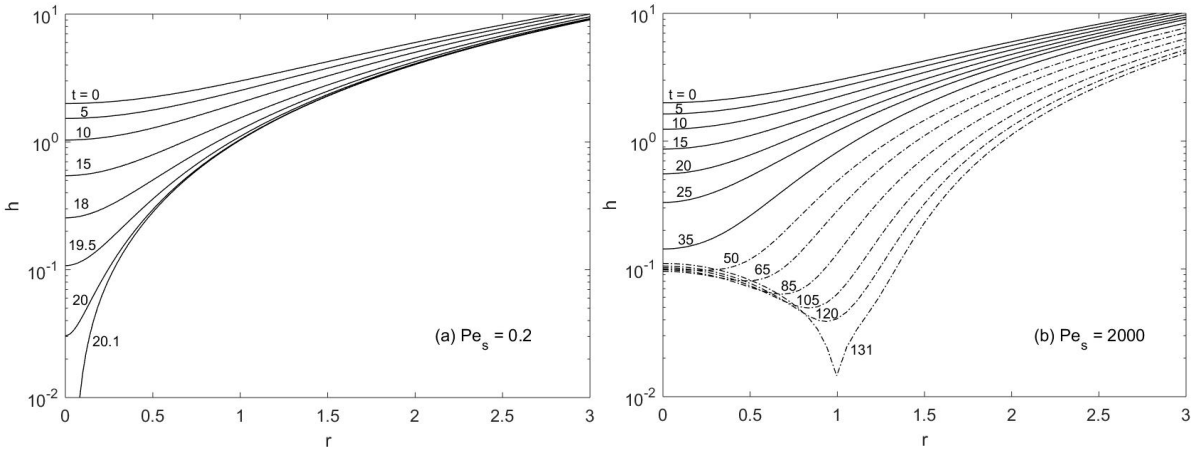

Figure 39: Time evolution of the film thickness profiles for (a) Pe_s = 0.2 and (b) Pe_s = 2000. All results are obtained at $|\sigma_\Gamma'\Gamma_0|$ = 0.5, V_{app} = 0.1, λ^* = 10^{-4}, A^* = 10^{-4}, h_{00} = 2, and r_∞ = 30.

The effect of Pe_s in slowing down the drainage rate is also evident in Figure 40 where the minimum film thickness starts to behave differently at $\min(h) \approx 0.1$. For relatively low values of Pe_s, $Pe_s \leq 20$, there is no delayed decreases in $\min(h)$ and the nose rupture occurs within these cases. Meanwhile, the three largest values of Pe_s shows a delay in the decreasing $\min(h)$ which corresponds to the rims formation as described in Figure 39 (b). As Pe_s reaches very high values, the behavior of the film drainage becomes more similar to the one for the immobile case. This implies that the effect of Pe_s in increasing the nonuniformity of the surfactant distribution promotes the Marangoni stresses which causes the interfaces to be more immobilized.

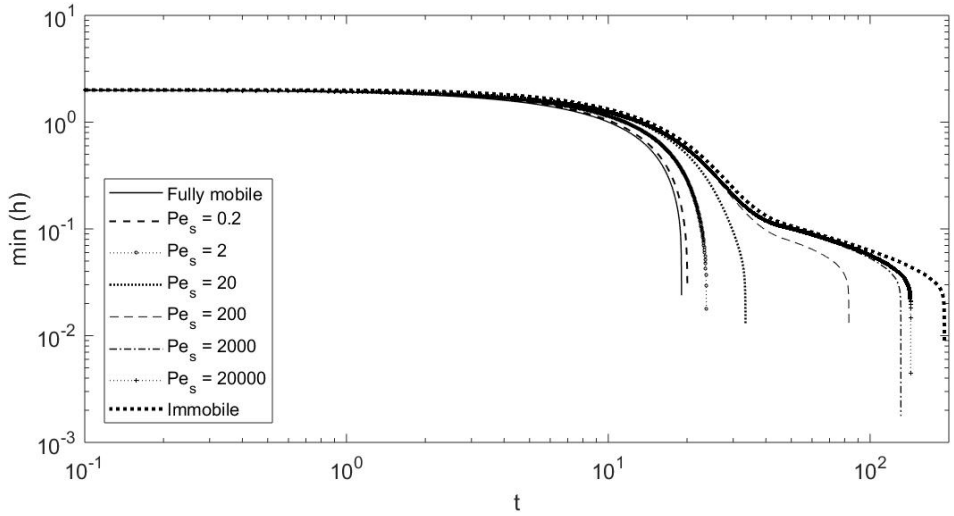

Figure 40: Minimum film thickness for different Pe_s as a function of time, with $|\sigma_\Gamma'\Gamma_0|$ = 0.5, V_{app} = 0.1, λ^* = 10^{-4}, A^* = 10^{-4}, h_{00} = 2, and r_∞ = 30

Figure 41 shows the time evolution of the surface excess concentration and its gradient for the corresponding Pe_s values. In cases (a) and (b), the surface excess concentration is found to decrease with time. Compared to $Pe_s = 0.2$, where the decrease in the Γ profiles only reaches $\Delta\Gamma \approx 5\,x\,10^{-6}$, $Pe_s = 2000$ decreases the Γ profiles up to $\Delta\Gamma \approx 4.5\,x\,10^{-5}$ which is approximately 10 times higher than the case with $Pe_s = 0.2$. This shows that higher Pe_s tends to drive the surfactants further from the center towards r_∞ which results in higher concentration gradient as presented in cases (c) and (d). It is clearly seen that $Pe_s = 2000$ results in the concentration gradient 100 times higher than the one obtained for $Pe_s = 0.2$. This behavior is consistent with Eq. (129), where larger concentration gradients result in slower tangential velocity, U_t. As also shown in Figure 42, the order of magnitude of U_t for $Pe_s = 2000$ is substantially lower than that of $Pe_s = 0.2$, which consequently reduces the tangential mobility of the interface.

As the drainage progresses, the Γ profiles in Figure 41 (b) change at $t \geq 50$, unlike the profiles in Figure 41 (a) which consistently decreases until coalescence occurs. These different behaviors correspond to the shapes of the interface. As can be seen in Figure 39 (b), the dimple starts to appear at $t = 50$, similarly as the time at which the surfactant concentrations begin to rise with time. Starting at $t = 150$, the dimple becomes more visible and the minimum Γ occurs at a further position away from $r = 0$ until $r \approx 1$, at which the film ruptures at $t_c \approx 130$. The increasing concentration at $r = 0$ implies that the surfactants migrate towards the center which may be caused by some backward flows within the deformed domain. These backward flows correspond to the negative values of U_t which are shown in Figure 42 (b) at $t \geq 50$. The impact of the behavior changes is also shown in Figure 41 (d) within the corresponding times.

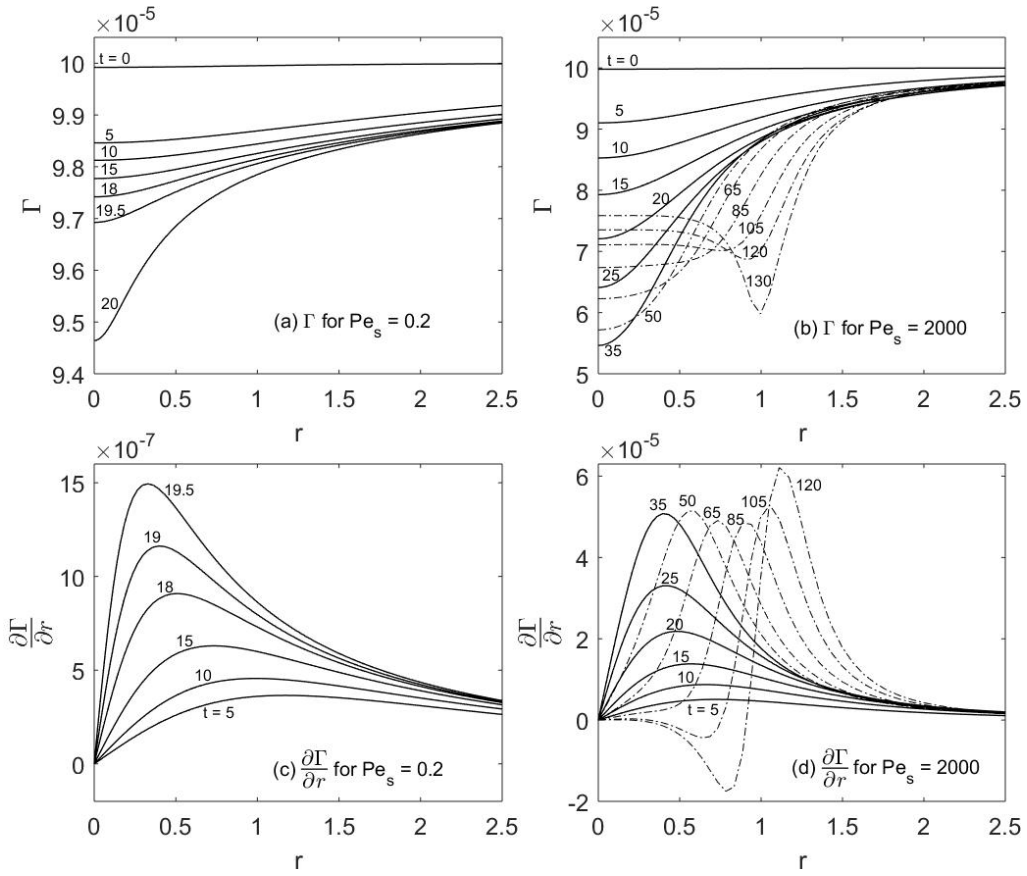

Figure 41: Time evolution of (a)-(b) the concentration and (c)-(d) the concentration gradient profiles for low and high Pe_s values. All results are obtained at V_{app} = 0.1, $|\sigma_\Gamma' \Gamma_0|$ = 0.5, λ^* = 10^{-4}, A^* = 10^{-4}, h_{00} = 2, and r_∞ = 30.

The effect of Pe_s in reducing the tangential mobility can be shown more clearly in Figure 42. In comparison to $Pe_s = 0.2$ where U_t increases with time, the case with $Pe_s = 2000$ shows decreasing U_t profiles throughout the drainage process. These contrast behaviors seem to occur due to the contrary effects of the pressure gradients and the surface tension gradients on the tangential stresses, which are described in Eq. (129). The increasing U_t values appear due to the pressure gradients which keep raising as the film is squeezed by the approaching bubbles. Meanwhile, the surface tension gradients, i.e., the Marangoni stresses, tend to pull the tangential flows back to the center, which lowers U_t values. The dominance between the two mechanisms depends on the extent of the Marangoni flows, which scale with Pe_s. When Pe_s is relatively lower, the nonuniformity of the surfactant distribution becomes less, resulting in weaker Marangoni flows. Consequently, the tangential mobility is dominated by the pressure gradients which yield the increasing trend of U_t in case (a). On the other hand, as Pe_s gets higher, the surfactants are distributed more non-uniformly which promotes Marangoni flows that may start to act more significantly in reducing U_t as shown in case (b).

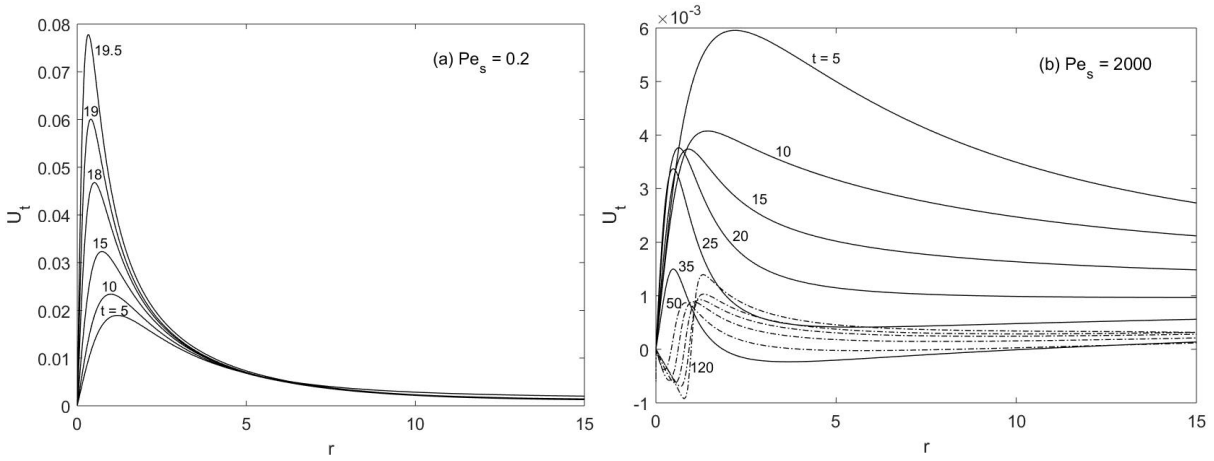

Figure 42: Time evolution of the tangential velocity for (a) Pe_s = 0.2 and (b) Pe_s = 2000 with V_{app} = 0.1, $|\sigma_\Gamma'\Gamma_0|$ = 0.5, λ^* = 10^{-4}, A^* = 10^{-4}, h_{00} = 2, and r_∞ = 30

The strength of the Marangoni flows is also found to depend on the product $|\sigma_\Gamma'\Gamma_0|$ which is investigated by varying $|\sigma_\Gamma'\Gamma_0|$ for fixed values of Pe_s. The results given in Figure 43 show different extent of tangential mobility, i.e., different strength of the Marangoni flows, ranging from the fully mobile to the completely immobile interfaces. Compared to the fully mobile case ($\lambda^* \to 0$), which represents a clean system without surfactants, the drainage behavior for all Pe_s values remains unchanged when $|\sigma_\Gamma'\Gamma_0| = 0.05$. This implies that the surfactants are not influential enough to create surface tension gradients unless $|\sigma_\Gamma'\Gamma_0| > 0.05$. When this requirement is satisfied, the coalescence time becomes distinguishable from that of the fully mobile case, which indicates that the interface starts to get immobilized by the presence of surfactants in the system. This immobilizing effect becomes more pronounced with larger $|\sigma_\Gamma'\Gamma_0|$, resulting in the t_c curves to approach the immobile case. Similarly for Pe_s, its effect in immobilizing the interface is shown for fixed values of $|\sigma_\Gamma'\Gamma_0|$, for example, at $|\sigma_\Gamma'\Gamma_0| = 0.5$ or $|\sigma_\Gamma'\Gamma_0| = 5$.

As the Marangoni stresses grow stronger with $|\sigma_\Gamma'\Gamma_0|$ and Pe_s, the tangential mobility becomes lower and lower until U_t vanishes completely, resulting in the same drainage behavior as the immobile interface ($U_t = 0$). In this case, $|Pe_s\sigma_\Gamma'\Gamma_0|$ is found to attain the same value on the order of 10^3 for $Pe_s \leq 200$. As Pe_s gets larger, the distribution of the surfactants may be uneven enough to create sufficient Marangoni stresses in immobilizing the interface completely even for smaller $|\sigma_\Gamma'\Gamma_0|$, i.e., when the surfactants are present in less quantities or with less significant impact on the surface tension gradients. For very high Pe_s values, however, the drainage behavior becomes independent of Pe_s. As can be seen in cases (e) and (f), the t_c curves look similar for both $Pe_s = 2000$ and $Pe_s = 20000$. In these cases, the rule of the

complete immobilization does not apply anymore, leading to a minimum requirement of $|\sigma_\Gamma'\Gamma_0| = 5$ instead.

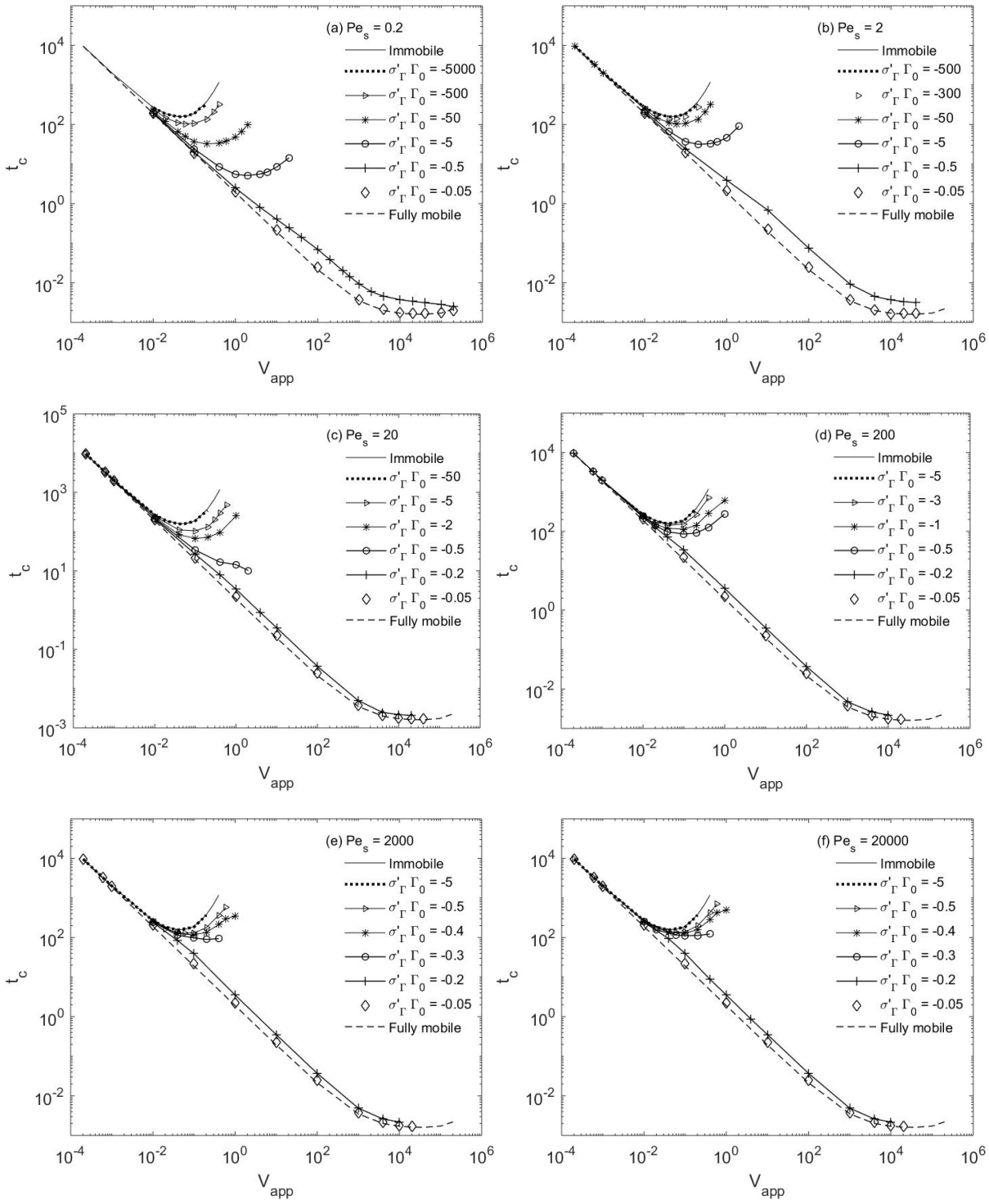

Figure 43: Coalescence time as a function of V_{app} for different $|\sigma_\Gamma'\Gamma_0|$ and Pe_s. All results are obtained at $\lambda^* = 10^{-4}$, $A^* = 10^{-4}$, $h_{00} = 2$, and $r_\infty = 30$.

The effect of surfactants is summarized in Figure 44 where the determining parameters, $|\sigma_\Gamma'\Gamma_0|$ and Pe_s, represent the tangential mobility of the interface. The dotted line at $|\sigma_\Gamma'\Gamma_0| \approx 0.05$

represents the minimum requirement for the surfactants to start immobilizing the interface, which seems to be independent of Pe_s values. Below this condition, the effect of the surfactant presence appears to be insignificant and the drainage behavior stays the same as the fully mobile case. This implies that the surfactants need to be present in the system with sufficient quantities or with adequate effect on the surface tension gradient in order for them to affect the drainage behavior. When this condition is satisfied, the surfactants start to change the coalescence time by immobilizing the system, resulting in less mobile interfaces with different levels of mobility. As Pe_s and $|\sigma_\Gamma'\Gamma_0|$ get higher, the region may pass the solid line towards the top zone where U_t goes to zero and the interfaces become completely immobilized. This condition requires specific values of $|\sigma_\Gamma'\Gamma_0|$ and Pe_s which compensate each other. As Pe_s increases, the minimum requirement for $|\sigma_\Gamma'\Gamma_0|$ decreases until $Pe \geq 200$ where Pe_s is too larger already to affect the system, hence, $|\sigma_\Gamma'\Gamma_0| \geq 5$ needs to be satisfied within this range.

Considering the realistic systems for chemical- or bioreactors, the surface diffusivity of surfactants may range from 10^{-11} to 10^{-8} m^2/s (Chang and Franses, 1995; López-Esparza et al., 2006; Pereira et al., 2014). By taking 1 mm air bubbles dispersed in water as the default case and assuming $0.01 \leq \epsilon \leq 0.1$, Pe_s can be estimated to range from 10^{-2} to 10^{7}. The surfactants may be present as impurities or cells which are typically low in the concentrations, giving an estimate for the highest initial concentration as $\Gamma_0 = 0.01\Gamma_m$. Then, by assuming $\Delta\sigma/\Delta\Gamma = -0.5$, i.e., the surface tension decreases to half when the critical micelle concentration is reached, the largest value of $|\sigma_\Gamma'|$ can be roughly estimated to reach $|\sigma_\Gamma'| \approx 5000$ for $0.01 \leq \epsilon \leq 0.1$. This yields the maximum value of $|\sigma_\Gamma'\Gamma_0|$ to be approximately 50, which becomes a limit of the complete immobilization in real systems. Therefore, the systems with $Pe \leq 2$ may not be possible to give the complete immobilization since the requirement for $|\sigma_\Gamma'\Gamma_0| \geq 500$ is physically unrealistic. This indicates that the Marangoni flows induced by the surfactant presence are insufficient to result in the complete immobilization, especially in systems with $|\sigma_\Gamma'\Gamma_0| \approx 50$ and $Pe_s \leq 20$. These cases require other immobilization mechanism, such as the surface viscosities studied by Ozan and Jakobsen (2019b), to explain the complete immobilization.

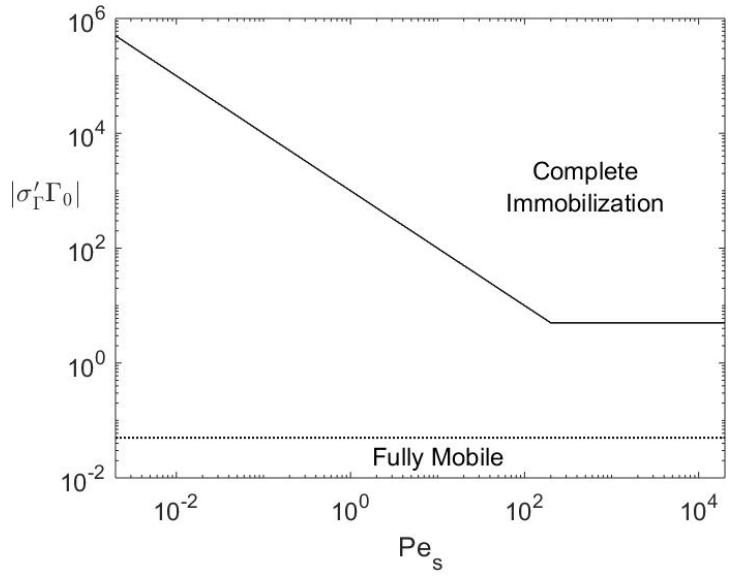

Figure 44: Conditions at which the complete immobilization is estimated to be obtained. The solid line indicates the minimum requirement of the product $|\sigma'_\Gamma\Gamma_0|$ as a function of Pe_s for the surfactants to immobilize the system completely. The dotted line reflects the minimum $|\sigma'_\Gamma\Gamma_0|$ required for the surfactants to affect the system.

4.3 The Combined Effect of Gas Dissolution and Surfactant Presence on Coalescence

In comparison to the effect of dissolution, the presence of surfactants in the system seems to be more influential on the drainage behavior. This can be shown by investigating the constant mass flux together with the surfactant presence. Although it is not the most realistic case, the constant mass flux can be taken as the extreme case since it is the one that changes the behavior the most. The results presented in Figure 45 are obtained at $|\sigma'_\Gamma\Gamma_0| = 0.5$ for different Pe_s and different M values. For fully mobile case, i.e., no surfactants, there is no apparent effect of dissolution on the drainage behavior. As the surfactants start to induce the Marangoni stresses, the drainage rate is slowed down due to the immobilization effect which becomes more influential with larger Pe_s. This results in the approaching bubbles to have longer contact period which allows more mass to pass across interface, i.e., more significant effect of dissolution on the drainage behavior. Although the effect of dissolution appears at relatively high V_{app} in cases (d)-(f), this should be unrealistic since V_{app} promotes film saturation which stops the mass transfer at earlier time.

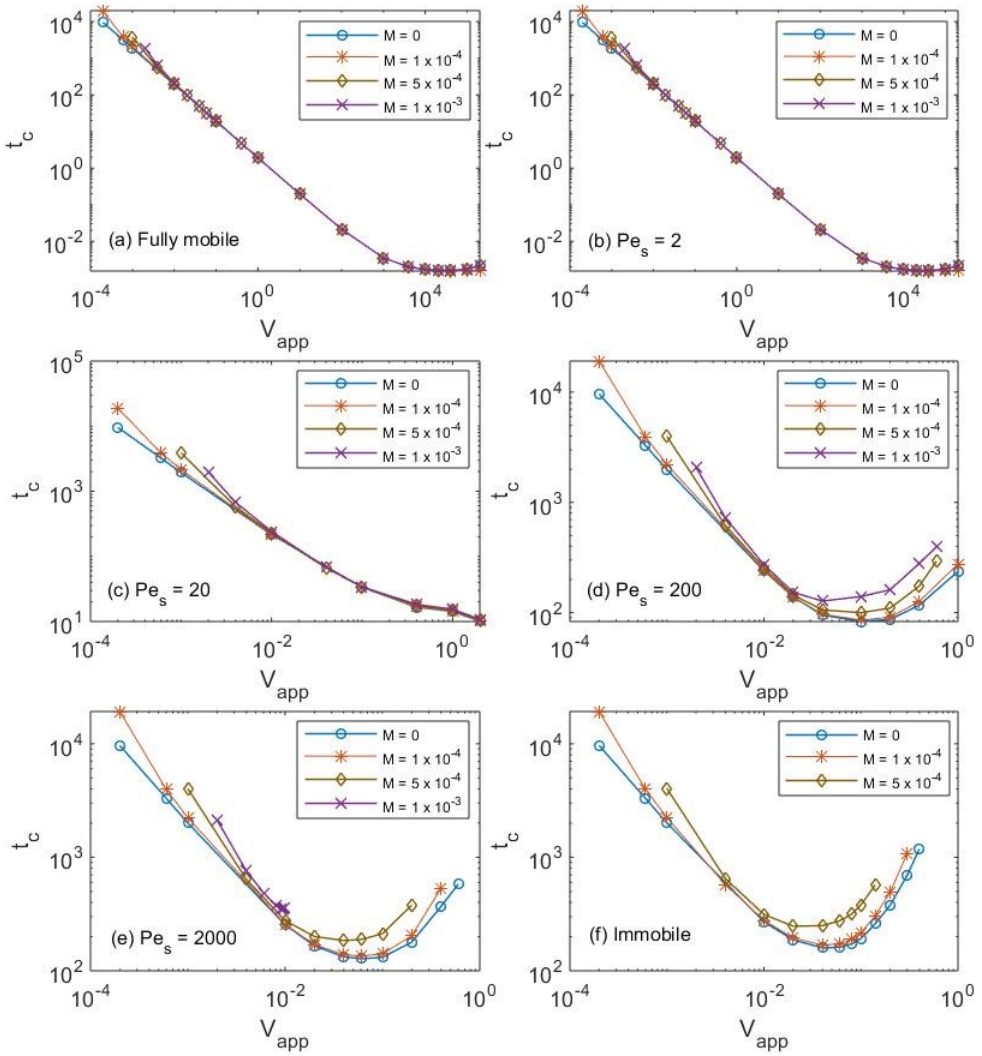

Figure 45: Coalescence time for different M as a function of V_{app} for (a) fully mobile, (b)-(e) different Pe_s, and (f) immobile cases. All results are obtained at $|\sigma_\Gamma'\Gamma_0| = 0.5$, $\lambda^* = 10^{-4}$, $A^* = 10^{-4}$, $h_{00} = 2$, and $r_\infty = 30$.

The same cases are examined with a different way of plotting as given in Figure 46. It can be seen that both dissolution and surfactants increase the coalescence time respectively by enlarging the distance between the bubbles and inducing the surface tension gradients which immobilize the interfaces. At low V_{app} values, the effect of dissolution may appear to be relatively more significant compared to the surfactants' effect. As V_{app} gets higher, the slopes of $t_c/\log(Pe_s)$ increase which implies that the surfactants become more influential on the coalescence time. On the other hand, the curves merge closer to each other, indicating negligible effect of dissolution at high V_{app}. These behaviors also apply for the 2D case with even less significant effect of dissolution due to film saturation.

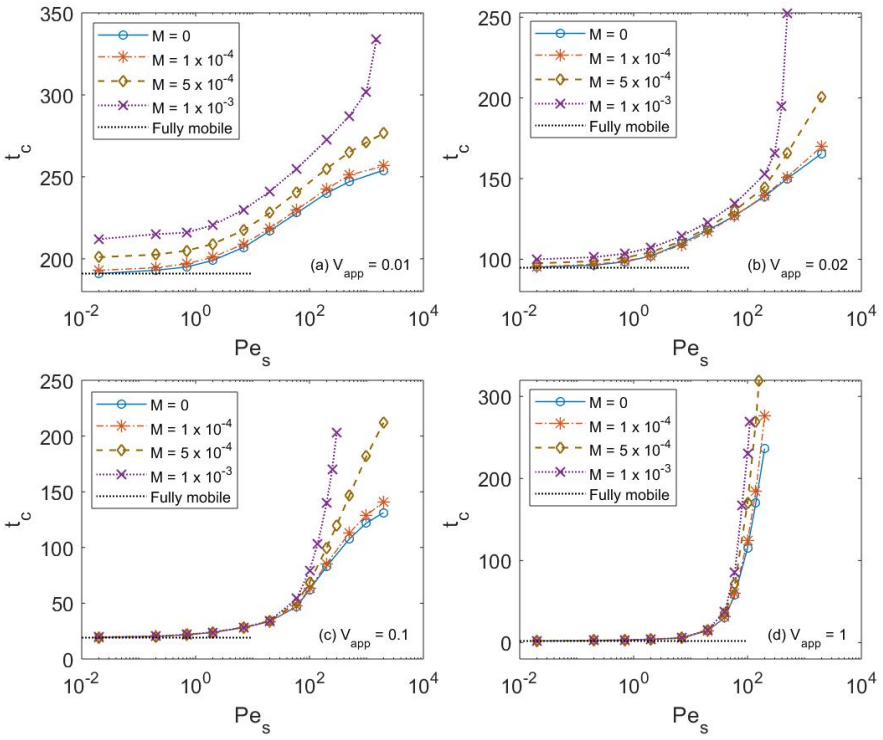

Figure 46: Coalescence time for different M as a function of Pe_s for (a) V_{app} = 0.01, (b) V_{app} = 0.02, (c) V_{app} = 0.1, and (d) V_{app} = 1. All results are obtained at $|\sigma'_\Gamma \Gamma_0|$ = 0.5, λ^* = 10^{-4}, $A^* = 10^{-4}$, h_{00} = 2, and r_∞ = 30

Based on these results, the dissolution of gas may influence the drainage behavior more significantly with the presence of surfactant. However, its effect on the coalescence time seems to be negligible compared to the immobilizing effect of surfactants.

5 Conclusion

In this study, the behavior of two approaching bubbles is investigated through a film drainage model by considering the gas dissolution and the surfactant presence in the system. Both phenomena are found to prolong the coalescence time under specific conditions where the former tends to enlarge the distance of the two bubbles and the latter creates the Marangoni flows which decrease the tangential mobility of the interface.

The effect of the gas dissolution is analyzed for three cases: assuming low Pe for negligible convective transport, constant mass flux, and variable mass flux that applies for all Pe values. The first two cases seem inadequate to represent the behavior of the gas dissolution. In the low Pe case, the effect of possible reactions is also studied and found to be negligible. Meanwhile, the constant mass flux case is unable to model the saturation phenomena during the drainage which results in the overestimation of the coalescence time. In the third case, where the component mass balance of the dissolved gas is resolved in two dimensions, it is revealed that the extent of the gas dissolution effect depends on how much it stimulates the film saturation. It is concluded that the dissolution starts to affect the drainage behavior when the gas solubility reaches 10^{-2} kg/kg water and $Pe \leq 1$, with relatively low values of approach velocity and tangential mobility.

In comparison to the gas dissolution, the effect of the surfactant presence appears to be more influential, especially within large approach velocities. The extent of this effect is determined by the amount of the surfactants present in the system (Γ_0), their strength in changing the surface tension (σ_Γ'), and the nonuniformity of the surfactant distribution characterized by the surface Péclet number (Pe_s). The surfactants start to immobilize the system when $|\sigma_\Gamma'\Gamma_0| \geq 0.05$ by inducing the Marangoni stresses along the interface. The immobilizing effect becomes more significant with $|\sigma_\Gamma'\Gamma_0|$ and Pe_s until the tangential velocity disappears, resulting in the complete immobilization of the interfaces. This condition is obtained at $|\sigma_\Gamma'\Gamma_0 Pe_s| \geq 10^3$ for $Pe_s \leq 200$ and at $|\sigma_\Gamma'\Gamma_0| \approx 5$ for $Pe_s \geq 200$. However, for some realistic cases with $|\sigma_\Gamma'\Gamma_0| \approx 50$ and $Pe_s \leq 20$, the Marangoni stresses are unable to immobilize the system completely without other immobilization mechanisms.

For further investigation, it may be important to extend this study by considering the non-Newtonian fluids which can be encountered in chemical- and bioreactors. In addition, the gas dissolution may also change the coalescence behavior through other mechanisms, for example,

the gas may dissociate and create the surface charges that generate the electric double layer repulsions between the interfaces. In the meantime, the solver developed so far still encounters some numerical stability issues in resolving the flow within the film, which may need to be improved for further studies in future.

Reference

Abid, S., & Chesters, A. K. (1994). The drainage and rupture of partially-mobile films between colliding drops at constant approach velocity. *International Journal of Multiphase Flow*, *20*(3), 613–629.

Alexandrova, S. (2014). Film Drainage and Coalescence of Drops in the Presence of Surfactant. *Journal of Chemical Technology and Metallurgy*, *49*, 321–328.

Alexandrova, S., Karsheva, M., Spasic, A., & Saboni, A. (2018). The influence of surfactants on the drainage and rupture of mobile liquid films between drops: A parametric numerical study. *Journal of Chemical Technology and Metallurgy*, *53*.

Ban, T., Kawaizumi, F., Susunu, N., & Takahashi, K. (2000). Study of Drop Coalescence Behavior for Liquid-Liquid Extraction Operation. *Chemical Engineering Science*, *55*, 5385–5391.

Bazhlekov, I. B., Chesters, A. K., & van de Vosse, F. N. (2000). The effect of the dispersed to continuous-phase viscosity ratio on film drainage between interacting drops. *International Journal of Multiphase Flow*, *26*(3), 445–466.

Chan, D. Y. C., Klaseboer, E., & Manica, R. (2011). Film drainage and coalescence between deformable drops and bubbles. *Soft Matter*, *7*(6), 2235–2264.

Chang, C.-H., & Franses, E. I. (1995). Adsorption dynamics of surfactants at the air/water interface: A critical review of mathematical models, data, and mechanisms. *Colloids and Surfaces A: Physicochemical and Engineering Aspects*, *100*, 1–45.

Chesters, A. K. (1991). The modelling of coalescence processes in fluid-liquid dispersions: A review of current understanding. *Chemical Engineering Research and Design*, *69*(A4), 259–270.

Chesters, A. K., & Hofman, G. (1982). Bubble coalescence in pure liquids. In L. van Wijngaarden (Ed.), *Mechanics and Physics of Bubbles in Liquids* (pp. 353–361). Springer Netherlands.

Chevaillier, J.-P., Klaseboer, E., Masbernat, O., & Gourdon, C. (2006). Effect of mass transfer on the film drainage between colliding drops. *Journal of Colloid and Interface Science*, *299*(1), 472–485.

Coulaloglou, C., (1975). *Dispersed phase interactions in an agitated flow vessel*. Ph.D. Dissertation, Chicago: Illinois Institute of Technology.

Davis, R. H., Schonberg, J. A., & Rallison, J. M. (1989). The lubrication force between two viscous drops. *Physics of Fluids A: Fluid Dynamics*, *1*(1), 77–81.

Del Castillo, L. A., Ohnishi, S., & Horn, R. G. (2011). Inhibition of bubble coalescence: Effects of salt concentration and speed of approach. *Journal of Colloid and Interface Science*, *356*(1), 316–324.

Doran, P. M. (2013). Mass Transfer. In *Bioprocess Engineering Principles* (pp. 379–444). Elsevier.

Duineveld, P. C. (1997). Bouncing and Coalescence of Bubble Pairs Rising at High Reynolds Number in Pure Water or Aqueous Surfactant Solutions. *Applied Scientific Research*, *58*(1), 409–439.

Farajzadeh, R., Vincent-Bonnieu, S., & Bourada Bourada, N. (2014). Effect of Gas Permeability and Solubility on Foam. *Journal of Soft Matter*, *2014*, 1–7.

Gomez, E., Santos, V. E., Alcon, A., Martin, A. B., & Garcia-Ochoa, F. (2006). Oxygen-Uptake and Mass-Transfer Rates on the Growth of *Pseudomonas p utida* CECT5279: Influence on Biodesulfurization (BDS) Capability. *Energy & Fuels*, *20*(4), 1565–1571.

Gourdon, C., & Casamatta, G. (1991). Influence of mass transfer direction on the operation of a pulsed sieve-plate pilot column. *Chemical Engineering Science*, *46*(11), 2799–2808.

Guo, W., Labrosse, G., & Narayanan, R. (2013). The Application of the Chebyshev-Spectral Method in Transport Phenomena.

Horn, R. G., Del Castillo, L. A., & Ohnishi, S. (2011). Coalescence map for bubbles in surfactant-free aqueous electrolyte solutions. *Advances in Colloid and Interface Science*, *168*(1), 85–92.

Howarth, W. J. (1964). Coalescence of drops in a turbulent flow field. *Chemical Engineering Science*, *19*(1), 33–38.

Jakobsen, H. A. (2008). *Chemical reactor modeling: Multiphase reactive flows*. Springer.

Johns, L. E., & Narayanan, R. (2007). *Interfacial Instability*. Springer Science & Business Media.

Kamp, J., & Kraume, M. (2014). Influence of drop size and superimposed mass transfer on coalescence in liquid/liquid dispersions – Test cell design for single drop investigations. *Chemical Engineering Research and Design*, *92*(4), 635–643.

Katsir, Y., & Marmur, A. (2014). Rate of Bubble Coalescence following Quasi-Static Approach: Screening and Neutralization of the Electric Double Layer. *Scientific Reports*, *4*(1), 4266.

Kirkpatrick, R. D., & Lockett, M. J. (1974). The influence of approach velocity on bubble coalescence. *Chemical Engineering Science*, *29*(12), 2363–2373.

Klaseboer, E., Chevaillier, J. Ph., Gourdon, C., & Masbernat, O. (2000). Film Drainage between Colliding Drops at Constant Approach Velocity: Experiments and Modeling. *Journal of Colloid and Interface Science*, *229*(1), 274–285.

Kourio, M.J. (1989). *Conception d'un dispositif experimental pour l'éude de la coalescence goutte-interface*. PhD thesis, Institut National Polytechnique de Toulouse.

Kourio, M. J., Gourdon, C., & Casamatta, G. (1994). Study of drop-interface coalescence: Drainage time measurement. *Chemical Engineering & Technology*, *17*(4), 249–254.

Ladyzhenskaya, O. A. (1969). *The mathematical theory of viscous incompressible flow* (Vol. 2). Gordon and Breach New York.

Lainioti, G. C., & Karaiskakis, G. (2013). New Approaches to the Kinetic Study of Alcoholic Fermentation by Chromatographic Techniques. *Journal of Chromatographic Science*, *51*(8), 764–779.

Lee, J. C., & Hodgson, T. D. (1968). Film flow and coalescence-I Basic relations, film shape and criteria for interface mobility. *Chemical Engineering Science*, *23*(11), 1375–1397.

Lehr, F., Millies, M., & Mewes, D. (2002). Bubble-Size distributions and flow fields in bubble columns. *AIChE Journal*, *48*(11), 2426–2443.

Li, X., Wang, W., Zhang, P., Li, J., & Chen, G. (2019). Interactions between gas–liquid mass transfer and bubble behaviours. *Royal Society Open Science*, *6*(5), 190136.

Liao, Y., & Lucas, D. (2010). A literature review on mechanisms and models for the coalescence process of fluid particles. *Chemical Engineering Science*, *65*(10), 2851–2864.

Lopes, M., Belo, I., & Mota, M. (2014). Over-pressurized bioreactors: Application to microbial cell cultures. *Biotechnology Progress*, *30*(4), 767–775.

López-Esparza, R., Guedeau-Boudeville, M.-A., Gambin, Y., Rodríguez-Beas, C., Maldonado, A., & Urbach, W. (2006). Interaction between poly(ethylene glycol) and two surfactants investigated by diffusion coefficient measurements. *Journal of Colloid and Interface Science*, *300*(1), 105–110.

Lu, J., Corvalan, C., Chew, J., & Huang, J.-Y. (2018). Coalescence of small bubbles with surfactants. *Chemical Engineering Science*, *196*.

Orvalho, S., Ruzicka, M. C., Olivieri, G., & Marzocchella, A. (2015). Bubble coalescence: Effect of bubble approach velocity and liquid viscosity. *Chemical Engineering Science*, *134*, 205–216.

Ozan, S. C., Hosen, H. F., & Jakobsen, H. A. (2021). On the prediction of coalescence and rebound of fluid particles: A film drainage study. *International Journal of Multiphase Flow*, *135*, 103521.

Ozan, S. C., & Jakobsen, H. A. (2019a). On the effect of the approach velocity on the coalescence of fluid particles. *International Journal of Multiphase Flow*, *119*, 223–236.

Ozan, S. C., & Jakobsen, H. A. (2019b). On the role of the surface rheology in film drainage between fluid particles. *International Journal of Multiphase Flow*, *120*, 103103.

Ozan, S. C., & Jakobsen, H. A. (2020a). Effect of surface viscoelasticity on the film drainage and the interfacial mobility. *International Journal of Multiphase Flow*, *130*, 103377.

Ozan, S. C., & Jakobsen, H. A. (2020b). Momentum jump condition for deformable Newtonian interfaces: Rigorous derivation. *European Journal of Mechanics - B/Fluids*, *84*, 367–445.

Pereira, L. A. M., Martins, L. F. G., Ascenso, J. R., Morgado, P., Ramalho, J. P. P., & Filipe, E. J. M. (2014). Diffusion Coefficients of Fluorinated Surfactants in Water: Experimental Results and Prediction by Computer Simulation. *Journal of Chemical & Engineering Data*, *59*(10), 3151–3159.

Pozrikidis, C. (1992). *Boundary integral and singularity methods for linearized viscous flow*. Cambridge university press.

Ribeiro, C. P., & Mewes, D. (2007). The effect of electrolytes on the critical velocity for bubble coalescence. *Chemical Engineering Journal*, *126*(1), 23–33.

Saboni, A. (2002). Interdrop coalescence with mass transfer: Comparison of the approximate drainage models with numerical results. *Chemical Engineering Journal*, *88*(1–3), 127–139.

Saboni, A., Gourdon, C., & Chesters, A. K. (1995). Drainage and Rupture of Partially Mobile Films during Coalescence in Liquid-Liquid Systems under a Constant Interaction Force. *Journal of Colloid and Interface Science*, *175*(1), 27–35.

Saboni, A., Gourdon, C., & Chesters, A. K. (1999). The influence of inter-phase mass transfer on the drainage of partially-mobile liquid films between drops undergoing a constant interaction force. *Chemical Engineering Science*, *54*(4), 461–473.

Sander, R. (2015). Compilation of Henry's law constants (version 4.0) for water as solvent. *Atmospheric Chemistry and Physics*, *15*(8), 4399–4981.

Shinnar, R. (1961). On the behaviour of liquid dispersions in mixing vessels. *Journal of Fluid Mechanics*, *10*(02), 259.

Shinnar, Reuel., & Church, J. M. (1960). Statistical Theories of Turbulence in Predicting Particle Size in Agitated Dispersions. *Industrial & Engineering Chemistry*, *52*(3), 253–256.

Yaminsky, V. V., Ohnishi, S., Vogler, E. A., & Horn, R. G. (2010). Stability of Aqueous Films between Bubbles. Part 1. The Effect of Speed on Bubble Coalescence in Purified Water and Simple Electrolyte Solutions. *Langmuir*, *26*(11), 8061–8074.

Yiantsios, S. G., & Davis, R. H. (1991). Close approach and deformation of two viscous drops due to gravity and van der waals forces. *Journal of Colloid and Interface Science*, *144*(2), 412–433.

Appendices

Appendix A: Mathematical Derivation

A.1 Vector and Tensor Operations

The mathematical model of the film drainage in this study involves two coordinate systems: the cylindrical coordinates for the bulk phases and the surface coordinates for the interface of the bubbles. The radial, angular, and axial components of the cylindrical coordinates are described by the base vectors: $\mathbf{e}_r$, $\mathbf{e}_\theta$, $\mathbf{e}_z$ while the tangential and normal components of the surface coordinates are notated by the unit vectors: $\mathbf{t}_1$, $\mathbf{t}_2$, and $\mathbf{n}$ which are defined as functions of the cylindrical base vectors. In general, the mathematical derivation requires the identity tensor, I, and the vector differential operator, ∇, defined in cylindrical coordinates as

$$\nabla = \mathbf{e}_r \frac{\partial}{\partial r} + \mathbf{e}_\theta \frac{1}{r}\frac{\partial}{\partial \theta} + \mathbf{e}_z \frac{\partial}{\partial z} \tag{A.1}$$

$$\mathrm{I} = \sum_i \sum_j \mathbf{e}_i \mathbf{e}_j \delta_{ij} = \mathbf{e}_r \mathbf{e}_r + \mathbf{e}_\theta \mathbf{e}_\theta + \mathbf{e}_z \mathbf{e}_z \tag{A.2}$$

In addition, the inclusion of surfactants into the model requires the surface gradient operator and the surface identity tensor, ∇_s and I_s, which are expressed in the surface coordinate system:

$$\nabla_s = \frac{\mathbf{t}_1}{\sqrt{1+\frac{1}{4}\left(\frac{\partial h}{\partial r}\right)^2}}\frac{\partial}{\partial r} + \frac{\mathbf{t}_2}{r}\frac{\partial}{\partial \theta} \tag{A.3}$$

$$\mathrm{I}_s = \mathbf{t}_1 \mathbf{t}_1 + \mathbf{t}_2 \mathbf{t}_2 \tag{A.4}$$

The flow within the film relates to the bulk velocity in the continuous phase, $\mathbf{v}_c$:

$$\mathbf{v}_c = v_r \mathbf{e}_r + v_\theta \mathbf{e}_\theta + v_z \mathbf{e}_z \tag{A.5}$$

In this study, the velocity in θ-component is assumed to be zero ($v_\theta = 0$), thus the velocity vector becomes

$$\mathbf{v}_c = v_r \mathbf{e}_r + v_z \mathbf{e}_z \tag{A.6}$$

Cross Product of Two Vectors

The cross product between two vectors, $\mathbf{e}_i \times \mathbf{e}_j$, equals to $\varepsilon_{ijk}\mathbf{e}_k$ where ε_{ijk} is the permutation symbol, given as

$$\mathbf{e}_i \times \mathbf{e}_j = \varepsilon_{ijk}\mathbf{e}_k \quad \begin{cases} \varepsilon_{ijk} = \ \ 1, & \text{if } ijk = 123, 231, \text{ or } 312 \\ \varepsilon_{ijk} = -1, & \text{if } ijk = 321, 132, \text{ or } 213 \\ \varepsilon_{ijk} = \ \ 0, & \text{if any two indices are alike} \end{cases} \tag{A.7}$$

This operation is required in Section 2 to derive the normal unit vector, $\mathbf{n}$, in Eq. (4) from the cross product of the tangent vectors $\mathbf{t}_1$ and $\mathbf{t}_2$:

$$\mathbf{n} = \mathbf{t}_1 \times \mathbf{t}_2 = \frac{\mathbf{e}_r + \frac{1}{2}\frac{\partial h}{\partial r}\mathbf{e}_z}{\sqrt{1+\frac{1}{4}\left(\frac{\partial h}{\partial r}\right)^2}} \times \mathbf{e}_\theta = \frac{(\mathbf{e}_r \times \mathbf{e}_\theta) + \frac{1}{2}\frac{\partial h}{\partial r}(\mathbf{e}_z \times \mathbf{e}_\theta)}{\sqrt{1+\frac{1}{4}\left(\frac{\partial h}{\partial r}\right)^2}} \tag{A.8}$$

By implementing the cross product rule in Eq. (A.7), the normal vector $\mathbf{n}$ becomes

$$\mathbf{n} = \frac{(\varepsilon_{r\theta z})\mathbf{e}_z + \frac{1}{2}\frac{\partial h}{\partial r}(\varepsilon_{z\theta r})\mathbf{e}_r}{\sqrt{1+\frac{1}{4}\left(\frac{\partial h}{\partial r}\right)^2}} = \frac{\mathbf{e}_z - \frac{1}{2}\frac{\partial h}{\partial r}\mathbf{e}_r}{\sqrt{1+\frac{1}{4}\left(\frac{\partial h}{\partial r}\right)^2}} \tag{A.9}$$

Dot Product of Two Vectors

The dot product between $\mathbf{e}_i \cdot \mathbf{e}_j$ is equivalent to the Kronecker delta δ_{ij} which reads

$$\mathbf{e}_i \cdot \mathbf{e}_j = \delta_{ij} \quad \begin{cases} \delta_{ij} = 1, & \text{if } i = j \\ \delta_{ij} = 0, & \text{if } i \neq j \end{cases} \tag{A.10}$$

This operation is frequently involved throughout the derivation to obtain the normal and tangential components of model equations, which will be shown in more details in Appendices A.2 - A.11.

Differential Operations

The differential operation for the cylindrical coordinate system involves the spatial derivatives of the base vectors $\frac{\partial}{\partial i}\mathbf{e}_j$:

$$\begin{aligned} &\frac{\partial}{\partial r}\mathbf{e}_r = 0, && \frac{\partial}{\partial r}\mathbf{e}_\theta = 0, && \frac{\partial}{\partial r}\mathbf{e}_z = 0 \\ &\frac{\partial}{\partial \theta}\mathbf{e}_r = \mathbf{e}_\theta, && \frac{\partial}{\partial \theta}\mathbf{e}_\theta = -\mathbf{e}_r, && \frac{\partial}{\partial \theta}\mathbf{e}_z = 0 \\ &\frac{\partial}{\partial z}\mathbf{e}_r = 0, && \frac{\partial}{\partial z}\mathbf{e}_\theta = 0, && \frac{\partial}{\partial z}\mathbf{e}_z = 0 \end{aligned} \tag{A.11}$$

This operation normally appears in some derivations involving ∇ and vectors such as the velocity gradient, $\nabla \mathbf{v}_c$, which is derived by applying Eqs. (A.1) and (A.6):

$$\nabla \mathbf{v}_c = \left(\mathbf{e}_r \frac{\partial}{\partial r} + \mathbf{e}_\theta \frac{1}{r}\frac{\partial}{\partial \theta} + \mathbf{e}_z \frac{\partial}{\partial z}\right)(v_r \mathbf{e}_r + v_z \mathbf{e}_z)$$

$$= \mathbf{e}_r \frac{\partial v_r}{\partial r}\mathbf{e}_r + \mathbf{e}_r \frac{\partial}{\partial r}\mathbf{e}_r v_r + \mathbf{e}_r \frac{\partial v_z}{\partial r}\mathbf{e}_z + \mathbf{e}_r \frac{\partial}{\partial r}\mathbf{e}_z v_z + \mathbf{e}_\theta \frac{1}{r}\frac{\partial v_r}{\partial \theta}\mathbf{e}_r$$
$$+\mathbf{e}_\theta \frac{\partial}{\partial \theta}\mathbf{e}_r \frac{v_r}{r} + \mathbf{e}_\theta \frac{1}{r}\frac{\partial v_z}{\partial \theta}\mathbf{e}_z + \mathbf{e}_\theta \frac{\partial}{\partial \theta}\mathbf{e}_z \frac{v_z}{r} + \mathbf{e}_z \frac{\partial v_r}{\partial z}\mathbf{e}_r$$
$$+\mathbf{e}_z \frac{\partial}{\partial z}\mathbf{e}_r v_r + \mathbf{e}_z \frac{\partial v_z}{\partial z}\mathbf{e}_z + \mathbf{e}_z \frac{\partial}{\partial z}\mathbf{e}_z v_z \tag{A.12}$$

Implementing Eq. (A.11) eliminates the spatial derivative of vectors except for $\frac{\partial}{\partial \theta}\mathbf{e}_r$, hence, simplifies Eq. (A.12) into

$$\nabla \mathbf{v}_c = \mathbf{e}_r \frac{\partial v_r}{\partial r}\mathbf{e}_r + \mathbf{e}_r \frac{\partial v_z}{\partial r}\mathbf{e}_z + \mathbf{e}_\theta \frac{1}{r}\frac{\partial v_r}{\partial \theta}\mathbf{e}_r + \mathbf{e}_\theta \mathbf{e}_\theta \frac{v_r}{r} + \mathbf{e}_\theta \frac{1}{r}\frac{\partial v_z}{\partial \theta}\mathbf{e}_z$$
$$+ \mathbf{e}_z \frac{\partial v_r}{\partial z}\mathbf{e}_r + \mathbf{e}_z \frac{\partial v_z}{\partial z}\mathbf{e}_z$$
$$= \mathbf{e}_r \frac{\partial v_r}{\partial r}\mathbf{e}_r + \mathbf{e}_r \frac{\partial v_z}{\partial r}\mathbf{e}_z + \mathbf{e}_\theta \mathbf{e}_\theta \frac{v_r}{r} + \mathbf{e}_z \frac{\partial v_r}{\partial z}\mathbf{e}_r + \mathbf{e}_z \frac{\partial v_z}{\partial z}\mathbf{e}_z \tag{A.13}$$

where the gradient in θ-direction is neglected due to the axisymmetry assumption.

The involvement of ∇_s in the tangential stress balance and the excess concentration balance requires the derivatives of $\mathbf{n}$ and $\mathbf{t}_1$with respect to r and θ which are derived as

$$\frac{\partial}{\partial r}\mathbf{n} = \frac{\partial}{\partial r}\left[\frac{1}{\sqrt{1+\frac{1}{4}\left(\frac{\partial h}{\partial r}\right)^2}}\mathbf{e}_z\right] - \frac{\partial}{\partial r}\left[\frac{\frac{1}{2}\frac{\partial h}{\partial r}}{\sqrt{1+\frac{1}{4}\left(\frac{\partial h}{\partial r}\right)^2}}\mathbf{e}_r\right]$$
$$= -\frac{1}{2}\left[1+\frac{1}{4}\left(\frac{\partial h}{\partial r}\right)^2\right]^{-3/2}\frac{1}{2}\frac{\partial h}{\partial r}\frac{\partial^2 h}{\partial r^2}\mathbf{e}_z$$
$$-\left\{\frac{1}{2}\frac{\partial^2 h}{\partial r^2}\frac{1}{\sqrt{1+\frac{1}{4}\left(\frac{\partial h}{\partial r}\right)^2}} - \frac{1}{2}\frac{\partial h}{\partial r}\frac{1}{2}\left[1+\frac{1}{4}\left(\frac{\partial h}{\partial r}\right)^2\right]^{-3/2}\frac{1}{2}\frac{\partial h}{\partial r}\frac{\partial^2 h}{\partial r^2}\right\}\mathbf{e}_r$$
$$= -\frac{1}{4}\left[1+\frac{1}{4}\left(\frac{\partial h}{\partial r}\right)^2\right]^{-3/2}\frac{\partial h}{\partial r}\frac{\partial^2 h}{\partial r^2}\mathbf{e}_z - \frac{1}{2}\frac{\partial^2 h}{\partial r^2}\frac{1}{\sqrt{1+\frac{1}{4}\left(\frac{\partial h}{\partial r}\right)^2}}\left[1-\frac{\frac{1}{4}\left(\frac{\partial h}{\partial r}\right)^2}{1+\frac{1}{4}\left(\frac{\partial h}{\partial r}\right)^2}\right]\mathbf{e}_r$$
$$= -\frac{1}{4}\left[1+\frac{1}{4}\left(\frac{\partial h}{\partial r}\right)^2\right]^{-3/2}\frac{\partial h}{\partial r}\frac{\partial^2 h}{\partial r^2}\mathbf{e}_z - \frac{1}{2}\frac{\partial^2 h}{\partial r^2}\frac{1}{\sqrt{1+\frac{1}{4}\left(\frac{\partial h}{\partial r}\right)^2}}\left[\frac{1}{1+\frac{1}{4}\left(\frac{\partial h}{\partial r}\right)^2}\right]\mathbf{e}_r$$
$$= -\frac{1}{4}\left[1+\frac{1}{4}\left(\frac{\partial h}{\partial r}\right)^2\right]^{-3/2}\frac{\partial h}{\partial r}\frac{\partial^2 h}{\partial r^2}\mathbf{e}_z - \frac{1}{2}\frac{\partial^2 h}{\partial r^2}\left[1+\frac{1}{4}\left(\frac{\partial h}{\partial r}\right)^2\right]^{-3/2}\mathbf{e}_r \tag{A.14}$$

$$\frac{\partial}{\partial\theta}\mathbf{n} = \frac{\partial}{\partial\theta}\left[\frac{1}{\sqrt{1+\frac{1}{4}\left(\frac{\partial h}{\partial r}\right)^2}}\mathbf{e}_z\right] - \frac{\partial}{\partial\theta}\left[\frac{\frac{1}{2}\frac{\partial h}{\partial r}}{\sqrt{1+\frac{1}{4}\left(\frac{\partial h}{\partial r}\right)^2}}\mathbf{e}_r\right]$$
$$= -\frac{\frac{1}{2}\frac{\partial h}{\partial r}}{\sqrt{1+\frac{1}{4}\left(\frac{\partial h}{\partial r}\right)^2}}\mathbf{e}_\theta \tag{A.15}$$

$$\frac{\partial}{\partial r}\mathbf{t}_1 = \frac{\partial}{\partial r}\left[\frac{1}{\sqrt{1+\frac{1}{4}\left(\frac{\partial h}{\partial r}\right)^2}}\mathbf{e}_r\right] + \frac{\partial}{\partial r}\left[\frac{\frac{1}{2}\frac{\partial h}{\partial r}}{\sqrt{1+\frac{1}{4}\left(\frac{\partial h}{\partial r}\right)^2}}\mathbf{e}_z\right]$$
$$= -\frac{1}{2}\left[1+\frac{1}{4}\left(\frac{\partial h}{\partial r}\right)^2\right]^{-3/2}\frac{1}{2}\frac{\partial h}{\partial r}\frac{\partial^2 h}{\partial r^2}\mathbf{e}_r$$
$$+\left\{\frac{1}{2}\frac{\partial^2 h}{\partial r^2}\frac{1}{\sqrt{1+\frac{1}{4}\left(\frac{\partial h}{\partial r}\right)^2}} - \frac{1}{2}\frac{\partial h}{\partial r}\frac{1}{2}\left[1+\frac{1}{4}\left(\frac{\partial h}{\partial r}\right)^2\right]^{-3/2}\frac{1}{2}\frac{\partial h}{\partial r}\frac{\partial^2 h}{\partial r^2}\right\}\mathbf{e}_z$$
$$= -\frac{1}{4}\left[1+\frac{1}{4}\left(\frac{\partial h}{\partial r}\right)^2\right]^{-3/2}\frac{\partial h}{\partial r}\frac{\partial^2 h}{\partial r^2}\mathbf{e}_r + \frac{1}{2}\frac{\partial^2 h}{\partial r^2}\frac{1}{\sqrt{1+\frac{1}{4}\left(\frac{\partial h}{\partial r}\right)^2}}\left[1-\frac{\frac{1}{4}\left(\frac{\partial h}{\partial r}\right)^2}{1+\frac{1}{4}\left(\frac{\partial h}{\partial r}\right)^2}\right]\mathbf{e}_z$$
$$= -\frac{1}{4}\left[1+\frac{1}{4}\left(\frac{\partial h}{\partial r}\right)^2\right]^{-3/2}\frac{\partial h}{\partial r}\frac{\partial^2 h}{\partial r^2}\mathbf{e}_r + \frac{1}{2}\frac{\partial^2 h}{\partial r^2}\frac{1}{\sqrt{1+\frac{1}{4}\left(\frac{\partial h}{\partial r}\right)^2}}\left[\frac{1}{1+\frac{1}{4}\left(\frac{\partial h}{\partial r}\right)^2}\right]\mathbf{e}_z$$
$$= -\frac{1}{4}\left[1+\frac{1}{4}\left(\frac{\partial h}{\partial r}\right)^2\right]^{-3/2}\frac{\partial h}{\partial r}\frac{\partial^2 h}{\partial r^2}\mathbf{e}_r + \frac{1}{2}\frac{\partial^2 h}{\partial r^2}\left[1+\frac{1}{4}\left(\frac{\partial h}{\partial r}\right)^2\right]^{-3/2}\mathbf{e}_z \tag{A.16}$$

$$\frac{\partial}{\partial\theta}\mathbf{t}_1 = \frac{\partial}{\partial\theta}\left[\frac{1}{\sqrt{1+\frac{1}{4}\left(\frac{\partial h}{\partial r}\right)^2}}\mathbf{e}_r\right] + \frac{\partial}{\partial\theta}\left[\frac{\frac{1}{2}\frac{\partial h}{\partial r}}{\sqrt{1+\frac{1}{4}\left(\frac{\partial h}{\partial r}\right)^2}}\mathbf{e}_z\right]$$
$$= \frac{1}{\sqrt{1+\frac{1}{4}\left(\frac{\partial h}{\partial r}\right)^2}}\mathbf{e}_\theta \tag{A.17}$$

A.2 Derivation of Equivalent Radius

Following Abid and Chesters (1994), the equivalent radius, R_p, for a thin film assuming gentle collision is derived from the normal stress balance of two bubbles with unequal radii, R_1 and R_2. The upper bubble having the interface position at $+z_1$ has a normal stress balance:

$$P_1 = \frac{2\sigma}{R_1} - \sigma\left(\frac{\partial^2 z_1}{\partial r^2} + \frac{1}{r}\frac{\partial z_1}{\partial r}\right) \tag{A.18}$$

while the other bubble located in the bottom position with $-z_2$ indicating the interface position has a normal stress balance:

$$P_2 = \frac{2\sigma}{R_2} + \sigma\left(\frac{\partial^2 z_2}{\partial r^2} + \frac{1}{r}\frac{\partial z_2}{\partial r}\right) \tag{A.19}$$

The excess pressure is independent of the coordinate z, $\frac{\partial P_c}{\partial z} = 0$, as indicated from the z-component of Navier-Stokes equation in Table 2. This implies that the two excess pressures in Eqs. (A.18) and (A.19) are identical and can be defined as one single variable P ($P_1 = P_2 = P$). Therefore, summing Eqs. (A.18) and (A.19) yields

$$2P = 2\sigma\left(\frac{1}{R_1} + \frac{1}{R_2}\right) - \sigma\left(\frac{\partial^2 (z_1 - z_2)}{\partial r^2} + \frac{1}{r}\frac{\partial (z_1 - z_2)}{\partial r}\right) \tag{A.20}$$

Since the film thickness is defined as the distance between the two bubble, $h = z_1 - z_2$, dividing Eq. (A.20) by 2 results in

$$\begin{aligned} P &= 2\sigma\left[\frac{1}{2}\left(\frac{1}{R_1} + \frac{1}{R_2}\right)\right] - \frac{\sigma}{2}\left(\frac{\partial^2 h}{\partial r^2} + \frac{1}{r}\frac{\partial h}{\partial r}\right) \\ &= 2\sigma\frac{1}{R_p} - \frac{\sigma}{2}\frac{1}{r}\frac{\partial}{\partial r}\left(r\frac{\partial h}{\partial r}\right) \end{aligned} \tag{A.21}$$

The first term in the right-hand side indicates the excess pressure for a spherical bubble described in Eq. (110) where $\frac{1}{R_p} = \frac{1}{2}\left(\frac{1}{R_1} + \frac{1}{R_2}\right)$. It is shown that the nondimensionalization of Eq. (A.21) results in the same formulation of the pressure equation as given in Eq. (112) and R_p is defined as $2\left(\frac{1}{R_1} + \frac{1}{R_2}\right)^{-1}$, as written in Eq. (2).

A.3 Derivation of the Continuity Equation

As expressed in Eqs. (5) and (6), the continuity equation reads

$$\frac{\partial \rho_c}{\partial t} + \nabla \cdot (\rho_c \mathbf{v}_c) = 0 \tag{A.22}$$

and simplifies into

$$\begin{aligned} \frac{\partial \rho_c}{\partial t} + \mathbf{v}_c \cdot \nabla \rho_c + \rho_c (\nabla \cdot \mathbf{v}_c) &= 0 \\ \rho_c (\nabla \cdot \mathbf{v}_c) &= 0 \end{aligned} \tag{A.23}$$

The implementation of Eqs. (A.1) and (A.6) yields

$$\begin{aligned} \nabla \cdot \mathbf{v}_c &= \left(\mathbf{e}_r \frac{\partial}{\partial r} + \mathbf{e}_\theta \frac{1}{r} \frac{\partial}{\partial \theta} + \mathbf{e}_z \frac{\partial}{\partial z} \right) \cdot (v_r \mathbf{e}_r + v_z \mathbf{e}_z) \\ &= \mathbf{e}_r \cdot \frac{\partial}{\partial r} (v_r \mathbf{e}_r) + \mathbf{e}_r \cdot \frac{\partial}{\partial r} (v_z \mathbf{e}_z) + \mathbf{e}_\theta \cdot \frac{1}{r} \frac{\partial}{\partial \theta} (v_r \mathbf{e}_r) + \mathbf{e}_\theta \cdot \frac{1}{r} \frac{\partial}{\partial \theta} (v_z \mathbf{e}_z) \\ &\quad + \mathbf{e}_z \cdot \frac{\partial}{\partial z} (v_r \mathbf{e}_r) + \mathbf{e}_z \cdot \frac{\partial}{\partial z} (v_z \mathbf{e}_z) \\ &= (\mathbf{e}_r \cdot \mathbf{e}_r) \frac{\partial v_r}{\partial r} + \left(\mathbf{e}_r \cdot \frac{\partial}{\partial r} \mathbf{e}_r \right) v_r + (\mathbf{e}_r \cdot \mathbf{e}_z) \frac{\partial v_z}{\partial r} + \left(\mathbf{e}_r \cdot \frac{\partial}{\partial r} \mathbf{e}_z \right) v_z \\ &\quad + (\mathbf{e}_\theta \cdot \mathbf{e}_r) \frac{1}{r} \frac{\partial v_r}{\partial \theta} + \left(\mathbf{e}_\theta \cdot \frac{\partial}{\partial \theta} \mathbf{e}_r \right) \frac{v_r}{r} + (\mathbf{e}_\theta \cdot \mathbf{e}_z) \frac{1}{r} \frac{\partial v_z}{\partial \theta} \\ &\quad + \left(\mathbf{e}_\theta \cdot \frac{\partial}{\partial \theta} \mathbf{e}_z \right) \frac{v_z}{r} + (\mathbf{e}_z \cdot \mathbf{e}_r) \frac{\partial v_r}{\partial z} + \left(\mathbf{e}_z \cdot \frac{\partial}{\partial z} \mathbf{e}_r \right) v_r \\ &\quad + (\mathbf{e}_z \cdot \mathbf{e}_z) \frac{\partial v_z}{\partial z} + \left(\mathbf{e}_z \cdot \frac{\partial}{\partial z} \mathbf{e}_z \right) v_z \end{aligned} \tag{A.24}$$

Applying the dot product rule and the differential operation in Eqs. (A.10) and (A.11) into Eq. (A.24) results in

$$\begin{aligned} \nabla \cdot \mathbf{v}_c &= \delta_{rr} \frac{\partial v_r}{\partial r} + (\mathbf{e}_r \cdot 0) v_r + \delta_{rz} \frac{\partial v_z}{\partial r} + (\mathbf{e}_r \cdot 0) v_z + \delta_{\theta r} \frac{1}{r} \frac{\partial v_r}{\partial \theta} + \delta_{\theta\theta} \frac{v_r}{r} + \delta_{\theta z} \frac{1}{r} \frac{\partial v_z}{\partial \theta} \\ &\quad + (\mathbf{e}_\theta \cdot 0) \frac{v_z}{r} + \delta_{zr} \frac{\partial v_r}{\partial z} + (\mathbf{e}_z \cdot 0) v_r + \delta_{zz} \frac{\partial v_z}{\partial z} + (\mathbf{e}_z \cdot 0) v_z \\ &= \frac{\partial v_r}{\partial r} + \frac{v_r}{r} + \frac{\partial v_z}{\partial z} \end{aligned} \tag{A.25}$$

By reformulating the first two terms of the right-hand side of Eq. (A.25): $\frac{\partial v_r}{\partial r} + \frac{v_r}{r} = \frac{1}{r} \frac{\partial}{\partial r} (r v_r)$, the substitution of Eq. (A.25) into Eq. (A.23) gives

$$\frac{1}{r} \frac{\partial}{\partial r} (r v_r) + \frac{\partial v_z}{\partial z} = 0 \tag{A.26}$$

as the final formulation of the continuity equation expressed in Eq. (9).

A.4 Derivation of the Navier-Stokes Equation

The derivation of the Navier-Stokes equation starts from Eq. (10):

$$\frac{\partial}{\partial t}(\rho_c \mathbf{v}_c) + \nabla \cdot (\rho_c \mathbf{v}_c \mathbf{v}_c) = -\nabla \mathrm{P}_c - \nabla \cdot \tau_c + \rho_c \mathbf{g} \tag{A.27}$$

The negligible gravitational forces in the last term of the right-hand side is indicated by estimating their magnitudes which are assumed constant and only act in z-direction:

$$\rho_c \mathbf{g} = \rho_c g_z = 1000 \frac{kg}{m^3}\ x\ 9.8 \frac{m}{s^2} = 9800 \frac{kg}{m^2 s^2} \tag{A.28}$$

It is found through the nondimensionalization of z-component of Navier-Stokes equation that the pressure term is the only significant term (shown in Table 2) and its magnitude for $\epsilon = 0.1$ is estimated based on the physical properties given in Table B.1, which results in

$$\frac{\partial P_c}{\partial z} = \frac{\bar{P}}{\bar{h}} \frac{\partial \tilde{P}_c}{\partial \tilde{z}} = \frac{\frac{\sigma}{R_p}}{\epsilon^2 R_p} \frac{\partial \tilde{P}_c}{\partial \tilde{z}} = \frac{72.8\ x\ 10^{-3} \frac{kg}{s^2}}{0.1^2\ x\ (5x10^{-4}\ m)^2} \frac{\partial \tilde{P}_c}{\partial \tilde{r}} = 2.91x10^7 \frac{kg}{m^2 s^2} \frac{\partial \tilde{P}_c}{\partial \tilde{r}} \tag{A.29}$$

The gravitational forces in Eq. (A.28) is shown to be much smaller than the magnitude of the pressure term in Eq. (A.29), thus, the last term of Eq. (A.27) is not considered. Considering constant ρ_c for an incompressible fluid, Eq. (A.29) can be rewritten as

$$\rho_c \frac{\partial \mathbf{v}_c}{\partial t} + \rho_c \nabla \cdot (\mathbf{v}_c \mathbf{v}_c) = -\nabla \mathrm{P}_c - \nabla \cdot \tau_c \tag{A.30}$$

Expanding the second term of the left-hand side of Eq. (A.30) yields

$$\begin{aligned} LHS_{2nd} &= \rho_c \nabla \cdot (\mathbf{v}_c \mathbf{v}_c) \\ &= \rho_c \mathbf{v}_c \cdot \nabla \mathbf{v}_c + \rho_c \mathbf{v}_c (\nabla \cdot \mathbf{v}_c) \\ &= \rho_c \mathbf{v}_c \cdot \nabla \mathbf{v}_c \end{aligned} \tag{A.31}$$

with $\nabla \cdot \mathbf{v}_c = 0$ coming from the continuity equation in Eq. (A.23).

For a Newtonian fluid, the deviatoric stress tensor, τ_c, contained in the last term of Eq. (A.30) is described as Eq. (11):

$$\tau_c = -\mu_c (\nabla \mathbf{v}_c + (\nabla \mathbf{v}_c)^T) + \frac{2}{3} \mu_c (\nabla \cdot \mathbf{v}_c) \mathrm{I} \tag{A.32}$$

Applying $\nabla \cdot \mathbf{v}_c = 0$ eliminates the last term of Eq. (A.32). Thus, the substitution of Eq. (A.32) to the second term of the right-hand side of Eq. (A.30) gives

$$\begin{aligned} RHS_{2nd} &= -\nabla \cdot \tau_c \\ &= \mu_c \nabla \cdot [\nabla \mathbf{v}_c + (\nabla \mathbf{v}_c)^T] \\ &= \mu_c \nabla \cdot \nabla \mathbf{v}_c + \mu_c \nabla \cdot (\nabla \mathbf{v}_c)^T \end{aligned} \tag{A.33}$$

where the Laplacian of the vectors defines each term of the right-hand side as

$$\mu_c \nabla \cdot \nabla \mathbf{v}_c = \mu_c \nabla^2 \mathbf{v}_c \quad \text{and} \quad \mu_c \nabla \cdot (\nabla \mathbf{v}_c)^T = \mu_c \nabla (\nabla \cdot \mathbf{v}_c) = 0 \tag{A.34}$$

Applying Eqs. (A.31) and (A.33) to Eq. (A.30) results in

$$\rho_c \frac{\partial \mathbf{v}_c}{\partial t} + \rho_c \mathbf{v}_c \cdot \nabla \mathbf{v}_c = -\nabla \mathrm{P}_c + \mu_c \nabla^2 \mathbf{v}_c \tag{A.35}$$

By using ∇ and $\nabla \mathbf{v}_c$ defined in Eqs. (A.1) and (A.13), elaborating the left-hand side of Eq. (A.35) gives the first term as

$$LHS_{1st} = \rho_c \frac{\partial}{\partial t}(v_r \mathbf{e}_r + v_z \mathbf{e}_z) = \rho_c \frac{\partial v_r}{\partial t}\mathbf{e}_r + \rho_c \frac{\partial v_z}{\partial t}\mathbf{e}_z \tag{A.36}$$

and the second term as

$$\begin{aligned} LHS_{2nd} &= \rho_c \mathbf{v}_c \cdot \nabla \mathbf{v}_c \\ &= \rho_c (v_r \mathbf{e}_r + v_z \mathbf{e}_z) \\ &\quad \cdot \left[\mathbf{e}_r \frac{\partial v_r}{\partial r}\mathbf{e}_r + \mathbf{e}_r \frac{\partial v_z}{\partial r}\mathbf{e}_z + \mathbf{e}_\theta \mathbf{e}_\theta \frac{v_r}{r} + \mathbf{e}_z \frac{\partial v_r}{\partial z}\mathbf{e}_r + \mathbf{e}_z \frac{\partial v_z}{\partial z}\mathbf{e}_z \right] \end{aligned} \tag{A.37}$$

The dot product is taken by applying Eq. (A.10), yielding

$$\begin{aligned} LHS_{2nd} = \rho_c \Big[& v_r (\mathbf{e}_r \cdot \mathbf{e}_r) \frac{\partial v_r}{\partial r}\mathbf{e}_r + v_r (\mathbf{e}_r \cdot \mathbf{e}_r) \frac{\partial v_z}{\partial r}\mathbf{e}_z + v_r (\mathbf{e}_r \cdot \mathbf{e}_\theta)\mathbf{e}_\theta \frac{v_r}{r} \\ & + v_r (\mathbf{e}_r \cdot \mathbf{e}_z) \frac{\partial v_r}{\partial z}\mathbf{e}_r + v_r (\mathbf{e}_r \cdot \mathbf{e}_z) \frac{\partial v_z}{\partial z}\mathbf{e}_z + v_z (\mathbf{e}_z \cdot \mathbf{e}_r) \frac{\partial v_r}{\partial r}\mathbf{e}_r \\ & + v_z (\mathbf{e}_z \cdot \mathbf{e}_r) \frac{\partial v_z}{\partial r}\mathbf{e}_z + v_z (\mathbf{e}_z \cdot \mathbf{e}_\theta)\mathbf{e}_\theta \frac{v_r}{r} + v_z (\mathbf{e}_z \cdot \mathbf{e}_z) \frac{\partial v_r}{\partial z}\mathbf{e}_r \\ & + v_z (\mathbf{e}_z \cdot \mathbf{e}_z) \frac{\partial v_z}{\partial z}\mathbf{e}_z \Big] \\ = \rho_c \Big[& v_r \delta_{rr} \frac{\partial v_r}{\partial r}\mathbf{e}_r + v_r \delta_{rr} \frac{\partial v_z}{\partial r}\mathbf{e}_z + v_r \delta_{r\theta}\mathbf{e}_\theta \frac{v_r}{r} + v_r \delta_{rz} \frac{\partial v_r}{\partial z}\mathbf{e}_r \\ & + v_r \delta_{rz} \frac{\partial v_z}{\partial z}\mathbf{e}_z + v_z \delta_{zr} \frac{\partial v_r}{\partial r}\mathbf{e}_r + v_z \delta_{zr} \frac{\partial v_z}{\partial r}\mathbf{e}_z + v_z \delta_{z\theta}\mathbf{e}_\theta \frac{v_r}{r} \\ & + v_z \delta_{zz} \frac{\partial v_r}{\partial z}\mathbf{e}_r + v_z \delta_{zz} \frac{\partial v_z}{\partial z}\mathbf{e}_z \Big] \\ = \rho_c \Big[& v_r \frac{\partial v_r}{\partial r}\mathbf{e}_r + v_r \frac{\partial v_z}{\partial r}\mathbf{e}_z + v_z \frac{\partial v_r}{\partial z}\mathbf{e}_r + v_z \frac{\partial v_z}{\partial z}\mathbf{e}_z \Big] \end{aligned} \tag{A.38}$$

By compiling Eqs. (A.36) and (A.38) together, the left-hand side of Eq. (A.35) becomes

$$\begin{aligned} LHS &= \rho_c \frac{\partial v_r}{\partial t}\mathbf{e}_r + \rho_c \frac{\partial v_z}{\partial t}\mathbf{e}_z + \rho_c \left[v_r \frac{\partial v_r}{\partial r}\mathbf{e}_r + v_r \frac{\partial v_z}{\partial r}\mathbf{e}_z + v_z \frac{\partial v_r}{\partial z}\mathbf{e}_r + v_z \frac{\partial v_z}{\partial z}\mathbf{e}_z \right] \\ &= \rho_c \left(\frac{\partial v_r}{\partial t} + v_r \frac{\partial v_r}{\partial r} + v_z \frac{\partial v_r}{\partial z} \right) \mathbf{e}_r + \rho_c \left(\frac{\partial v_z}{\partial t} + v_r \frac{\partial v_z}{\partial r} + v_z \frac{\partial v_z}{\partial z} \right) \mathbf{e}_z \end{aligned} \tag{A.39}$$

Decomposing the right-hand side of Eq. (A.35) gives the first term as

$$RHS_{1st} = -\nabla \mathrm{P}_c = -\left(\mathbf{e}_r \frac{\partial}{\partial r} + \mathbf{e}_\theta \frac{1}{r}\frac{\partial}{\partial \theta} + \mathbf{e}_z \frac{\partial}{\partial z}\right)\mathrm{P}_c$$
$$= -\left(\mathbf{e}_r \frac{\partial \mathrm{P}_c}{\partial r} + \mathbf{e}_\theta \frac{1}{r}\frac{\partial \mathrm{P}_c}{\partial \theta} + \mathbf{e}_z \frac{\partial \mathrm{P}_c}{\partial z}\right) \quad \text{(A.40)}$$

The pressure gradient in θ-direction vanishes due to the axisymmetry assumption, resulting in

$$RHS_{1st} = -\mathbf{e}_r \frac{\partial \mathrm{P}_c}{\partial r} - \mathbf{e}_z \frac{\partial \mathrm{P}_c}{\partial z} \quad \text{(A.41)}$$

Meanwhile, the second term of the right-hand side in Eq. (A.35) is expanded by taking $\nabla \mathbf{v}_c$ from Eq. (A.13), giving

$$RHS_{2nd} = \mu_c \nabla^2 \mathbf{v}_c = \mu_c \nabla \cdot \nabla \mathbf{v}_c$$
$$= \mu_c \left(\mathbf{e}_r \frac{\partial}{\partial r} + \mathbf{e}_\theta \frac{1}{r}\frac{\partial}{\partial \theta} + \mathbf{e}_z \frac{\partial}{\partial z}\right)$$
$$\cdot \left[\mathbf{e}_r \frac{\partial v_r}{\partial r}\mathbf{e}_r + \mathbf{e}_r \frac{\partial v_z}{\partial r}\mathbf{e}_z + \mathbf{e}_\theta \mathbf{e}_\theta \frac{v_r}{r} + \mathbf{e}_z \frac{\partial v_r}{\partial z}\mathbf{e}_r + \mathbf{e}_z \frac{\partial v_z}{\partial z}\mathbf{e}_z\right] \quad \text{(A.42)}$$

Expanding Eq. (A.42), eliminating the gradient in θ-direction, and implementing Eqs. (A.10) and (A.11) give

$$RHS_{2nd} = \mu_c \left[\mathbf{e}_r \cdot \frac{\partial}{\partial r}\left(\mathbf{e}_r \frac{\partial v_r}{\partial r}\mathbf{e}_r + \mathbf{e}_r \frac{\partial v_z}{\partial r}\mathbf{e}_z + \mathbf{e}_\theta \mathbf{e}_\theta \frac{v_r}{r} + \mathbf{e}_z \frac{\partial v_r}{\partial z}\mathbf{e}_r + \mathbf{e}_z \frac{\partial v_z}{\partial z}\mathbf{e}_z\right)\right.$$
$$+ \mathbf{e}_\theta \cdot \frac{1}{r}\frac{\partial}{\partial \theta}\left(\mathbf{e}_r \frac{\partial v_r}{\partial r}\mathbf{e}_r + \mathbf{e}_r \frac{\partial v_z}{\partial r}\mathbf{e}_z + \mathbf{e}_\theta \mathbf{e}_\theta \frac{v_r}{r} + \mathbf{e}_z \frac{\partial v_r}{\partial z}\mathbf{e}_r + \mathbf{e}_z \frac{\partial v_z}{\partial z}\mathbf{e}_z\right)$$
$$\left. + \mathbf{e}_z \cdot \frac{\partial}{\partial z}\left(\mathbf{e}_r \frac{\partial v_r}{\partial r}\mathbf{e}_r + \mathbf{e}_r \frac{\partial v_z}{\partial r}\mathbf{e}_z + \mathbf{e}_\theta \mathbf{e}_\theta \frac{v_r}{r} + \mathbf{e}_z \frac{\partial v_r}{\partial z}\mathbf{e}_r + \mathbf{e}_z \frac{\partial v_z}{\partial z}\mathbf{e}_z\right)\right]$$
$$= \mu_c \left[(\mathbf{e}_r \cdot \mathbf{e}_r)\frac{\partial}{\partial r}\left(\frac{\partial v_r}{\partial r}\right)\mathbf{e}_r + (\mathbf{e}_r \cdot \mathbf{e}_r)\frac{\partial}{\partial r}\left(\frac{\partial v_z}{\partial r}\right)\mathbf{e}_z + (\mathbf{e}_\theta \cdot \mathbf{e}_\theta)\frac{1}{r}\frac{\partial v_r}{\partial r}\mathbf{e}_r\right.$$
$$+ (\mathbf{e}_\theta \cdot \mathbf{e}_\theta)\frac{1}{r}\frac{\partial v_z}{\partial r}\mathbf{e}_z - (\mathbf{e}_\theta \cdot \mathbf{e}_\theta)\frac{v_r}{r^2}\mathbf{e}_r + (\mathbf{e}_z \cdot \mathbf{e}_z)\frac{\partial}{\partial z}\left(\frac{\partial v_r}{\partial z}\right)\mathbf{e}_r$$
$$\left. + (\mathbf{e}_z \cdot \mathbf{e}_z)\frac{\partial}{\partial z}\left(\frac{\partial v_z}{\partial z}\right)\mathbf{e}_z\right]$$
$$= \mu_c \left[\delta_{rr}\frac{\partial^2 v_r}{\partial r^2}\mathbf{e}_r + \delta_{rr}\frac{\partial^2 v_z}{\partial r^2}\mathbf{e}_z + \delta_{\theta\theta}\frac{1}{r}\frac{\partial v_r}{\partial r}\mathbf{e}_r + \delta_{\theta\theta}\frac{1}{r}\frac{\partial v_z}{\partial r}\mathbf{e}_z - \delta_{\theta\theta}\frac{v_r}{r^2}\mathbf{e}_r\right.$$
$$\left. + \delta_{zz}\frac{\partial^2 v_r}{\partial z^2}\mathbf{e}_r + \delta_{zz}\frac{\partial^2 v_z}{\partial z^2}\mathbf{e}_z\right]$$
$$= \mu_c \left[\frac{\partial^2 v_r}{\partial r^2}\mathbf{e}_r + \frac{1}{r}\frac{\partial v_r}{\partial r}\mathbf{e}_r - \frac{v_r}{r^2}\mathbf{e}_r + \frac{\partial^2 v_r}{\partial z^2}\mathbf{e}_r + \frac{\partial^2 v_z}{\partial r^2}\mathbf{e}_z + \frac{1}{r}\frac{\partial v_z}{\partial r}\mathbf{e}_z + \frac{\partial^2 v_z}{\partial z^2}\mathbf{e}_z\right] \quad \text{(A.43)}$$

Equation (A.43) is simplified by reformulating the 1st-3rd terms $\frac{\partial^2 v_r}{\partial r^2}\mathbf{e}_r + \frac{1}{r}\frac{\partial v_r}{\partial r}\mathbf{e}_r - \frac{v_r}{r^2}\mathbf{e}_r$ into

$$\frac{\partial^2 v_r}{\partial r^2}\mathbf{e}_r + \frac{1}{r}\frac{\partial v_r}{\partial r}\mathbf{e}_r - \frac{v_r}{r^2}\mathbf{e}_r = \frac{\partial}{\partial r}\left(\frac{1}{r}\frac{\partial}{\partial r}(rv_r)\right)\mathbf{e}_r \tag{A.44}$$

and the 5th-6th terms $\frac{\partial^2 v_z}{\partial r^2}\mathbf{e}_z + \frac{1}{r}\frac{\partial v_z}{\partial r}\mathbf{e}_z$ into

$$\frac{\partial^2 v_z}{\partial r^2}\mathbf{e}_z + \frac{1}{r}\frac{\partial v_z}{\partial r}\mathbf{e}_z = \frac{1}{r}\frac{\partial}{\partial r}\left(r\frac{\partial v_z}{\partial r}\right)\mathbf{e}_z \tag{A.45}$$

which yields

$$RHS_{2nd} = \mu_c\left[\frac{\partial}{\partial r}\left(\frac{1}{r}\frac{\partial}{\partial r}(rv_r)\right)\mathbf{e}_r + \frac{\partial^2 v_r}{\partial z^2}\mathbf{e}_r + \frac{1}{r}\frac{\partial}{\partial r}\left(r\frac{\partial v_z}{\partial r}\right)\mathbf{e}_z + \frac{\partial^2 v_z}{\partial z^2}\mathbf{e}_z\right] \tag{A.46}$$

Combining Eqs. (A.41) and (A.46) gives the right-hand side of Eq. (A.35) as

$$\begin{aligned} RHS = &-\mathbf{e}_r\frac{\partial \mathrm{P}_c}{\partial r} - \mathbf{e}_z\frac{\partial \mathrm{P}_c}{\partial z} \\ &+\mu_c\left[\frac{\partial}{\partial r}\left(\frac{1}{r}\frac{\partial}{\partial r}(rv_r)\right)\mathbf{e}_r + \frac{\partial^2 v_r}{\partial z^2}\mathbf{e}_r + \frac{1}{r}\frac{\partial}{\partial r}\left(r\frac{\partial v_z}{\partial r}\right)\mathbf{e}_z + \frac{\partial^2 v_z}{\partial z^2}\mathbf{e}_z\right] \end{aligned} \tag{A.47}$$

Equating Eqs. (A.39) and (A.47) results in the Navier-Stokes equation:

$$\begin{aligned} &\rho_c\left(\frac{\partial v_r}{\partial t} + v_r\frac{\partial v_r}{\partial r} + v_z\frac{\partial v_r}{\partial z}\right)\mathbf{e}_r + \rho_c\left(\frac{\partial v_z}{\partial t} + v_r\frac{\partial v_z}{\partial r} + v_z\frac{\partial v_z}{\partial z}\right)\mathbf{e}_z \\ &= -\mathbf{e}_r\frac{\partial \mathrm{P}_c}{\partial r} - \mathbf{e}_z\frac{\partial \mathrm{P}_c}{\partial z} + \mu_c\left[\frac{\partial}{\partial r}\left(\frac{1}{r}\frac{\partial}{\partial r}(rv_r)\right)\mathbf{e}_r + \frac{1}{r}\frac{\partial}{\partial r}\left(r\frac{\partial v_z}{\partial r}\right)\mathbf{e}_z + \frac{\partial^2 v_r}{\partial z^2}\mathbf{e}_r + \frac{\partial^2 v_z}{\partial z^2}\mathbf{e}_z\right] \end{aligned} \tag{A.48}$$

which can be decomposed into:

$$\text{r-component:}\quad \rho_c\left(\frac{\partial v_r}{\partial t} + v_r\frac{\partial v_r}{\partial r} + v_z\frac{\partial v_r}{\partial z}\right) = -\frac{\partial P_c}{\partial r} + \mu_c\left[\frac{\partial}{\partial r}\left(\frac{1}{r}\frac{\partial}{\partial r}(rv_r)\right) + \frac{\partial^2 v_r}{\partial z^2}\right] \tag{A.49}$$

$$\text{z-component:}\quad \rho_c\left(\frac{\partial v_z}{\partial t} + v_r\frac{\partial v_z}{\partial r} + v_z\frac{\partial v_z}{\partial z}\right) = -\frac{\partial P_c}{\partial z} + \mu_c\left[\frac{1}{r}\frac{\partial}{\partial r}\left(r\frac{\partial v_z}{\partial r}\right) + \frac{\partial^2 v_z}{\partial z^2}\right] \tag{A.50}$$

A.5 Derivation of the Component Mass Balance Equation

The component mass balance of species A follows Eq. (15):

$$\frac{\partial(\rho_c \omega_{A,c})}{\partial t} + \nabla \cdot (\rho_c \mathbf{v}_c \omega_{A,c}) = -\nabla \cdot \mathbf{j}_A + r_A \tag{A.51}$$

where the mass flux $\mathbf{j}_A$ is estimated by the Fick's law:

$$\mathbf{j}_A = -\rho_c D_{AB} \nabla \omega_{A,c} \tag{A.52}$$

By having constant ρ_c due to the incompressible fluid assumption, taking ρ_c out of the differential operator and substituting Eq. (A.52) into Eq. (A.51) yield

$$\rho_c \frac{\partial \omega_{A,c}}{\partial t} + \rho_c \nabla \cdot (\mathbf{v}_c \omega_{A,c}) = -\rho_c \nabla \cdot (-D_{AB} \nabla \omega_{A,c}) + r_A \tag{A.53}$$

Elaborating the second term in the left-hand side gives

$$\begin{aligned} LHS_{2nd} = \rho_c \nabla \cdot (\mathbf{v}_c \omega_{A,c}) &= \rho_c (\mathbf{v}_c \cdot \nabla \omega_A) + \rho_c \omega_{A,c} (\nabla \cdot \mathbf{v}_c) \\ &= \rho_c (\mathbf{v}_c \cdot \nabla \omega_A) \end{aligned} \tag{A.54}$$

noting that $\nabla \cdot \mathbf{v}_c = 0$ as defined in Eq. (A.23). The mass diffusivity, D_{AB}, in the first term of the right-hand side of Eq. (A.53) is considered constant, hence, can be taken out of the differential operator, resulting in

$$\begin{aligned} RHS_{1st} = -\rho_c \nabla \cdot (-D_{AB} \nabla \omega_{A,c}) &= D_{AB} \rho_c \nabla \cdot \nabla \omega_{A,c} \\ &= D_{AB} \nabla^2 \omega_A \end{aligned} \tag{A.55}$$

where ∇^2 denotes the Laplace operator. Substituting Eqs. (A.54) and (A.55) into Eq. (A.53) and dividing both sides with ρ_c formulates

$$\frac{\partial \omega_{A,c}}{\partial t} + \mathbf{v}_c \cdot \nabla \omega_A = D_{AB} \nabla^2 \omega_A + \frac{r_A}{\rho_c} \tag{A.56}$$

Applying ∇ and $\mathbf{v}_c$ as Eqs. (A.11) and (A.6) expands Eq. (A.56) into

$$\begin{aligned} &\frac{\partial \omega_{A,c}}{\partial t} + (v_r \mathbf{e}_r + v_z \mathbf{e}_z) \cdot \left(\mathbf{e}_r \frac{\partial \omega_{A,c}}{\partial r} + \mathbf{e}_\theta \frac{1}{r} \frac{\partial \omega_{A,c}}{\partial \theta} + \mathbf{e}_z \frac{\partial \omega_{A,c}}{\partial z} \right) \\ &\quad = D_{AB} \left[\mathbf{e}_r \cdot \frac{\partial}{\partial r} \left(\mathbf{e}_r \frac{\partial \omega_{A,c}}{\partial r} + \mathbf{e}_\theta \frac{1}{r} \frac{\partial \omega_{A,c}}{\partial \theta} + \mathbf{e}_z \frac{\partial \omega_{A,c}}{\partial z} \right) + \mathbf{e}_\theta \right. \\ &\qquad \cdot \frac{1}{r} \frac{\partial}{\partial \theta} \left(\mathbf{e}_r \frac{\partial \omega_{A,c}}{\partial r} + \mathbf{e}_\theta \frac{1}{r} \frac{\partial \omega_{A,c}}{\partial \theta} + \mathbf{e}_z \frac{\partial \omega_{A,c}}{\partial z} \right) + \mathbf{e}_z \\ &\qquad \left. \cdot \frac{\partial}{\partial z} \left(\mathbf{e}_r \frac{\partial \omega_{A,c}}{\partial r} + \mathbf{e}_\theta \frac{1}{r} \frac{\partial \omega_{A,c}}{\partial \theta} + \mathbf{e}_z \frac{\partial \omega_{A,c}}{\partial z} \right) \right] + \frac{r_A}{\rho_c} \end{aligned} \tag{A.57}$$

By following the dot product rule in Eq. (A.10), the left-hand side of Eq. (A.57) is derived into

$$\begin{aligned} LHS &= \frac{\partial \omega_{A,c}}{\partial t} + \left[v_r(\mathbf{e}_r \cdot \mathbf{e}_r)\frac{\partial \omega_{A,c}}{\partial r} + v_r(\mathbf{e}_r \cdot \mathbf{e}_\theta)\frac{1}{r}\frac{\partial \omega_{A,c}}{\partial \theta} + v_r(\mathbf{e}_r \cdot \mathbf{e}_z)\frac{\partial \omega_{A,c}}{\partial z} \right. \\ &\qquad \left. + v_z(\mathbf{e}_z \cdot \mathbf{e}_r)\frac{\partial \omega_{A,c}}{\partial r} + v_z(\mathbf{e}_z \cdot \mathbf{e}_\theta)\frac{1}{r}\frac{\partial \omega_{A,c}}{\partial \theta} + v_z(\mathbf{e}_z \cdot \mathbf{e}_z)\frac{\partial \omega_{A,c}}{\partial z} \right] \\ &= \frac{\partial \omega_{A,c}}{\partial t} + \left[v_r\delta_{rr}\frac{\partial \omega_{A,c}}{\partial r} + v_r\delta_{r\theta}\frac{1}{r}\frac{\partial \omega_{A,c}}{\partial \theta} + v_r\delta_{rz}\frac{\partial \omega_{A,c}}{\partial z} + v_z\delta_{zr}\frac{\partial \omega_{A,c}}{\partial r} \right. \\ &\qquad \left. + v_z\delta_{z\theta}\frac{1}{r}\frac{\partial \omega_{A,c}}{\partial \theta} + v_z\delta_{zz}\frac{\partial \omega_{A,c}}{\partial z} \right] \\ &= \frac{\partial \omega_{A,c}}{\partial t} + v_r\frac{\partial \omega_{A,c}}{\partial r} + v_z\frac{\partial \omega_{A,c}}{\partial z} \end{aligned} \tag{A.58}$$

while the right-hand side of Eq. (A.57) is derived by also implementing Eq. (A.11) and neglecting the gradient in θ-direction due to axisymmetric assumption, yielding

$$\begin{aligned} RHS &= D_{AB}\left[(\mathbf{e}_r \cdot \mathbf{e}_r)\frac{\partial}{\partial r}\left(\frac{\partial \omega_{A,c}}{\partial r}\right) + (\mathbf{e}_\theta \cdot \mathbf{e}_\theta)\frac{1}{r}\left(\frac{\partial \omega_{A,c}}{\partial r}\right) + (\mathbf{e}_z \cdot \mathbf{e}_z)\frac{\partial}{\partial z}\left(\frac{\partial \omega_{A,c}}{\partial z}\right) \right] + \frac{r_A}{\rho_c} \\ &= D_{AB}\left[\delta_{rr}\frac{\partial}{\partial r}\left(\frac{\partial \omega_{A,c}}{\partial r}\right) + \delta_{\theta\theta}\frac{1}{r}\left(\frac{\partial \omega_{A,c}}{\partial r}\right) + \delta_{zz}\frac{\partial}{\partial z}\left(\frac{\partial \omega_{A,c}}{\partial z}\right) \right] + \frac{r_A}{\rho_c} \\ &= D_{AB}\left[\frac{\partial^2 \omega_{A,c}}{\partial r^2} + \frac{1}{r}\frac{\partial \omega_{A,c}}{\partial r} + \frac{\partial^2 \omega_{A,c}}{\partial z^2} \right] + \frac{r_A}{\rho_c} \end{aligned} \tag{A.59}$$

Substituting Eqs. (A.58) and (A.59) to the left-hand and the righ-hand sides of Eq. (A.57) gives

$$\frac{\partial \omega_{A,c}}{\partial t} + v_r\frac{\partial \omega_{A,c}}{\partial r} + v_z\frac{\partial \omega_{A,c}}{\partial z} = D_{AB}\left[\frac{\partial^2 \omega_{A,c}}{\partial r^2} + \frac{1}{r}\frac{\partial \omega_{A,c}}{\partial r} + \frac{\partial^2 \omega_{A,c}}{\partial z^2} \right] + \frac{r_A}{\rho_c} \tag{A.60}$$

The term $\frac{\partial^2 \omega_{A,c}}{\partial r^2} + \frac{1}{r}\frac{\partial \omega_{A,c}}{\partial r}$ in the right-hand side is equivalent to $\frac{1}{r}\frac{\partial}{\partial r}\left(r\frac{\partial \omega_{A,c}}{\partial r}\right)$ which formulates the mass fraction profile into

$$\frac{\partial \omega_{A,c}}{\partial t} + v_r\frac{\partial \omega_{A,c}}{\partial r} + v_z\frac{\partial \omega_{A,c}}{\partial z} = D_{AB}\left[\frac{1}{r}\frac{\partial}{\partial r}\left(r\frac{\partial \omega_{A,c}}{\partial r}\right) + \frac{\partial^2 \omega_{A,c}}{\partial z^2} \right] + \frac{r_A}{\rho_c} \tag{A.61}$$

A.6 Derivation of the No-Slip Condition

The no-slip condition stems from Eq. (22):

$$\mathbf{v}_c|_{z=h/2} \cdot \mathbf{t}_1 = \mathbf{u} \cdot \mathbf{t}_1 \tag{A.62}$$

Defining the right-hand side as the tangential velocity of the interface, U_t, and substituting $\mathbf{t}_1$ and $\mathbf{v}_c$ in Eqs. (3) and (A.6) into Eq. (A.62) result in

$$(v_r \mathbf{e}_r + v_z \mathbf{e}_z) \cdot \frac{\mathbf{e}_r + \frac{1}{2}\frac{\partial h}{\partial r}\mathbf{e}_z}{\sqrt{1 + \frac{1}{4}\left(\frac{\partial h}{\partial r}\right)^2}} = U_t \tag{A.63}$$

Elaborating the dot product of the left-hand side in Eq. (A.63) and implementing (A.10) give

$$\begin{aligned} LHS &= \frac{1}{\sqrt{1 + \frac{1}{4}\left(\frac{\partial h}{\partial r}\right)^2}} \left[v_r(\mathbf{e}_r \cdot \mathbf{e}_r) + \frac{v_r}{2}\frac{\partial h}{\partial r}(\mathbf{e}_r \cdot \mathbf{e}_z) + v_z(\mathbf{e}_z \cdot \mathbf{e}_r) \right. \\ &\qquad \left. + \frac{v_z}{2}\frac{\partial h}{\partial r}(\mathbf{e}_z \cdot \mathbf{e}_z) \right] \\ &= \frac{1}{\sqrt{1 + \frac{1}{4}\left(\frac{\partial h}{\partial r}\right)^2}} \left[v_r(\delta_{rr}) + \frac{v_r}{2}\frac{\partial h}{\partial r}(\delta_{rz}) + v_z(\delta_{zr}) + \frac{v_z}{2}\frac{\partial h}{\partial r}(\delta_{zz}) \right] \\ &= \frac{1}{\sqrt{1 + \frac{1}{4}\left(\frac{\partial h}{\partial r}\right)^2}} \left[v_r + \frac{v_z}{2}\frac{\partial h}{\partial r} \right] \end{aligned} \tag{A.64}$$

Noting that the left-hand side is evaluated at the interface, $z = h/2$, substituting Eq. (A.64) to Eq. (A.63) yields

$$\frac{v_r|_{z=h/2} + \frac{1}{2}\frac{\partial h}{\partial r} v_z|_{z=h/2}}{\sqrt{1 + \frac{1}{4}\left(\frac{\partial h}{\partial r}\right)^2}} = U_t \tag{A.65}$$

A.7 Derivation of the Kinematic Conditions

Referring to Section 2.2.2, the kinematic condition with the inclusion of the mass transfer has been derived in detail until Eq. (32):

$$\left(1-\omega_{A,c}\big|_{z=h/2}\right)\left(\mathbf{v}_c|_{z=h/2}-\mathbf{u}\right)\cdot\mathbf{n}=-D_{AB}\nabla\omega_{A,c}\big|_{z=h/2}\cdot\mathbf{n} \tag{A.66}$$

which can be re-arranged into

$$\left(\mathbf{v}_c|_{z=h/2}\cdot\mathbf{n}\right)-(\mathbf{u}\cdot\mathbf{n})=-\frac{D_{AB}}{1-\omega_{A,c}\big|_{z=h/2}}\left(\nabla\omega_{A,c}\big|_{z=h/2}\cdot\mathbf{n}\right)$$

$$\mathbf{u}\cdot\mathbf{n}=\mathbf{v}_c|_{z=h/2}\cdot\mathbf{n}+\frac{D_{AB}\nabla\omega_{A,c}\big|_{z=h/2}\cdot\mathbf{n}}{\left(1-\omega_{A,c}\big|_{z=h/2}\right)} \tag{A.67}$$

The left-hand side is identified as the normal velocity of the interface, U_n, while the right-hand side is expanded by employing ∇, $\mathbf{v}_c$, and $\mathbf{n}$ in Eqs. (A.1), (A.6), and (A.8), yielding

$$U_n=(v_r\mathbf{e}_r+v_z\mathbf{e}_z)\cdot\frac{\left(\mathbf{e}_z-\frac{1}{2}\frac{\partial h}{\partial r}\mathbf{e}_r\right)}{\sqrt{1+\frac{1}{4}\left(\frac{\partial h}{\partial r}\right)^2}}$$

$$+\frac{D_{AB}}{\left(1-\omega_{A,c}\right)}\left(\mathbf{e}_r\frac{\partial\omega_{A,c}}{\partial r}+\mathbf{e}_\theta\frac{1}{r}\frac{\partial\omega_{A,c}}{\partial\theta}+\mathbf{e}_z\frac{\partial\omega_{A,c}}{\partial z}\right)\cdot\frac{\left(\mathbf{e}_z-\frac{1}{2}\frac{\partial h}{\partial r}\mathbf{e}_r\right)}{\sqrt{1+\frac{1}{4}\left(\frac{\partial h}{\partial r}\right)^2}} \tag{A.68}$$

The expansion of the dot product gives

$$U_n=\frac{1}{\sqrt{1+\frac{1}{4}\left(\frac{\partial h}{\partial r}\right)^2}}\left[v_r(\mathbf{e}_r\cdot\mathbf{e}_z)-\frac{v_r}{2}\frac{\partial h}{\partial r}(\mathbf{e}_r\cdot\mathbf{e}_r)+v_z(\mathbf{e}_z\cdot\mathbf{e}_z)-\frac{v_z}{2}\frac{\partial h}{\partial r}(\mathbf{e}_z\cdot\mathbf{e}_r)\right]$$

$$+\frac{D_{AB}}{\left(1-\omega_{A,c}\right)}\frac{1}{\sqrt{1+\frac{1}{4}\left(\frac{\partial h}{\partial r}\right)^2}}\left[(\mathbf{e}_r\cdot\mathbf{e}_z)\frac{\partial\omega_{A,c}}{\partial r}-(\mathbf{e}_r\cdot\mathbf{e}_r)\frac{1}{2}\frac{\partial\omega_{A,c}}{\partial r}\frac{\partial h}{\partial r}\right.$$

$$+(\mathbf{e}_\theta\cdot\mathbf{e}_z)\frac{1}{r}\frac{\partial\omega_{A,c}}{\partial\theta}-(\mathbf{e}_\theta\cdot\mathbf{e}_r)\frac{1}{2}\frac{1}{r}\frac{\partial\omega_{A,c}}{\partial\theta}\frac{\partial h}{\partial r}+(\mathbf{e}_z\cdot\mathbf{e}_z)\frac{\partial\omega_{A,c}}{\partial z}$$

$$\left.-(\mathbf{e}_z\cdot\mathbf{e}_r)\frac{1}{2}\frac{\partial\omega_{A,c}}{\partial z}\frac{\partial h}{\partial r}\right] \tag{A.69}$$

Applying Eq. (A.10) formulates Eq. (A.69) into

$$U_n = \frac{1}{\sqrt{1+\frac{1}{4}\left(\frac{\partial h}{\partial r}\right)^2}}\left(v_r\delta_{rz} - \frac{v_r}{2}\frac{\partial h}{\partial r}\delta_{rr} + v_z\delta_{zz} - \frac{v_z}{2}\frac{\partial h}{\partial r}\delta_{zr}\right)$$

$$+ \frac{D_{AB}}{\left(1-\omega_{A,c}\right)}\frac{1}{\sqrt{1+\frac{1}{4}\left(\frac{\partial h}{\partial r}\right)^2}}\left[\delta_{rz}\frac{\partial \omega_{A,c}}{\partial r} - \delta_{rr}\frac{1}{2}\frac{\partial \omega_{A,c}}{\partial r}\frac{\partial h}{\partial r}\right.$$

$$\left. + \delta_{\theta z}\frac{1}{r}\frac{\partial \omega_{A,c}}{\partial \theta} - \delta_{\theta r}\frac{1}{2}\frac{1}{r}\frac{\partial \omega_{A,c}}{\partial \theta}\frac{\partial h}{\partial r} + \delta_{zz}\frac{\partial \omega_{A,c}}{\partial z} - \delta_{zr}\frac{1}{2}\frac{\partial \omega_{A,c}}{\partial z}\frac{\partial h}{\partial r}\right]$$

$$= \frac{\left(-\frac{v_r}{2}\frac{\partial h}{\partial r} + v_z\right)}{\sqrt{1+\frac{1}{4}\left(\frac{\partial h}{\partial r}\right)^2}} + \frac{D_{AB}}{\left(1-\omega_{A,c}\right)}\frac{1}{\sqrt{1+\frac{1}{4}\left(\frac{\partial h}{\partial r}\right)^2}}\left[-\frac{1}{2}\frac{\partial \omega_{A,c}}{\partial r}\frac{\partial h}{\partial r} + \frac{\partial \omega_{A,c}}{\partial z}\right] \tag{A.70}$$

Evaluating the right-hand side at the interface position, $z = h/2$, with some rearrangements results in

$$U_n = \frac{v_z|_{z=h/2} - \frac{1}{2}\frac{\partial h}{\partial r}v_r|_{z=h/2}}{\sqrt{1+\frac{1}{4}\left(\frac{\partial h}{\partial r}\right)^2}}$$

$$+ \frac{1}{\sqrt{1+\frac{1}{4}\left(\frac{\partial h}{\partial r}\right)^2}}\frac{D_{AB}}{\left(1-\omega_{A,c}\big|_{z=h/2}\right)}\left(\frac{\partial \omega_{A,c}}{\partial z}\Big|_{z=h/2} - \frac{1}{2}\frac{\partial h}{\partial r}\frac{\partial \omega_{A,c}}{\partial r}\Big|_{z=h/2}\right) \tag{A.71}$$

The normal velocity U_n is derived according Johns and Narayanan (2007) in their Appendix C. Then, by following Ozan and Jakobsen (2019b)'s derivation for a thin film, the surface position is described in its implicit form, $f = z - h(r,t)/2$, and used to determine U_n as

$$U_n = -\frac{\frac{\partial f}{\partial t}}{|\nabla f|} = \frac{\frac{1}{2}\frac{\partial h}{\partial t}}{\sqrt{1+\frac{1}{4}\left(\frac{\partial h}{\partial r}\right)^4}} \approx \frac{1}{2}\frac{\partial h}{\partial t} \tag{A.72}$$

A.8 Derivation of the Normal Stress Balance

The normal stress balance considering the mass transfer is expressed in Eq. (34) as

$$2H\sigma\mathbf{n}\cdot\mathbf{n}+\nabla_s\sigma\cdot\mathbf{n}=\|\mathrm{T}\|:\mathbf{nn}-\left\|\rho\big((\mathbf{u}-\mathbf{v})\cdot\mathbf{n}\big)^2\right\| \tag{A.73}$$

The left-hand side indicates the dot product of two identical vectors, $\mathbf{n}\cdot\mathbf{n}=1$. The twice of the mean curvature of deformable interfaces, $2H$, stems from the surface divergence of $\mathbf{n}$ as described in Eq. (35), which is derived by applying ∇_s in Eq. (A.3) and expanding the dot product:

$$\begin{aligned}2H=-\nabla_\mathrm{s}\cdot\mathbf{n}&=-\left(\frac{\mathbf{t}_1}{\sqrt{1+\frac{1}{4}\left(\frac{\partial h}{\partial r}\right)^2}}\frac{\partial}{\partial r}+\frac{\mathbf{t}_2}{r}\frac{\partial}{\partial\theta}\right)\cdot\mathbf{n}\\&=-\frac{1}{\sqrt{1+\frac{1}{4}\left(\frac{\partial h}{\partial r}\right)^2}}\left(\mathbf{t}_1\cdot\frac{\partial}{\partial r}\mathbf{n}\right)-\frac{1}{r}\left(\mathbf{t}_2\cdot\frac{\partial}{\partial\theta}\mathbf{n}\right)\end{aligned} \tag{A.74}$$

The term $\left(\mathbf{t}_1\cdot\frac{\partial}{\partial r}\mathbf{n}\right)$ is derived by substituting Eqs. (3) and (A.14) to take the dot product as

$$\begin{aligned}\mathbf{t}_1\cdot\frac{\partial}{\partial r}\mathbf{n}&=\frac{\mathbf{e}_r+\frac{1}{2}\frac{\partial h}{\partial r}\mathbf{e}_z}{\sqrt{1+\frac{1}{4}\left(\frac{\partial h}{\partial r}\right)^2}}\cdot\left\{-\frac{\frac{1}{4}\frac{\partial h}{\partial r}\frac{\partial^2 h}{\partial r^2}\mathbf{e}_z}{\left[1+\frac{1}{4}\left(\frac{\partial h}{\partial r}\right)^2\right]^{3/2}}-\frac{\frac{1}{2}\frac{\partial^2 h}{\partial r^2}\mathbf{e}_r}{\left[1+\frac{1}{4}\left(\frac{\partial h}{\partial r}\right)^2\right]^{3/2}}\right\}\\&=-\frac{\frac{1}{2}\frac{\partial^2 h}{\partial r^2}}{\left[1+\frac{1}{4}\left(\frac{\partial h}{\partial r}\right)^2\right]^2}-\frac{\frac{1}{8}\left(\frac{\partial h}{\partial r}\right)^2\frac{\partial^2 h}{\partial r^2}}{\left[1+\frac{1}{4}\left(\frac{\partial h}{\partial r}\right)^2\right]^2}\\&=-\frac{\frac{1}{2}\frac{\partial^2 h}{\partial r^2}\left[1+\frac{1}{4}\left(\frac{\partial h}{\partial r}\right)^2\right]}{\left[1+\frac{1}{4}\left(\frac{\partial h}{\partial r}\right)^2\right]^2}\\&=-\frac{\frac{1}{2}\frac{\partial^2 h}{\partial r^2}}{1+\frac{1}{4}\left(\frac{\partial h}{\partial r}\right)^2}\end{aligned} \tag{A.75}$$

while the term $\left(\mathbf{t}_2\cdot\frac{\partial}{\partial\theta}\mathbf{n}\right)$ is found by applying Eqs. (3) and (A.15):

$$\mathbf{t}_2\cdot\frac{\partial}{\partial\theta}\mathbf{n}=\mathbf{e}_\theta\cdot-\frac{\frac{1}{2}\frac{\partial h}{\partial r}}{\sqrt{1+\frac{1}{4}\left(\frac{\partial h}{\partial r}\right)^2}}\mathbf{e}_\theta=-\frac{\frac{1}{2}\frac{\partial h}{\partial r}}{\sqrt{1+\frac{1}{4}\left(\frac{\partial h}{\partial r}\right)^2}} \tag{A.76}$$

The substitution of Eqs. (A.75) and (A.76) to (A.74) results in

$$2H = -\nabla_s \cdot \mathbf{n} = -\frac{1}{\sqrt{1+\frac{1}{4}\left(\frac{\partial h}{\partial r}\right)^2}}\left(-\frac{\frac{1}{2}\frac{\partial^2 h}{\partial r^2}}{1+\frac{1}{4}\left(\frac{\partial h}{\partial r}\right)^2}\right)-\frac{1}{r}\left(-\frac{\frac{1}{2}\frac{\partial h}{\partial r}}{\sqrt{1+\frac{1}{4}\left(\frac{\partial h}{\partial r}\right)^2}}\right)$$

$$= \frac{1}{\sqrt{1+\frac{1}{4}\left(\frac{\partial h}{\partial r}\right)^2}}\left[\frac{\frac{1}{2}\frac{\partial^2 h}{\partial r^2}}{1+\frac{1}{4}\left(\frac{\partial h}{\partial r}\right)^2}+\frac{1}{2}\frac{1}{r}\frac{\partial h}{\partial r}\right]$$

$$= \left[1+\frac{1}{4}\left(\frac{\partial h}{\partial r}\right)^2\right]^{-3/2}\left\{\frac{1}{2}\frac{\partial^2 h}{\partial r^2}+\frac{1}{2}\frac{1}{r}\frac{\partial h}{\partial r}\left[1+\frac{1}{4}\left(\frac{\partial h}{\partial r}\right)^2\right]\right\} \tag{A.77}$$

Since $\frac{\bar{h}}{\bar{r}} = \epsilon \ll 1$ holds as defined in Section 2.3, the term $1+\frac{1}{4}\left(\frac{\partial h}{\partial r}\right)^2$ is approximately 1 and the curvature is obtained as

$$2H = \frac{1}{2}\frac{\partial^2 h}{\partial r^2}+\frac{1}{2}\frac{1}{r}\frac{\partial h}{\partial r} = \frac{1}{2r}\frac{\partial}{\partial r}\left(r\frac{\partial h}{\partial r}\right) \tag{A.78}$$

The complete derivation is discussed in Ozan and Jakobsen (2020b) with Eq. 4.43 of their work showing the same final expression as Eq. (A.78), which is also consistent with Eq. (7) of Chesters and Hofman (1982). Substituting Eq. (A.78) to the left-hand side of Eq. (A.73) gives

$$LHS = 2H\sigma = \frac{\sigma}{2r}\frac{\partial}{\partial r}\left(r\frac{\partial h}{\partial r}\right) \tag{A.79}$$

The first term of the right-hand side of Eq. (A.73) contains the bulk stress tensors for Newtonian fluids which are expressed as Eq. (37):

$$\mathrm{T} = -P\mathrm{I}+\mu(\nabla\mathbf{v}+(\nabla\mathbf{v})^T) \tag{A.80}$$

where I and $\nabla\mathbf{v}$ are given in Eqs. (A.2) and (A.13). The transpose of the velocity gradient, $(\nabla\mathbf{v})^T$, equals to the switched components of $\nabla\mathbf{v}$ from $(\partial/\partial x_i)v_j$ to $(\partial/\partial x_j)v_i$:

$$\nabla\mathbf{v} = \sum_i\sum_j \mathbf{e}_i\mathbf{e}_j\frac{\partial}{\partial x_i}v_j \;;\quad (\nabla\mathbf{v})^T = \sum_i\sum_j \mathbf{e}_i\mathbf{e}_j\frac{\partial}{\partial x_j}v_i \tag{A.81}$$

This implies that the last term in Eq. (A.80) can be formulated as

$$\mu(\nabla\mathbf{v}+(\nabla\mathbf{v})^T)$$

$$= \mu\left(2\frac{\partial v_r}{\partial r}\mathbf{e}_r\mathbf{e}_r+\frac{\partial v_z}{\partial r}\mathbf{e}_r\mathbf{e}_z+\frac{\partial v_z}{\partial r}\mathbf{e}_z\mathbf{e}_r+2\frac{v_r}{r}\mathbf{e}_\theta\mathbf{e}_\theta+\frac{\partial v_r}{\partial z}\mathbf{e}_z\mathbf{e}_r\right.$$

$$\left.+\frac{\partial v_r}{\partial z}\mathbf{e}_r\mathbf{e}_z+2\frac{\partial v_z}{\partial z}\mathbf{e}_z\mathbf{e}_z\right) \tag{A.82}$$

Implementing Eq. (A.80) to the first term of the right-hand side in Eq. (A.73) gives

$$\mathrm{T}:\mathbf{nn}=\left[-P\mathrm{I}+\mu(\nabla\mathbf{v}+(\nabla\mathbf{v})^{T})\right]:\mathbf{nn}=-P\mathrm{I}:\mathbf{nn}+\mu[\nabla\mathbf{v}+(\nabla\mathbf{v})^{T}]:\mathbf{nn}$$
$$=\left[-P\mathrm{I}\cdot\mathbf{n}\right]\cdot\mathbf{n}+\mu\left[[\nabla\mathbf{v}+(\nabla\mathbf{v})^{T}]\cdot\mathbf{n}\right]\cdot\mathbf{n} \qquad \text{(A.83)}$$

For gas bubbles in liquid, μ_d is much smaller than μ_c, implying that the deviatoric stress of the dispersed phase can be omitted. This simplifies the normal stress of the dispersed phase into

$$\mathrm{T}_d:\mathbf{nn}=-P_d \qquad \text{(A.84)}$$

By applying Eqs. (A.2), (A.8), and (A.10), the evaluation of Eq. (A.83) for the continuous phase gives the first dot product in the second term of the left-hand side as

$$-P_c\mathrm{I}\cdot\mathbf{n}=-P_c\left(\mathbf{e}_r\mathbf{e}_r+\mathbf{e}_\theta\mathbf{e}_\theta+\mathbf{e}_z\mathbf{e}_z\right)\cdot\frac{\left(\mathbf{e}_z-\frac{1}{2}\frac{\partial h}{\partial r}\mathbf{e}_r\right)}{\sqrt{1+\frac{1}{4}\left(\frac{\partial h}{\partial r}\right)^2}}$$
$$=-\frac{P_c}{\sqrt{1+\frac{1}{4}\left(\frac{\partial h}{\partial r}\right)^2}}\Bigg[\mathbf{e}_r(\mathbf{e}_r\cdot\mathbf{e}_z)-\mathbf{e}_r(\mathbf{e}_r\cdot\mathbf{e}_r)\frac{1}{2}\frac{\partial h}{\partial r}+\mathbf{e}_\theta(\mathbf{e}_\theta\cdot\mathbf{e}_z)-\mathbf{e}_\theta(\mathbf{e}_\theta\cdot\mathbf{e}_r)\frac{1}{2}\frac{\partial h}{\partial r}$$
$$+\mathbf{e}_z(\mathbf{e}_z\cdot\mathbf{e}_z)-\mathbf{e}_z(\mathbf{e}_z\cdot\mathbf{e}_r)\frac{1}{2}\frac{\partial h}{\partial r}\Bigg]$$
$$=-\frac{P_c}{\sqrt{1+\frac{1}{4}\left(\frac{\partial h}{\partial r}\right)^2}}\left[\mathbf{e}_r\delta_{rz}-\mathbf{e}_r\delta_{rr}\frac{1}{2}\frac{\partial h}{\partial r}+\mathbf{e}_\theta\delta_{\theta z}-\mathbf{e}_\theta\delta_{\theta r}\frac{1}{2}\frac{\partial h}{\partial r}+\mathbf{e}_z\delta_{zz}-\mathbf{e}_z\delta_{zr}\frac{1}{2}\frac{\partial h}{\partial r}\right]$$
$$=-\frac{P_c}{\sqrt{1+\frac{1}{4}\left(\frac{\partial h}{\partial r}\right)^2}}\left[-\mathbf{e}_r\frac{1}{2}\frac{\partial h}{\partial r}+\mathbf{e}_z\right] \qquad \text{(A.85)}$$

Taking the dot product between Eqs. (A.85) and (A.8) yields the double dot product of the pressure term in Eq. (A.83):

$$-P_c\mathrm{I}:\mathbf{nn}=\left[-P_c\mathrm{I}\cdot\mathbf{n}\right]\cdot\mathbf{n}=-\frac{P_c}{\sqrt{1+\frac{1}{4}\left(\frac{\partial h}{\partial r}\right)^2}}\left[-\mathbf{e}_r\frac{1}{2}\frac{\partial h}{\partial r}+\mathbf{e}_z\right]\cdot\frac{\left(\mathbf{e}_z-\frac{1}{2}\frac{\partial h}{\partial r}\mathbf{e}_r\right)}{\sqrt{1+\frac{1}{4}\left(\frac{\partial h}{\partial r}\right)^2}}$$
$$=-\frac{P_c}{1+\frac{1}{4}\left(\frac{\partial h}{\partial r}\right)^2}\left[-\mathbf{e}_r\cdot\mathbf{e}_z\frac{1}{2}\frac{\partial h}{\partial r}+\mathbf{e}_r\cdot\mathbf{e}_r\left(\frac{1}{2}\frac{\partial h}{\partial r}\right)^2+\mathbf{e}_z\cdot\mathbf{e}_z-\mathbf{e}_z\cdot\mathbf{e}_r\frac{1}{2}\frac{\partial h}{\partial r}\right]$$
$$=-\frac{P_c}{1+\frac{1}{4}\left(\frac{\partial h}{\partial r}\right)^2}\left[-\delta_{rz}\frac{1}{2}\frac{\partial h}{\partial r}+\delta_{rr}\left(\frac{1}{2}\frac{\partial h}{\partial r}\right)^2+\delta_{zz}-\delta_{zr}\frac{1}{2}\frac{\partial h}{\partial r}\right]$$
$$=-\frac{P_c}{1+\frac{1}{4}\left(\frac{\partial h}{\partial r}\right)^2}\left[\frac{1}{4}\left(\frac{\partial h}{\partial r}\right)^2+1\right]$$
$$=-P_c \qquad \text{(A.86)}$$

The deviatoric stress term is derived by taking the first dot product between Eqs. (A.82) and (A.8) using the dot product rule in Eq. (A.10):

$$\mu_c \left[\nabla \mathbf{v} + (\nabla \mathbf{v})^T \right] \cdot \mathbf{n}$$

$$= \mu_c \left[2\frac{\partial v_r}{\partial r}\mathbf{e}_r\mathbf{e}_r + \frac{\partial v_z}{\partial r}\mathbf{e}_r\mathbf{e}_z + \frac{\partial v_z}{\partial r}\mathbf{e}_z\mathbf{e}_r + 2\frac{v_r}{r}\mathbf{e}_\theta\mathbf{e}_\theta + \frac{\partial v_r}{\partial z}\mathbf{e}_z\mathbf{e}_r + \frac{\partial v_r}{\partial z}\mathbf{e}_r\mathbf{e}_z + 2\frac{\partial v_z}{\partial z}\mathbf{e}_z\mathbf{e}_z \right] \cdot \frac{\left(\mathbf{e}_z - \frac{1}{2}\frac{\partial h}{\partial r}\mathbf{e}_r\right)}{\sqrt{1+\frac{1}{4}\left(\frac{\partial h}{\partial r}\right)^2}}$$

$$= \frac{\mu_c}{\sqrt{1+\frac{1}{4}\left(\frac{\partial h}{\partial r}\right)^2}} \left[2\frac{\partial v_r}{\partial r}\mathbf{e}_r(\mathbf{e}_r\cdot\mathbf{e}_r)\left(-\frac{1}{2}\frac{\partial h}{\partial r}\right) + \frac{\partial v_z}{\partial r}\mathbf{e}_r(\mathbf{e}_z\cdot\mathbf{e}_z) + \frac{\partial v_z}{\partial r}\mathbf{e}_z(\mathbf{e}_r\cdot\mathbf{e}_r)\left(-\frac{1}{2}\frac{\partial h}{\partial r}\right) + \frac{\partial v_r}{\partial z}\mathbf{e}_z(\mathbf{e}_r\cdot\mathbf{e}_r)\left(-\frac{1}{2}\frac{\partial h}{\partial r}\right) + \frac{\partial v_r}{\partial z}\mathbf{e}_r(\mathbf{e}_z\cdot\mathbf{e}_z) + 2\frac{\partial v_z}{\partial z}\mathbf{e}_z(\mathbf{e}_z\cdot\mathbf{e}_z) \right]$$

$$= \frac{\mu_c}{\sqrt{1+\frac{1}{4}\left(\frac{\partial h}{\partial r}\right)^2}} \left[-\frac{\partial v_r}{\partial r}\frac{\partial h}{\partial r}\mathbf{e}_r + \frac{\partial v_z}{\partial r}\mathbf{e}_r - \frac{1}{2}\frac{\partial v_z}{\partial r}\frac{\partial h}{\partial r}\mathbf{e}_z - \frac{1}{2}\frac{\partial v_r}{\partial z}\frac{\partial h}{\partial r}\mathbf{e}_z + \frac{\partial v_r}{\partial z}\mathbf{e}_r + 2\frac{\partial v_z}{\partial z}\mathbf{e}_z \right] \quad \text{(A.87)}$$

The double dot product is then obtained by taking the dot product between Eqs. (A.87) and (A.8) with the same rule as in Eq. (A.10), resulting in

$$\mu_c \left[\nabla \mathbf{v} + (\nabla \mathbf{v})^T \right] : \mathbf{nn} = \mu_c \left[[\nabla \mathbf{v} + (\nabla \mathbf{v})^T] \cdot \mathbf{n} \right] \cdot \mathbf{n}$$

$$= \frac{\mu_c}{\sqrt{1+\frac{1}{4}\left(\frac{\partial h}{\partial r}\right)^2}} \left[-\frac{\partial v_r}{\partial r}\frac{\partial h}{\partial r}\mathbf{e}_r + \frac{\partial v_z}{\partial r}\mathbf{e}_r - \frac{1}{2}\frac{\partial v_z}{\partial r}\frac{\partial h}{\partial r}\mathbf{e}_z - \frac{1}{2}\frac{\partial v_r}{\partial z}\frac{\partial h}{\partial r}\mathbf{e}_z + \frac{\partial v_r}{\partial z}\mathbf{e}_r + 2\frac{\partial v_z}{\partial z}\mathbf{e}_z \right] \cdot \frac{\left(\mathbf{e}_z - \frac{1}{2}\frac{\partial h}{\partial r}\mathbf{e}_r\right)}{\sqrt{1+\frac{1}{4}\left(\frac{\partial h}{\partial r}\right)^2}}$$

$$= \frac{\mu_c}{1+\frac{1}{4}\left(\frac{\partial h}{\partial r}\right)^2} \left[\frac{1}{2}\frac{\partial v_r}{\partial r}\left(\frac{\partial h}{\partial r}\right)^2 - \frac{1}{2}\frac{\partial v_z}{\partial r}\frac{\partial h}{\partial r} - \frac{1}{2}\frac{\partial v_z}{\partial r}\frac{\partial h}{\partial r} - \frac{1}{2}\frac{\partial v_r}{\partial z}\frac{\partial h}{\partial r} - \frac{1}{2}\frac{\partial v_r}{\partial z}\frac{\partial h}{\partial r} + 2\frac{\partial v_z}{\partial z} \right]$$

$$= \frac{\mu_c}{1+\frac{1}{4}\left(\frac{\partial h}{\partial r}\right)^2} \left[\frac{1}{2}\frac{\partial v_r}{\partial r}\left(\frac{\partial h}{\partial r}\right)^2 - \frac{\partial v_z}{\partial r}\frac{\partial h}{\partial r} - \frac{\partial v_r}{\partial z}\frac{\partial h}{\partial r} + 2\frac{\partial v_z}{\partial z} \right]$$

$$= \frac{\mu_c}{1+\frac{1}{4}\left(\frac{\partial h}{\partial r}\right)^2} \left[\frac{1}{2}\left(\frac{\partial h}{\partial r}\right)^2\frac{\partial v_r}{\partial r} + \left(\frac{\partial v_r}{\partial z} + \frac{\partial v_z}{\partial r}\right)\left(-\frac{\partial h}{\partial r}\right) + 2\frac{\partial v_z}{\partial z} \right] \quad \text{(A.88)}$$

Combining Eqs. (A.86) and (A.88) yields the normal stress balance in the continuous phase:

$$\begin{aligned}\mathrm{T}_c:\mathbf{nn} &= -P_c\mathrm{I}:\mathbf{nn} + \mu_c[\nabla\mathbf{v} + (\nabla\mathbf{v})^T]:\mathbf{nn} \\ &= -P_c + \frac{\mu_c}{1+\frac{1}{4}\left(\frac{\partial h}{\partial r}\right)^2}\left[\frac{1}{2}\left(\frac{\partial h}{\partial r}\right)^2\frac{\partial v_r}{\partial r} + \left(\frac{\partial v_r}{\partial z}+\frac{\partial v_z}{\partial r}\right)\left(-\frac{\partial h}{\partial r}\right) + 2\frac{\partial v_z}{\partial z}\right]\end{aligned} \quad \text{(A.89)}$$

The subtraction between Eqs. (A.84) and (A.89) gives the jump condition in the first term of the right-hand side of Eq. (A.73) as

$$\begin{aligned}RHS_{1st} &= \|\mathrm{T}\|:\mathbf{nn} = \mathrm{T}_c:\mathbf{nn} - \mathrm{T}_d:\mathbf{nn} \\ &= -P_c + \frac{\mu_c}{1+\frac{1}{4}\left(\frac{\partial h}{\partial r}\right)^2}\left[\frac{1}{2}\left(\frac{\partial h}{\partial r}\right)^2\frac{\partial v_r}{\partial r} + \left(\frac{\partial v_r}{\partial z}+\frac{\partial v_z}{\partial r}\right)\left(-\frac{\partial h}{\partial r}\right) + 2\frac{\partial v_z}{\partial z}\right] + P_d\end{aligned} \quad \text{(A.90)}$$

The dot product in the last term of the right-hand side of Eq. (A.73) is defined as the normal velocity in bulk phases, v_n, and the normal velocity of the interface, U_n, which gives:

$$\begin{aligned}RHS_{2nd} &= -\left\|\rho\left((\mathbf{u}-\mathbf{v})\cdot\mathbf{n}\right)^2\right\| \\ &= -\|\rho(\mathbf{u}\cdot\mathbf{n} - \mathbf{v}\cdot\mathbf{n})^2\| \\ &= -\|\rho(U_n - v_n)^2\|\end{aligned} \quad \text{(A.91)}$$

Finally, Eqs. (A.79), (A.90), and (A.91) are substituted into Eq. (A.73) as

$$\begin{aligned}2H\sigma\mathbf{n}\cdot\mathbf{n} &= \|\mathrm{T}\|:\mathbf{nn} - \left\|\rho\left((\mathbf{u}-\mathbf{v})\cdot\mathbf{n}\right)^2\right\| \\ \frac{\sigma}{2r}\frac{\partial}{\partial r}\left(r\frac{\partial h}{\partial r}\right) &= -P_c + \frac{\mu_c}{1+\frac{1}{4}\left(\frac{\partial h}{\partial r}\right)^2}\left[\frac{1}{2}\left(\frac{\partial h}{\partial r}\right)^2\frac{\partial v_r}{\partial r} + \left(\frac{\partial v_r}{\partial z}+\frac{\partial v_z}{\partial r}\right)\left(-\frac{\partial h}{\partial r}\right) + 2\frac{\partial v_z}{\partial z}\right] \\ &\quad + P_d - \|\rho(U_n - v_n)^2\| = 0\end{aligned} \quad \text{(A.92)}$$

Arranging Eq. (A.92) gives the final expression of the normal stress balance as Eq. (39):

$$\begin{aligned}\frac{\sigma}{2r}\frac{\partial}{\partial r}\left(r\frac{\partial h}{\partial r}\right) &= P_d - P_c + \frac{\mu_c}{1+\frac{1}{4}\left(\frac{\partial h}{\partial r}\right)^2}\left[\frac{1}{2}\left(\frac{\partial h}{\partial r}\right)^2\frac{\partial v_r}{\partial r} + \left(\frac{\partial v_r}{\partial z}+\frac{\partial v_z}{\partial r}\right)\left(-\frac{\partial h}{\partial r}\right) + 2\frac{\partial v_z}{\partial z}\right] \\ &\quad - \|\rho(U_n - v_n)^2\|\end{aligned} \quad \text{(A.93)}$$

A.9 Derivation of the Tangential Stress Balance

The tangential stress balance with the presence of surfactants follows Eq. (40):

$$2H\sigma\mathbf{n}\cdot\mathbf{t}_1+\nabla_s\sigma\cdot\mathbf{t}_1=\|\mathrm{T}\|:\mathbf{n}\mathbf{t}_1 \tag{A.94}$$

with $\|\mathrm{T}\|=[\mathrm{T_c}-\mathrm{T_d}]$. The dot product between two orthogonal vectors, $\mathbf{n}$ and $\mathbf{t}_1$, gives zero to the first term of the left-hand side, simplifying Eq. (A.94) into

$$\nabla_s\sigma\cdot\mathbf{t}_1=\left[\mathrm{T}_c|_{z=h/2}:\mathbf{n}\mathbf{t}_1-\mathrm{T}_d|_{z=h/2}:\mathbf{n}\mathbf{t}_1\right] \tag{A.95}$$

Substituting ∇_s in Eq. (A.3) to the left-hand side of Eq. (A.95) yields

$$\nabla_s\sigma\cdot\mathbf{t}_1=\left[\left(\frac{\mathbf{t}_1}{\sqrt{1+\frac{1}{4}\left(\frac{\partial h}{\partial r}\right)^2}}\frac{\partial\sigma}{\partial r}+\frac{\mathbf{t}_2}{r}\frac{\partial\sigma}{\partial\theta}\right)\right]\cdot\mathbf{t}_1 \tag{A.96}$$

Noting that the dot product of two identical vectors gives 1 and the one between two orthogonal vectors gives 0, Eq. (A.96) becomes

$$\nabla_s\sigma\cdot\mathbf{t}_1=\frac{1}{\sqrt{1+\frac{1}{4}\left(\frac{\partial h}{\partial r}\right)^2}}\frac{\partial\sigma}{\partial r} \tag{A.97}$$

The first term of the right-hand side in Eq. (A.95) is derived by substituting the Newtonian stress tensor in Eq. (A.80) for the continuous phase:

$$\begin{aligned}\mathrm{T}_c:\mathbf{n}\mathbf{t}_1&=\left[-P_c\mathrm{I}+\mu_c(\nabla\mathbf{v}_c+(\nabla\mathbf{v}_c)^T)\right]:\mathbf{n}\mathbf{t}_1\\&=-P_c\mathrm{I}:\mathbf{n}\mathbf{t}_1+\mu_c[\nabla\mathbf{v}_c+(\nabla\mathbf{v}_c)^T]:\mathbf{n}\mathbf{t}_1\\&=\left[-P_c\mathrm{I}\cdot\mathbf{n}\right]\cdot\mathbf{t}_1+\mu_c\left\{[\nabla\mathbf{v}_c+(\nabla\mathbf{v}_c)^T]\cdot\mathbf{n}\right\}\cdot\mathbf{t}_1\end{aligned} \tag{A.98}$$

By expanding the pressure term of Eq. (A.98) with $-P_c\mathrm{I}\cdot\mathbf{n}$ and $\mathbf{t}_1$ in Eqs. (A.85) and (3), taking the dot product according to Eq. (A.10) give

$$\begin{aligned}-P_c\mathrm{I}:\mathbf{n}\mathbf{t}_1=\left(-P_c\mathrm{I}\cdot\mathbf{n}\right)\cdot\mathbf{t}_1&=-\frac{P_c}{\sqrt{1+\frac{1}{4}\left(\frac{\partial h}{\partial r}\right)^2}}\left[-\mathbf{e}_r\frac{1}{2}\frac{\partial h}{\partial r}+\mathbf{e}_z\right]\cdot\frac{\mathbf{e}_r+\frac{1}{2}\frac{\partial h}{\partial r}\mathbf{e}_z}{\sqrt{1+\frac{1}{4}\left(\frac{\partial h}{\partial r}\right)^2}}\\&=-\frac{P_c}{1+\frac{1}{4}\left(\frac{\partial h}{\partial r}\right)^2}\left[-\mathbf{e}_r\cdot\mathbf{e}_r\frac{1}{2}\frac{\partial h}{\partial r}-\mathbf{e}_r\cdot\mathbf{e}_z\left(\frac{1}{2}\frac{\partial h}{\partial r}\right)^2+\mathbf{e}_z\cdot\mathbf{e}_r+\mathbf{e}_z\cdot\mathbf{e}_z\frac{1}{2}\frac{\partial h}{\partial r}\right]\\&=-\frac{P_c}{1+\frac{1}{4}\left(\frac{\partial h}{\partial r}\right)^2}\left[-\delta_{rr}\frac{1}{2}\frac{\partial h}{\partial r}-\delta_{rz}\left(\frac{1}{2}\frac{\partial h}{\partial r}\right)^2+\delta_{zr}+\delta_{zz}\frac{1}{2}\frac{\partial h}{\partial r}\right]\\&=-\frac{P_c}{1+\frac{1}{4}\left(\frac{\partial h}{\partial r}\right)^2}\left[-\frac{1}{2}\frac{\partial h}{\partial r}+\frac{1}{2}\frac{\partial h}{\partial r}\right]\\&=0\end{aligned} \tag{A.99}$$

The last term of Eq. (A.98) is derived by following the dot product with $\mathbf{n}$ described in Eq. (A.87), then applying Eqs. (3) and (A.10) to take the dot product with $\mathbf{t}_1$ as

$$\mu_c\left[\nabla\mathbf{v}_c+(\nabla\mathbf{v}_c)^T\right]:\mathbf{n}\mathbf{t}_1=\mu_c\left[[\nabla\mathbf{v}_c+(\nabla\mathbf{v}_c)^T]\cdot\mathbf{n}\right]\cdot\mathbf{t}_1$$

$$=\frac{\mu_c}{\sqrt{1+\frac{1}{4}\left(\frac{\partial h}{\partial r}\right)^2}}\left[-\frac{\partial v_r}{\partial r}\frac{\partial h}{\partial r}\mathbf{e}_r+\frac{\partial v_z}{\partial r}\mathbf{e}_r-\frac{1}{2}\frac{\partial v_z}{\partial r}\frac{\partial h}{\partial r}\mathbf{e}_z\right.$$

$$\left.-\frac{1}{2}\frac{\partial v_r}{\partial z}\frac{\partial h}{\partial r}\mathbf{e}_z+\frac{\partial v_r}{\partial z}\mathbf{e}_r+2\frac{\partial v_z}{\partial z}\mathbf{e}_z\right]\cdot\frac{\mathbf{e}_r+\frac{1}{2}\frac{\partial h}{\partial r}\mathbf{e}_z}{\sqrt{1+\frac{1}{4}\left(\frac{\partial h}{\partial r}\right)^2}}$$

$$=\frac{\mu_c}{1+\frac{1}{4}\left(\frac{\partial h}{\partial r}\right)^2}\left[-\frac{\partial v_r}{\partial r}\frac{\partial h}{\partial r}+\frac{\partial v_z}{\partial r}-\frac{1}{4}\frac{\partial v_z}{\partial r}\left(\frac{\partial h}{\partial r}\right)^2-\frac{1}{4}\frac{\partial v_r}{\partial z}\left(\frac{\partial h}{\partial r}\right)^2+\frac{\partial v_r}{\partial z}+\frac{\partial v_z}{\partial z}\frac{\partial h}{\partial r}\right]$$

$$=\frac{\mu_c}{1+\frac{1}{4}\left(\frac{\partial h}{\partial r}\right)^2}\left[-\frac{\partial h}{\partial r}\frac{\partial v_r}{\partial r}+\frac{\partial v_z}{\partial r}\left(1-\frac{1}{4}\left(\frac{\partial h}{\partial r}\right)^2\right)+\frac{\partial v_r}{\partial z}\left(1-\frac{1}{4}\left(\frac{\partial h}{\partial r}\right)^2\right)+\frac{\partial h}{\partial r}\frac{\partial v_z}{\partial z}\right]$$

$$=\frac{\mu_c}{1+\frac{1}{4}\left(\frac{\partial h}{\partial r}\right)^2}\left[-\frac{\partial h}{\partial r}\frac{\partial v_r}{\partial r}+\left(\frac{\partial v_r}{\partial z}+\frac{\partial v_z}{\partial r}\right)\left(1-\frac{1}{4}\left(\frac{\partial h}{\partial r}\right)^2\right)+\frac{\partial h}{\partial r}\frac{\partial v_z}{\partial z}\right] \quad \text{(A.100)}$$

By substituting Eqs. (A.99) and (A.100) to Eq. (A.98), the tangential stress of the film side is found as

$$\mathrm{T}_c:\mathbf{n}\mathbf{t}_1=-P_c\mathrm{I}:\mathbf{n}\mathbf{t}_1+\mu_c[\nabla\mathbf{v}_c+(\nabla\mathbf{v}_c)^T]:\mathbf{n}\mathbf{t}_1$$

$$=0+\frac{\mu_c}{1+\frac{1}{4}\left(\frac{\partial h}{\partial r}\right)^2}\left[-\frac{\partial h}{\partial r}\frac{\partial v_r}{\partial r}+\left(\frac{\partial v_r}{\partial z}+\frac{\partial v_z}{\partial r}\right)\left(1-\frac{1}{4}\left(\frac{\partial h}{\partial r}\right)^2\right)+\frac{\partial h}{\partial r}\frac{\partial v_z}{\partial z}\right] \quad \text{(A.101)}$$

The tangential stress for the dispersed phase in the last term of Eq. (A.95) is defined as $\tau_d=-(\mathrm{T}_d\cdot\mathbf{n})\cdot\mathbf{t}_1$. Applying this together with Eqs. (A.97) and (A.101) to Eq. (A.95) yields the tangential stress balance as

$$\frac{1}{\sqrt{1+\frac{1}{4}\left(\frac{\partial h}{\partial r}\right)^2}}\frac{\partial\sigma}{\partial r}$$

$$=\frac{\mu_c}{1+\frac{1}{4}\left(\frac{\partial h}{\partial r}\right)^2}\left[-\frac{\partial h}{\partial r}\frac{\partial v_r}{\partial r}+\left(\frac{\partial v_r}{\partial z}+\frac{\partial v_z}{\partial r}\right)\left(1-\frac{1}{4}\left(\frac{\partial h}{\partial r}\right)^2\right)+\frac{\partial h}{\partial r}\frac{\partial v_z}{\partial z}\right]+\tau_d \quad \text{(A.102)}$$

A.10 Derivation of the Surface Excess Concentration Balance

The excess concentration of the surfactant along the interface is given as Eq. (45):

$$\frac{\partial \Gamma}{\partial t} + \nabla_s \cdot (\Gamma \mathbf{u}) + \nabla_s \cdot (\mathbf{J}_I \cdot \mathrm{I}_s) = 0 \tag{A.103}$$

where $\mathbf{J}_I$ is defined in Eq. (46):

$$\mathbf{J}_I = -D_I \nabla_s \Gamma \tag{A.104}$$

Expanding the second term of the left-hand side of Eq. (A.103) yields

$$\begin{aligned}
LHS_{2nd} &= \nabla_s \cdot (\Gamma \mathbf{u}) \\
&= \mathbf{u} \cdot \nabla_s \Gamma + \Gamma (\nabla_s \cdot \mathbf{u}) \\
&= \left[U_n \mathbf{n} + U_t \mathbf{t}_1\right] \cdot \left[\frac{\mathbf{t}_1}{\sqrt{1+\frac{1}{4}\left(\frac{\partial h}{\partial r}\right)^2}} \frac{\partial \Gamma}{\partial r} + \frac{\mathbf{t}_2}{r} \frac{\partial \Gamma}{\partial \theta}\right] + \left[\frac{\Gamma\, \mathbf{t}_1}{\sqrt{1+\frac{1}{4}\left(\frac{\partial h}{\partial r}\right)^2}} \frac{\partial}{\partial r} + \frac{\Gamma\, \mathbf{t}_2}{r} \frac{\partial}{\partial \theta}\right] \cdot \left[U_n \mathbf{n} + U_t \mathbf{t}_1\right] \\
&= U_n \left[\frac{(\mathbf{n} \cdot \mathbf{t}_1)}{\sqrt{1+\frac{1}{4}\left(\frac{\partial h}{\partial r}\right)^2}} \frac{\partial \Gamma}{\partial r} + \frac{(\mathbf{n} \cdot \mathbf{t}_2)}{r} \frac{\partial \Gamma}{\partial \theta}\right] + U_t \left[\frac{(\mathbf{t}_1 \cdot \mathbf{t}_1)}{\sqrt{1+\frac{1}{4}\left(\frac{\partial h}{\partial r}\right)^2}} \frac{\partial \Gamma}{\partial r} + \frac{(\mathbf{t}_1 \cdot \mathbf{t}_2)}{r} \frac{\partial \Gamma}{\partial \theta}\right] \\
&\quad + \frac{\Gamma}{\sqrt{1+\frac{1}{4}\left(\frac{\partial h}{\partial r}\right)^2}} \frac{\partial U_n}{\partial r}\left(\mathbf{t}_1 \cdot \mathbf{n}\right) + \frac{\Gamma U_n}{\sqrt{1+\frac{1}{4}\left(\frac{\partial h}{\partial r}\right)^2}} \left(\mathbf{t}_1 \cdot \frac{\partial}{\partial r} \mathbf{n}\right) \\
&\quad + \frac{\Gamma}{\sqrt{1+\frac{1}{4}\left(\frac{\partial h}{\partial r}\right)^2}} \frac{\partial U_t}{\partial r}\left(\mathbf{t}_1 \cdot \mathbf{t}_1\right) + \frac{\Gamma U_t}{\sqrt{1+\frac{1}{4}\left(\frac{\partial h}{\partial r}\right)^2}} \left(\mathbf{t}_1 \cdot \frac{\partial}{\partial r} \mathbf{t}_1\right) \\
&\quad + \frac{\Gamma}{r} \frac{\partial U_n}{\partial \theta}\left(\mathbf{t}_2 \cdot \mathbf{n}\right) + \frac{\Gamma U_n}{r} \left(\mathbf{t}_2 \cdot \frac{\partial}{\partial \theta} \mathbf{n}\right) + \frac{\Gamma}{r} \frac{\partial U_t}{\partial \theta}\left(\mathbf{t}_2 \cdot \mathbf{t}_1\right) \\
&\quad + \frac{\Gamma U_t}{r} \left(\mathbf{t}_2 \cdot \frac{\partial}{\partial \theta} \mathbf{t}_1\right)
\end{aligned} \tag{A.105}$$

The term $\left(\mathbf{t}_1 \cdot \frac{\partial}{\partial r} \mathbf{t}_1\right)$ is derived by substituting Eqs. (3) and (A.16) to yield

$$\begin{aligned}
\mathbf{t}_1 \cdot \frac{\partial}{\partial r} \mathbf{t}_1 &= \frac{\mathbf{e}_r + \frac{1}{2}\frac{\partial h}{\partial r} \mathbf{e}_z}{\sqrt{1+\frac{1}{4}\left(\frac{\partial h}{\partial r}\right)^2}} \cdot \left\{ -\frac{\frac{1}{4}\frac{\partial h}{\partial r}\frac{\partial^2 h}{\partial r^2} \mathbf{e}_r}{\left[1+\frac{1}{4}\left(\frac{\partial h}{\partial r}\right)^2\right]^{3/2}} + \frac{\frac{1}{2}\frac{\partial^2 h}{\partial r^2} \mathbf{e}_z}{\left[1+\frac{1}{4}\left(\frac{\partial h}{\partial r}\right)^2\right]^{3/2}} \right\} \\
&= -\frac{\frac{1}{4}\frac{\partial h}{\partial r}\frac{\partial^2 h}{\partial r^2}}{\left[1+\frac{1}{4}\left(\frac{\partial h}{\partial r}\right)^2\right]^2} + \frac{\frac{1}{4}\frac{\partial h}{\partial r}\frac{\partial^2 h}{\partial r^2}}{\left[1+\frac{1}{4}\left(\frac{\partial h}{\partial r}\right)^2\right]^2} \\
&= 0
\end{aligned} \tag{A.106}$$

The term $\left(\mathbf{t}_2 \cdot \frac{\partial}{\partial\theta}\mathbf{t}_1\right)$ is computed by substituting Eqs. (3) and (A.17) to give

$$\mathbf{t}_2 \cdot \frac{\partial}{\partial\theta}\mathbf{t}_1 = \mathbf{e}_\theta \cdot \frac{1}{\sqrt{1+\frac{1}{4}\left(\frac{\partial h}{\partial r}\right)^2}}\mathbf{e}_\theta = \frac{1}{\sqrt{1+\frac{1}{4}\left(\frac{\partial h}{\partial r}\right)^2}} \tag{A.107}$$

Implementing Eqs. (A.75) - (A.76) and (A.106) - (A.107), taking the dot product between two vectors orthogonal to each other as zero, and having $\mathbf{t}_1 \cdot \mathbf{t}_1 = 1$ simplify Eq. (A.105) into

$$\begin{aligned} LHS_{2nd} &= \nabla_s \cdot (\Gamma\mathbf{u}) \\ &= \frac{U_t}{\sqrt{1+\frac{1}{4}\left(\frac{\partial h}{\partial r}\right)^2}}\frac{\partial\Gamma}{\partial r} - \frac{1}{2}\frac{\Gamma U_n}{\left[1+\frac{1}{4}\left(\frac{\partial h}{\partial r}\right)^2\right]^{3/2}}\frac{\partial^2 h}{\partial r^2} + \frac{\Gamma}{\sqrt{1+\frac{1}{4}\left(\frac{\partial h}{\partial r}\right)^2}}\frac{\partial U_t}{\partial r} \\ &\quad - \frac{\Gamma U_n}{2r}\frac{\frac{\partial h}{\partial r}}{\sqrt{1+\frac{1}{4}\left(\frac{\partial h}{\partial r}\right)^2}} + \frac{\Gamma U_t}{r}\frac{1}{\sqrt{1+\frac{1}{4}\left(\frac{\partial h}{\partial r}\right)^2}} \end{aligned} \tag{A.108}$$

The third term of the left-hand side of Eq. (A.103) decomposes by substituting Eqs. (A.104), (A.3), and (A.4) into

$$\begin{aligned} LHS_{3rd} &= \nabla_s \cdot (\mathbf{J}_I \cdot \mathrm{I}_s) \\ &= \nabla_s \cdot \left[(-D_I \nabla_s \Gamma) \cdot (\mathbf{t}_1\mathbf{t}_1 + \mathbf{t}_2\mathbf{t}_2)\right] \\ &= \nabla_s \cdot \left[\left(-D_I \frac{\mathbf{t}_1}{\sqrt{1+\frac{1}{4}\left(\frac{\partial h}{\partial r}\right)^2}}\frac{\partial\Gamma}{\partial r} - D_I \frac{\mathbf{t}_2}{r}\frac{\partial\Gamma}{\partial\theta}\right) \cdot (\mathbf{t}_1\mathbf{t}_1 + \mathbf{t}_2\mathbf{t}_2)\right] \end{aligned} \tag{A.109}$$

The axisymmetry condition eliminates the concentration gradient with respect to θ-direction. By considering constant D_I, applying ∇_s from Eq. (A.3) and the dot product rules gives

$$\begin{aligned} LHS_{3rd} &= \nabla_s \cdot \left[\left(-D_I \frac{\mathbf{t}_1 \cdot (\mathbf{t}_1\mathbf{t}_1 + \mathbf{t}_2\mathbf{t}_2)}{\sqrt{1+\frac{1}{4}\left(\frac{\partial h}{\partial r}\right)^2}}\frac{\partial\Gamma}{\partial r}\right)\right] \\ &= \left[\frac{\mathbf{t}_1}{\sqrt{1+\frac{1}{4}\left(\frac{\partial h}{\partial r}\right)^2}}\frac{\partial}{\partial r} + \frac{\mathbf{t}_2}{r}\frac{\partial}{\partial\theta}\right] \cdot \left[\left(-\frac{D_I}{\sqrt{1+\frac{1}{4}\left(\frac{\partial h}{\partial r}\right)^2}}\frac{\partial\Gamma}{\partial r}\mathbf{t}_1\right)\right] \end{aligned}$$

$$= \frac{-D_I(\mathbf{t}_1 \cdot \mathbf{t}_1)}{\sqrt{1+\frac{1}{4}\left(\frac{\partial h}{\partial r}\right)^2}}\left[\frac{\partial^2 \Gamma}{\partial r^2}\frac{1}{\sqrt{1+\frac{1}{4}\left(\frac{\partial h}{\partial r}\right)^2}} - \frac{\partial \Gamma}{\partial r}\frac{1}{2}\frac{\frac{1}{2}\frac{\partial h}{\partial r}\frac{\partial^2 h}{\partial r^2}}{\left[1+\frac{1}{4}\left(\frac{\partial h}{\partial r}\right)^2\right]^{\frac{3}{2}}}\right]$$

$$- \frac{D_I}{1+\frac{1}{4}\left(\frac{\partial h}{\partial r}\right)^2}\frac{\partial \Gamma}{\partial r}\left(\mathbf{t}_1 \cdot \frac{\partial}{\partial r}\mathbf{t}_1\right) - \frac{D_I}{\sqrt{1+\frac{1}{4}\left(\frac{\partial h}{\partial r}\right)^2}}\frac{1}{r}\frac{\partial \Gamma}{\partial r}\left(\mathbf{t}_2 \cdot \frac{\partial}{\partial \theta}\mathbf{t}_1\right)$$

$$= \frac{-D_I}{1+\frac{1}{4}\left(\frac{\partial h}{\partial r}\right)^2}\left[\frac{\partial^2 \Gamma}{\partial r^2} - \frac{1}{4}\frac{\partial \Gamma}{\partial r}\frac{\frac{\partial h}{\partial r}\frac{\partial^2 h}{\partial r^2}}{1+\frac{1}{4}\left(\frac{\partial h}{\partial r}\right)^2}\right] - \frac{D_I}{1+\frac{1}{4}\left(\frac{\partial h}{\partial r}\right)^2}\frac{1}{r}\frac{\partial \Gamma}{\partial r}$$

$$= \frac{-D_I}{1+\frac{1}{4}\left(\frac{\partial h}{\partial r}\right)^2}\left[\frac{1}{r}\frac{\partial}{\partial r}\left(r\frac{\partial \Gamma}{\partial r}\right) - \frac{1}{4}\frac{\partial \Gamma}{\partial r}\frac{\frac{\partial h}{\partial r}\frac{\partial^2 h}{\partial r^2}}{1+\frac{1}{4}\left(\frac{\partial h}{\partial r}\right)^2}\right] \tag{A.110}$$

Note that $\mathbf{t}_1 \cdot \frac{\partial}{\partial r}\mathbf{t}_1 = 0$ and $\mathbf{t}_2 \cdot \frac{\partial}{\partial \theta}\mathbf{t}_1 = \frac{1}{\sqrt{1+\frac{1}{4}\left(\frac{\partial h}{\partial r}\right)^2}}$ according to Eqs. (A.106) and (A.107).

Applying Eqs. (A.108) and (A.110) into Eq. (A.103) results in

$$\frac{\partial \Gamma}{\partial t} + \frac{U_t}{\sqrt{1+\frac{1}{4}\left(\frac{\partial h}{\partial r}\right)^2}}\frac{\partial \Gamma}{\partial r} - \frac{1}{2}\frac{\Gamma U_n}{\left[1+\frac{1}{4}\left(\frac{\partial h}{\partial r}\right)^2\right]^{3/2}}\frac{\partial^2 h}{\partial r^2} + \frac{\Gamma}{\sqrt{1+\frac{1}{4}\left(\frac{\partial h}{\partial r}\right)^2}}\frac{\partial U_t}{\partial r}$$

$$- \frac{\Gamma U_n}{2r}\frac{\frac{\partial h}{\partial r}}{\sqrt{1+\frac{1}{4}\left(\frac{\partial h}{\partial r}\right)^2}} + \frac{\Gamma U_t}{r}\frac{1}{\sqrt{1+\frac{1}{4}\left(\frac{\partial h}{\partial r}\right)^2}}$$

$$- \frac{D_I}{1+\frac{1}{4}\left(\frac{\partial h}{\partial r}\right)^2}\left[\frac{1}{r}\frac{\partial}{\partial r}\left(r\frac{\partial \Gamma}{\partial r}\right) - \frac{1}{4}\frac{\partial \Gamma}{\partial r}\frac{\frac{\partial h}{\partial r}\frac{\partial^2 h}{\partial r^2}}{1+\frac{1}{4}\left(\frac{\partial h}{\partial r}\right)^2}\right] = 0 \tag{A.111}$$

which is reformulated by using the relation: $U_t\frac{\partial \Gamma}{\partial r} + \Gamma\frac{\partial U_t}{\partial r} + \frac{\Gamma U_t}{r} = \frac{1}{r}\frac{\partial}{\partial r}(r\Gamma U_t)$ to yield

$$\frac{\partial \Gamma}{\partial t} + \frac{\frac{1}{r}\frac{\partial}{\partial r}(r\Gamma U_t)}{\sqrt{1+\frac{1}{4}\left(\frac{\partial h}{\partial r}\right)^2}} - \frac{1}{2}\frac{\Gamma U_n}{\left[1+\frac{1}{4}\left(\frac{\partial h}{\partial r}\right)^2\right]^{3/2}}\frac{\partial^2 h}{\partial r^2} - \frac{\Gamma U_n}{2r}\frac{\frac{\partial h}{\partial r}}{\sqrt{1+\frac{1}{4}\left(\frac{\partial h}{\partial r}\right)^2}}$$

$$- \frac{D_I}{1+\frac{1}{4}\left(\frac{\partial h}{\partial r}\right)^2}\left[\frac{1}{r}\frac{\partial}{\partial r}\left(r\frac{\partial \Gamma}{\partial r}\right) - \frac{1}{4}\frac{\partial \Gamma}{\partial r}\frac{\frac{\partial h}{\partial r}\frac{\partial^2 h}{\partial r^2}}{1+\frac{1}{4}\left(\frac{\partial h}{\partial r}\right)^2}\right] = 0 \tag{A.112}$$

A.11 Derivation of the Thinning Equation

In this section, all equations are present in terms of dimensionless variables.

The thinning equation in Eq. (101) comes from the kinematic condition in Eq. (59):

$$U_n = \frac{1}{2}\frac{\partial h}{\partial t} = v_z|_{z=h/2} - \frac{1}{2}\frac{\partial h}{\partial r}v_r|_{z=h/2} + \frac{1}{Pe}\frac{1}{\left(1-\omega_{A,c}\big|_{z=h/2}\right)}\frac{\partial \omega_{A,c}}{\partial z}\bigg|_{z=h/2} \tag{A.113}$$

by evaluating v_r and v_z at the interface. Applying $z = h/2$ into Eq. (100) gives the v_z profiles at the interface as:

$$v_z|_{z=h/2} = -\frac{1}{3}\frac{1}{r}\frac{\partial}{\partial r}\left(\frac{r}{2}\frac{\partial P_c}{\partial r}\right)z^3\bigg|_{z=h/2} - \frac{1}{r}\frac{\partial}{\partial r}(rU_t)z\bigg|_{z=h/2} + \frac{1}{r}\frac{\partial}{\partial r}\left[\frac{r}{2}\frac{\partial P_c}{\partial r}\left(\frac{h}{2}\right)^2\right]z\bigg|_{z=h/2}$$

$$= -\frac{1}{3}\frac{1}{r}\frac{\partial}{\partial r}\left(\frac{r}{2}\frac{\partial P_c}{\partial r}\right)\left(\frac{h}{2}\right)^3 - \frac{1}{r}\frac{\partial}{\partial r}(rU_t)\left(\frac{h}{2}\right) + \frac{1}{r}\frac{\partial}{\partial r}\left[\frac{r}{2}\frac{\partial P_c}{\partial r}\left(\frac{h}{2}\right)^2\right]\frac{h}{2} \tag{A.114}$$

Expanding the last term of the right-hand side in Eq. (A.114) gives

$$\frac{1}{r}\frac{\partial}{\partial r}\left[\frac{r}{2}\frac{\partial P_c}{\partial r}\left(\frac{h}{2}\right)^2\right]\frac{h}{2} = \frac{1}{r}\frac{\partial}{\partial r}\left(\frac{r}{2}\frac{\partial P_c}{\partial r}\right)\left(\frac{h}{2}\right)^2\left(\frac{h}{2}\right) + \frac{1}{r}\left(\frac{r}{2}\frac{\partial P_c}{\partial r}\right)\frac{\partial}{\partial r}\left[\left(\frac{h}{2}\right)^2\right]\left(\frac{h}{2}\right) \tag{A.115}$$

Thus, Eq. (A.115) becomes

$$v_z|_{z=h/2} = -\frac{1}{3}\frac{1}{r}\frac{\partial}{\partial r}\left(\frac{r}{2}\frac{\partial P_c}{\partial r}\right)\left(\frac{h}{2}\right)^3 - \frac{1}{r}\frac{\partial}{\partial r}(rU_t)\left(\frac{h}{2}\right) + \frac{1}{r}\frac{\partial}{\partial r}\left(\frac{r}{2}\frac{\partial P_c}{\partial r}\right)\left(\frac{h}{2}\right)^3 + \frac{1}{2}\left(\frac{\partial P_c}{\partial r}\right)\frac{\partial}{\partial r}\left[\left(\frac{h}{2}\right)^2\right]\left(\frac{h}{2}\right) \tag{A.116}$$

The first and the third terms in the right-hand side of Eq. (A.116) are summed up into

$$v_z|_{z=\frac{h}{2}} = \frac{2}{3}\frac{1}{r}\frac{\partial}{\partial r}\left(\frac{r}{2}\frac{\partial P_c}{\partial r}\right)\left(\frac{h}{2}\right)^3 - \frac{1}{r}\frac{\partial}{\partial r}(rU_t)\left(\frac{h}{2}\right) + \frac{1}{2}\left(\frac{\partial P_c}{\partial r}\right)\frac{\partial}{\partial r}\left[\left(\frac{h}{2}\right)^2\right]\left(\frac{h}{2}\right) \tag{A.117}$$

Expanding the last term of Eq. (A.117) yields

$$\frac{1}{2}\left(\frac{\partial P_c}{\partial r}\right)\frac{\partial}{\partial r}\left[\left(\frac{h}{2}\right)^2\right]\left(\frac{h}{2}\right) = \frac{1}{2}\left(\frac{\partial P_c}{\partial r}\right)2\left(\frac{h}{2}\right)\frac{\partial}{\partial r}\left(\frac{h}{2}\right)\left(\frac{h}{2}\right)$$

$$= \frac{1}{2}\left(\frac{\partial P_c}{\partial r}\right)2\left(\frac{h}{2}\right)^2\frac{\partial}{\partial r}\left(\frac{h}{2}\right) \tag{A.118}$$

By applying $\frac{\partial}{\partial r}\left[\left(\frac{h}{2}\right)^3\right] = 3\left(\frac{h}{2}\right)^2\frac{\partial}{\partial r}\left(\frac{h}{2}\right)$, Eq. (A.118) is reformulated into

$$\frac{1}{2}\left(\frac{\partial P_c}{\partial r}\right)\frac{\partial}{\partial r}\left[\left(\frac{h}{2}\right)^2\right]\left(\frac{h}{2}\right)=\frac{1}{2}\left(\frac{\partial P_c}{\partial r}\right)\frac{2}{3}\frac{\partial}{\partial r}\left[\left(\frac{h}{2}\right)^3\right]=\frac{2}{3}\left\{\frac{1}{2}\left(\frac{\partial P_c}{\partial r}\right)\frac{\partial}{\partial r}\left[\left(\frac{h}{2}\right)^3\right]\right\} \quad \text{(A.119)}$$

Then, Eq. (A.119) is substituted to Eq. (A.117) to yield (A.124)

$$v_z|_{z=h/2}=\frac{2}{3}\frac{1}{r}\frac{\partial}{\partial r}\left(\frac{r}{2}\frac{\partial P_c}{\partial r}\right)\left(\frac{h}{2}\right)^3-\frac{1}{r}\frac{\partial}{\partial r}(rU_t)\left(\frac{h}{2}\right)+\frac{2}{3}\left\{\frac{1}{2}\left(\frac{\partial P_c}{\partial r}\right)\frac{\partial}{\partial r}\left[\left(\frac{h}{2}\right)^3\right]\right\} \quad \text{(A.120)}$$

Merging the first and the last terms of the right-hand side of Eq. (A.120) results in the axial velocity profiles at the interface:

$$v_z|_{z=h/2}=\frac{2}{3}\frac{1}{r}\frac{\partial}{\partial r}\left[\frac{r}{2}\frac{\partial P_c}{\partial r}\left(\frac{h}{2}\right)^3\right]-\frac{1}{r}\frac{\partial}{\partial r}(rU_t)\left(\frac{h}{2}\right) \quad \text{(A.121)}$$

The evaluation of v_r in Eq. (99) at the interface yields

$$\begin{aligned}-\frac{1}{2}\frac{\partial h}{\partial r}v_r|_{z=h/2}&=-\frac{1}{2}\frac{\partial h}{\partial r}\left\{\frac{1}{2}\frac{\partial P_c}{\partial r}\left[z^2-\left(\frac{h}{2}\right)^2\right]\Big|_{z=h/2}+U_t\right\}\\&=-\frac{1}{2}\frac{\partial h}{\partial r}\left\{\frac{1}{2}\frac{\partial P_c}{\partial r}\left[\left(\frac{h}{2}\right)^2-\left(\frac{h}{2}\right)^2\right]+U_t\right\}=-\frac{1}{2}\frac{\partial h}{\partial r}U_t\end{aligned} \quad \text{(A.122)}$$

Implementing Eqs. (A.121) and (A.122) to the first two terms in the right-hand side of Eq. (A.113) gives the kinematic condition as

$$\begin{aligned}\frac{1}{2}\frac{\partial h}{\partial t}=\frac{2}{3}\frac{1}{r}\frac{\partial}{\partial r}\left[\frac{r}{2}\frac{\partial P_c}{\partial r}\left(\frac{h}{2}\right)^3\right]-\frac{1}{r}\frac{\partial}{\partial r}(rU_t)\left(\frac{h}{2}\right)-\frac{1}{2}\frac{\partial h}{\partial r}U_t\\+\frac{1}{Pe}\frac{1}{\left(1-\omega_{A,c}|_{z=h/2}\right)}\frac{\partial\omega_{A,c}}{\partial z}\Big|_{z=h/2}\end{aligned} \quad \text{(A.123)}$$

The second and the third terms in the right-hand side of Eq. (A.123) are merged into $-\frac{1}{2r}\frac{\partial}{\partial r}(rU_th)$ by following the partial derivative rule. With some rearrangements of the first term in the right-hand side of Eq. (A.123), the thinning equation is obtained as in Eq. (101):

$$\frac{\partial h}{\partial t}=\frac{1}{12}\frac{1}{r}\frac{\partial}{\partial r}\left[r\frac{\partial P_c}{\partial r}h^3\right]-\frac{1}{r}\frac{\partial}{\partial r}(rU_th)+M \quad \text{(A.124)}$$

where M describes the interfacial displacement rate due to mass transfer, specified in Eq. (118):

$$M=\frac{2}{Pe}\frac{1}{(1-K')}\frac{\partial\omega_{A,c}}{\partial z}\Big|_{z=h/2} \quad \text{(A.125)}$$

A.12 Derivation of the Component Mass Balance for Low Pe Case

All equations in this section are expressed in dimensionless variable. In the limit of low Pe, the left-hand side of Eq. (68) disappears due to negligible convective mass rates, yielding Eq. (119) as

$$0 = \frac{1}{Pe}\frac{\partial^2 \omega_{A,c}}{\partial z^2} + Q \tag{A.126}$$

The dimensionless reaction term Q is specified in Table 1 which is also described as a function of $\bar{t}$ as Eq. (69):

$$Q = \frac{R_p \mu_c}{\sigma \epsilon^2}\frac{r_A}{\rho_c} = \bar{t}\frac{r_A}{\rho_c} \tag{A.127}$$

The two boundary conditions are taken from Eq. (117):

$$\left.\frac{\partial \omega_{A,c}}{\partial z}\right|_{z=0} = 0 \qquad\qquad \omega_{A,c}\big|_{z=h/2} = \frac{k_H P_{A,d}}{\rho_c} = K' \tag{A.128}$$

Analytical Solution for Zero-order Reactions

The zero-order reactions consider the consumption rate r_A to be independent on $\omega_{A,c}$, which gives constant Q. The first and the second integrations of Eq. (A.126) with respect to z yields the concentration gradient and the mass fraction profiles, respectively, as:

$$\frac{\partial \omega_{A,c}}{\partial z} = -\left(PeQ \right) z + C_1 \tag{A.129}$$

$$\omega_{A,c} = -\frac{1}{2}\left(PeQ \right) z^2 + C_1 z + C_2 \tag{A.130}$$

By substituting the first boundary condition in Eq. (A.128) to Eq. (A.129), the constant C_1 is obtained as

$$\begin{aligned} \left.\frac{\partial \omega_{A,c}}{\partial z}\right|_{z=0} &= -\left(PeQ \right) z\big|_{z=0} + C_1 \\ &= C_1 = 0 \end{aligned} \tag{A.131}$$

Then, C_1 and the second boundary condition in Eqs. (A.131) and (A.128) are applied to Eq. (A.130) to determine C_2 as

$$\begin{aligned} C_2 &= \omega_{A,c}\big|_{z=h/2} + \frac{1}{2}\left(PeQ \right) z^2\Big|_{z=h/2} \\ &= K' + \frac{1}{2}\left(PeQ \right)\left(\frac{h}{2} \right)^2 \end{aligned} \tag{A.132}$$

The substitution of Eqs. (A.131) and (A.132) to Eqs. (A.129) and (A.130) results in the concentration gradient profile as

$$\frac{\partial \omega_{A,c}}{\partial z} = -\left(PeQ \right) z \tag{A.133}$$

and the mass fraction profiles as

$$\begin{aligned} \omega_{A,c} &= -\frac{1}{2}\left(PeQ \right) z^2 + K' + \frac{1}{2}\left(PeQ \right)\left(\frac{h}{2} \right)^2 \\ &= -\frac{1}{2}\left(PeQ \right)\left[z^2 - \left(\frac{h}{2} \right)^2 \right] + K' \end{aligned} \tag{A.134}$$

Finally, M for the zero-order reaction is obtained by evaluating Eq. (A.133) at the interface position $z = h/2$:

$$\left.\frac{\partial \omega_{A,c}}{\partial z}\right|_{z=h/2} = -\left(PeQ \right)\frac{h}{2} \tag{A.135}$$

and substituting Eq. (A.135) to Eq. (A.125) to yield the same formula as Eq. (121):

$$M = \frac{2}{Pe}\frac{1}{(1-K')}\left[-\left(PeQ \right)\frac{h}{2} \right] = -\frac{Qh}{(1-K')} \tag{A.136}$$

Analytical Solution for First-order Reactions

The first-order reactions indicate a linear relationship between r_A and $\omega_{A,c}$ as

$$r_A = k_1 \rho_{A,c} = k_1 \omega_{A,c} \rho_c \tag{A.137}$$

Here, $\rho_{A,c}$ and k_1 respectively stand for the mass concentration of A in the continuous phase and the reaction rate constant for first-order kinetics. In this case, the mass balance in Eq. (A.126) is solved by applying Q and r_A in Eqs. (A.127) and (A.137) to yield

$$\begin{aligned} 0 &= \frac{1}{Pe}\frac{\partial^2 \omega_{A,c}}{\partial z^2} + \bar{t}\frac{R_A}{\rho_c} \\ &= \frac{1}{Pe}\frac{\partial^2 \omega_{A,c}}{\partial z^2} + \bar{t}\frac{k_1 \omega_{A,c} \rho_c}{\rho_c} = \frac{1}{Pe}\frac{\partial^2 \omega_{A,c}}{\partial z^2} + \bar{t} k_1 \omega_{A,c} \end{aligned} \tag{A.138}$$

The analytical solution of the second-order homogeneous linear differential equation suggests the reformulation of Eq. (A.138) into its characteristic polynomial form:

$$0 = \frac{1}{Pe} D^2 + \bar{t} k_1 \tag{A.139}$$

Here, D denotes the differential operator with an order of 2, i.e., there are two solutions for D:

$$D = \pm\sqrt{-\bar{t} k_1 Pe} \tag{A.140}$$

The solution for $\omega_{A,c}$ is obtained with two unknown constants, C_1 and C_2:

$$\omega_{A,c} = C_1 e^{\sqrt{-\bar{t} k_1 Pe}\, z} + C_2 e^{-\sqrt{-\bar{t} k_1 Pe}\, z} \tag{A.141}$$

The first derivative of Eq. (A.141) is evaluated at $z = 0$ by implementing the first boundary condition of Eq. (A.128) to yield

$$\frac{\partial \omega_{A,c}}{\partial z} = \sqrt{-\bar{t}k_1 Pe}\, C_1 e^{\sqrt{-\bar{t}k_1 Pe}\, z} - \sqrt{-\bar{t}k_1 Pe}\, C_2 e^{-\sqrt{-\bar{t}k_1 Pe}\, z} \tag{A.142}$$

$$\begin{aligned}\left.\frac{\partial \omega_{A,c}}{\partial z}\right|_{z=0} &= \left.\sqrt{-\bar{t}k_1 Pe}\, C_1 e^{\sqrt{-\bar{t}k_1 Pe}\, z}\right|_{z=0} - \left.\sqrt{-\bar{t}k_1 Pe}\, C_2 e^{-\sqrt{-\bar{t}k_1 Pe}\, z}\right|_{z=0} \\ &= \sqrt{-\bar{t}k_1 Pe}\, C_1 - \sqrt{-\bar{t}k_1 Pe}\, C_2 \\ &= \sqrt{-\bar{t}k_1 Pe}\,\left(C_1 - C_2 \right) = 0 \end{aligned} \tag{A.143}$$

Equation (A.143) implies that $C_1 = C_2$, thus, applying the second boundary condition in Eq. (A.128) gives

$$\begin{aligned}\left.\omega_{A,c}\right|_{z=h/2} &= \left. C_1 e^{\sqrt{-\bar{t}k_1 Pe}\, z}\right|_{z=h/2} + \left. C_1 e^{-\sqrt{-\bar{t}k_1 Pe}\, z}\right|_{z=h/2} \\ &= C_1 \left[e^{\sqrt{-\bar{t}k_1 Pe}\frac{h}{2}} + e^{-\sqrt{-\bar{t}k_1 Pe}\frac{h}{2}} \right] = K' \end{aligned} \tag{A.144}$$

and determines C_1 and C_2 as

$$C_1 = C_2 = \frac{K'}{e^{\sqrt{-\bar{t}k_1 Pe}\frac{h}{2}} + e^{-\sqrt{-\bar{t}k_1 Pe}\frac{h}{2}}} \tag{A.145}$$

Implementing Eq. (A.145) to Eqs. (A.141) and (A.142) results in the mass fraction and the concentration gradient profiles respectively:

$$\omega_{A,c} = \frac{K'}{e^{\sqrt{-\bar{t}k_1 Pe}\frac{h}{2}} + e^{-\sqrt{-\bar{t}k_1 Pe}\frac{h}{2}}} \left[e^{\sqrt{-\bar{t}k_1 Pe}\, z} + e^{-\sqrt{-\bar{t}k_1 Pe}\, z} \right] \tag{A.146}$$

$$\begin{aligned}\frac{\partial \omega_{A,c}}{\partial z} &= \frac{K'}{e^{\sqrt{-\bar{t}k_1 Pe}\frac{h}{2}} + e^{-\sqrt{-\bar{t}k_1 Pe}\frac{h}{2}}} \left[\sqrt{-\bar{t}k_1 Pe}\, e^{\sqrt{-\bar{t}k_1 Pe}\, z} - \sqrt{-\bar{t}k_1 Pe}\, e^{-\sqrt{-\bar{t}k_1 Pe}\, z} \right] \\ &= \frac{K'\sqrt{-\bar{t}k_1 Pe}}{e^{\sqrt{-\bar{t}k_1 Pe}\frac{h}{2}} + e^{-\sqrt{-\bar{t}k_1 Pe}\frac{h}{2}}} \left[e^{\sqrt{-\bar{t}k_1 Pe}\, z} - e^{-\sqrt{-\bar{t}k_1 Pe}\, z} \right] \end{aligned} \tag{A.147}$$

Then, the concentration gradient in Eq. (A.147) is evaluated at the interface position $z = h/2$ and applied to Eq. (A.125) to determine M for the first-order reactions:

$$\begin{aligned} M &= \frac{2}{Pe}\frac{1}{(1-K')} \left\{ \frac{K'\sqrt{-\bar{t}k_1 Pe}}{e^{\sqrt{-\bar{t}k_1 Pe}\frac{h}{2}} + e^{-\sqrt{-\bar{t}k_1 Pe}\frac{h}{2}}} \left[e^{\sqrt{-\bar{t}k_1 Pe}\frac{h}{2}} - e^{-\sqrt{-\bar{t}k_1 Pe}\frac{h}{2}} \right] \right\} \\ &= 2\frac{\sqrt{-\bar{t}k_1 Pe}}{Pe}\frac{K'}{(1-K')}\frac{e^{\sqrt{-\bar{t}k_1 Pe}\frac{h}{2}} - e^{-\sqrt{-\bar{t}k_1 Pe}\frac{h}{2}}}{e^{\sqrt{-\bar{t}k_1 Pe}\frac{h}{2}} + e^{-\sqrt{-\bar{t}k_1 Pe}\frac{h}{2}}} \end{aligned} \tag{A.148}$$

Appendix B: Parameter Estimation

B.1 Physical Properties and Parameter Conditions

Table B.1: Physical properties for 1 mm O_2 bubbles in water and parameter conditions for typical bioreactor systems

Parameters	Unit	Values	References
Chemical and physical properties			
k_H	kg/m^3.atm	10^{-2}	(Doran, 2013; Sander, 2015)
ρ_c	kg/m^3	10^3	
μ_c	kg/m.s	10^{-3}	
R_p	m	5 x 10^{-4}	
σ	kg/s^2	72.8 x 10^{-3}	
k_0	mol/L.s	10^{-6}	(Doran, 2013; Gomez et al., 2006)
k_1	1/s	10^{-5}	(Lainioti & Karaiskakis, 2013)
D_{AB}	m^2/s	10^{-9}	(Doran, 2013; Gomez et al., 2006)
Operating parameters			
$P_{A,d}$	atm	1 - 15	(Lopes et al., 2014)

B.2 Estimation of M for CO_2 Bubbles

The estimation of M for CO_2 bubbles is made by calculating the mass flux, $N|_{z=h/2}$, of a 1 mm CO_2 bubble according to Li et al. (2019) using their Eq. (3.2):

$$N|_{z=h/2} = 4\,x\,10^{-8}\left(2R_p\right)^{-0.947} = 4\,x\,10^{-8}(0.1)^{-0.947} = 3.5\,x\,10^{-7}\ \mathrm{g/cm^2.s} \tag{B.1}$$

with R_p is in cm and $N|_{z=h/2}$ is in g/cm^2.s.

The mass flux is assigned to Eq. (29) as

$$N|_{z=h/2} = -\rho\mathbf{u}_{mt}\cdot\mathbf{n} = -\rho_c(\mathbf{u}-\mathbf{v}_c)\cdot\mathbf{n} = -3.5\,x\,10^{-6}\ \mathrm{kg/m^2.s} \tag{B.2}$$

with the negative sign indicating the mass transfer from the dispersed to the continuous phase. The dot product results in the normal bulk velocity, $v_{c,n}$, and the normal interface velocity, $U_n = \frac{1}{2}\frac{\partial h}{\partial t}$ (Johns and Narayanan, 2007; Ozan and Jakobsen, 2019b), which rearranges Eq. (B.2) into

$$U_n = v_{c,n} + \frac{3.5\,x\,10^{-6}\ \mathrm{kg/m^2.s}}{\rho_c} = \frac{1}{2}\frac{\partial h}{\partial t} \tag{B.3}$$

The non-dimensionalization of Eq. (B.3) gives

$$\frac{\partial \tilde{h}}{\partial \tilde{t}} = 2\tilde{v}_{c,n} + 2\,\frac{3.5\,x\,10^{-6}\ \mathrm{kg/m^2.s}}{\bar{v}_z\rho_c} = 2\tilde{v}_{c,n} + M \tag{B.4}$$

Therefore, M can be determined as

$$M = 2\,\frac{3.5\,x\,10^{-6}\ \mathrm{kg/m^2.s}}{\bar{v}_z\rho_c} \tag{B.5}$$

The velocity scale $\bar{v}_z$ is determined from Eq. (91):

$$\bar{v}_z = \frac{\sigma_0}{\mu_c}\epsilon^4 = 72.8\,\epsilon^4\ \mathrm{m/s} \tag{B.6}$$

By assuming $0.01 < \epsilon < 0.1$ as in App. B.1, $\bar{v}_z$ is estimated to range from $7.28\,x\,10^{-7} - 7.28\,x\,10^{-3}$ m/s. Substituting these values to Eq. (B.5) gives an estimation on the magnitude of M to be on the order of $10^{-6} - 10^{-2}$.

Appendix C: Analysis of Numerical Issues

In this section, the numerical issues encountered in the two-step solver (the 2D solver) is discussed.

C.1 Initial Attempts to Resolve the Inconsistencies in the Solver

During the initial trials of the (the 2D solver), the estimated coalescence time, t_c, for different K' are presented in Figure C.1.

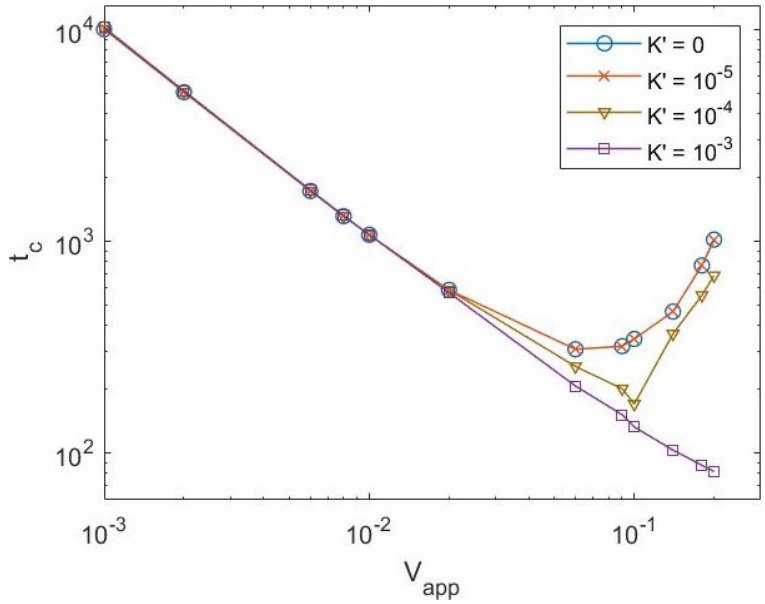

Figure C.1: The first trial of estimating t_c for 2D case

It can be seen that the t_c curves do not follow the expected behavior, represented by $K' = 0$. The t_c curve for $K' = 10^{-4}$ turns up sharply at $V_{app} = 0.1$ while the one for $K' = 10^{-3}$ keeps decreasing with V_{app}. This may indicate some inaccuracies occurred during the numerical computation, which can be detected from the minimum film thickness $\min(h)$ plot as shown in Figure C.2. This plot is expected to behave like the no-flux case ($K' = 0$), represented by the blue curve, which decreases smoothly along the time. In addition, all curves should reach approximately the same critical minimum thickness for the same V_{app} regardless of K' values. Here, the critical minimum thickness is defined as the minimum thickness at which the attractive van der Waals forces start to act significantly, giving a fast decreasing trend on the $\min(h)$ values before coalescence is estimated to occur. Figure C.2 shows that the $\min(h)$ plots for $K' = 10^{-4}$ and $K' = 10^{-3}$ with $\Delta t = 0.05$ drop sharply at earlier critical thickness. These unexpected behaviors may occur due to the unsuitable parameter settings, for example, the solver may require smaller Δt to compute more accurately.

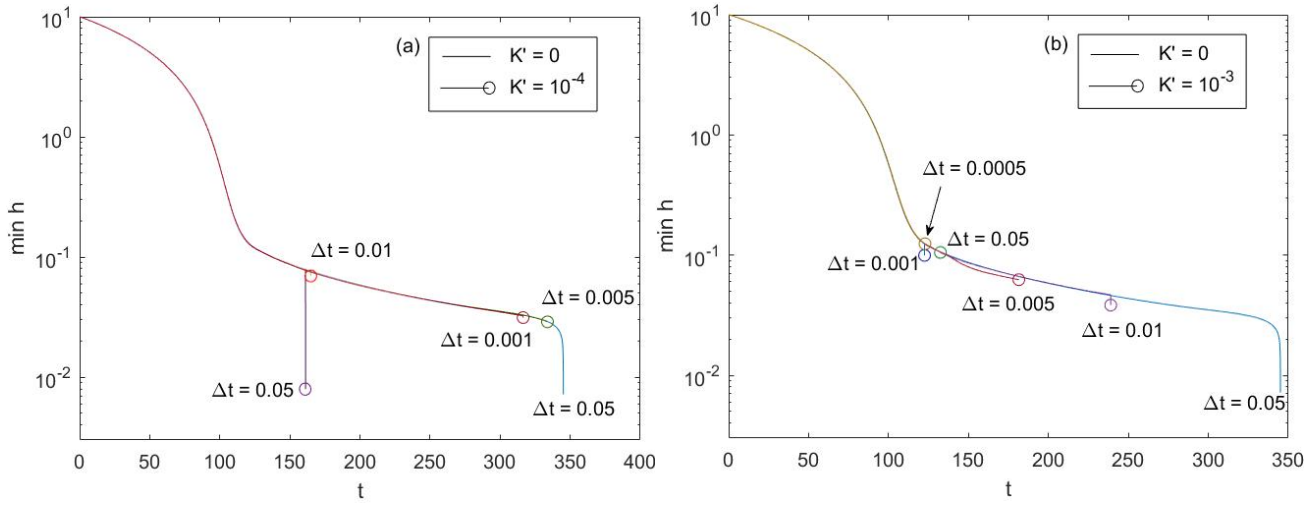

Figure C.2: The time evolution of the minimum film thickness evaluated at different Δt values for (a) $K' = 10^{-4}$ at $V_{app} = 0.1$ and (b) $K' = 10^{-3}$ at $V_{app} = 0.1$ with the blue curve representing the expected behavior which is obtained for $K' = 0$

By verifying the behavior of $\min(h)$ for other Δt values and comparing the results with the one for the no-flux case, it is shown in Figure C.2 (a) that $\min(h)$ drops unexpectedly at $\min(h) \approx 0.1$ even when Δt is set to $\Delta t = 0.01$. In comparison, the results for $\Delta t = 0.005$ and $\Delta t = 0.001$ seem to give relatively smoother trends until $\min(h) \approx 0.03$, which is close enough tothe critical minimum thickness of the no-flux case. Therefore, $\Delta t = 0.005$ is taken to estimate t_c in this case. However, setting Δt into smaller values may not always result in more accurate solutions as it is found in Figure C.2 (b) that the two smallest Δt, at 0.001 and 0.0005, give a sudden decrease earlier than the larger Δt values. Furthermore, the results in Figure C.3 indicates that there are still some numerical issues although the parameter Δt has been adjusted.

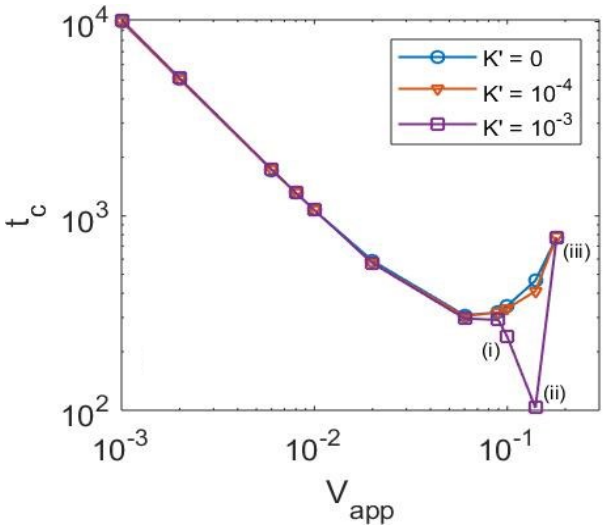

Figure C.3: Coalescence time with adjusted Δt

Compared to Figure C.1, the results in Figure C.3 seem more reasonable except for the three cases (i)-(iii). In case (iii), all K' values result in similar t_c which seems to be unreasonable for the curves to merge once again after they separate at around their minimum t_c. In these cases, it is found that the interface deforms wider than 50% of r_∞, which indicates that the gentle collision assumption does not hold for $V_{app} = 0.18$, thus, case (iii) is excluded from this study.

Cases (i) and (ii) seem to correspond to Figure C.2 (b), where all Δt values are unable to satisfy the two requirements for accurate t_c estimate, which are a smooth trend of $\min(h)$ and a similar critical minimum thickness as the no-flux case. Therefore, the two cases need to be investigated further by evaluating the number of grids for z and the M criterion as presented in Figure C.4.

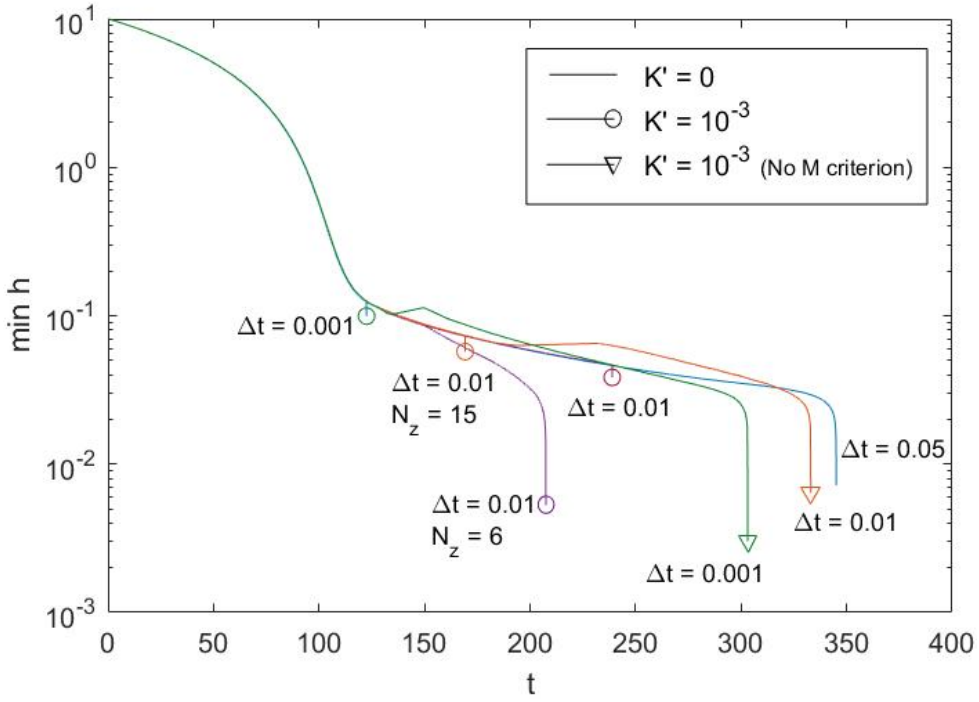

Figure C.4: The time evolution of the minimum thickness evaluated at different N_z values and re-consideration of M criterion for $K' = 10^{-3}$ at $V_{app} = 0.1$ with the blue curve representing the expected behavior which is obtained for $K' = 0$

At this stage, the simulation is run for 11 grid points of z domain, i.e., $N_z = 10$. Although the resulting surface profiles in Figure 16 look smooth enough to indicate that $N_z = 10$ is sufficient, the two cases, (i) and (ii), in Figure C.3 are re-evaluated at different N_z values. As shown in Figure C.4, $\min(h)$ for $N_z = 15$ falls even earlier than the one for $N_z = 10$, which implies that higher N_z does not always result in more accurate estimation of t_c. On the other hand, the decreasing $\min(h)$ for $N_z = 6$ looks smoother with unreasonably faster t_c as plotted in Figure C.3. This indicates that N_z might be not the source of the problems, leading to the

next attempt which is to exclude the M criterion from the code. Although this criterion was originally created due to the negative M values appearing to be unexpected direction of the mass transfer, they are physically acceptable to occur at high V_{app} since the emergence of the dimple may change the behavior of M. The results for no M criterion in Figure C.4 show smoother trend of $\min(h)$ where the critical minimum thickness is approximately the same as the no-flux case. This implies that the current M criterion might result in further instabilities in the solver, which therefore, needs to be excluded for cases (i) and (ii). By taking $\Delta t = 0.001$ and excluding M criterion, the updated results are shown in Figure C.5.

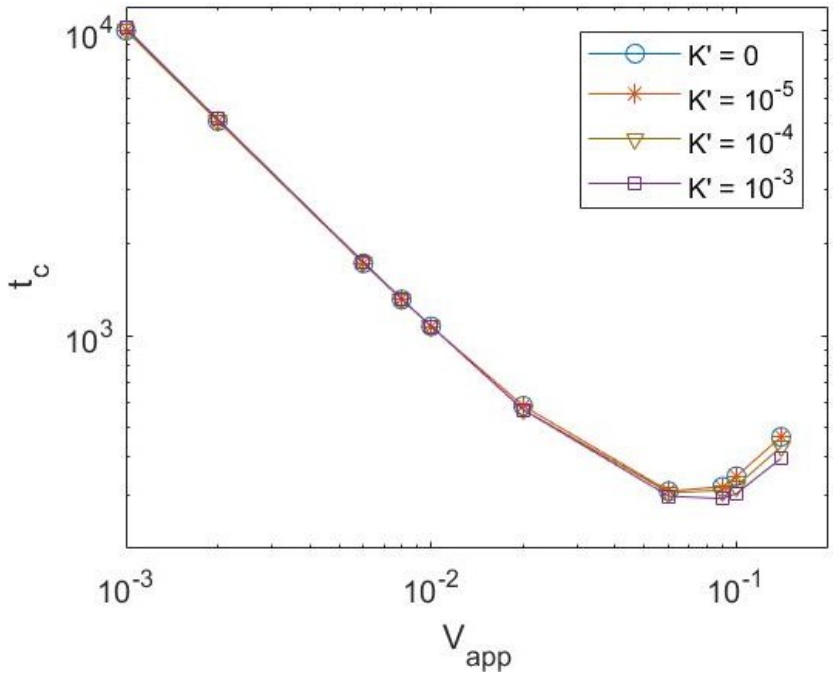

Figure C.5: Corrected t_c after re-evaluation of parameter settings and re-consideration of M criterion

Although Figure C.5 seems to be the most reliable results compared to the previous plots in Figure C.1 and Figure C.3, there are some other numerical issues detected in Figure C.6 and Figure C.7 for immobile and mobile cases, respectively, which are discussed in Section 4.1.3.2 as incorrect results.

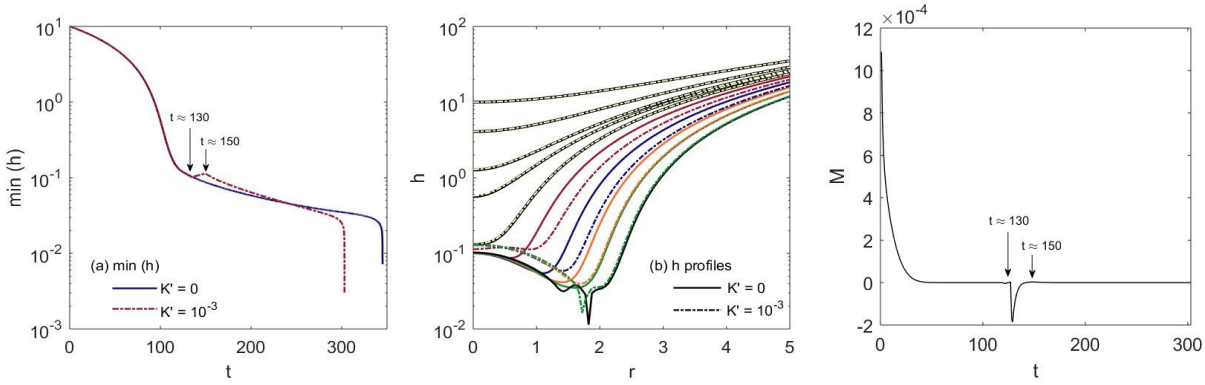

Figure C.6: Incorrect results for the immobile case due to numerical issues showing some increases in min(h) at the same time as the instabilities in M

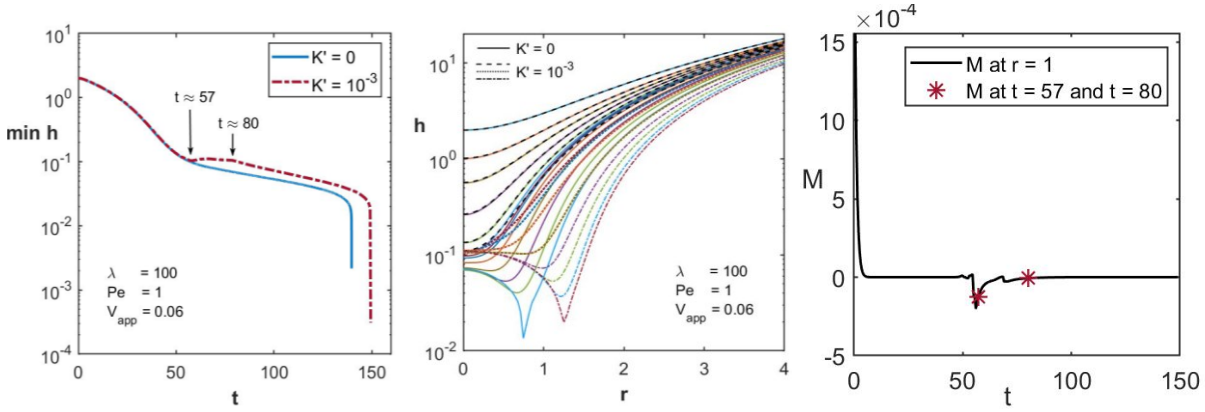

Figure C.7: Incorrect results for the mobile case due to numerical issues showing some increases in min(h) at the same time as the instabilities in M

C.2 Analysis of v_z Computation as the Main Source of the Issues

The analytical solution to v_z is expressed in Eq. (100) as

$$\tilde{v}_z = -\frac{1}{3}\frac{1}{\tilde{r}}\frac{\partial}{\partial\tilde{r}}\left(\frac{\tilde{r}}{2}\frac{\partial\tilde{P}}{\partial\tilde{r}}\right)\tilde{z}^3 - \frac{1}{\tilde{r}}\frac{\partial}{\partial\tilde{r}}\left(\tilde{r}\tilde{U}_t\right)\tilde{z} + \frac{1}{\tilde{r}}\frac{\partial}{\partial\tilde{r}}\left[\frac{\tilde{r}}{2}\frac{\partial\tilde{P}}{\partial\tilde{r}}\left(\frac{\tilde{h}}{2}\right)^2\right]\tilde{z} \tag{C.1}$$

The connection between v_z computation and the time evolution of M is analyzed by neglecting term by term of Eq. (C.1). It is found that the unexpected behavior of M dissapears when the second derivative of the pressure in the first term of Eq. (C.1) is neglected. This can be shown by expanding the first term into

$$1^{st}\ term = -\frac{1}{3}\frac{1}{\tilde{r}}\frac{\partial}{\partial\tilde{r}}\left(\frac{\tilde{r}}{2}\frac{\partial\tilde{P}}{\partial\tilde{r}}\right)\tilde{z}^3 = -\left\{\frac{1}{6}\frac{\partial^2\tilde{P}}{\partial\tilde{r}^2} + \frac{1}{6}\frac{1}{\tilde{r}}\frac{\partial\tilde{P}}{\partial\tilde{r}}\right\}\tilde{z}^3 \tag{C.2}$$

Then, the second derivative term in Eq. (C.2) is excluded to yield

$$\tilde{v}_z{}' = -\frac{1}{6}\frac{\partial^2\tilde{P}}{\partial\tilde{r}^2}\tilde{z}^3 - \frac{1}{\tilde{r}}\frac{\partial}{\partial\tilde{r}}\left(\tilde{r}\tilde{U}_t\right)\tilde{z} + \frac{1}{\tilde{r}}\frac{\partial}{\partial\tilde{r}}\left[\frac{\tilde{r}}{2}\frac{\partial\tilde{P}}{\partial\tilde{r}}\left(\frac{\tilde{h}}{2}\right)^2\right]\tilde{z} \tag{C.3}$$

The results given in Figure C.8 show that the discontinuities in case (a) dissappear when the second derivative of the first term in Eq. (C.1) is neglected. However, Figure C.9 and Figure C.10 indicate that the second derivative is important in determining the behavior, thus, cannot be neglected in this case.

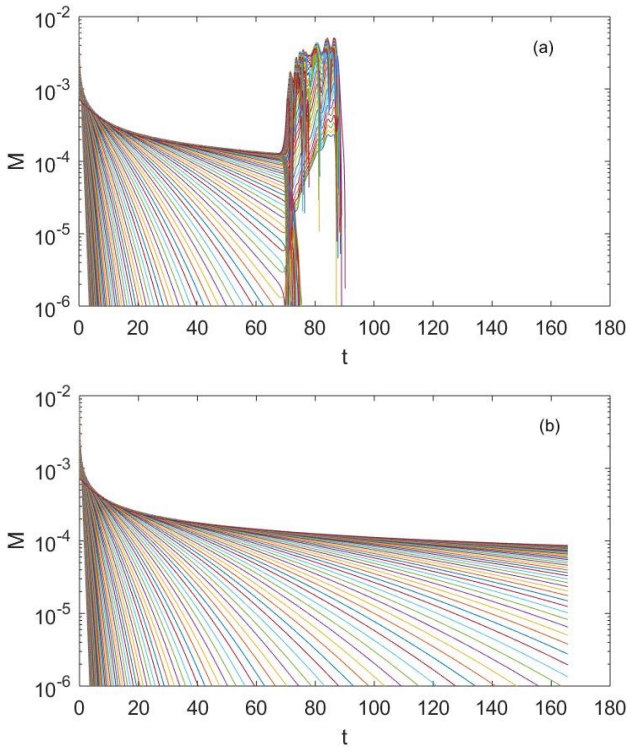

Figure C.8: (a) Unexpected behavior of M due to numerical issues in v_z computation and (b) the expected behavior of M obtained by neglecting the second derivative of the first term in v_z

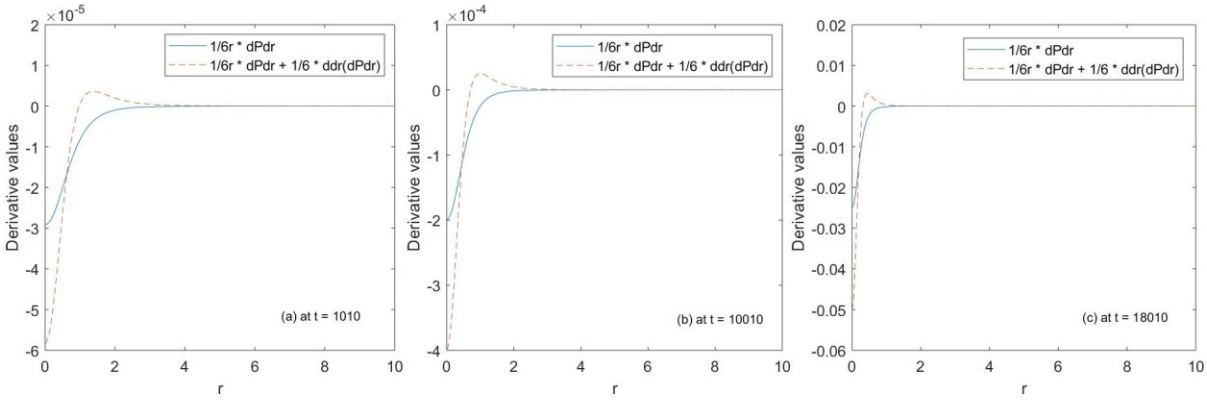

Figure C.9: Significance of the second derivative term of v_z in the nose rupture regime

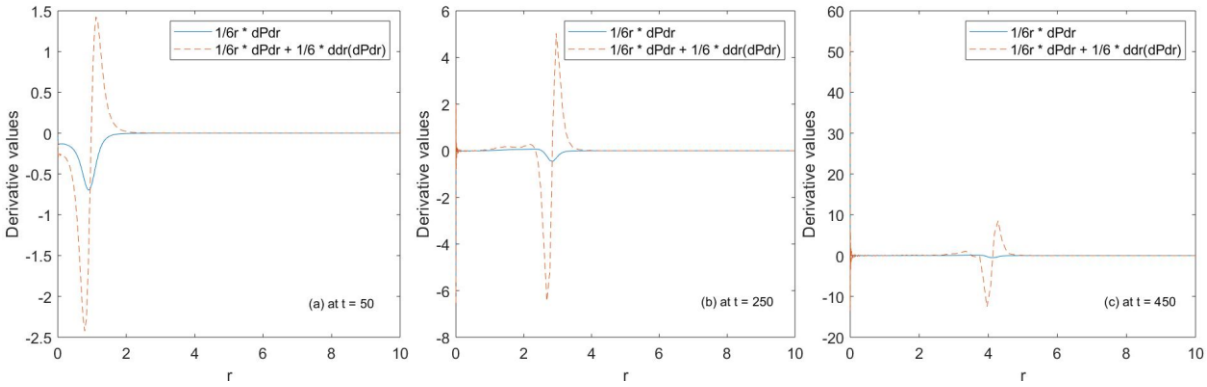

Figure C.10: Significance of the second derivative term of v_z in the rim rupture regime

Appendix D: Estimation of M Expression

D.1 Expression of $M(h)$ for Some r Values

The M expression is estimated by approximating the relationship between M and h for fixed r positions through the linear regression as shown in Figure D.1 which yields the constants a and b for the corresponding r as Table D.1.

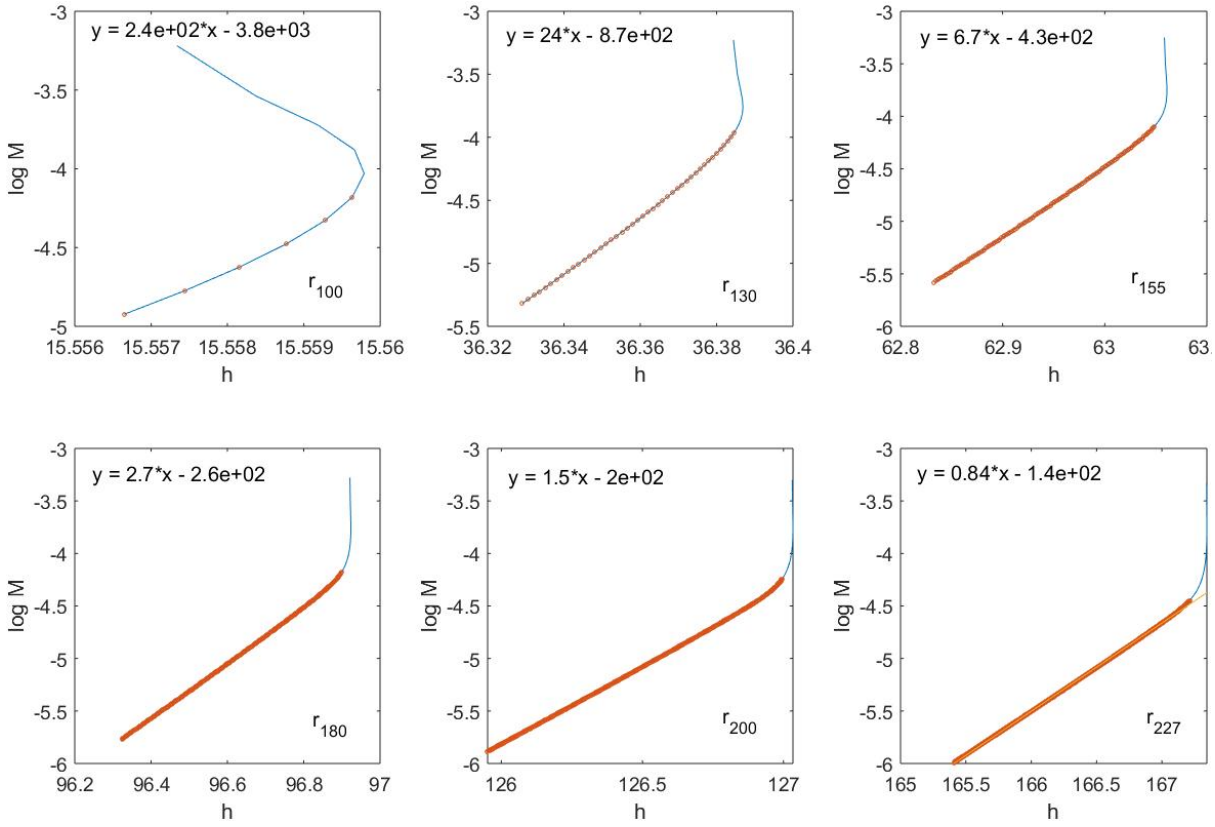

Figure D.1: Linear regression of log (M) and h for fixed r values

Table D.1: The constants a and b obtained from the linear regression of log (M) and h for fixed r values

r_pos	r	y	=	a	x	+	b
105	4.0253	log M	=	150	h	-	2700
110	4.3779	log M	=	95	h	-	2000
130	5.8639	log M	=	24	h	-	870
155	7.8141	log M	=	6.7	h	-	430
180	9.7428	log M	=	2.7	h	-	260
200	11.1818	log M	=	1.5	h	-	200
227	12.8585	log M	=	0.84	h	-	140
250	13.9556	log M	=	0.61	h	-	120
280	14.8194	log M	=	0.48	h	-	110
301	15	log M	=	0.46	h	-	110

D.2 Estimation of $M(h, r)$

The resulting constants a and b are plotted against r to determine their relationships in Figure D.2.

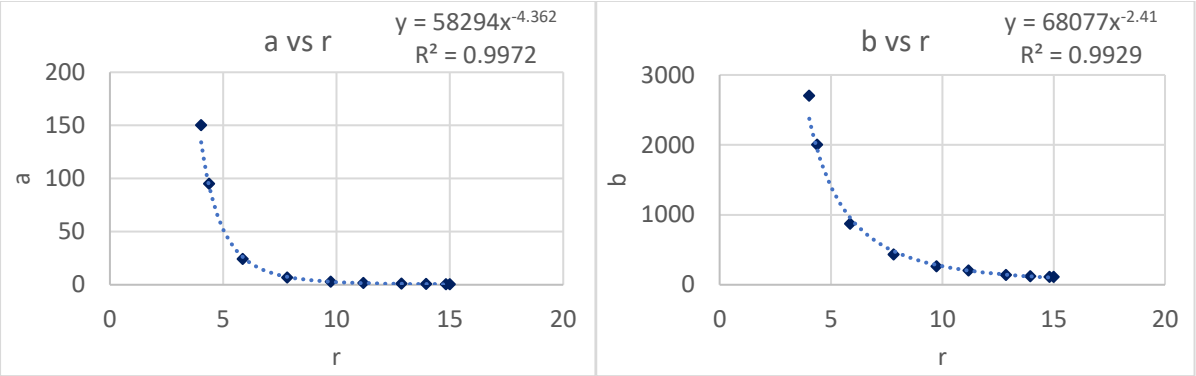

Figure D.2: Estimation of the constants a and b as functions of r, obtained from power regression

Finally, the value of M can be estimated as a function of h and r as

$$\log M = 58290\, r^{-4.362} h - 68100\, r^{-2.4} \tag{D.1}$$

Appendix E: MATLAB Codes

The parameters involved in the MATLAB codes are defined using different notations from the main report in Section 3 with the corresponding notations shown in Table E.1.

Table E.1: Notations defined in the main report and in the MATLAB code

Parameters	Notation	
	Main report	MATLAB
The lower limit of r domain at $r = 0$	r_0	`L`
The upper limit of r domain at $r = r_\infty$	r_∞	`R`
Number of grids for r	N_r	`N`
Number of grids for z	N_z	`M`
Time step	Δt	`dt`
Differentiation matrix for r	$D_{r,ij}$	`D`
Differentiation matrix for z evaluated at $r = r_i$	$D_{z,mn}\big\|_{r=r_i}$	`Dz`
Relative approach velocity	V_{app}	`vapp`
Solubility of the gas	K'	`Kp`
Dimensionless Hamaker constant	A^*	`A_star`
Viscosity ratio	λ^*	`lambda`
Surface Peclet number	Pe_s	`Pe_s`
Dependence	σ'_Γ	`sigma`
Product of dependence and initial surface excess concentration	$\sigma'_\Gamma \Gamma_0$	`sigma_times_Gamma00`
The i^{th} element of the film thickness at the $(k-1)^{th}$ time step	h_i^{k-1}	`hkm1`
The i^{th} element of the film thickness at the k^{th} time step	h_i^k	`hk`
The i^{th} element of the film thickness at the $(k+1)^{th}$ time step	h_i^{k+1}	`Hkp1`
The i^{th} element of the excess pressure at the $(k-1)^{th}$ time step	P_i^{k-1}	`Pkm1`

Parameters	Notation	
	Main report	MATLAB
The i^{th} element of the excess pressure at the k^{th} time step	P_i^k	`Pk`
The i^{th} element of the excess pressure at the $(k+1)^{th}$ time step	P_i^{k+1}	`Pkp1`
The i^{th} element of the tangential velocity at the k^{th} time step	U_i^k	`Uk`
The i^{th} element of the tangential velocity at the $(k+1)^{th}$ time step	U_i^{k+1}	`Ukp1`
The i^{th} element of the surfaces excess concentration at the $(k-1)^{th}$ time step	Γ_i^{k-1}	`Gammakm1`
The i^{th} element of the surface excess concentration at the k^{th} time step	Γ_i^k	`Gammak`
The i^{th} element of the surface excess concentration at the $(k+1)^{th}$ time step	Γ_i^{k+1}	`Gammakp1`
The m^{th} element of the mass fraction at the k^{th} time step at the position of $r = r_i$	$\omega_m^k\|_{r=r_i}$	`wk`
The m^{th} element of the mass fraction at the $(k+1)^{th}$ time step at the position of $r = r_i$	$\omega_m^{k+1}\|_{r=r_i}$	`wkp1`
The i^{th} element of the rate of interface displacement due to mass transfer	M_i	`MT`
An array with a value of zero in all elements	$[0\ 0\ 0\ \ldots 0]_{size}$	`zeros(1,size)`
An array with a value of one in all elements	$[1\ 1\ 1\ \ldots 1]_{size}$	`ones(1,size)`

E.1 The First Part of the Solver

```
%clearing previous outcomes and turning off any warnings when
running the simulation
clear all
clc
close all
warning off
load('integration_matrix_N_300') %call the integral matrix
that has been stored


%Step 1 - Specifying domain, number of grids, and time step
L = 0; R = 15;    %domain for r (r_0 and r_∞)
N = 300; M = 10; %number of grids for r (N_r) and z (N_z)
dt= 0.05;         %time step (Δt)

%Step 2 - Cheb function for discretization of r
[Dc,zc] = cheb(N);

%Step 3 - Mapping function to adjust the domain
[a,b,r] = mapping(L,R,zc);
D = a*Dc;       %differentiation matrix for r (D_r)

%Step 4a - Physical parameters
vapp   = 0.0006; %approach velocity (V_app)
Kp     = 10^-3;  %solubility (K')
Pe     = 1;      %bulk Peclet number (Pe)
A_star = 10^-4;  %Hamaker constant (A*)
lambda = 10^-4;  %viscosity ratio (λ*)
Pe_s   = 50;     %surface Peclet number (Pe_s)
sigma_times_Gamma00=-20; %merged parameter (σ'_Γ Γ_0)
sigma  = -5000; %dependence of the surface tension on the
surface excess concentration (σ'_Γ)
Gamma00= sigma_times_Gamma00/sigma;%initial surface excess
concentration (Γ_0)


%Step 4b - Initial conditions
h00    = 2; %initial minimum thickness
h0     = h00 + r.^2;
P0     = zeros(N+1,1);
w0     = zeros(N+1,M+1);
U0     = zeros(N+1,1);
Gamma0 = ones(N+1,1)*Gamma00;
t      = 0;

hkm1 = h0; hk = h0;
Pkm1 = P0; Pk = P0;
```

```
wk    = w0;
wkm1 = w0;
dwdz = zeros(N+1,1);
Uk    = U0;
Gammakm1 = Gamma0; Gammak = Gamma0;

mass_flux_zero_maker=ones(N+1,1); %an array to multiply the
computed M as a part of the new M criterion
MT = 2/Pe./(1-wk(:,end)).*dwdz; %computed M

hstore=[];Pstore=[];tstore=[];MTstore=[];Ustore=[];Gammastore=[];

%%%%%%Integration matrix calculations, called AA in the code
ep=10^-4.2;
% AA is only a function of number of grids, meaning that the
code is run for once, for the defined N (number of grids for r)
% The stored AA is then loaded at the beginning of the code

[Zcheb,rhoI] = newforBIMnonsing(r,ep);

cc = ones(N+1,1);
   cc(1)=2;
   cc(N+1)=2;

   for mm = 0:N
       for nn = 0:N
           invT(mm+1,nn+1) = 2*(-
1)^mm*cos(mm*nn*pi/N)/(N*cc(mm+1)*cc(nn+1));
       end
   end

   weights=zeros(N+1,1);
for j=1:N+1
for i=1:2:length(invT)
weights(j)=weights(j)-2*invT(i,j)/((i-1)^2-1);
end
end
weights=weights/a;
W=repmat(weights,1,N+1)';
AA=Zcheb.*W/2/pi;
%%%%%%%%%%%%%%%%%%%%%%%%%%%%%%%%%%%%%%%%%%%%%%%%%%%%%%%%%%%%

% Parts of matrix A that are independent of dt, thus, do not
need to be included in the iteration to save time
I     = eye(N+1,N+1); %Identity matrix

A11 = 3/2*I;
A14 = zeros(N+1,N+1);

A21 = 1/2*diag(1./r)*D*diag(r)*D;
A22 = I;
```

```
A23 = zeros(N+1,N+1);
A24 = zeros(N+1,N+1);

A31 = zeros(N+1,N+1);
A33 = I;
A34 = -1/lambda*sigma*AA*D;

A41 = zeros(N+1,N+1);
A42 = zeros(N+1,N+1);


freq=20; %defining frequency of saving data

%Starting the iteration
for k=2:(10^8)

    t=t+dt;

%Step 5 - Build A and RHS matrices
A12 = -dt/12*diag(1./r)*D*diag(r)*diag(hk.^3)*D;
A13 = dt*diag(1./r)*D*diag(r)*diag(hk);

A32 = 1/lambda*AA*diag(hk/2)*D;

A43 = dt*Pe_s*diag(1./r)*D*diag(r)*diag(Gammak);
A44 = 3/2*I*Pe_s-dt*diag(1./r)*D*diag(r)*D;

RHS1 = 2*hk-hkm1/2+dt*MT;       %Including M to the model
RHS2 = 2*ones(N+1,1)+A_star./(hk.^3);
RHS3 = zeros(N+1,1);
RHS4 = 2*Pe_s*Gammak - 1/2*Pe_s*Gammakm1;

A = [A11 A12 A13 A14; A21 A22 A23 A24; A31 A32 A33 A34; A41
A42 A43 A44];
RHS = [RHS1; RHS2; RHS3; RHS4];

%Step 6 - BCs
A(1,:) = [ D(1,:) zeros(1,3*(N+1))];
RHS(1) = 0; %dhdr=0 at r=0

A(N+1,:) = [zeros(1,N) 1 zeros(1,3*(N+1))];
RHS(N+1) = ((-vapp + MT(end))*dt + 2*hk(N+1)-
1/2*hkm1(N+1))*2/3; %dh/dt=-Vapp + M at r=r_inf

A(N+2,:) = [zeros(1,N+1) D(1,:) zeros(1,2*(N+1))];
RHS(N+2) = 0; %dPdr=0 at r=0

A(2*(N+1), :) = [zeros(1,N+1) zeros(1,N) 1 zeros(1,2*(N+1))];
RHS(2*(N+1)) = 0; %P=0 at r=r_inf
```

```
A(2*(N+1)+1,:)= [zeros(1,2*(N+1)) 1 zeros(1,N) zeros(1,N+1)];
RHS(2*(N+1)+1) = 0; %U=0 at r=0

A(3*(N+1),:)  = [zeros(1,2*(N+1)) D(end,:) zeros(1,N+1)];
RHS(3*(N+1)) = 0; %dUdr=0 at r=r_inf

A(3*(N+1)+1,:)= [zeros(1,3*(N+1)) D(1,:)]; RHS(3*(N+1)+1) = 0;
%dGammadr=0 at r=0

A(4*(N+1),:)  = [zeros(1,3*(N+1)) D(end,:)]; RHS(4*(N+1)) = 0;
%dGammadr=0 at r=r_inf


%Step 7 - solve
sol=A\RHS;

hkp1 = sol(1:N+1);
Pkp1 = sol(N+2:end);
Ukp1 = sol(2*(N+1)+1:3*(N+1));
Gammakp1 = sol(3*(N+1)+1:end);

%Calling the outcomes from the second part of the solver
[RHSw,Aw,wkp1,dwdz,dwdr,z,vr,vz,Dz] =
code_massfracH_spec(M,N,hkp1,Pkp1,wk,D,r,Kp,Pe,dt);


%Computing M for the next time step
MT = 2/Pe./(1-Kp).*dwdz;

%New M criterion
for rr2=1:N+1
    if MT(rr2) <= 10^-15
       mass_flux_zero_maker(rr2)=0;
    end
end

MT=MT.*mass_flux_zero_maker; %applying the new M criterion

%Defining the solutions as the inputs for the next time step
hkm1=hk; hk=hkp1; Pkm1=Pk; Pk=Pkp1; wk=wkp1; Uk=Ukp1;
Gammakm1=Gammak; Gammak=Gammakp1;

%Saving data
minhstore(k-1)=min(hkp1);
minh=min(minhstore);
MTmax(k-1)=max(MT);


if mod(k,freq)==2
    minh
    hstore=[hstore hkp1];
```

```
    Pstore=[Pstore Pkp1];
    tstore=[tstore t];
    MTstore=[MTstore MT];
    Ustore=[Ustore Ukp1];
    Gammastore=[Gammastore Gammakp1];
end

%Coalescence criterion with critical film thickness of 10^-3
[criterion,min_pos]=min(hkp1);
if criterion<10^-3
    if min_pos==1
        outcome=sprintf('nose rupture')
    else
        outcome=sprintf('rim rupture')
    end
    tc=t
    break
%No coalescence criterion when film thickness > 1.5 of the
initial minimum thickness
elseif criterion>1.5*h00;
    outcome=sprintf('bye')
    tc=0
    break
end
end

%Summarizing the saved data
hstore=[hstore hkp1];
    Pstore=[Pstore Pkp1];
    tstore=[tstore t];
    MTstore=[MTstore MT];
    Ustore=[Ustore Ukp1];
    Gammastore=[Gammastore Gammakp1];

%Step 8 - plotting
figure
semilogy(r,hstore)
xlabel('r')
ylabel('h')
figure
plot(r,Pstore)
xlabel('r')
ylabel('P')
figure
semilogy(r,MTstore(:,1:end-1))
xlabel('r')
ylabel('MT')
```

E.2 The Second Part of the Solver

```
%Specifying the inputs from the first part of the solver and
the outputs from this part
function [RHSw,Aw,wkp1,dwdz,dwdr,z,vr,vz,Dz] =
code_massfracH_spec(M,N,hkp1,Pkp1,wk,D,r,Kp,Pe,dt)

% Cheb function for discretization of z: only depend on M,
which in here is defined as the number of grids for z
[Dc2,zc2] = cheb(M);

% Mapping function to adjust the domain of z: for each r point
for i = 1:N+1
[az(i),bz(i),z(:,i)] = mapping(0,hkp1(i)/2,zc2);
Dz(:,:,i) = az(i)*Dc2;

% velocity profiles for each r point
dP   = D*Pkp1;
drP1 = D*(r/2.*dP);
drP2 = D*(r/2.*dP.*(hkp1/2).^2);
dwdr = D*wk;

vr(:,i) = 1/2*dP(i)*(z(:,i).^2-(ones(M+1,1)*hkp1(i)/2).^2);
end

for ii = 2:N+1
vz(:,ii) = -
1/3*(1/r(ii))*drP1(ii)*z(:,ii).^3+(1/r(ii))*drP2(ii)*z(:,ii);
end
%BC for r
vz(:,1)=vz(:,2);

%Computing the mass fraction for each r value
for n = 2:N
% A and RHS
Aw(:,:,n) = eye(M+1)*Pe+dt*Pe*diag(vz(:,n))*Dz(:,:,n)-
dt*Dz(:,:,n)^2;
RHSw(:,n) = (wk(n,:)*Pe)'-dt*Pe*vr(:,n).*(dwdr(n,:))';

% BCs for z
Aw(1,:,n) = [Dz(1,:,n)]; RHSw(1,n) = 0;
Aw(end,:,n) = [zeros(1,M) 1]; RHSw(end,n) = Kp(n);

% solve
wkp1(:,n) = Aw(:,:,n)\RHSw(:,n);

% dwdz at interface
dwdz(n,:)=Dz(end,:,n)*wkp1(:,n);

end
```

```
%Transpose the matrix before getting called to the first part
of the solver
wkp1=wkp1';

%Mass fraction criterion
for rr=1:N
    for zz=1:M+1
        if (wkp1(rr,zz))<=10^-15
            wkp1(rr,zz)=0;
%Saturation condition
        elseif abs(wkp1(rr,zz)-Kp(rr))/Kp(rr) <=10^-5
            wkp1(rr,zz)=Kp(rr);

        end

    end
end

wkp1(1,:)=wkp1(2,:); %BC at r=0, dwdr=0
wkp1(N+1,:) = wkp1(N,:); %BC at r_inf, dwdr=0

% dwdz at interface
for nn=1:N+1
dwdz(nn)=(wkp1(nn,end)-wkp1(nn,end-1))/(z(end,nn)-z(end-
1,nn));
end
dwdz=dwdz';


end
```

Hauna Fathmadinda Hosen

NTNU
Norwegian University of
Science and Technology